

**Acoustic and Thermal Characterization of  
Oil Migration, Gas Hydrates Formation and Silica Diagenesis**

Gilles Guerin

Submitted in partial fulfillment of the  
requirements for the degree  
of Doctor of Philosophy  
in the Graduate School of Arts and Sciences

COLUMBIA UNIVERSITY  
2000

© 2000  
Gilles Guerin  
All Rights Reserved

## ABSTRACT

### Acoustic and Thermal Characterization of Oil Migration, Gas Hydrates Formation and Silica Diagenesis

Gilles Guerin

This dissertation presents four processes occurring in marine sediments with distinct signatures in standard geophysical datasets. The diagenetic transformation of Opal-A to Opal-CT, the formation of gas hydrates, fluid substitution in hydrocarbon reservoirs, and fluid migrations in a fault are described with a common approach: identify the specificity of each process and reproduce their 'distinct' signature to quantify how it affects the sediments.

In Chapter 1 we describe the changes occurring when dissolved Opal-A re-precipitates into Opal-CT in siliceous sediments. This diagenetic transformation produces regional Bottom Simulating Reflectors (BSRs) in seismic surveys. We use geophysical logs to calculate the elastic moduli of sediments through a BSR offshore New Jersey. Comparison with classic consolidation models shows that the mechanical changes are controlled by a decrease in porosity following the "Gassmann" formulation.

A more common BSR is associated with the occurrence of gas hydrates and underlying free gas. In Chapter 2, logging results from the Blake Ridge show that classic models cannot describe elastic properties of hydrated sediments. The cementation theory describing interactions between grains uniformly coated by hydrates reproduces best the observations. According to this model, Gas hydrates occupy about 10% of the pore space above the BSR and coexist with free gas below.

In Chapter 3, we use various elastic models to interpret changes observed between successive 3D seismic surveys of producing reservoirs. The models are applied to the

results of reservoir simulation to translate seismic impedance differences into fluid substitution and bypassed hydrocarbon. This time-lapse methodology is applied to two reservoirs in the Gulf of Mexico.

In the last chapter, we present the thermal regime in the Eugene Island 330 oil field, within an active fault. The temperature distribution reconstructed from 600 Bottom Hole Temperatures displays  $\sim 10^{\circ}\text{C}$  anomalies overlying salt diapirs and the fault. 3D numerical modeling of heat transfers is used to estimate the contributions of the diapirs and of fluid migrations along the fault. Some of the observed anomalies could result from 5,000 years-long fluid circulations.

## CONTENTS

List of figures	vi
Acknowledgements	ix
Preface	xii
References	xvii

### **Chapter 1: Acoustic and elastic properties of calcareous sediments across a siliceous diagenetic front on the eastern U.S. continental slope**

1.1 Abstract	1
1.2 Introduction	1
1.3 Logging Results	3
1.4 Velocity-Porosity Models	5
1.4.1 Models description	5
1.4.2 Hole 902D	6
1.5 Elastic Moduli and Porosity	7
1.6 Discussion	7
1.7 Conclusion	9
References	9
Tables	11

### **Chapter 2: Characterization of *in situ* elastic properties of gas hydrate-bearing sediments on the Blake Ridge**

2.1 Abstract	17
2.2 Introduction	18

2.3 Logging data	20
2.3.1 Sonic logging	22
2.3.2 Data Interpretation	24
2.3.3 Porosity correction and gas hydrate saturation from the resistivity log	26
2.4 Elastic Moduli of Hydrate-bearing sediments	28
2.5 Methane Saturation from elastic moduli	32
2.6 Determination of the free gas concentration	35
2.7 Discussion	36
2.7.1 Quality of the logging data	36
2.7.2 Comparison of the Models	37
2.7.3 Coexistence of hydrates and free gas from logs at Site 995	38
2.7.4 Mechanisms for coexistence of hydrates and free gas	39
2.7.5 Comparison between Sites 994, 995 and 997	40
2.8 Conclusions	41
References	42
Tables	47

### **Chapter 3: Simulation of production and elastic properties of reservoirs to validate time-lapse seismics.**

3.1 Introduction	59
3.2 The 4D seismic loop	60
3.2.1 Registration and normalization of seismic datasets	60
3.2.2 Non linear inversion of successive 3D datasets	61
3.2.3 Preliminary 4D interpretation of the K8 sand	62
3.3 Elastic properties of reservoir sediments	63
3.3.1 Elastic models	63

3.3.1.1 Theoretical formulations	64
3.3.1.2 Experimental relationships	65
3.3.2 Fluid properties	66
3.3.2.1 Properties of fluid mixtures	66
3.3.2.2 Elastic properties of reservoir fluids	67
3.3.2.3 Original fluids in place	69
3.3.3 Stochastic reservoir characterization	70
3.3.4 From saturation to impedance	71
3.3.5 Comparison with vertical sweep	72
3.4 Reservoir Simulation	73
3.4.1 Permeability distribution	73
3.4.2 Multiple-phase fluid flows in porous media	74
3.4.3 Simulator description	75
3.4.4 Simulation of K8	77
3.4.4.1 Constraint on the simulation: production history analysis	77
3.4.4.2 Simulation results	78
3.4.4.2.1 History match	78
3.4.4.2.2 Fluid saturations and impedance	79
3.5 LF sand, Eugene Island 330	80
3.5.1 Geological setting and history	81
3.5.2 Preliminary 4-D impedance analysis	82
3.5.3 Reservoir characterization of LF330	82
3.5.4 Fluid properties and initial conditions	83
3.5.5 Simulation results	84
3.6 Discussion - End of the 4D loop	86
3.6.1 Discussion of the LF sand results	86
3.6.2 Closing the 4D analysis loop - optimization	87

3.7 Conclusions	90
References	92
Tables	95
Appendix: Reservoir fluid properties	96

## **Chapter 4: 3D Temperature distribution and numerical modeling of heat transfers in an active fault zone: Eugene Island 330, Offshore Louisiana.**

4.1 Abstract	125
4.2 Introduction	126
4.3 Geological Setting	127
4.4 The Temperature distribution in Eugene Island 330	129
4.4.1 Data Correction	129
4.4.2 Heat transfer in sedimentary basins	131
4.4.3 Heat sources	133
4.4.3.1 Radiogenic heat	133
4.4.3.2 Heat generation from oil maturation	133
4.4.4 The effect of sedimentation	135
4.4.5 Analysis of the present-day temperature distribution	138
4.4.6 One dimensional analysis of heat advection	139
4.5 Numerical modeling of the conductive regime	140
4.5.1 Model description	140
4.5.2 Results	142
4.6 Numerical simulation of fluid migration	143
4.6.1 Indications for fluid circulation within the Red Fault	143
4.6.2 3D Numerical simulation of the pressure and temperature	144

4.6.2.1 Numerical formulation	145
4.6.2.2 Properties at the interface	146
4.6.2.3 Sources	146
4.6.2.4 Lithology description	147
4.6.2.5 Numerical controls	147
4.6.2.6 Fault simulation	149
4.6.3 Results	150
4.6.4 Discussion	152
4.6.5 Limitations of the results	154
4.7 Conclusion	156
References	158
Tables	162

## List of figures

**Preliminary Figure:** Overview of the manifestation of the processes described in this dissertation . xviii

### Chapter 1

<b>Figure 1.1.</b> Logs measured in Hole 904A, ODP Leg 150.	12
<b>Figure 1.2.</b> Relationship between $\square$ and (a) $1/V_P$ and (b) $1/V_S$ in Hole 904A.	13
<b>Figure 1.3.</b> Elastic moduli calculated from logs in Hole 904A.	14
<b>Figure 1.4.</b> <i>In situ</i> velocity measurements in Hole 902D.	15
<b>Figure 1.5.</b> Relationships between $\square$ and $K$ and $\square\square$ in Hole 904A.	16

### Chapter 2

<b>Figure 2.1:</b> Seismic profile across the Blake Ridge along the transect of ODP Leg 164.	48
<b>Figure 2.2:</b> Location map of ODP Leg 164 and regional BSR.	49
<b>Figure 2.3:</b> Logs recorded in Hole 995B.	50
<b>Figure 2.4:</b> Shear sonic logging tool configuration and typical waveforms in Holes 995B and 997A.	52
<b>Figure 2.5:</b> Sonic waveforms recorded in Holes 995A and 997B.	53
<b>Figure 2.6:</b> Elastic moduli calculated from logs in Hole 995A.	54
<b>Figure 2.7:</b> Relationship between frame modulus and porosity in Hole 995A.	55
<b>Figure 2.8:</b> Cement and grain configurations in the cementation theory.	56
<b>Figure 2.9:</b> Estimation of gas hydrate and free gas saturations in Hole 995A from the different elastic models.	57

<b>Figure 2.10:</b> Summary of logs and methane concentrations in Hole 995A.	58
--	----

### Chapter 3

<b>Figure 3.1</b> Location map of the ST295 and EI330 oil fields, Offshore Louisiana.	100
<b>Figure 3.2</b> Structure of the K8 reservoir, South Timbalier 295.	101
<b>Figure 3.3:</b> Production history of K8.	102
<b>Figure 3.4:</b> Impedance inversion results for K8 in 1988 and 1994.	103
<b>Figure 3.5:</b> Initial pressure distribution and simulator grid in K8.	104
<b>Figure 3.6:</b> Stochastic reservoir characterization of K8.	105
<b>Figure 3.7:</b> Comparison of the petrophysic models with the 1988 impedance inversion.	106
<b>Figure 3.8:</b> Evolution of the reservoir impedance in the case of a uniform sweep.	107
<b>Figure 3.9:</b> Permeability / porosity relationship from K8 core samples.	108
<b>Figure 3.10:</b> Permeability distribution in K8.	109
<b>Figure 3.11:</b> Simulated production history match in K8.	110
<b>Figure 3.12:</b> Oil migration stream line in K8 at various dates.	111
<b>Figure 3.13:</b> Simulated pressure distribution evolution in K8.	112
<b>Figure 3.14:</b> Simulated Oil and gas saturation at the end of the simulation of K8.	113
<b>Figure 3.15:</b> Impedances calculated from the reservoir simulation results in K8.	114
<b>Figure 3.16:</b> Comparison of the petrophysic models at the end of the simulation with the 1994 impedance inversion.	115
<b>Figure 3.17:</b> Structure of the LF sand, Eugene Island 330.	116
<b>Figure 3.18:</b> Production history from the fault block B in the LF sand.	117
<b>Figure 3.19:</b> Impedance inversion results in the LF sand in 1985 and 1992.	118

<b>Figure 3.20:</b> Results of the reservoir characterization of the LF sand.	119
<b>Figure 3.21:</b> Permeability/porosity relationship from LF core samples.	120
<b>Figure 3.22:</b> Simulated production history match in the LF sand.	121
<b>Figure 3.23:</b> Simulated oil saturation in the LF sand.	

122

<b>Figure 3.24:</b> Simulated gas saturation in the LF sand.	123
<b>Figure 3.25:</b> Impedances calculated from the simulation results in the LF sand.	124

## Chapter 4

<b>Figure 4.1:</b> Location of the Eugene Island Block 330 field, off-shore Louisiana.	163
<b>Figure 4.2:</b> Salt structure interpreted from the 3D seismics.	164
<b>Figure 4.3:</b> Transgressive surfaces used to define the data cube lithology.	165
<b>Figure 4.4:</b> Bottom Hole Temperatures before and after correction.	166
<b>Figure 4.5:</b> Corrected temperature distribution at four different depths.	167
<b>Figure 4.6:</b> Influence of sedimentation on the conductive regime.	168
<b>Figure 4.7:</b> Representation of the lithology used in the conductive model.	169
<b>Figure 4.8:</b> Results of the conductive regime simulation.	170
<b>Figure 4.9:</b> Difference between measured temperatures and the simulated conductive regime.	171
<b>Figure 4.10:</b> Lithology and grid used in the simulation of the complete thermal regime.	172
<b>Figure 4.11-14:</b> Simulation results for various parameter values.	173
<b>Figure 4.15:</b> Best-matching simulation results after 5,000 years.	181
<b>Figure 4.16:</b> Advective temperature anomaly in the best-matching results.	182

## **Acknowledgements**

This voyage took many years, and I won't be able to express my gratitude to everyone whom by helping me, making me laugh, or just being themselves contributed to its completion and to maintain the little sanity I have left.

Roger Anderson and Dave Goldberg, offered me the opportunity to work with them, and kept me their trust and support all along while giving me all the independence that I value so much. My gratitude for their patience, their generosity, their trust and for their friendship goes beyond words. Bill Menke, Marc Spiegelman and Ulisses Mello were kind enough to review this dissertation and provided me with precious advices on how to improve it.

Robert Gable from the BRGM, France, provided me with crucial support during my first years and was always here for guidance and encouragements. I wish him the most fulfilling retirement.

My most sincere thanks also go to the members of the two groups that had to bear with me on a daily basis: the Borehole Research Group and 4-D Technology. Among them Wei He, Gerry Iturrino, Candace Major and Erich Scholz stand out as invaluable friends. Cristina Broglia, Greg Myers, Mary Reagan, Dave Roach, Joan Totton, LiQing Xu, among others, provided me with the finest and most friendly assistance. During the final months, Ule Ninnemann and Julie Carlut also greatly helped bearing the lightness of being.

By their fidelity to the rituals of TG, Drs Jeff Weissel and John Marra, Sean Higgins, Dan Barker, Del Bohnenstiehl, a few others, and most of the Borehole Group contributed to fulfill joyfully even the most frustrating weeks. The support of more occasional 'customers' was also wholeheartedly appreciated. I hope they enjoyed it as much as I did.

And to my family and friends in France, who helped me maintain my few roots and kept wondering if I would ever come back: I will.

To my parents and brothers.

They are examples of generosity, courage, dignity, simplicity, honesty.

All I know that matters comes from them - I am the most fortunate to have such models.

To Shit Head - *in memoriam*.

What do we believe  
To live with ? Answer.  
Not invent - just answer - all  
That verse attempts.

--“Blood from the stone” - George Oppen

This is the raw data.  
A mystery translates it  
into feeling and perception;  
then imagination;  
finally the hard  
inevitable quartz,  
figure of will  
and language.

-- Carl Rakozi

## **Preface**

From the time they settle on the seafloor, marine sediments are the locus of active processes involving the fluids present in the pore space. Most of these processes can have distinct signatures detectable by standard exploration techniques. The dissolution/re-precipitation of Opal-A (biogenic silica) into Opal-CT (porcellanite) is at the origin of time transgressive Bottom Simulating Reflectors (BSR) in seismic surveys of marine sediments across the world. The dissociation of gas hydrates at the base of the gas-hydrates stability zone has been associated with reverse polarity BSR. The presence of hydrocarbons in reservoirs can be identified by high negative-amplitude events. The changes occurring in a reservoir because of production can be identified by 4D, or time-lapse, seismics. The longer term migrations that feed shallow reservoirs in active oil field are too slow for such characterization, but can be identified by their influence on the temperature distribution.

This dissertation presents techniques to characterize and quantify these processes with a common approach: 1) identify the specificity of each process through the comparison with accepted models describing ‘normal’, passive attributes, and, if necessary, 2) the numerical modeling of the ‘anomalous’ or, more appropriately, ‘distinct’ signature in order to quantify how it affects the sediments. Under this general methodology, the techniques used are specific to each characterization.

In Chapter 1, (published in *Geophysical Research Letters*, vol.23, No 19, pp 2697-2700, 09/15/1996), we describe the elastic properties of marine calcareous sediments across a siliceous diagenetic front. During Ocean Drilling Program Leg 150, a transect was drilled across the on the Eastern U.S. continental slope off New Jersey. At three sites, a diagenetic boundary was recovered, across which Opal-A (biogenic silica, mostly diatoms) is replaced by Opal-CT. By re-precipitating dissolved silica into porcellanite

lepispheres, this transformation can generate a sharp increase in the density and velocity of the sediments that creates a positive high amplitude reflector in seismic surveys. Because temperature and depositional history are the primary parameters controlling the reaction, this diagenetic boundary is sub-parallel to the seafloor, producing a time transgressive positive BSR (see Preliminary Figure a). The deployment of a dipole shear sonic tool allowed to measure the elastic moduli of the calcareous marine sediments. The comparison with the classic consolidation models of Gassmann and Wood shows that porosity is the principal factor controlling the properties of the sediments, and that the Gassmann model can be used to describe their mechanical behavior. In particular we show that this model is still valid to describe the change in properties across the diagenetic front, indicating that despite an anomalously strong seismic signature, silica diagenesis can be characterized mostly by a change in porosity preserving the normal elastic behavior of the sediments.

By comparison, Chapter 2 (published in the Journal of Geophysical Research, Vol. 104, No B8, pp. 17,781-17,795, 08/1999) shows how a similar seismic signature can be associated with a profound changes in the mechanical behavior of marine sediments. In this chapter, we present the results of the first deployment of a dipole shear sonic tool in gas-hydrate bearing sediments. Gas hydrates are ice-like particles forming in the sediment pore space under specific conditions of pressure, temperature and free gas influx. In areas with steady seafloor topography, the limit of the hydrate stability zone is merely an isotherm sub-parallel to the seafloor. In most locations, free gas liberated by hydrate decomposition remains trapped under the impermeable hydrated sediments. The contrast between the properties of hydrated sediments above and partially free-gas saturated sediments below creates a negative amplitude BSR that has been used to identify hydrate reserves worldwide (Preliminary Figure b). The most striking difference between the two BSRs in Figures a) and b) is the change in the character of the seismic

waveform across the two reflectors. The stiffening of the sediments because of porcellanite precipitation generates lower seismic amplitudes below the Opal-A/Opal-CT BSR. The free gas produces higher seismic amplitudes below the Gas-Hydrate BSR, while the seismic amplitudes are particularly low above this reflector, which has been called the “Blanking effect” of hydrates. The first recording of a shear sonic velocity log in hydrated sediments during ODP Leg 164 allowed us to characterize the *in situ* elastic properties of such sediments. Comparison with the Gassmann model shows that the presence of hydrates deeply transforms the properties of the sediments. Investigating alternate models to explain these observations, we use the cementation theory to establish the mode of deposition of hydrates in the pore space and the amounts responsible for the observed anomalies. We can however use the Gassmann model to estimate the amount of free gas below the BSR.

Despite being particularly noticeable features in seismic surveys because of their extent, BSR's have little economic relevance beside possible landslide assessment - at least until technology allows the exploitation of the estimated  $2 \times 10^{16}$  m<sup>3</sup> of hydrocarbons trapped in hydrated sediments worldwide. In Chapter 3, we present a more pragmatic application of the same elastic models: to estimate the changes in reservoir fluids associated with differences observed between successive 3D seismic surveys of producing reservoirs. As part of an integrated time-lapse seismic interpretation methodology, petrophysical models are used in combination with reservoir simulation to characterize the changes detected through seismic inversion of 3D surveys (Preliminary Figure c) and to identify bypassed hydrocarbon. This chapter is therefore partly devoted to the selection of the most reliable formulation to convert observed impedance changes into producible resources. Because our objective is to develop a methodology applicable to the time lapse analysis of any reservoir, we present various possible formulations and a complete description of fluid properties. we then apply the methodology to two specific

cases in the Gulf of Mexico. The different successes of the two reservoir simulations show the difficulties of time-lapse analysis and allow discussion of the additional steps necessary to conclude the interpretation loop before spudding a new well.

Finally, whereas the present-day dynamics of a producing reservoir can be identified by time-lapse seismics, this technique can not be used to study the natural migrations filling shallow reservoirs with mature hydrocarbons in active oil fields. Such migrations can cover several kilometers vertically and span centuries of periodic fluid expulsions in active faults, and they are too slow to produce noticeable changes in reservoir seismic attributes over a few years. However, the ascension of large amount of fluids from deep sources can generate temperature anomalies detectable for thousands of years. In Chapter 4, we present a complete analysis of the thermal regime in the Eugene Island 330 area, offshore Louisiana, located at the center of an active growth fault system. The reconstruction of the present-day temperature field is done by the correction and the interpolation of 600 Bottom Hole Temperatures (Preliminary Figure d). The analysis of the temperature distribution identifies several high temperature anomalies. Because the area is underlain by high relief salt diapirs, some of these anomalies are produced by the highly conductive salt. This is confirmed by the 3D numerical simulation of the regional conductive regime. The anomalies remaining after removal of the conductive component are attributed to fluid migrations within the active fault, and we use the 3D numerical modeling of the complete thermal regime to estimate the mechanism and duration of the migrations.

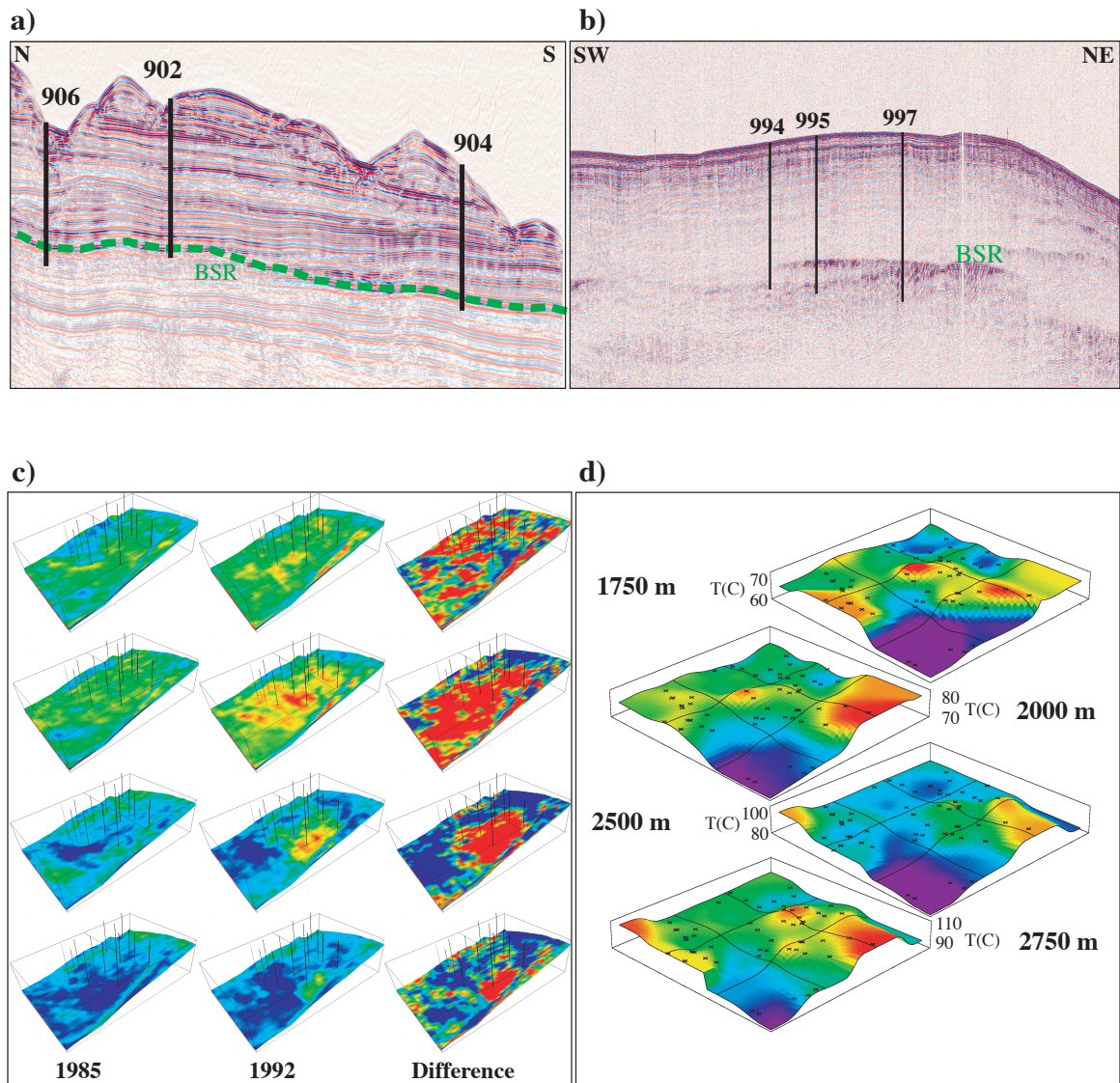
This last chapter shows how combining the insight of seismic surveys with the knowledge of the temperature distribution can help understand the dynamics of deep underground processes. In every study presented here, the use of thermal and acoustic signature to characterize the processes presented is related to the time scales involved. The migrations within a fault zone can occur over a few thousand years, but are induced

by relatively low pressure gradients with pressure changes to low for time lapse seismic identification. They have however a significant thermal signature because of the large volumes of fluid and of the vertical extent of the migrations. In this study seismic data are only used for the characterization of static features of the system. By comparison, the forced pressure depletion in a reservoir under production and the resulting fluid substitutions can generate impedance changes of about 10% over a few years. As a result, these changes can be detected by the comparison of successive 3D seismic surveys, but are not associated with significant thermal signatures and temperature is here a static attribute. The primary importance of temperature on both silica diagenesis and hydrate stability allows to combine both acoustic and thermal characterization of these processes, but the very distinct reaction rates of opal-CT formation and hydrate decomposition require different interpretation of the thermal significance of the two BSRs. Both reactions obey Arrhenius-type laws but the rate of hydrate decomposition at the BSR is of the order of mol/min [Kim *et al.*, 1987], while it is of the order of mol/kyear at opaline BSR [Mizutani, 1966]. Hydrate decomposition is merely an instantaneous process on a sedimentation time scale and the BSR represents simply a phase change boundary defined by pressure and temperature at the present time. The precipitation of Opal CT in passive margin sediments requires millions of year to produce a BSR [Hein *et al.*, 1978] and the location of the reflector is the result of the integrated deposition history of the overlaying sediments [Langseth and Tamaki, 1992]. In both cases, the depth of the BSR can be used to estimate the regional thermal regime, providing or requiring additional constraints on stratigraphic history in the case of silica diagenesis [Langseth and Tamaki, 1992, Townend, 1997, Ruppel *et al.* 1995, Barstow *et al.*, 1997]. Proceeding with such thermal characterization of the Blake Ridge and of the New Jersey margin could complete the cycle of the present work. It would also mostly underline what is already apparent in the present chapters and what *Baudelaire* [1857] already said so much better

of sounds, scents and colors: into one deep and shadowy unison, sound, heat and pore fluids correspond.

**References:**

- Barstow, N., G. Guerin, D. Goldberg and T. Chabernaud, 1997, Equilibrium borehole temperatures in the Ocean Drilling Program, *Eos, Transactions, AGU*, 78(46), p. F686 (abstract).
- Baudelaire, C., 1857, *Les Fleurs du Mal*, Poulet-Malassis et de Broise, Paris.
- Langseth, M., and K. Tamaki, 1992, Geothermal measurements: Thermal evolution of the Japan Sea basins and sediments, *Proc. ODP, Sci. Results.*, 127/128, College Station, TX, (Ocean Drilling Program), 1,297-1,309.
- Ruppel, C., R.P. Von Herzen and A. Bonneville, 1995, Heat flux through an old (~175 Ma) passive margin: Offshore southeastern United States, *J. Geophys. Res.*, 100(B10), 20,037-20,057.
- Townend, J., 1997, Estimates of conductive heat flow through bottom-simulating reflectors on the Hikurangi and southwest Fiordland continental margins, New Zealand, *Marine Geology*, 141, 209-220.



**Preliminary Figure:** a) **Chapter 1:** Opal-A/Opal-CT Diagenetic front across the New Jersey Continental Slope. b) **Chapter 2:** Bottom Simulating Reflector indicating the presence of Gas Hydrates across the Blake Ridge. c) **Chapter 3:** Acoustic impedance changes in a producing reservoir, Eugene Island 330, Gulf of Mexico. d) **Chapter 4:** Temperature distribution in an active fault zone, Eugene Island 330.

## **Chapter 1:**

# **Acoustic and elastic properties of calcareous sediments across a siliceous diagenetic front on the eastern U.S. continental slope**

## **1.1 Abstract**

The Ocean Drilling Program drilled Hole 904A on the upper continental slope offshore New Jersey through 230 m of Eocene chalks and an opal-A/opal-CT diagenetic front. In addition to a suite of standard logging tools, a dipole sonic tool was deployed to determine the *in situ* shear sonic velocity and the elastic properties of these slow, highly porous, sediments. While porosity decreases by 20% across the diagenetic front, the compressional velocity and the density are observed to increase by 30%, the shear sonic velocity and the bulk modulus by about 60%, and the shear modulus by almost 300%. It is shown that shear and compressional velocities are both controlled by porosity and consolidation, and that existing models for the prediction of elastic properties and shear velocity from standard logs are still valid through the diagenetic front. The strong effect of diagenesis on rigidity makes the shear velocity log a highly sensitive indicator of pore shape and pore filling transformations.

## **1.2 Introduction**

The Ocean Drilling Program Leg 150 drilled and collected logging data at 4 Sites (902, 903, 904 and 906) on the eastern U.S. continental slope where it recovered a thick section of Eocene chalks [Mountain, Miller, Blum, et al., 1994]. At all four sites, a diachronous high amplitude seismic reflector was recovered which had previously been identified as a siliceous diagenetic front below which biogenic opal-A has been converted to porcellanite [Tucholke, Vogt et al., 1979; Poag, Watts, et al., 1987]. In this paper we investigate the *in situ* elastic properties of the chalks through the diagenetic front and their relationship to porosity and consolidation.

Compressional velocity ( $V_p$ ) and density ( $\rho$ ) are both routinely measured *in situ* and on core samples. These data are critical for log-seismic correlation (synthetic seismograms) and for the identification of seismic sequence boundaries [e.g. *Goldberg et al.*, 1987], but in order to describe the elastic behavior of the formation, its dynamic elastic constants must also be known. The shear modulus,  $\mu$ , and the bulk modulus,  $K$ , can be defined by:

$$V_p = \sqrt{\frac{1}{\rho} \left( K + \frac{4}{3} \mu \right)} \quad \text{and} \quad V_s = \sqrt{\frac{\mu}{\rho}} \quad (1)$$

where  $V_s$  is the shear wave velocity. Because neither of the elastic moduli can be directly measured *in situ*, the measurement of  $\rho$ ,  $V_p$  and  $V_s$  is necessary for the resolution of equation (1). When using standard acoustic logging tools, however, there is no detectable shear wave in slow, poorly consolidated formations such as on the New Jersey continental slope, and it is not possible to measure  $V_s$  directly [*Toksöz and Cheng*, 1991]. Dipole sonic logging technologies, which initiate flexural waves in the formation using a directional pressure source [*Chen*, 1988], usually allow for estimates of  $V_s$  through waveform analysis, over a wide range of wave speeds and formation porosity. During ODP Leg 150, a commercial dipole tool was used in addition to a suite of standard tools which made possible the estimation of  $V_s$  and of the elastic moduli in these high-porosity sediments.

In previous work on the New Jersey continental slope at adjacent DSDP Sites 612 and 613, Poag, Watts, *et al.* [1987] and Wilkens *et al.* [1987] identified a sharp change in core and log physical properties related to the conversion of biogenic Opal-A to porcellanite. Wilkens *et al.* [1987] linked the density and porosity changes to the transformation in the micro-structure of the chalks: the re-precipitation of the dissolved biogenic silica (opal-A) into silica lepispheres (opal-CT). This diagenetic transformation cements the matrix of the sediments and partially fills the large calcareous fossils, reducing porosity by about

20% over just a few meters and without affecting the overall chemical composition of the grains or their density.

The dipole sonic tool used during Leg 150 enabled direct measurement of  $V_s$  in the chalks and through this same diagenetic front. We discuss the results at Site 904 and at nearby Site 902 and the suitability of current models for velocity-porosity relationships and sediment elastic properties.

### 1.3 Logging Results

In Hole 904A, an extensive suite of logs was run over a 230 m-thick calcareous chalk section, including porosity ( $\Phi$ ),  $\rho$ ,  $V_p$  and  $V_s$  measurements. The borehole conditions were excellent over this interval and the data clearly show the opal-A/opal-CT diagenetic front penetrated at 525 meters below seafloor (mbsf). In Figure 1.1 porosity ( $\Phi$ ) decreases by 20 % across this boundary, density and  $V_p$  increase by about 30% and  $V_s$  by 60%. Mountain, Miller, Blum, *et al.*, [1994] observe that the grain density in core samples remains unchanged, or even decreases slightly, below 525 mbsf, which suggests that the increase in bulk density and compressional velocity are controlled uniquely by changes in the porosity and the nature of the pore space.

The strong correlation between velocities and porosity in Figure 1.2a and 2b underlines the velocity dependence on porosity. The chalks drilled in Hole 904A have been divided into three distinct subunits, identified by Mountain, Miller, Blum *et al.*, [1994]: above (+) and below (o) an abrupt drop in clay content at 419 mbsf; and below (•) the diagenetic boundary at 525 mbsf (see Figure 1.1). Least square regressions distinguish different trends between these three groups of data (Table 1.1). The increase in slope with increasing depth and decreasing porosity can be attributed mainly to compaction. Part of this increase between (+) and (o) may also be attributed to a clay content reduction which increases the contribution of higher-velocity calcite and silica minerals. Data recorded below the diagenetic front (•) are particularly distinct, showing

reduced scatter (increased correlation coefficients in Table 1.1), but no significant change in chemical composition. This behavior is interpreted to be characteristic of the change in mechanical state of the sediments.

In the past, a lack of direct  $V_s$  measurements has precluded the development of empirical relations between  $V_s$  and porosity. The shear velocity and the rigidity of marine sediments have not been easily computed from their physical components and properties because of the diversity in grain sizes, shapes, and other parameters affecting particle interlocking and sediment rigidity [Hamilton, 1971]. Figure 1.2b shows, however, that a consistent correlation exists between  $\Phi$  and  $V_s$ . Least square regressions for the same three subunits described above appear in Table 1.1. The relationships for  $1/V_s$  and  $1/V_p$  vs.  $\Phi$  through the chalks and the diagenetic front are similar with a reduction in scatter and a steepening of slopes as  $\Phi$  decreases with depth (Table 1.1). Figures 2a and 2b show that  $V_s$  increases faster than  $V_p$  with decreasing porosity, although this is more apparent in the evolution of their ratio  $V_p/V_s$  as a function of depth. Figure 1.3 (column a) shows  $V_p/V_s$ , representative of the Poisson's ratio and of the stiffness of the material, steadily decreasing with depth as a result of compaction, and dropping sharply from 3.0 to 2.5 at the diagenetic front. This change is consistent with the stiffening of sediments during the early stages of diagenesis also observed by Wilkens *et al.*[1992].

Having acquired log data for  $V_p$ ,  $V_s$  and  $\rho$ , equation (1) can be used to estimate  $\mu$  and  $K$ , the shear and bulk moduli, as a function of depth. Figure 1.3 (column b) illustrates the sharp increase in the two moduli and the mechanical change occurring through the diagenetic front at 525 mbsf. The relative increase in bulk modulus is about 60%, and the shear modulus increases by about 300%. Therefore a five times greater relative increase in rigidity than in incompressibility results from diagenesis in these sediments.

## 1.4 Velocity-Porosity Models

### 1.4.1 Models description

Several models have been proposed for the determination of elastic moduli in sediments from porosity, in the absence of shear velocity measurements. Particularly, Wood [1941] and Gassmann [1951] derived equations that have been used by different authors to address the changes in elastic properties of marine sediments through consolidation. Wood assumes that the shear modulus of unconsolidated sediments, considered to be high porosity aggregates of fluid and grains, is zero and that the bulk modulus is the geometric average of the bulk moduli of the grains ( $K_s$ ) and of water ( $K_w$ ):

$$\frac{1}{K_{\text{Wood}}} = \frac{\Phi}{K_w} + \frac{(1-\Phi)}{K_s} \quad \text{and} \quad V_p = \sqrt{\frac{K_{\text{Wood}}}{\rho}}. \quad (2)$$

Hamilton [1971], Hamilton *et al.*[1982] and Wilkens *et al.* [1992] suggest that this formulation is not valid for marine sediments, which have some rigidity, but still can be used to obtain a maximum estimate of the shear velocity. Assuming that the difference between compressional velocities estimated from Wood's equation and measured velocities can be attributed to non-zero rigidity, the dynamic shear modulus predicted by Wilkens *et al.*[1992] is  $\mu = 3/4(\rho V_p^2 - K_{\text{Wood}})$ .

In Gassman's equation [1951], the bulk modulus is considered as the combination of three moduli:  $K_s$ ,  $K_w$  and the frame bulk modulus ( $K_f$ ) which represents a rigidity component introduced by grain-to-grain contacts:

$$K = K_s \frac{K_f + Q}{K_s + Q} \quad \text{with} \quad Q = \frac{K_w(K_s - K_f)}{\Phi(K_s - K_w)}. \quad (3)$$

Hamilton [1971] and Hamilton *et al.*[1982] defined an empirical relation between  $K_f$  and  $\Phi$  for calcareous sediments similar to those encountered on the eastern U.S. continental slope:

$$\log(K_f \text{ (Pa)} \times 10^{-9}) = 1.87355 - 3.41062\Phi. \quad (4)$$

Once  $K$  has been estimated from porosity using equation (2) (Wood's model) or using equations (3) and (4) (Gassmann-Hamilton's model),  $\mu$  and  $V_s$  can be deduced from  $V_p$  and  $\rho$  measurements.

Using the logging data recorded at Site 904, we have compared the results of these two models to the  $V_s$  log data in Figure 1.3 (column c). Both models assume a grain bulk modulus  $K_g = 74.74 \times 10^9$  Pa (mostly calcite) and  $K_w = 2.25 \times 10^9$  Pa (after Hamilton *et al.*, [1982]). As expected, the shear velocity estimated from Wood's model is higher than the log data, while on average the results from the Gassmann-Hamilton model agree with the log data within 10 %. In the absence of other *in situ* measurements of  $V_s$ , this observation supports the prediction of  $V_s$  in these sediments using the Gassmann-Hamilton model. We use this model for the estimation of  $V_s$  in adjacent Hole 902D, where no direct shear waves were recorded.

#### 1.4.2 Hole 902D

Hole 902D was drilled 7 km upslope from Site 904 through similar, uniform lithologies and with good hole conditions. Only a monopole sonic tool was used in this hole and measured  $V_p$ , but no direct shear waves were detected. The second arrival detected was almost invariably the fluid wave at a constant velocity of  $V_f = 1.6$  km/s, as shown in Figure 1.4. In order to estimate  $V_s$  at this site, we applied the Gassmann-Hamilton model using the density,  $V_p$  and  $\Phi$  logging data measured in Hole 902D. The results are also shown in Figure 1.4. Based on the comparison with Hole 904A, this estimate reasonably represents the shear velocity in Hole 902D because: (1) the limited range of  $\rho$ ,  $\Phi$  or  $V_p$  data is similar at Site 904; (2)  $V_s$  is clearly less than  $V_f$  and could not have been measured with a monopole source in this hole; and (3) in one interval where  $V_s$  is higher than  $V_f$  (at about 613 mbsf), a refracted shear wave was measured and agrees with the model.

A limitation of this method for estimating  $V_s$  is that it requires similar lithologies. When direct  $V_s$  measurements are not available, however, a reasonable estimate can be provided from standard logs by a well-constrained formulation. With more direct measurements of  $V_s$  (in combination with  $V_p$ ,  $\rho$  and  $\Phi$ ) in different types of sediments, the empirical parameters in equations (3) and (4) could be defined broadly over a wide range of minerals and porosity, which could eventually allow for estimates of  $V_s$  in any environment using conventional logging data.

### 1.5 Elastic Moduli and Porosity

Figure 1.5 displays the relationships between porosity and the bulk and shear moduli calculated from logging data at Site 904, and the curve representing the Gassmann-Hamilton model in calcareous sediments. The same symbols are used as in Figure 1.2, except for  $\mu$  below the diagenetic front (■). The bulk moduli data agree reasonably well with the model and confirm its validity at this site, even through the diagenetic front. In itself, such a strong correlation points to the porosity as a dominant parameter in the elastic properties of the chalks.

Figure 1.5 also illustrates the difference in the elastic moduli across the diagenetic front. While  $K$  and the gradient  $\partial K/\partial\Phi$  increase progressively with decreasing  $\Phi$ ,  $\mu$  increases steadily and  $\partial\mu/\partial\Phi$  changes sharply at  $\Phi=45\%$ , from 2.19 to 8.37 (Table 1.2).

### 1.6 Discussion

The discontinuity in rigidity may be explained by the formation of silica lepispheres in open pore space due to diagenesis. The abrupt increase in stiffness at the diagenetic front is clearly illustrated by the increase in  $V_p/V_s$  ratio (Figure 1.3a) and the discontinuous change in  $\partial\mu/\partial\Phi$  suggests a coincident discontinuity in the mechanical properties of the chalks and in the lithification process. Whether this process is actually

discontinuous or not, however, the increase in rigidity is the most significant change in the elastic properties of the chalks through diagenesis.

The Gassmann-Hamilton model accurately predicts shear sonic velocities through the entire chalk interval and through the diagenetic front in the absence of direct  $V_S$  measurements. This suggests that there is no major change in the nature of the consolidation process, or in the grain structure, due to silica diagenesis. If there is a change, its quantitative effect on the elastic properties of the sediments is limited, so that they remain predictable by the same algebraic formulation shown in equations (3) and (4).

Wood's model, by comparison, predicts velocities less satisfactorily than observed by Wilkens *et al.* [1992] for the same lithological formation a few miles downslope at Site 613, and the velocities which result from using this model are much higher than the velocities measured *in situ* by the dipole sonic tool. However the difference between the model and the  $V_S$  log increases with depth, or greater consolidation, as also observed by Wilkens *et al.* [1992]. The greater burial depth and higher consolidation of the chalks at Site 904 than at Site 613 may partially explain the difference in the application of Wood's model at the two sites. There is also a considerable difference between the results of the inversion described by Wilkens *et al.* [1992] and the  $V_S$  logging data, particularly above the diagenetic front where the inversion process produces shear velocity values much higher than the present logging data. Wilkens *et al.* [1992] note that the inversion process breaks down at very low shear wave velocities (i.e. lower than about 800 m/s) which accounts for most of the interval above the diagenetic front both at Sites 904 and 613. Consequently we suggest that the results of the inversion study overestimate  $V_S$  at Site 613 above the diagenetic front, and that Wood's model overestimates  $V_S$  at both sites. Dipole log measurements and alternatively the Hamilton-Gassmann model are more representative of  $V_S$  in these marine sediments.

## 1.7 Conclusion

The primary role of porosity on the evolution of the mechanical properties of carbonates has been here observed and documented over an intermediate porosity range from 30 to 65% on the eastern U.S. continental slope. The Hamilton-Gassmann model provides a reliable empirical estimation of elastic moduli and  $V_s$  from porosity and conventional logs and agrees well with the dipole sonic log data. More *in situ* shear velocity measurements are needed to calibrate similar models in a variety of sedimentary environments.

At Site 904, the infilling of foraminifer chambers by diagenetic re-precipitation of Opal-CT from dissolved Opal-A generates a noticeable change in the lithification process, whose most apparent mechanical effect is a sharp increase in sediment rigidity. Shear velocity logs can indicate, and to some extent quantify, this specific diagenetic transformation in the absence of sediment core analyses. With adequate data for calibration, these observations could be extended to other mechanical or geochemical processes that affect grain-to-grain contacts and alter the pore space and the matrix through different types of transformations, such as the formation of ice (gas hydrates) or the precipitation of diverse types of minerals. The shear velocity log is a highly sensitive indicator of such processes that primarily affect the sediment rigidity.

## References

- Chen, S.T., Shear wave logging with dipole sources, *Geophysics*, 53, 659-667, 1988.
- Gassmann, F., Elastic waves through a packing of spheres, *Geophysics*, 16, 673-685, 1951.
- Goldberg, D. S., Wilkens, R. H., and Moos, D., Seismic modeling of diagenetic effects in Cenozoic marine sediments at Deep Sea Drilling Project Sites 612 and 613, in Poag, C. W., Watts, A. B., *et al.*, *Init. Repts. DSDP*, 95, 589-599, 1987.

- Hamilton, E. L., Elastic properties of marine sediments, *J. Geophys. Res.*, 76, 579-601, 1971.
- Hamilton, E. L., Bachman, R. T., Berger, W. H., Johnson, T. C., and Mayer, L. A., Acoustic and related properties of Calcareous deep-sea sediments, *J. Sed. Pet.*, 52(3), 733-753, 1982.
- Mountain, G.S., Miller, K.G., Blum, P., *et al.*, *Proc. ODP, Init. Repts.*, 150, College Station, TX (Ocean Drilling Program), 1994.
- Poag, C. W., Watts, A. B., *et al.*, *Init. Repts. DSDP*, 95, Washington (U.S. Govt. Printing Office), 1987.
- Toksöz, M.N., and Cheng, C.H., Wave propagation in a borehole, in *Shear waves in marine sediments*, edited by J.M. Hovem, M.D. Richardson, and R.D. Stoll, pp. 257-265, Kluwer Academic Publishers, 1991.
- Tucholke, B.E., Vogt, P.R., *et al.*, *Init. Repts.*, *DSDP*, 43, Washington (U.S. Govt. Printing Office), 1979.
- Wilkins, R. H., Schreiber, B. C., Caruso, L., and Simmons, G., The effects of diagenesis on the micro structure of Eocene sediments bordering the Baltimore Canyon Trough, in Poag, C. W., Watts, A. B., *et al.*, *Init. Repts. DSDP*, 95, Washington (U.S. Govt. Printing Office), 527-536, 1987.
- Wilkins, R. H., Cheng, C. H., and Meredith, J.A., Evaluation and prediction of shear wave velocities in calcareous marine sediment and rocks, *J. Geophys. Res.*, 97, 9297-9305, 1992.
- Wood, A.B., *A textbook of sound*, G. Bell and Sons, Ltd, London, 1941.

## Tables

**Table 1.1:** Linear regressions for slowness vs. porosity (with correlation coefficients).

Unit	$1/V_p$	$1/V_s$
+	$0.475 + 0.159\Phi$ (0.441)	$1.217 + 1.079\Phi$ (0.404)
o	$0.378 + 0.310\Phi$ (0.636)	$0.621 + 2.064\Phi$ (0.586)
•	$0.231 + 0.586\Phi$ (0.817)	$-0.324 + 3.897\Phi$ (0.855)

**Table 1.2:** Linear regressions for elastic moduli vs. porosity (with correlation coefficients in brackets).

Unit	Bulk Modulus (K, in $10^9\text{Pa}$ )	Shear Modulus ( $\mu$ , in $10^9\text{Pa}$ )
+	$7.21 - 4.50\Phi$ [0.410]	$1.05 - 0.95\Phi$ [0.429]
o	$10.31 - 10.17\Phi$ [0.642]	$1.73 - 2.19\Phi$ [0.636]
•	$15.26 - 19.76\Phi$ [0.777]	$4.69 - 8.37\Phi$ [0.821]

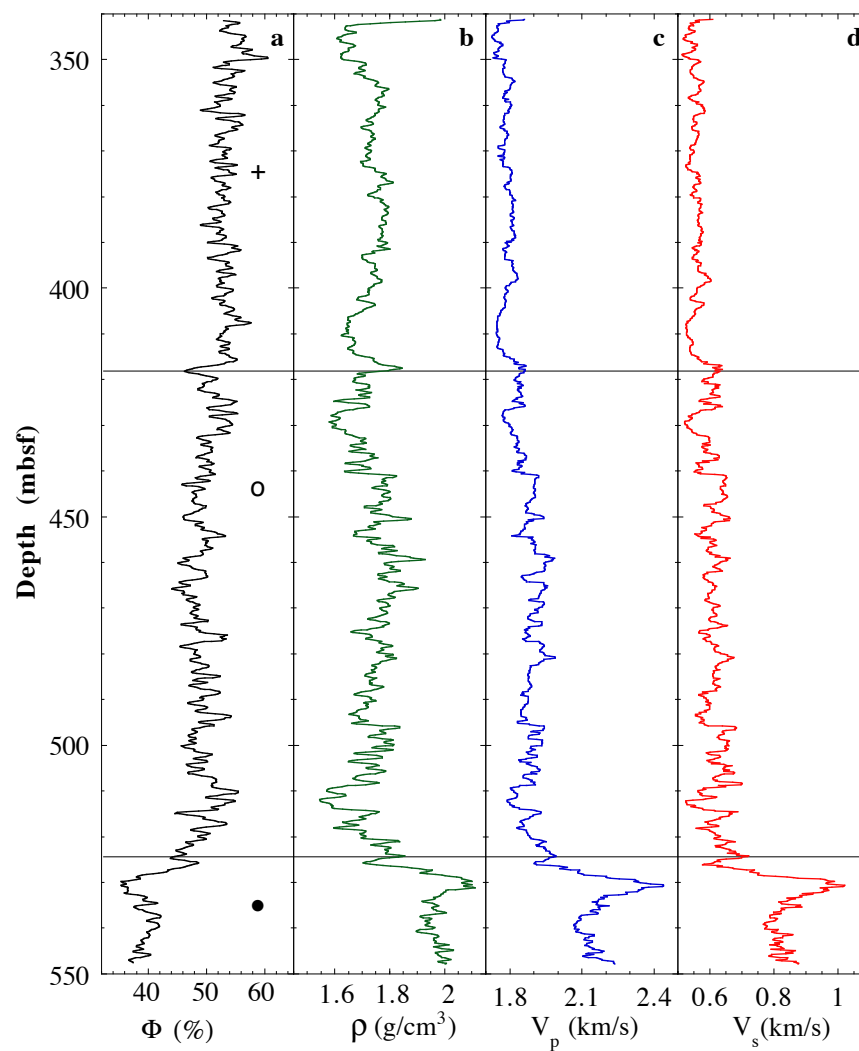


**Figure 1.1:** Logs measured in hole 904A (a)  $\Phi$ , (b)  $\rho$ , (c)  $V_p$  and (d)  $V_s$ . The interval logged is divided into three subunits (see text). The sharp change in all the measurements at about 525 mbsf corresponds to the diagenetic change from Opal A to Opal CT.

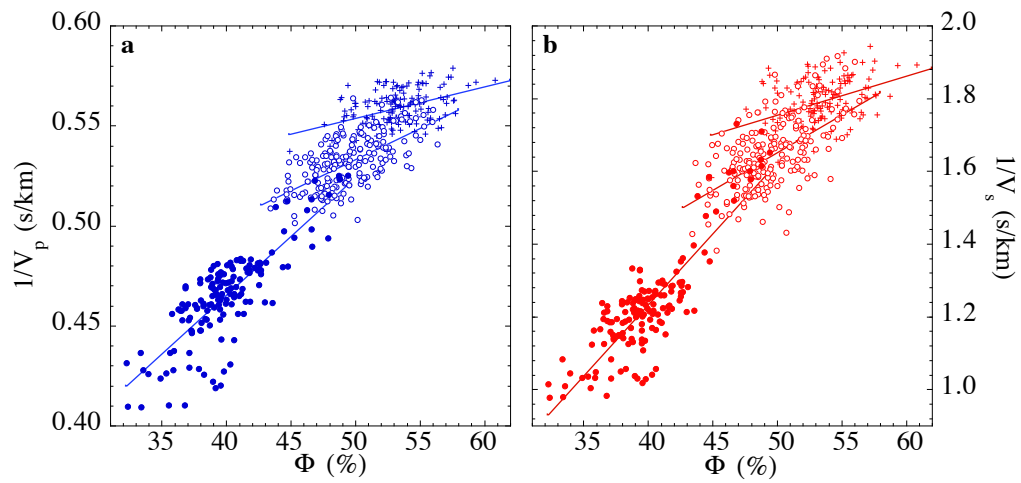


**Figure 1.2:** Relationship between porosity ( $\Phi$ ) and (a)  $1/V_p$  and (b)  $1/V_s$  in Hole 904A. Least square linear regressions are displayed for each lithologic subunit (same as in Figure 1.1: cross above 419 mbsf, hollow circle above the diagenetic front and filled circles below ).

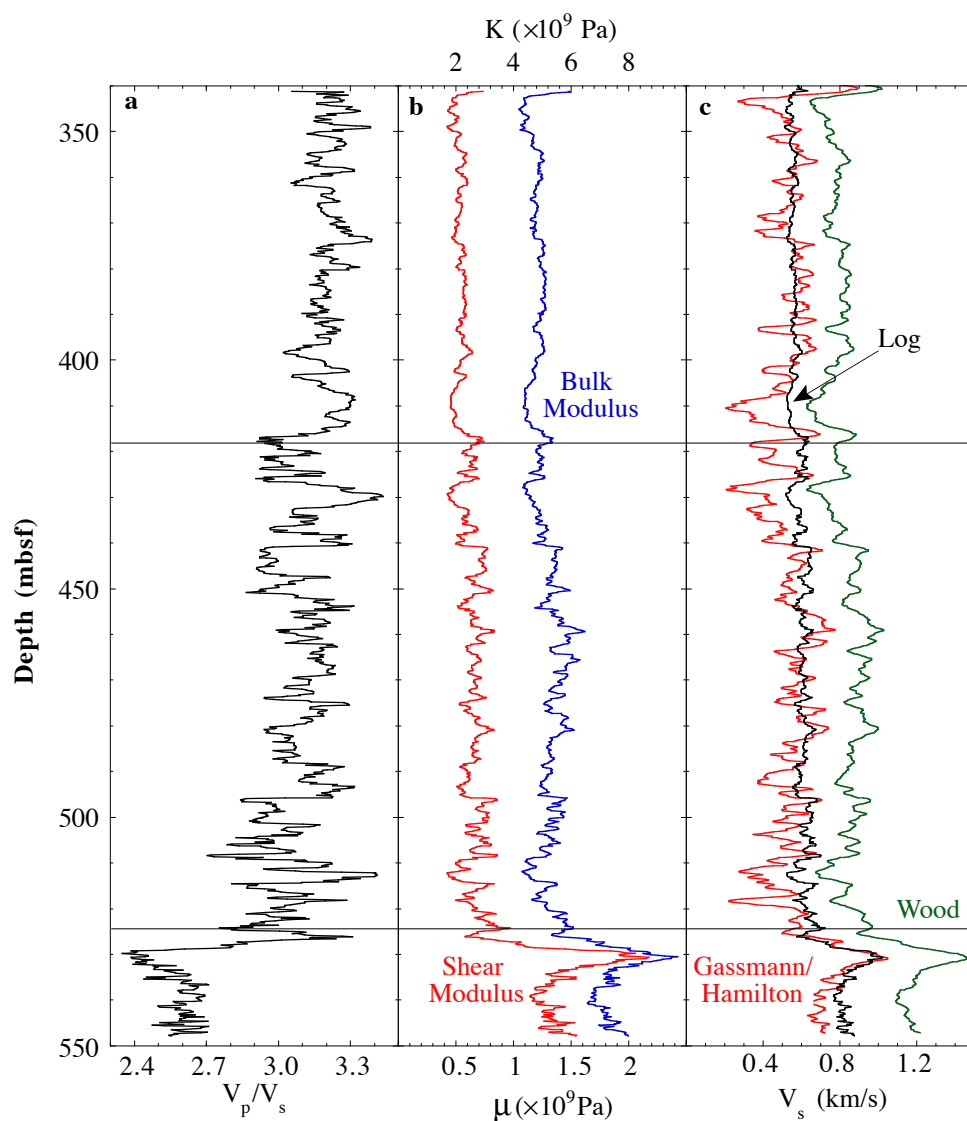


**Figure 1.3.** (a) In situ  $V_p/V_s$  from logging data in Hole 904A. (b) Bulk and shear moduli calculated from  $\rho$ ,  $V_p$  and  $V_s$  logs in Hole 904A. (c) Comparison between direct  $V_s$  measurements in Hole 904A and the Wood and Gassmann-Hamilton models.

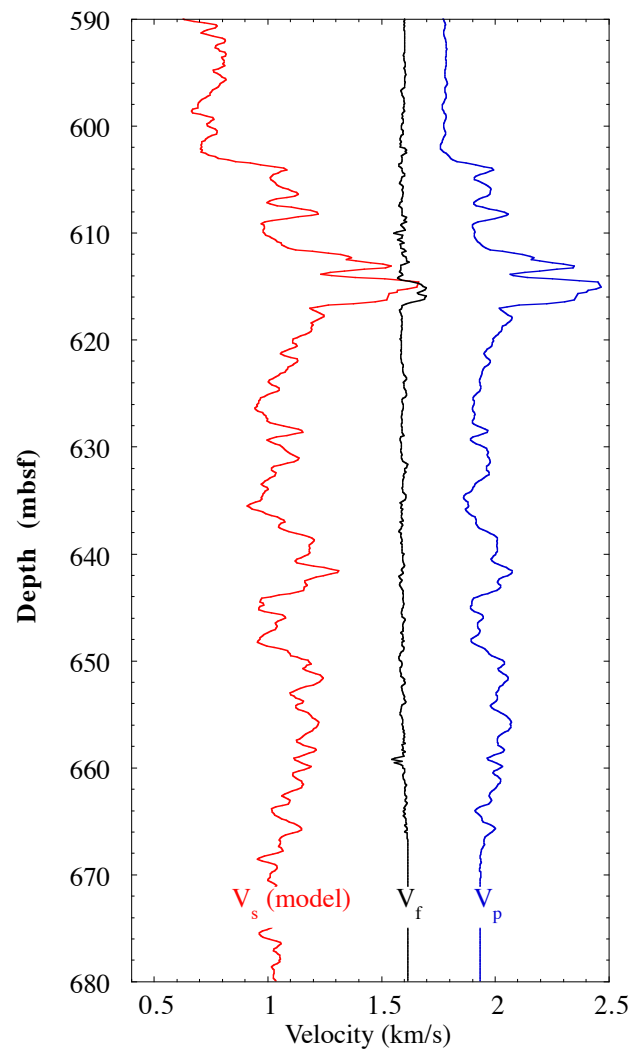


**Figure 1.4:** In situ velocity measurements in Hole 902D (similar lithology as Site 904) and  $V_s$  estimated by the Gassmann-Hamilton model. A direct refracted shear wave measurement around 613 mbsf matches the model results.

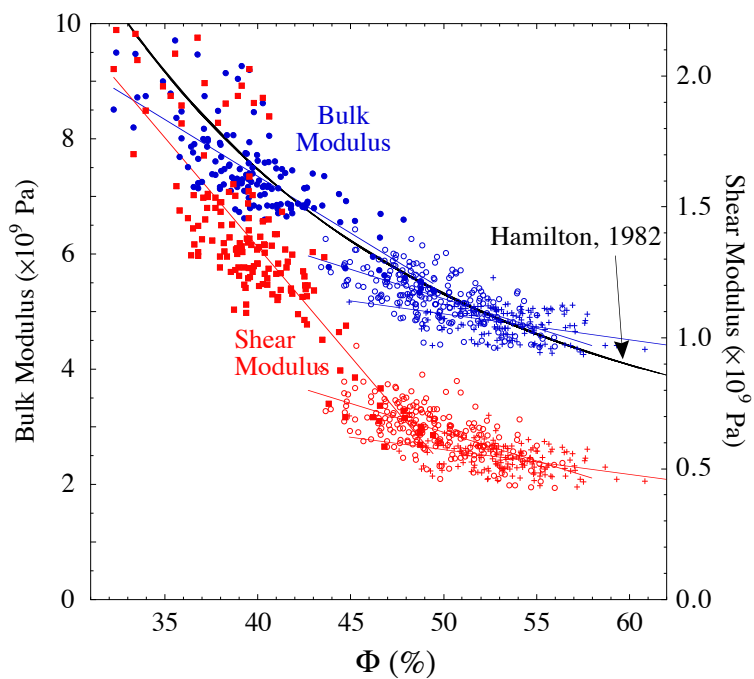


**Figure 1.5:** Relationships between porosity and bulk and shear moduli in Hole 904A. The symbols are the same as in Figure 2. The measurements of  $K$  compare well with the Gassmann-Hamilton model.

## Chapter 2:

### Characterization of *in situ* elastic properties of gas hydrate-bearing sediments on the Blake Ridge

#### 2.1 Abstract

During ODP Leg 164, shear sonic velocity and other geophysical logs were acquired in gas-hydrate bearing sediments on the Blake Ridge to characterize the very distinct seismic signature of such formations: anomalous low amplitudes overlying a strong Bottom Simulating Reflector (BSR). A comparison of the bulk moduli derived from the logs to standard elastic consolidation models shows that the sediments are over-consolidated above the BSR at 440 mbsf because of the presence of hydrates. Below the bottom of the thermodynamic hydrate stability zone at ~520 mbsf, the high compressibility of the formation and the attenuation of the monopole sonic waveforms are typical of sediments partially saturated with free gas. Between these two depths, gas hydrate and free gas seem to coexist. Within the Gas Hydrate Stability Zone, we estimate the amount of gas hydrates using different models based on theories for wave scattering in multi-phase media and for grain cementation. In close agreement with measurements made on discrete *in situ* samples, the latter describes most accurately the interactions between the matrix, the pore fluids and the hydrates. This model indicates that 5 to 10% of the pore space is occupied by hydrates deposited uniformly on the surface of the grains. The comparison with Gassmann's model also show that the amount of free gas below the BSR never exceeds 5% of the pore space, but is high enough to generate the BSR. The coexistence of free gas and gas hydrates below the BSR may be explained by capillary effects in the smaller pores or by remaining crystalline structures after partial hydrate decomposition.

## 2.2 Introduction

Gas Hydrates are crystalline solids formed of a cage of water molecules surrounding a natural gas molecule under specific conditions of relatively high pressure and low temperature. The supply of gas also must be sufficient to initiate and stabilize the hydrate structure [Sloan, 1990, Kvenvolden, 1994]. These restrictive thermodynamic conditions are satisfied on many continental slopes and rises around the globe, in particular on the U.S. Eastern Continental Margin.

A common seismic signature of hydrate accumulation is the presence of a strong diachronous reflector sub-parallel to the seafloor called Bottom Simulating Reflector (BSR). As seen in Figure 2.1, it is commonly overlain by anomalously low-amplitude seismic reflections often referred as “blanking effect” [Shipley *et al.*, 1979]. One of the most extensively studied locations with such characteristics is the Blake-Bahamas Ridge, a pronounced topographic feature extending more than 500 km downslope to the south east off South Carolina and approximately perpendicular to the general trend of the continental margin (Figure 2.2). The Blake Ridge is a major Neogene and Quaternary sediment drift consisting of hemipelagic silt and clay-rich contourite deposits that accumulated at unusually high rates [Tucholke *et al.*, 1977, Paull *et al.*, 1996]. The strong BSR underlying the Blake Ridge was first observed in the late 1960s, and its identification as the bottom of the hydrate stability zone was suggested after Deep Sea Drilling Project (DSDP) Leg 11 [Hollister, Ewing, *et al.*, 1972]. This hypothesis was then supported by the recovery of hydrate-bearing samples during DSDP Leg 76 [Sheridan *et al.*, 1983], but the final confirmation only came during Ocean Drilling Program (ODP) Leg 164 when the BSR was penetrated at Sites 995 and 997 along a transect across the Blake Ridge [Paull *et al.*, 1996]. One of the main objectives of Leg 164 was to quantify the amount of methane present on the Blake Ridge and determine the characteristics of the particularly well-developed BSR. Leg 164 was a key study for characterizing and quantifying the hydrocarbon accumulation in similar geologic environments, which have

been observed worldwide and are considered as a potential energy reserve for the future [Kvenvolden, 1994].

The very distinct seismic signature indicates that changes in the elastic and mechanical properties of the host sediments are a fundamental manifestation of the presence of gas hydrates and free gas. One way to address these changes is to measure the velocity of elastic waves using a variety of direct and inverse methods. Velocities in this area and in similar environments have been estimated by many authors using seismic inversion and Amplitude Versus Offset (AVO) analysis [Ecker *et al.*, 1996, Wood *et al.*, 1994, Lee *et al.*, 1993, Hyndman and Davis, 1992, Shipley *et al.*, 1979], and by Vertical Seismic Profiling (VSP) [Pecher *et al.*, 1997, Holbrook *et al.*, 1996]. However, such estimates are indirect and have vertical resolutions on the order of meters for the VSP to tens of meters for seismic surveys. Due to this resolution limit, the pore-scale nature of the hydrate accumulation process can only be broadly inferred from these studies. Moreover, owing to the instability of the hydrate compound under standard atmospheric conditions, the mechanical properties of hydrated sediments are extremely difficult to assess in the laboratory. One of the primary achievements of Leg 164 was the deployment of several downhole logging instruments, including a dipole sonic tool capable of measuring shear velocities in “slow” sediments [Guerin *et al.*, 1996]. These measurements of *in situ* properties are made at a cm-to-meter scale resolution.

In this paper, the qualitative analysis of the logs and of the sonic log waveforms delineates several sections with distinct characteristics associated with the presence of hydrate and free gas. The comparison of the elastic moduli of the formation calculated from the geophysical logs with the elastic formulation established by Gassmann [1951] and Hamilton [1971] shows that the hydrate-bearing sediments overlying the BSR are more consolidated, or less compressible, than normally compacting clastic sediments described by these models [Guerin *et al.*, 1996, Guerin and Goldberg, 1997]. In order to estimate the amount of hydrate responsible for this anomalous consolidation, we compare

our data to models based on numerical formulations of wave scattering in multi-phase media and of grain cementation. We use the Gassmann/Hamilton model to determine the amount of free gas beneath the BSR.

### 2.3 Logging data

Downhole measurements are used to assess the *in situ* physical, chemical, and structural properties of the formation surrounding a borehole. After completion of drilling, probes are lowered into the borehole with an electrical wireline and record data at a typical vertical sampling interval of 15 cm. Various tools, originally developed for oil exploration, have been routinely deployed at most of the sites drilled by ODP. The data recorded at Site 995 included standard geophysical measurements (density, resistivity, porosity, natural radioactivity) as well as compressional- and shear-wave velocities ( $V_p$  and  $V_s$ ). Our analysis will mostly concern the data from Hole 995B since the data recorded at Sites 994 and 997 were more severely affected by enlarged hole conditions.

Figure 2.3 shows some of the log data recorded in Hole 995B. The caliper log (Figure 2.3a) gives an estimate of the diameter of the hole and is an indicator of the quality of the other logs - large or highly variable readings indicate likely poorer data quality. In particular, the intervals from 180 to 230 meters below seafloor (mbsf), from 390 to 410 mbsf, and several thin intervals between 460 and 510 mbsf display rugged hole conditions. The density log (Figure 2.3b) was overall affected by the enlarged hole. The log values are consistently lower than the discrete density measurements made on core samples collected in the same hole (dots), which suggests that the caliper arm had incomplete contact with the formation and that the measurements are affected by an intermediate layer of fluid. Despite these effects, the density log follows the trend of the core data with depth.

The neutron porosity log was most adversely affected by the hole rugosity and by the hydrogen bound in clay-rich sediments because it measures neutron scattering which is

controlled by the total hydrogen content [Schlumberger, 1989]. As the density log was also of poor quality, the most reliable porosity estimation ( $\Phi$ ) was derived from the resistivity log (Figure 2.3c) which is commonly the least sensitive log to poor hole conditions [Schlumberger, 1989]. Archie [1942] established an empirical relationship between porosity, the measured resistivity ( $R_t$ ) and the pore water resistivity ( $R_w$ ) in sandy formations:

$$R_t/R_w = a/\Phi^m \text{ or } \Phi = (a.R_w/R_t)^{1/m} \quad (1)$$

where  $m$  and  $a$  are two empirical parameters derived from cross-correlation between log resistivity and porosity measurements made on core samples from the same formation. The values for  $a$  and  $m$  calculated from the cores and logs collected at site 995 were respectively 0.9 and 2.7 [Paull *et al.*, 1996]. The resistivity of seawater,  $R_w$ , was calculated as a function of temperature ( $T$ ) and salinity using an empirical formula:

$$R_w = R_0(T_0 + 21.5)/(T + 21.5) \quad (2)$$

where  $R_0$  is the resistivity of the seawater with the same salinity at a reference temperature  $T_0$  [Schlumberger, 1994]. The salinity was assumed to be 32 ppt, [Paull *et al.*, 1996], yielding a water resistivity at surface temperature ( $T_0 = 18^\circ\text{C}$ ) of 240 ohm.m [Schlumberger, 1994]. The temperature was assumed to follow a linear gradient of  $38.5^\circ\text{C}/\text{km}$  established by *in situ* temperature measurements, with a seafloor temperature of  $3^\circ\text{C}$  [Paull *et al.*, 1996]. Collett [1998] and Collett and Ladd [1998] provide extensive descriptions of the different porosity estimates on the Blake Ridge. Although Archie's relationship was originally defined for sand-rich formations, Jarrard *et al.* [1989] observed that the effect of clay minerals is moderate in high-porosity terrigenous sediments, and the relationship is commonly used to estimate porosity in clay-rich formations with poor borehole conditions [Collett, 1998, Jarrard *et al.*, 1989, Srivastava *et al.*, 1987]. The resulting porosity log is shown in Figure 2.3d, where it compares well with the discrete porosity measured on core samples at Site 995. The consistently lower porosity between  $\sim 200$  and  $\sim 440$  mbsf reflects the higher resistivity measured in this

interval (Figure 2.3c) which is attributed to the presence of hydrates (see discussion in a later section).

The gamma ray log (GR) is a measure of the natural radioactivity of the formation, which is directly proportional to the amount of clay minerals. The log can be scaled to represent an approximation of the shaliness of the formation (0 = no shales to 100 = only shales). In Figure 2.3e this ‘pseudo’ shaliness log can be compared with the clay minerals percentage observed on smear slides from core samples (dots) [Paull *et al.* 1996]. While the log does not reproduce the exact variability of the core observations, it remains in the range of the observed clay fraction. Both log and core data indicate only limited compositional changes over the entire hole [Paull *et al.*, 1996] and give a reasonable estimate of the proportions of the principal lithological components.

### 2.3.1 Sonic logging

In poorly consolidated sediments, when  $V_s$  is lower than the sound velocity in water, the shear waves generated by monopole acoustic sources are refracted away from the borehole and  $V_s$  can not be measured directly using conventional logging tools [Toksöz and Cheng, 1991]. On the Blake Ridge, an experimental dipole tool was deployed in which a standard monopole source (for  $V_p$ ) and a wide-band dipole source are used. The dipole directional source generates flexural waves that propagate in the formation at a velocity close to  $V_s$  [Chen, 1988]. The waveforms generated by both sources are each recorded at three separate receivers (see tool geometry Figure 2.4a). Figures 4b and 4c display three sets of dipole waveforms representative of the data recorded at different depths at Sites 995 and 997. Except for the greatest depths, the waveforms recorded by the farthest receiver (3) are all very weak. The straight lines on these figures mark the detection of the flexural wave and are indicative of the velocity - steeper slopes indicate higher shear velocities. The differences between these waveforms will be discussed below.

The  $V_s$  log was computed from the dipole waveforms by a semi-automatic cross-correlation analysis between receivers, similar to the cross correlation method described by *Willis and Toksöz* [1985]. A time window is selected for each trace to specify the approximate arrival time and the duration of a given event. A velocity window is specified to limit the allowable shifts on the cross correlation function, and the event's slowness is calculated by determining the shift resulting in a global maximum in the cross correlation function. This procedure was applied to the different receiver pairs (1-2, 1-3, 2-3) along the entire interval logged in Hole 995B. At each depth, we chose the value of slowness corresponding to the highest correlation coefficient. These correlation coefficients are displayed in Figure 2.3f. In most cases, the highest correlation was obtained between receivers 1 and 2, the furthest waveform being generally too weak for strong correlation (see Figure 2.4B). Low correlation values of the dipole waveforms in Figure 2.3f also generally correspond to large or irregular caliper readings (Figure 2.3a).

The entire set of monopole and dipole waveforms recorded in Holes 995B and 997A are shown in Figure 2.5, where red and blue colors indicate positive and negative amplitudes, respectively. Despite the poorer hole conditions in Hole 997A, some significant similarities and differences can be seen between the waveforms at the two sites. At both sites, the dipole waveforms recorded by receivers 2 and 3 are extremely attenuated in the upper part of the hole and show a distinct increase in amplitude with depth. This change occurs at ~440 mbsf in Hole 997A and at ~530 mbsf in Hole 995B. Below these depths, the monopole waveforms are more attenuated than in the overlying units, most noticeably between 530 and 630 mbsf in Hole 995B and below 600 mbsf in Hole 997A. The most significant differences between the two sites occur between 440 mbsf and 530 mbsf, where the dipole waveform recorded by receivers 2 and 3 have high amplitudes in Hole 997A and low amplitudes in 995B. In Figure 2.4, this is seen more clearly by comparing the waveform recorded at 475m in Hole 995B (Figure 2.4b) and at 485 m in 997 (4c). The monopole waveforms in Hole 997A are also slightly attenuated

between 440 and 480 mbsf. Hole 995B does not show an equivalent feature. These comparisons indicate different elastic properties at the two sites immediately below ~440 mbsf, which is the depth of the BSR [Paull *et al.*, 1996].

The  $V_p$  and  $V_s$  logs derived from the waveforms recorded in Hole 995B are shown in Figures 3g and 3h, respectively. The  $V_p$  log values are similar to interval velocities interpreted from offset VSP experiments (dots) reported by *Holbrook et al.*, [1996].  $V_s$  values less than 800 m/s were measured over most of the logged interval and are too low to have been recorded with a monopole source. The  $V_s$  log has a slightly higher gradient with depth above the BSR than the trend compiled by *Hamilton* [1979] for marine clastic sediments (dotted line). Below 440 mbsf,  $V_s$  follows the *Hamilton* trend, with value systematically lower than this reference profile. To our knowledge, these data represent the first open hole shear wave log ever recorded in hydrate-bearing sediments. In Figure 2.3j, we also show the  $V_p/V_s$  ratio, which is often used as an indicator of free gas [Hamilton, 1979]. The good comparison of  $V_p/V_s$  with the trend defined by *Hamilton* [1979] for marine clastic sediments (dotted line) suggests that the Blake Ridge sediments follow an overall normal trend with depth.

### 2.3.2 Data Interpretation

The qualitative interpretation of the logs and sonic waveforms in Figures 2.3 and 2.5 delineates four intervals with distinct signatures:

- (I) above ~200 mbsf
- (II) between ~200 and ~440 mbsf
- (III) between ~440 and ~520 mbsf
- (IV) below ~520 mbsf

The velocity gradients in these intervals are compiled in table 1.

In (I), the sediments are unconsolidated and the caliper log shows extremely poor hole conditions. No clear trend or correlation between the different logs is observed.

In (II), initial visual inspection, chemical analysis, and thermal measurements on the recovered cores, as well as pressurized samples collected with the Pressure Core Sampler (PCS) all indicate that gas hydrate is disseminated in the pore space throughout the formation [Paull *et al.* 1996; Dickens *et al.*, 1997]. A conversion from travel time to depth using the  $V_p$  log [Paull *et al.*, 1996] shows that the seismic blanking described in Figure 2.1 extends over this interval. Both  $V_p$  and  $V_s$  increase more rapidly with depth than in the other intervals (see Table 1). Although  $V_s$  values remain lower than the Hamilton [1979] profile, the gradient ( $0.817 \text{ s}^{-1}$ ) is higher than in the Hamilton curve ( $0.58 \text{ s}^{-1}$ , see Table 1). The high  $V_p$  and  $V_s$  gradients are interpreted to reflect an enhanced consolidation associated with the presence of hydrates within this interval.

The top of (III) corresponds to a strong decrease in  $V_p$  in both log and VSP data. Paull *et al.* [1996] attribute this decrease to the presence of free gas. The  $V_s$  gradient over this interval is lower than in the overlying unit and follows the trend of Hamilton [1979] (see Table 1) but there is no sharp decrease in  $V_s$  matching the change in  $V_p$ . Note that the low values of  $V_s$  between 470 and 490 mbsf are associated with low waveform correlation under degraded hole conditions and are not reliable (see correlation coefficient and caliper in Figure 2.3a). Anstey [1991] points out that the presence of free gas should not significantly affect the shear velocity of water-saturated marine sediments, as neither fluid transmits shear energy. The observation of a strong decrease in  $V_p$  with no clear change in  $V_s$  supports the interpretation of the presence of free gas in this interval. However, while the presence of free gas should cause a drop in  $V_p/V_s$  [Hamilton, 1979], the curve in Figure 2.3i does not decrease, suggesting that unit (III) has a mechanical behavior different from ‘normal’ partially gas-saturated sediments. Table 1 indicates that the lowest  $V_p$  and  $V_s$  gradients at Site 995 were measured in this unit, perhaps indicating the increasing dissociation of hydrates with depth, that would deprive progressively the sediments from the enhanced consolidation that they had while in the

core of the Hydrate Stability Zone. The nature of this transition zone will be discussed farther.

Although core observation, chloride analysis of pore fluid samples, and core temperature measurements did not indicate gas hydrate below 440 mbsf, the theoretical thermodynamic Gas Hydrate Stability Zone (GHSZ) is predicted by heat flow measurements to extend to ~540 mbsf [Paull *et al.*, 1996]. While the logs display differences across the BSR, the sonic waveforms have the same character in unit (III) as in unit (II): strong monopole waveforms and attenuated dipole. If, in particular, the strong attenuation of the dipole waveforms is indicative of the presence of hydrates above the BSR, some hydrates are also present in this deepest part of the GHSZ.

In (IV), the strong attenuation of the compressional waveforms and the high amplitude of the shear waveforms can be explained by the presence of partially gas-saturated sediments. *Murphy* [1982] made observations of similar phenomena in laboratory experiments on partially gas-saturated sediments. In this interval both log and VSP values show that  $V_p$  is anomalously low, particularly between 440 and 620 mbsf, and that  $V_p/V_s$  decreases significantly below ~530 mbsf. These observations are characteristic of normally consolidated sediments that are partially gas-saturated, but do not contain hydrates.

### 2.3.3 Porosity correction and gas hydrate saturation from resistivity log

Assuming that the higher log resistivity observed in interval (II) is caused by the presence of electrically resistive gas hydrates, the fractional hydrate saturation in the pore space ( $S$ ) can be expressed as a function of the ratio of the measured resistivity ( $R_t$ ) to the resistivity of the same formation saturated with water ( $R_0$ ). This is given by a modified version of Archie's relation :

$$S = 1 - (R_0/R_t)^{1/n} \quad (\text{Paull et al, 1996}) \quad (3)$$

In this formulation, it is assumed that the resistivity of water saturated sediments ( $R_o$ ) can be considered as a baseline function of depth. In Hole 995B, *Paull et al.* [1996] and *Collett and Ladd* [1998] approximate  $R_o$  by a least square linear fit with depth calculated in the hydrate-free sediments:  $R_o = 0.8495 + 2.986 \cdot 10^{-04}z$ . Laboratory experiments on hydrated sediments by *Pearson et al.* [1983] yielded a value of  $n = 1.9386$ . *Paull et al.* [1996], *Collett*, [1998] and *Collett and Ladd* [1998] give a complete description of this method, which compares well with more rigorous saturation evaluations that include in particular the variation of fluid salinity with depth. The resulting gas hydrate saturation is shown in Figure 2.3j, displaying saturation values consistently between 5 and 10% over interval (II). However, the dissociation of hydrates in the proximity of the borehole due to drilling reduces the salinity of the pore fluid [*Paull et al.*, 1996], which consequently increases the measured resistivity. Therefore, this saturation estimated from the resistivity log represents a maximum expected value.

The volume of methane recovered from each Pressure Core Sampler (PCS) core was used to calculate discrete *in situ* saturation values. The amount of methane in each sample was calculated by dividing the volume recovered by the molecular volume of methane at surface conditions (23.6 l/mol [*Dickens et al.*, 1996]). This amount was converted to an *in situ* volume of methane by multiplication by the *in situ* molecular volume of hydrate (136.2 cm<sup>3</sup>/mol [*Dickens et al.*, 1996]) or of free gas, depending on the depth of the sample. The molecular volume of free gas was calculated from *in situ* pressure and temperature assuming a perfect gas behavior. The methane saturation is the ratio of the *in situ* methane volume to the total pore space measured in the PCS core. Between the BSR and the bottom of the GHSZ, two possible methane saturations can be calculated, depending on whether the recovered methane is present as hydrate or as free gas. The various *in situ* methane saturation estimates and the saturation derived from the resistivity log are shown in Fig 3j. As anticipated, the saturations computed from the resistivity log

above the BSR are systematically higher than the PCS-derived hydrate saturation values (filled circle).

In interval (II), the presence of electrically-insulating hydrates decreases the connectivity between the pores and increases the bulk resistivity of the formation (Figure 2.3c). Archie's formulation [Archie, 1942] applied to the resistivity log then underestimates the porosity in this unit (see Figure 2.3d). In order to compensate for this effect, we use the hydrate saturation (S) calculated using Eq. (3) to correct the porosity in this interval. Assuming that the hydrates increase the resistivity only by occupying part of the pore space, the "corrected" porosity ( $\Phi_c$ ) can be calculated from the value estimated by Archie's law ( $\Phi$ ) by  $\Phi_c = \Phi/(1 - S)$ . This corrected value of the porosity is used in the elastic models described later.

## 2.4 Elastic Moduli of Hydrate-bearing sediments

While the qualitative analysis of the  $V_p$  and  $V_s$  logs suggests increased lithification within hydrate-bearing sediments, the characterization of the quantitative mechanical changes requires a more complete analysis of the elastic properties of the formation. The bulk (K) and shear (G) moduli can be used to directly relate changes in lithology and lithification to mechanical properties. They integrate  $V_p$ ,  $V_s$  and  $\rho$  and can be calculated from the log data using :

$$G = \rho V_s^2 \quad (4a) \quad \text{and} \quad K = \rho \left( V_p^2 - \frac{4}{3} V_s^2 \right) \quad (4b)$$

Despite the poor quality of the density log (Figure 2.3b), we chose to use its values to calculate the elastic moduli in order to preserve the high (15 cm.) vertical resolution of the logs in our analysis. As the log density data are consistently about 0.1 g/cc<sup>3</sup> lower than the core data (which corresponds to ~6% error for an average 1.7 g/cc<sup>3</sup> density), the moduli calculated from the log should underestimate the actual values. We will see later

that this underestimation does not affect significantly the quantitative hydrate saturation estimates based on the elastic moduli models.

The shear modulus calculated from the  $V_s$  and  $\rho$  logs and Eq.(4a) is shown in Figure 2.6a. Its variations are very similar to the shear velocity log as a result of the limited variability in the density log. The steady stiffening of the sediments with depth and slightly higher rigidity of the hydrated sediments is illustrated by a shift between the depth gradients above 440 mbsf and below 520 mbsf. The shear modulus is not affected at greater depth by the presence of free gas [Anstey, 1991]. Figure 2.6b shows that the bulk modulus displays more noticeable variations along the logged interval, which may correspond to very distinct mechanical behavior in the different units.

We compared  $K$  to two consolidation models relating the elastic properties of the sediments to their porosity and degree of lithification. *Wood* [1941] and *Gassmann* [1951] derived models which represent two end-members of the consolidation process of sediments, ranging from the suspension of particles in water (*Wood*) to consolidated sediments (*Gassmann*). The model originally described by *Wood* [1942] has been widely used [Guerin and Goldberg, 1996, Wilkens et al., 1992, Hamilton, 1971] and describes the mechanical behavior of unconsolidated sediments as particles in suspension. The compressibility (inverse of the bulk modulus) of such formations is given by a weighted average of the compressibilities of the grain aggregate ( $K_g$ ) and of the pore fluid ( $K_w$ ):

$$\frac{1}{K_{\text{Wood}}} = \frac{\Phi}{K_w} + \frac{1 - \Phi}{K_g} \quad (5)$$

where  $\Phi$  is in decimal fraction.

*Gassmann* [1951] established a relationship also widely used [Guerin and Goldberg, 1996, Hamilton et al., 1982, Hamilton, 1971] expressing the bulk modulus of sediments as a function of the pore fluid and grain properties and of the porosity of the formation. In this formulation the bulk modulus of the dry sediments is defined as the frame bulk

modulus ( $K_f$ ), which results from the interaction between grains, and the bulk modulus of the saturated sediments is calculated by:

$$K = K_g \frac{K_f + Q}{K_g + Q} \quad \text{with} \quad Q = \frac{K_w(K_g - K_f)}{\Phi(K_g - K_w)} \quad (6)$$

(notations same as in Eq. (5)).

*Hamilton* [1971] compiled a large amount of laboratory marine sample data to establish a relationship between the frame bulk modulus and the porosity of marine sediments. In particular, he defines the two following relationships for respectively silt clays and for fine sands:

$$\log(K_f(\times 10^{-9} \text{ Pa})) = 1.7358 - 4.25075\Phi \quad (7a)$$

$$\text{and} \quad \log(K_f(\times 10^{-9} \text{ Pa})) = 1.70932 - 4.25391\Phi \quad (7b)$$

with  $\Phi$  expressed as a decimal fraction. In these two formulas, the first term on the right represents the (logarithm of) the grain bulk modulus  $K_g$  which is the frame modulus at zero porosity. Note that we use here SI units for the moduli (i.e. Pa.), yielding a slightly different expression than in *Hamilton* [1971] where dynes/cm<sup>2</sup> were used. We simplified these two distinct relationships to define a single formula for clastic sediments:

$$\log(K_f) = \log(K_g) - 4.25\Phi \quad \text{or} \quad \log(K_f/K_g) = -4.25\Phi. \quad (8)$$

This simplification ensures that for any value of the aggregate grain modulus, the frame bulk modulus equals the grain bulk modulus at  $\Phi = 0$ . We refer to the combination of *Hamilton's* and *Gassmann's* equations as the *Gassmann/Hamilton* model.

The aggregate grain bulk modulus ( $K_g$ ) in the *Wood* and *Gassmann/Hamilton* models can be calculated by a *Voigt-Reuss-Hill* average of the grain moduli of the two main mineral phases, sand ( $K_s$ ) and clay ( $K_c$ ) [*Hamilton*, 1971]. Using the normalized *Gamma Ray* values ( $\gamma$ ) to define the clay mineral percentage in these sediments (see *Figure 2.3e*) and grain moduli values in *Table 2*, the grain bulk modulus can be calculated by:

$$K_g = \frac{1}{2} \left[ \gamma K_c + (1 - \gamma) K_s + \frac{K_s K_c}{K_s \gamma + K_c (1 - \gamma)} \right]. \quad (9)$$

We calculate the predictions of the Wood and Gassmann/Hamilton models at Site 995 to define an expected range of compressibility for the Blake Ridge sediments. In normal sediments, the degree of consolidation may be indicated by the closeness of the measured bulk modulus to either the Wood (unconsolidated) or Gassmann/Hamilton (consolidated) model [*Guerin and Goldberg, 1996*]. Because these sediments were deposited extremely quickly [*Paull et al., 1996*], their porosity is very high and the range between these two models is particularly narrow. This is illustrated by the very narrow range between the two fine dotted lines in Figure 2.6, representing respectively Wood's and Gassmann/Hamilton's models.

Above 250 mbsf, the bulk modulus is roughly in the range of the two models. The fluctuations can be likely attributed to poor hole conditions, rather than to consolidation differences. Below 520 mbsf, the presence of free gas reduces the bulk modulus to values lower than either model, which both assume the pore fluid to be water. Between these two depths, and more distinctly above 440 mbsf the measured bulk modulus is significantly greater than the Gassmann/Hamilton model [*Guerin et al., 1996, Guerin and Goldberg, 1997*]. Considering in addition that the poor log density data likely result in an underestimation of the bulk modulus, the anomalously high estimate may be due to the presence of hydrates. Below the BSR, the measured bulk modulus remains generally higher than the Gassmann/Hamilton model despite the indications that free gas is present. We interpret this to indicate that the elastic and mechanical properties of the sediments at Site 995 are dominated by the influence of hydrates down to the bottom of the GHSZ.

Considering that the sediments in unit (II) (~200 to 440 mbsf) are consolidated and that a frame bulk modulus exists, Eq. (6) can be reworked to calculate the frame bulk modulus when the bulk modulus of the saturated sediments is known:

$$\frac{K_f}{K_g} = \frac{K[\Phi(K_g - K_w) + K_w] - K_g K_w}{\Phi K_g (K_g - K_w) + K_w (K - K_g)} \quad (10).$$

Using the measured porosity and moduli from the logs in Hole 995B, we use Eq. (9) to compute the frame bulk modulus of hydrate-bearing sediments, shown as a function of porosity in Figure 2.7. These data can be fit by a logarithmic relationship similar to Eq.(8):

$$\log(K_f/K_g) = 3.02 - 7.372\Phi \quad (\text{regression coefficient} = 0.734) \quad (11).$$

Note that in order to define a statistically significant relationship, only data where the coherence of the shear wave processing was high ( $>0.7$ ) are used. Figure 2.7 shows that the frame modulus of hydrated sediment is about 20 times higher than the frame modulus of normal clastic sediments of the same porosity. The limited porosity range on the Blake Ridge (50-70 %) and the relatively low regression coefficient in Eq. (11) do not allow to extrapolate this equation much beyond this range. However we speculate that for low (0-20%) porosities, the strong interactions between grains will not be additionally increased by the presence of hydrates, whose elastic moduli are lower than those of the grains, and that the expression of the frame modulus becomes closer to Eq.(8) at very low porosity. At high ( $>80\%$ ) porosity, particles, grains and hydrates, are merely in suspension in water, having little rigidity [Wood, 1942]. Under these conditions, the influence of hydrates on the elastic moduli should also decrease at very high porosity.

## 2.5 Methane Saturation from elastic moduli

The deviation of the frame bulk modulus from the Hamilton trend shows that the presence of hydrates affects the interaction between grains and transforms the elastic moduli of the Blake Ridge sediments. Various existing models may be used to describe the elastic properties of a formation as a function of hydrate concentration. These models differ primarily by their assumption of how hydrates are arranged within the pore space.

Following *Kuster and Toksöz* [1974], *Zimmerman and King* [1986] and *Lee et al.* [1996] have formulated the propagation of seismic waves in hydrate- or ice-bearing unconsolidated sediments in terms of wave scattering through a three-phase medium. The

formation is represented by spherical clay grains embedded in a matrix composed of spherical inclusions of water within an hydrate or ice framework. For a two-phase medium composed of spherical inclusions within an uniform matrix, the effective bulk and shear moduli are given by Kuster and *Toksöz* as:

$$K = K_m \frac{1 + \left[ 4G_m (K_i - K_m) / ((3K_i + 4G_m)K_m) \right] I_c}{1 - \left[ 3(K_i - K_m) / (3K_i + 4G_m) \right] I_c} \quad (12),$$

$$\text{and } G = G_m \frac{(6K_m + 12G_m)G_i + (9K_m + 8G_m) \left[ (1 - I_c)G_m + I_c G_i \right]}{(9K_m + 8G_m)G_m + (6K_m + 12G_m) \left[ (1 - I_c)G_i + I_c G_m \right]} \quad (13),$$

where the i and m subscripts refer to the inclusion and the matrix properties, respectively, and  $I_c$  is the volumetric fraction of the inclusion. *Zimmerman and King* [1986] and *Lee et al.* [1996] extend these formulae to a three-phase medium. They first estimate the moduli of an ice-water matrix with (12) and (13), water being considered as the inclusion. The moduli of the three-phase medium are then calculated assuming that the clay grains are spherical inclusions within the ice-water matrix. The justifications for these assumptions are discussed in the two papers. Like *Lee et al.* [1996], we refer to this three-phase model as the K-T model. In order to estimate the hydrate concentration from the observed moduli, we use an inverse approach to this model. Using the porosity log and the parameter values in Table 2 and considering the grains as the inclusion material ( $I_c = 1 - \Phi$ ), we numerically increase the hydrate concentration, and consequently the hydrate-water compound moduli, in (12) and (13) until the calculated moduli matches the measured moduli. The saturations independently estimated by this method may be compared to the methane saturation estimates from the PCS and resistivity log. In Figure 2.9a, the results from the K-T model are shown to be generally greater than these previous estimates [*Guerin and Goldberg*, 1997].

An alternative model may be used which focuses on the interaction between the grains and hydrates acting as an intergranular cement [*Dvorkin et al.*, 1991 and 1994; *Dvorkin and Nur*, 1996]. It is based on the estimation of the shear and normal stiffness of

two-grain combinations with elastic cement at the contact. The frame is assumed to be a random pack of identical spherical grains, with an estimated average of  $n$  contacts per grain. The effective dry-rock bulk modulus ( $K_{\text{eff}}$ ) is defined by *Dvorkin and Nur* [1996] as:

$$K_{\text{eff}} = \frac{1}{6}n(1 - \Phi)M_c S_n, \quad \text{with} \quad M_c = \rho_c V_{pc}^2. \quad (14)$$

$M_c$  is the compressional wave modulus of the cement,  $\rho_c$  is its density, and  $V_{pc}$  its compressional velocity.  $S_n$  is proportional to the stiffness of a cemented two-grains combination and depends on the amount of cement and on the properties of the cement and the grains. The amount of cement is expressed by a parameter  $\alpha$ , which in the configuration where cement is deposited on circular layers between grains is the ratio of the radius  $a$  of the circular layer of cement to the grain radius  $R$  (Figure 2.8a). In this configuration,  $\alpha$  can be related to the hydrate fraction in the pore space ( $S$ ) by :

$$\alpha = \sqrt[4]{\frac{S\Phi}{3n(1 - \Phi)}} \quad (15a).$$

If the cement is deposited evenly on the grain surface (see Figure 2.8b),  $\alpha$  is given by:

$$\alpha = \sqrt{\frac{2S\Phi}{3(1 - \Phi)}} \quad (15b).$$

Statistical approximations of the solution of the rigorous cementation theory for the expression of  $S_n$  as a function of  $\alpha$  and of the properties of the grain and of the cement are given in the appendix of *Dvorkin and Nur* [1996].

Since Eq.(14) is defined for dry sediments, we use Eq. (10) to calculate the effective dry bulk modulus  $K_{\text{eff}}$  from our measured values of  $K$  and  $\Phi$ . Assuming an average value of  $n = 9$  contacts per grain [*Dvorkin and Nur*, 1996] and using the porosity log and the parameters in Table 2, we incrementally increase the hydrate concentrations in the two expressions of Eq.(15), and subsequently the stiffness  $S_n$  in Eq.(14), to match  $K_{\text{eff}} = K_r$ . Figure 2.9b shows the methane concentration from hydrate estimated by the cementation theory for the two different  $\alpha$  values. Above the BSR, the best agreement with the PCS

data is provided by the model assuming an uniform distribution of hydrate around sediment grains [*Guerin and Goldberg, 1997*].

To estimate the hydrate content where hydrates and free gas might coexist below the BSR, we applied the same procedure using the bulk modulus of a mixture of water and 1% gas for the fluid bulk modulus (see below for the methodology of fluid elastic moduli calculation). This gives the amount of hydrate that would be necessary to reproduce the observed data if as much as 1% of the pore space was occupied by free gas. The resulting hydrate saturation below 440 mbsf is shown in Figure 2.9c. These values compare well with the saturations estimated from the recovered PCS samples below the BSR.

Of the different hydrate saturation estimates derived from the logs, the best agreement with the PCS measurements is obtained with the cementation theory assuming a uniform hydrate distribution surrounding the grains (Figure 2.9b). All of the models suggest that hydrates are present down to ~520 mbsf, about 80 meters deeper than the BSR, and coexist with some free gas in this interval. We conclude therefore that the BSR marks the top of free gas occurrence rather than the bottom of the hydrate stability zone.

## **2.6 Determination of the free gas concentration**

Quantifying the free gas accumulation below the GHSZ is also crucial to the estimation of the total gas reserves on the Blake Ridge. For this, we again use the velocity logs and existing elastic wave models. Below 520 mbsf, the caliper log shows good hole conditions and the waveforms display high coherence, indicating that the bulk modulus reliably reflects changes in lithology or in the pore fluid. Because the gamma ray log remains relatively uniform, the strong variations in bulk modulus likely results from the presence of free gas, as discussed by *Paull et al.* [1996].

*Murphy* [1984] calculates the change in pore fluid compressibility due to the presence of free gas by a weighted average of the fluid moduli, assuming that the relative

configuration of the fluid phases has no effect on the velocities. This may be expressed by:

$$\frac{1}{K_{\text{fluid}}} = \frac{(1 - S_{\text{gas}})}{K_{\text{liq}}} + \frac{S_{\text{gas}}}{K_{\text{gas}}} \quad (16)$$

where  $S_{\text{gas}}$  is the fraction of pore space occupied by free gas, and  $K_{\text{liq}}$ ,  $K_{\text{gas}}$  and  $K_{\text{fluid}}$  are the bulk moduli of the liquid phase, the free gas, and of the fluid mixture, respectively. The amount of free gas in the sediments below 520 mbsf can be calculated by replacing  $K_w$  by this expression of  $K_{\text{fluid}}$  in the Gassmann/Hamilton model (Eq. 6) and numerically increasing the value of  $S_{\text{gas}}$  in Eq.(16) until reproducing the measured bulk modulus. Table 2 gives the values used for  $K_{\text{liq}}$  and  $K_{\text{gas}}$ . The estimated free gas saturation is shown in Figure 2.9c, together with the hydrate estimation derived below the BSR, assuming that 1% of the pore space was occupied by free gas. This figure shows the total amount of methane, in the form of hydrate and free gas, trapped under the BSR. As the compressibility of free gas is high and the formation has a high porosity, only a relatively small amount of gas (no more than 5%) is necessary to produce the low bulk modulus observed below 520 mbsf.

$S_{\text{gas}}$  estimates agree well below 520 mbsf with the methane saturation derived from the resistivity log using the modified Archie formulation (the grey area between 570 and 630 mbsf in Figures 9a,b). This is expected since the Archie relationship was originally derived for empirical estimations of free gas [Schlumberger, 1989]. Below the GHSZ, no hydrate is present and a free gas relationship fully applies.

## 2.7 Discussion

### 2.7.1 Quality of the logging data

Figure 2.10 summarizes the changes in sonic waveforms and bulk modulus in Hole 995B and a combined estimate of the total methane distribution. Because of the poor quality of the density data and of the limitations of Archie's law in clay-rich sediments to

calculate porosity, it is necessary to estimate the possible error resulting from the use of these values in our estimation of the moduli and of hydrate saturations. For this purpose we have used the density measured on core samples at Site 995 [Paull *et al.*, 1996] to recalculate the elastic moduli of the sediments and thereafter we used the porosity measured on cores to re-estimate hydrate saturations with the K-T model and the cementation theory. Both density and porosity are sampled at a lower resolution on core than in logs, hence the discrete data were interpolated between intervals to the closest measured value.

The resulting hydrate saturations were generally slightly lower using core than log data, however we reach the same conclusions regarding the general distribution of hydrates with depth. The cementation theory best describes the elastic properties of hydrate-bearing sediments on the Blake Ridge with either data set. In Figure 2.10, we compare the results of the cementation theory calculated with the core data (green curve) to the results derived from the log (blue line, as in Figure 2.9b) for the case of hydrates being uniformly distributed on the grains. The difference between the two curves is less than 5%, and they show similar hydrate distribution with depth.

### **2.7.2 Comparison of the Models**

Qualitatively, all the models indicate the presence of hydrates to ~520 mbsf at Site 995. Quantitatively, they produce considerably different methane saturation values. We use the values derived from the PCS data as a reference for comparison. As noted earlier, the insulating properties of hydrates cause methane saturation derived from the resistivity log to be systematically higher than the PCS values. Results of the K-T model are even higher. Lee *et al.* [1996] also concluded that the K-T model overestimated hydrate concentrations and they proposed a weighted equation as a more accurate and versatile alternative. We interpret the high estimates of the K-T model as a consequence of its statistical treatment of elastic waves propagation which does not account for the

interactions between inclusions [*Kuster and Toksöz, 1974*]. Without such interaction, hydrates increase the bulk modulus by partially replacing water within the pore space, increasing only the value of the pore fluid modulus in Eq.(12). This process requires more hydrate to produce the same consolidation than by stiffening the matrix frame modulus at the grains contacts. Because the frame bulk modulus of hydrate-bearing sediments may 20 times higher than in hydrate-free sediments (see Figure 2.7), the K-T model does not completely describe the effects of hydrate deposition on grain interactions and elastic wave propagation.

The cementation theory of *Dvorkin and Nur [1996]* agrees well with saturation estimates from the PCS when hydrates are assumed to uniformly coat grains, but very low values are obtained when hydrates are assumed to be only at the grain contacts. However, since the Blake Ridge sediments are clay-rich, they are not well represented by spherical grains, as this model assumes, and this single data set does not allow us to discriminate confidently between the two end-member configurations. In addition, this theory was actually developed and experimentally tested in sands with lower porosity (less than 36%) [*Dvorkin and Nur, 1996*]. Therefore, additional data in a variety of lithologies and porosity ranges, particularly in hydrate-bearing sands, are necessary to determine conclusively the actual hydrate-grain configuration. A combination of coated grain surfaces and grain contact cementation may be realistic. At this stage we consider the results of the cementation theory for uniformly hydrate-coated grains as the most accurate of our estimates of methane saturation near Hole 995B.

*Ecker et al. [1996]* applied the cementation theory to velocities derived from seismic by AVO analysis and concluded that hydrates form in the open pore space away from either grain contacts or surfaces. The reason for this interpretation is that the shear velocity values derived from AVO analysis are lower in the hydrate-bearing sediments than below the BSR. Such low values are not observed in the  $V_s$  log. Additional *in situ*  $V_s$  logs across other BSR's are needed to resolve this difference.

### 2.7.3 Coexistence of hydrates and free gas from logs at Site 995

Figure 2.10 summarizes the various indications from elastic data that gas hydrate is present below the BSR down to ~520 mbsf. *Paull et al.* [1996] and *Dickens et al.* [1997] conclude from chlorinity dilution profiles that gas hydrate is present only above ~440 mbsf. Our extension of this zone to the BGHSZ is based on four key observations: (1) Neither the monopole or the dipole waveforms display any change across the BSR at ~440 mbsf. In particular, the dipole waveforms remain strongly attenuated as in the hydrate-bearing sediments above the BSR. The strong attenuation of shear waveforms without attenuation of the compressional waveforms can be attributed to slight partial free gas saturation [*Murphy*, 1982]. The main change in the character of the waveforms, and in the elastic properties of the formation, occurs below ~520 mbsf where the dipole amplitudes increase and the monopole waveforms become attenuated, indicating higher free gas saturation. (2) Above 520 mbsf, the bulk modulus remains generally higher than the Gassmann/Hamilton model. It decreases to lower values below this depth, which is characteristic of the influence of free gas. Therefore, between the BSR and 520 mbsf, the bulk modulus and the sonic waveforms have characteristics similar to the hydrate-bearing sediments above the BSR. Below 520 mbsf both waveforms and bulk modulus are typical of the influence of free gas. (3) The single methane saturation value from the PCS between 440 and 520 mbsf (8% from one sample at 493 mbsf) is at least four times higher than the values (<2%) derived from the Gassmann/Hamilton model. If the amount of methane sampled was present as free gas in this interval, the measured bulk modulus would be much lower. (4) Finally, there is no lithological or structural change between the BSR and 520 mbsf, and no obstacle to the upwards migration of free gas. The presence of hydrates in part of the pore space above 520 mbsf may reduce the bulk permeability of the sediments and trap free gas below this depth as it migrates upwards.

#### **2.7.4 Mechanisms for coexistence of hydrates and free gas**

*Ruppel* [1997], *Hovland et al.*, [1997] and *Clennell et al.* [1995] reported a difference between the depth of the BSR and the theoretical bottom of the GHSZ. They associate this discrepancy with capillary forces that develop in fine grained sediments and reduce the temperature where hydrates dissociate. *Hovland et al.* [1997] underline that hydrates preferably initiate in larger pore space, and, reciprocally, dissociate first in smaller pores with strong capillary effects. In the interval between the BSR and the bottom of the GHSZ, therefore, hydrates in smaller pores may have dissociated and released free gas, while they remain present within the larger pores. The two phases would then coexist in this interval.

The coexistence of hydrates and free gas also proceeds as a normal stage during hydrate dissociation. *Christiansen and Sloan* [1994] describe the progressive heating in a reactor of synthetic hydrates and observe that “as the system is heated, visible hydrate agglomerates decompose into the liquid and vapor phase, but quasi-crystalline metastable cluster structures remain in the liquid up to a certain degree of heating”. Similarly, as sediments accumulate on the Blake Ridge and the BSR slowly migrates upwards, progressive heating and dissociation of hydrates would tend to create an interval where both crystalline and vapor gas coexist.

Also, since methane solubility in water increases with depth within the GHSZ [*Zatsepina and Buffet*, 1997], the pore fluid above 520 mbsf should be oversaturated with methane compared to the deeper sediments and the occurrence of free gas should be favored.

#### **2.7.5 Comparison between Sites 994, 995 and 997**

The coexistence of free gas and gas hydrates over 70 meters below the BSR on the Blake Ridge may explain some of the differences in seismic character at Sites 994, 995 and 997. The bad hole conditions at Site 994 did not allow the recording of reliable  $V_s$

data, but our analysis and the characteristics of the BSR at Site 995 suggest that it represents an intermediate location, and perhaps an intermediate process, between the other two sites (see Figure 2.1). At Site 997, the BSR at 4.25 sec (two-way travel time) is strong and immediately underlain by high seismic amplitudes for more than 100 milliseconds. At Site 994, there is no BSR and low seismic amplitudes persist to ~4.32 sec twtt (e.g. ~530 mbsf) [Paull *et al.*, 1996]. Since heat flow values are similar at the three sites (34-36 mW/m<sup>2</sup> [Paull *et al.*, 1996]), the theoretical GHSZ extends to the same depth and gas hydrates may be present to at least 520 mbsf. The differences between the three sites may be explained by the absence or presence of, and the amount of, free gas. The low seismic amplitudes to ~530 mbsf at Site 994 may indicate that gas hydrate is present to this depth, but that any free gas, either rising from a deeper source or resulting from gas hydrate dissociation, is driven past the south-west edge of the BSR through the numerous faults described by Dillon *et al.* [1996]. Lateral gas migration along such faults may also reduce the accumulation of free gas at Site 995. In contrast, the location of Site 997 on the topographic crest of the Blake Ridge favors the structurally-controlled accumulation of free gas, which is responsible for the high seismic amplitude below the BSR and for the high amplitude of the dipole waveforms below 440 mbsf in Hole 997A (Figure 2.5, see also Figure 2.4c at 485 mbsf). Besides a 40 m-thick interval below 440 mbsf, the monopole waveforms at Site 997 are not significantly attenuated between 440 mbsf and 550 mbsf. Hence, either the stiffness of the sediments is maintained by the occurrence of some hydrates to this depth despite the presence of free gas or the amount of free gas is not high enough to attenuate the monopole waveforms [Murphy, 1982]. In summary, at Site 997, a high concentration of free gas responsible for the attenuation of the monopole waveforms occurs from 440 to 480 mbsf. Between 480 and 550 mbsf, hydrates and free gas coexist as at site 995, but a higher concentration of free gas increases the dipole waveform amplitudes, despite the presence of hydrates. At greater

depths, and most notably below 600 mbsf, high concentrations of free gas are indicated by the strong attenuation of the monopole waveforms.

## 2.8 Conclusions

Our principal results on the distribution of methane and methane hydrate on the Blake Ridge are: (1) Hydrates appear to act as an intergranular cement and increase the rigidity and the bulk modulus of the host sediment; (2) the BSR marks the top of the occurrence of free gas, not the base of the gas hydrates; and (3) some form of hydrate exists below the BSR on the Blake Ridge, coexisting with free gas.

These conclusions are based only on the Blake Ridge dataset, recorded only in one hole under rugged marine borehole logging conditions. Additional shear sonic tool deployments are necessary, as well as further studies to refine the model for the configuration of hydrates in the pore space of clay-rich sediments. As a first step towards a better understanding, we recommend the evaluation of hydrate concentrations using *in situ*  $V_p$  and  $V_s$  logs in hydrate-bearing sands which correspond to the laboratory-tested models of the cementation theory.

Nevertheless, the quantification of the *in situ* elastic properties of the Blake Ridge hydrate-bearing sediments using cementation theory yields methane concentrations similar to *in situ* discrete sample measurements. The amplitudes of sonic logging waveforms are also effective qualitative indicators of the changes in the mechanical properties of the formation resulting from the presence of gas hydrates or free gas.

## References

- Anstey, N.A., Velocity in thin section, *First Break*, 9(10), 449-457, 1991.
- Archie, G.E., The electrical resistivity log as an aid in determining some reservoir characteristics, *J. Pet. Technol.*, 5, 1-8, 1942.
- Chen, S.T., Shear wave logging with dipole sources, *Geophysics*, 53, 659-667, 1988.

- Christiansen, R.L., and E.D. Sloan, Mechanisms and kinetics of hydrate formation, *in* International Conference on Natural Gas Hydrates, edited by E.D. Sloan, J. Happel, and M.A. Hnatow, *Ann. of the N.Y. Acad. of Sci.*, 715, 283-305, 1994.
- Clennell, M.B., M. Hovland, D. Lysne, and J.S. Booth, Role of capillary forces, coupled flows and sediment-water depletion in the habitat of gas hydrate, *Eos Transactions of the American Geophysical Union*, 76(16), 164-165, 1995.
- Collett, T.S., and J. Ladd, Detection of gas hydrate with downhole logs and assessment of gas hydrate concentrations (saturations) and gas volumes on the Blake Ridge with electrical resistivity log data, *submitted to Proc. ODP, Sci. Results*, 164, 1998.
- Collett, T.S., Well log evaluation of gas hydrate saturations, *Trans. SPWLA 39th Logging Symposium*, paper MM 1998.
- Dickens, G.R., C.K. Paull, P. Wallace, and the ODP Leg 164 Scientific Party, Direct measurements of in situ methane quantities in a large gas-hydrate reservoir, *Nature*, 385, 427-429, 1997.
- Dillon, W.P., D.R. Hutchinson, and R.M. Drury, Seismic reflection profiles on the Blake Ridge near sites 994, 995, and 997, in Paull, C.K., R. Matsumoto, P.J. Wallace, *et al.*, *Proc. ODP, Init. Repts., 164*: College Station, TX (Ocean Drilling Program), 47-56, 1996.
- Dvorkin, J., G. Mavko and A. Nur, The effect of cementation on the elastic properties of granular material, *Mechanics of Materials*, 12, 207-217, 1991.
- Dvorkin, J., A. Nur, and H. Yin, Effective properties of cemented granular material, *Mechanics of Materials*, 18, 351-366, 1994.
- Dvorkin, J., and A. Nur, Elasticity of high-porosity sandstones: theory for two North Sea data sets, *Geophysics*, 61, 1363-1370, 1996.
- Ecker, C., D. Lumlet, J. Dvorkin, and A. Nur, Structure of hydrated sediments from seismic and rock physics, *in* Proceedings, 2nd International Conference on Natural Gas Hydrates, Toulouse, 491-498, 1996.

- Gassmann, F., Elastic waves through a packing of spheres, *Geophysics*, 16, 673-685, 1951.
- Guerin, G., and D. Goldberg, Acoustic and elastic properties of calcareous sediments across a siliceous diagenetic front on the eastern U.S. continental slope, *Geophys. Res. Lett.*, 23(19), 2697-2700, 1996.
- Guerin, G., A. Meltser, and D. Goldberg, Results of acoustic and shear wave logging in gas hydrates; preliminary data from ODP Leg 164, *Eos, AGU Transactions*, 77(46), p. F322, 1996.
- Guerin, G., and D. Goldberg, Characterization of *in situ* elastic properties of hydrated sediments, *Eos, AGU Transactions*, 78(46), p. F339, 1997.
- Hamilton, E. L., Elastic properties of marine sediments, *J. Geophys. Res.*, 76, 579-601, 1971.
- Hamilton, E.L.,  $V_p/V_s$  and Poisson's ratios in marine sediments and rocks, *J. Acoust. Soc. Am.*, 66, 1093-1101, 1979.
- Hamilton, E. L., Bachman, R. T., Berger, W. H., Johnson, T. C., and Mayer, L. A., Acoustic and related properties of Calcareous deep-sea sediments, *J. Sed. Pet.*, 52(3), 733-753, 1982.
- Holbrook, W.S., H. Hoskins, W.T. Wood, R.A. Stephen, D. Lizarralde, and Leg 164 Science Party, Methane hydrate and free gas on the Blake Ridge from vertical seismic profiling, *Science*, 273, 1840-1843, 1996.
- Hollister, C.D., J.I. Ewing, *et al.*, *Init. Repts., DSDP, 11*, Washington (U.S. Govt. Printing Office), 1972.
- Hovland, M., J.W. Gallagher, M.B. Clennell, and K. Lekvam, Gas hydrate and free gas volumes in marine sediments: example from the Niger delta front, *Mar. Petr. Geol.*, 14, 245-255, 1997.

- Hyndman, R.D., and E.E. Davis, A mechanism for the formation of methane hydrate and seafloor bottom simulation reflectors by vertical fluid expulsion, *J. Geophys. Res.*, *97*, 7025-7041, 1992.
- Jarrard, R.D., K.A. Dadey and W.H. Busch, Velocity and density of sediments of Eirik Ridge, Labrador Sea: control by porosity and mineralogy, *Proc. ODP, Sci. Res.*, *105*, p. 811-835, 1989.
- Kvenvolden, K.A., Natural gas hydrate occurrence and issues, in *International Conference on Natural Gas Hydrates*, edited by E.D. Sloan, J. Happel, and M.A. Hnatow, *Ann. of the N.Y. Acad. of Sci.*, *715*, 232-246, 1994.
- Kuster, G.T., and M.N. Toksöz, Velocity and attenuation of seismic waves in two-phase media, 1, Theoretical formulation, *Geophysics*, *39*, 587-606, 1974.
- Lee, M.W., D.R. Hutchinson, W.P. Dillon, J.J. Miller, W.F. Agena, and A.B. Swift, Method of estimating the amount of in situ gas hydrates in deep marine sediments, *Mar. Petr. Geol.*, *10*, 493-506, 1993.
- Lee, M.W., D.R. Hutchinson, T.S. Collett, and W.P. Dillon, Seismic velocities for hydrate bearing sediments using weighted equation, *J. Geophys. Res.*, *101*, 20,347-20,358, 1996.
- Murphy, W.F., Massillon sandstone and Vycor porous glass, *J. Acoust. Soc. Am.*, *71(6)*, 1458-1468, 1982.
- Murphy, W.F., Acoustic measures of partial gas saturation in tight sandstones, *J. Geophys. Res.*, *89*, 11,549-11,559, 1984.
- Paull, C.K., R. Matsumoto, P.J. Wallace, et al., *Proc. ODP, Init. Repts.*, *164*, College Station, TX (Ocean Drilling Program), 1996.
- Pearson, C.F., P.M. Halleck, P.L. McGuire, R. Hermes, and M. Mathews, natural gas hydrates deposits: a review of in situ properties, *J. Phys. Chem.*, *87*, 4180-4185, 1983.
- Pecher, I. A., W.S. Holbrook, R.A. Stephen, H. Hoskins, D. Lizarralde, D.R. Hutchinson, W.T. Wood, Offset-vertical seismic profiling for marine gas hydrate exploration; is it a

- suitable technique? First results from ODP Leg 164, in *Proceedings of the 29th annual offshore technology conference*, Dallas, TX, 193-200, 1997.
- Ruppel, C., Anomalously cold temperatures observed at the base of the gas hydrate stability zone on the U.S. Atlantic passive margin, *Geology*, 25(8), 699-702, 1997.
- Sheridan, R.E., F.M. Gradstein, *et al.*, *Init. Repts. DSDP, 11*, Washington (U.S. Govt. Printing Office), 1983.
- Shipley, T.H., M.H. Houston, R.T. Buffler, F.J. Shaub, K.J. McMillen, J.W. Ladd, and J.L. Worzel, Seismic evidence for widespread possible gas hydrate horizons on continental slopes and rises, *AAPG Bull*, 63, 2204-2213, 1979.
- Schlumberger, Log interpretation principles/applications, Houston, TX (Schlumberger Educ. Services), 1989.
- Schlumberger, Log Interpretation Charts, Houston, TX (Schlumberger Wireline & Testing), 1994.
- Sloan, D.E., *Clathrate hydrates of natural gases*, Marcel Dekker, New York, 1990.
- Srivastava, W.B., M. Arthur, *et al.*, Proc. ODP, Init. Repts., 105: College Station, TX (Ocean Drilling Program), 1987.
- Toksöz, M.N., and Cheng, C.H., Wave propagation in a borehole, in *Shear waves in marine sediments*, edited by J.M. Hovem, M.D. Richardson, and R.D. Stoll, 257-265, Kluwer Academic Publishers, 1991.
- Tucholke, B.E., G.M. Bryan, and J.I. Ewing, Gas hydrate horizon detected in seismic reflection profiler data from the western North Atlantic, *AAPG Bull.*, 61, 698-707, 1977.
- Wilkins, R. H., C.H. Cheng, and J.A. Meredith, Evaluation and prediction of shear wave velocities in calcareous marine sediment and rocks, *J. Geophys. Res.*, 97, 9297-9305, 1992.
- Willis, M.E., and M.N. Toksöz, Automatic P and S velocity determination from full waveform digital acoustic logs, *Geophysics*, 48, 1631-1644, 1983.

Wood, W.T., P.L. Stoffa, and T.H. Shipley, Quantitative detection of methane hydrate through high-resolution seismic velocity analysis, *J. Geophys. Res.*, 99, 9681-9695, 1994.

Wood, A.B., *A textbook of sound*, G. Bell and Sons, Ltd, London, 1941.

Zastepina, O.Y., and B.A. Buffett, Phase equilibrium of gas hydrate: implications for the formation of hydrates in the deep sea floor, *Geophys. Res. Lett.*, 24(13), 1667-1570, 1997.

Zimmerman, R.W., and M.S. King, The effect of the extent of freezing on seismic velocities in unconsolidated permafrost, *Geophysics*, 51, 1285-1290, 1986.

## Tables

**Table 1:** Linear fit as a function of depth ( $z$ ) for data in Figs. 3 and 6a and equation of the  $V_s$  linear trend defined by *Hamilton* [1979]. The regression coefficient ( $R$ ) is given in brackets.

Unit	$V_p$ (m/s)	$V_s$ (m/s)	Shear modulus ( $\cdot 10^9$ Pa)
II	$1481.6 + 0.739z$ [0.873]	$220.7 + 0.817z$ [0.857]	$-0.1045 + 0.00158z$ [.813]
III	$1712.3 + 0.061z$ [0.473]	$389.6 + 0.325z$ [0.208]	
IV	$1464.0 + 0.411z$ [0.192]	$205.5 + 0.673z$ [0.556]	$-0.2549 + 0.00152$ [.690]
<i>Hamilton</i> [1979]		$322 + 0.58z$	

**Table 2:** Elastic parameters used in elastic models

Component	$\rho$ (g/cc)	$V_p$ (m/s)	$V_s$ (m/s)	K ( $\cdot 10^9$ Pa)	G ( $\cdot 10^9$ Pa)
Clay	2.6	3400	1600	21.2	6.666
Sand/ $\text{CaCO}_3$	2.7	5980	4040	38.0	44.0
Gas Hydrate	0.9	3300	1680	6.414	2.540
Water	1.05	1600	0	2.688	0
Gas	0.30	849	0	0.216	0

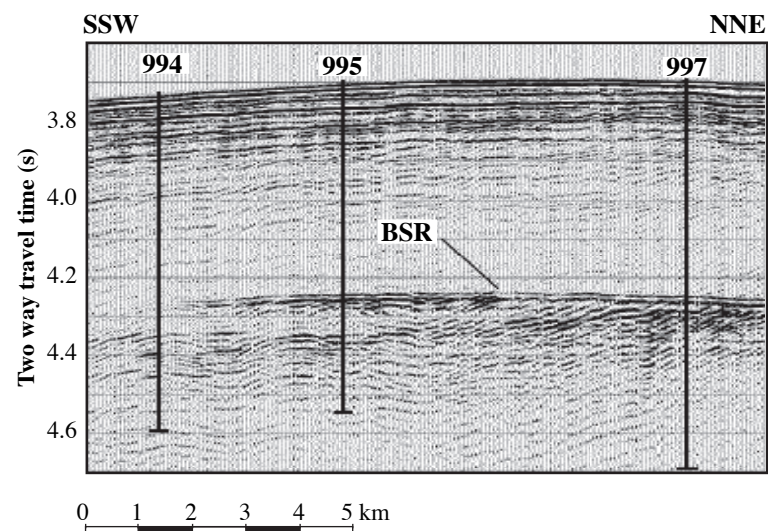


**Figure 2.1:** Seismic profile across the Blake Ridge along the transect drilled during ODP Leg 164. Site numbers are indicated. The strong reflector at about 4.3 s is the BSR [from Paull et al., 1996].

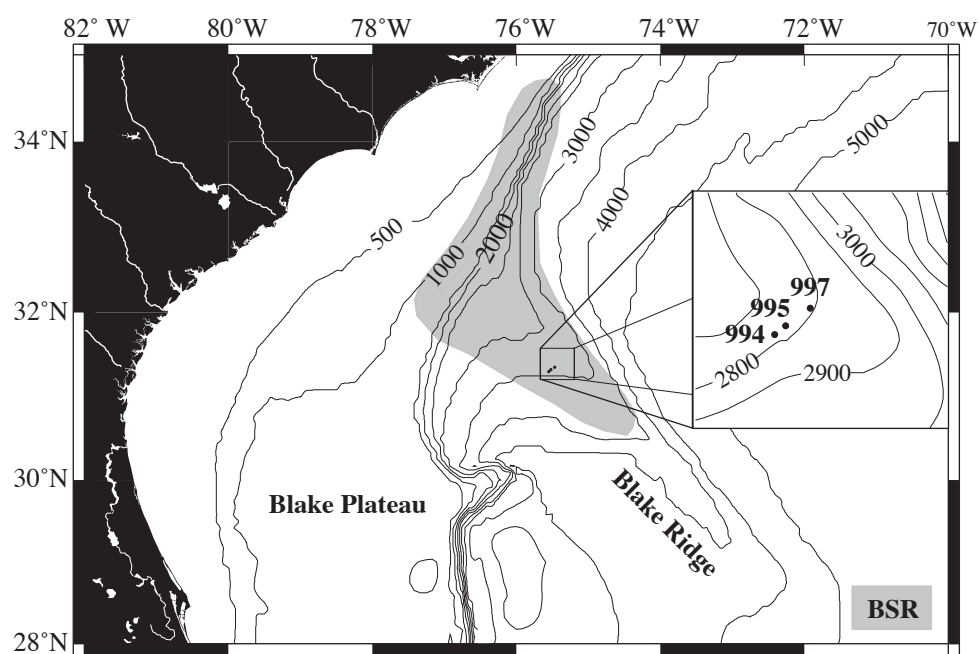


**Figure 2.2:** Location map of ODP Leg 164 drill sites on the Blake Ridge. The grey area shows the regional ex-tent of the Blake Ridge BSR as defined by seismic surveys. The inset shows the relative locations of Sites 994, 995 and 997.

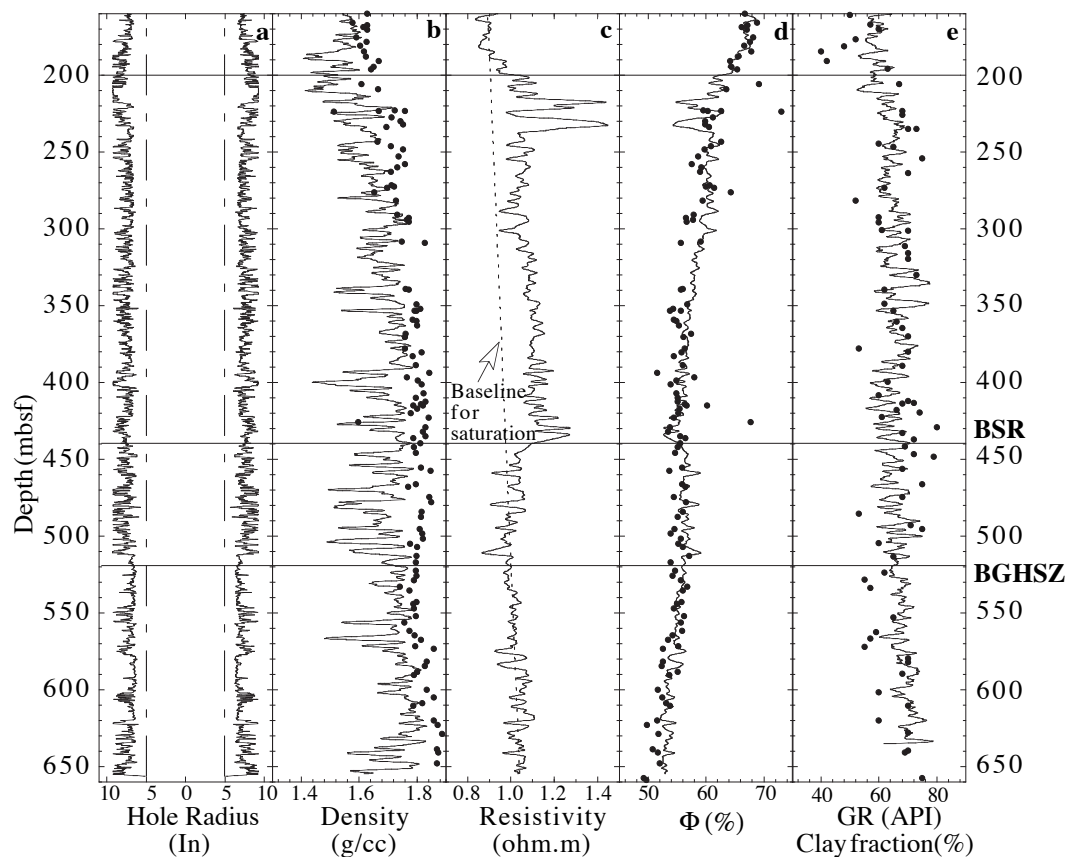


**Figure 2.3:** Logs recorded in Hole 995B. **(a)** The two symmetric curves of hole radius illustrate the shape of the hole. The vertical dashed lines indicate the diameter of the drill bit, showing the enlargements over the entire logged interval. **(b)** Density log ( $\rho$ ) and discrete density measurements (solid circles) from cores. **(c)** Deep induction resistivity log recorded with the digital induction tool. The dotted line represents the linear fit with depth established in hydrate-free sediments that is used as a baseline to calculate hydrate saturations from the resistivity log (see text). **(d)** Porosity ( $\Phi$ ) calculated from the resistivity log. Discrete porosity values (solid circles) were measured on shipboard core samples. **(e)** Natural gamma ray log (GR) scaled from 0 to 100% to represent the shaliness and clay fraction observed on smear slides from Site 995 (solid circles).

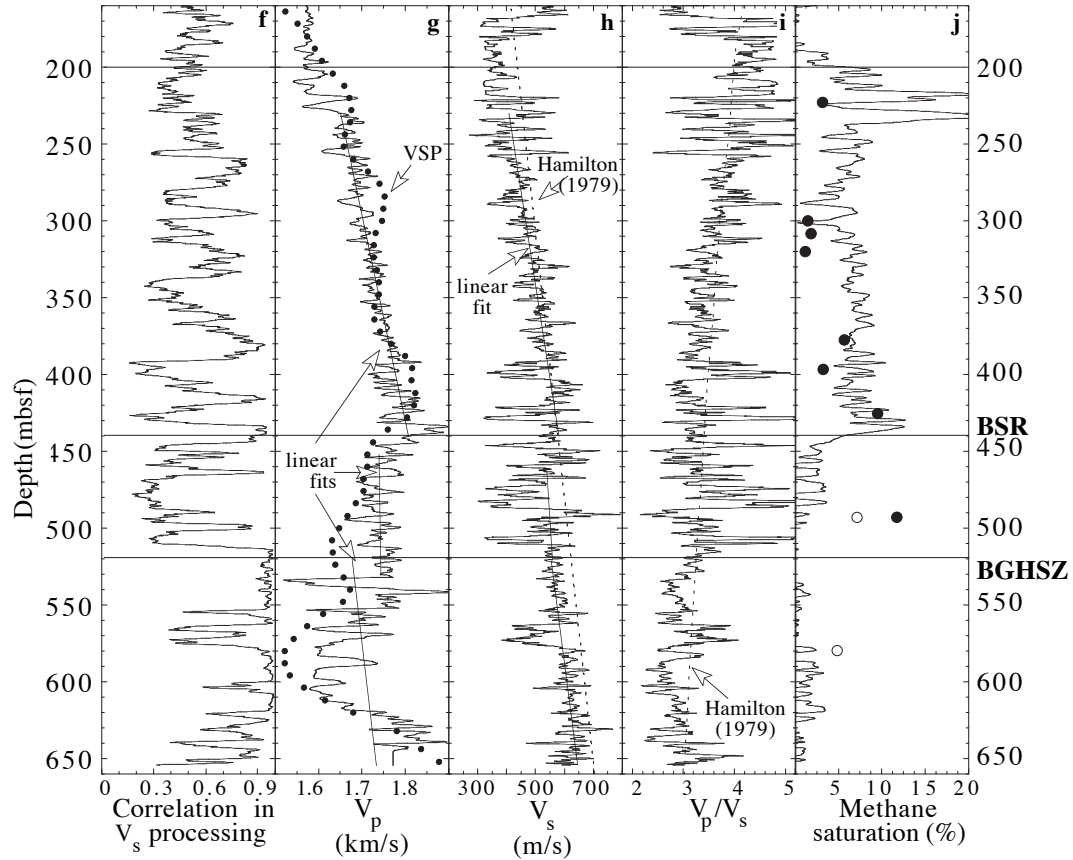


**Figure 2.3 (cont.):** (f) Correlation coefficients obtained in the processing of the dipole waveforms. Values closer to 1 indicate more reliable readings. (g)  $V_p$  log and  $V_p$  inverted from the VSP (solid circles). Solid straight lines are linear fits versus depth over various intervals. (h)  $V_s$  log and the linear trend defined by Hamilton [1979] (dotted line) for clay-rich marine sediments. Solid straight lines are linear fits versus depth. (i)  $V_p/V_s$  ratio, a common indicator of the presence of free gas. The dotted line is a trend defined by Hamilton [1979] for clay-rich marine sediments. (j) Methane saturation computed from the resistivity log using a modified Archie's law (see text). Also shown: methane saturation values measured from in situ pressure core sampler (PCS) data. Solid circles correspond to gas hydrate and empty circles correspond to free gas. The location of the BSR and the bottom of the gas hydrate stability zone (BGHSZ) are indicated by horizontal lines.

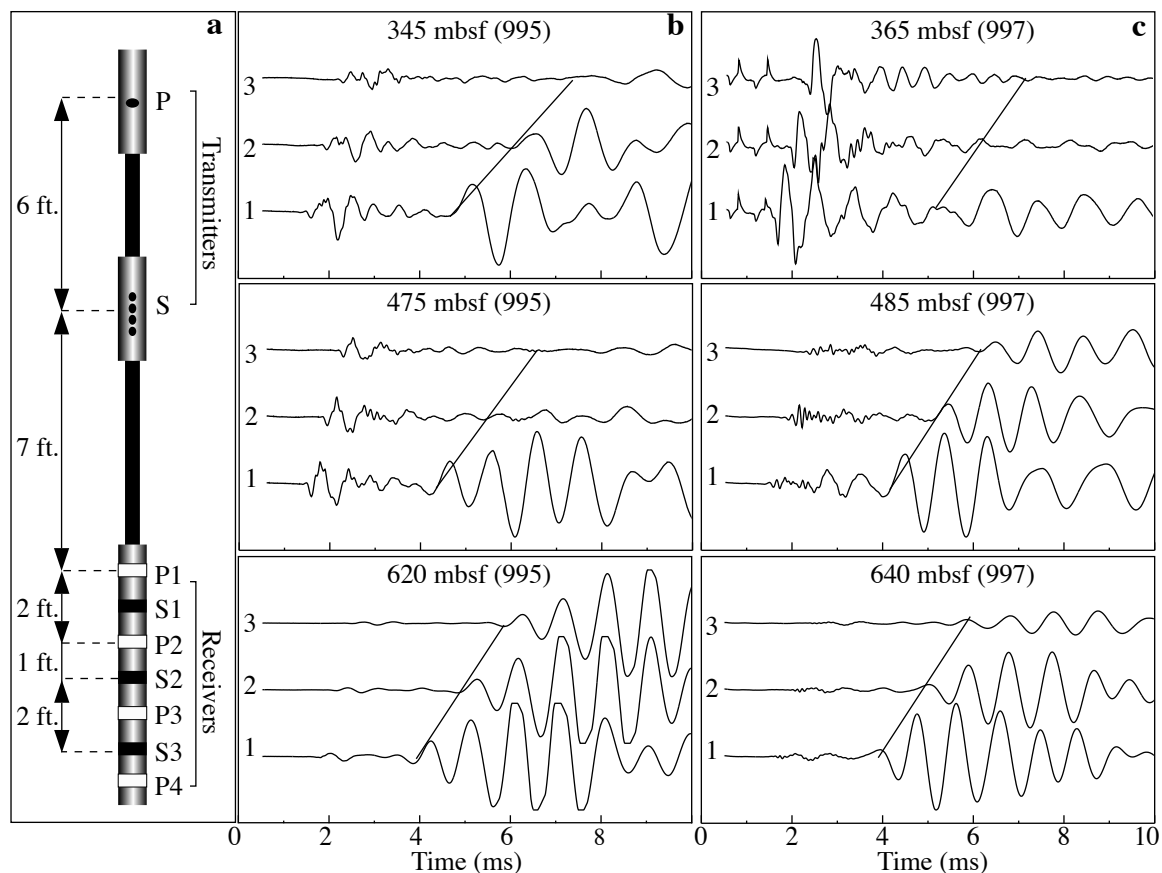


**Figure 2.4** (a) The Lamont-Doherty Earth Observatory sonic logging tool configuration showing the spacing between the different sources and receivers. (b) and (c) Waveforms recorded at various representative depths in Holes 995B and 997A, respectively. The depths of the measurements are indicated, the shallowest being recorded above the BSR, the second between the BSR and the BGHSZ, and the deepest below the BGHSZ. The number on the left of each waveform corresponds to the receiver number, receiver 1 being the closest to the source. The straight lines represent the arrival of the flexural wave; slopes are proportional to the shear velocity.

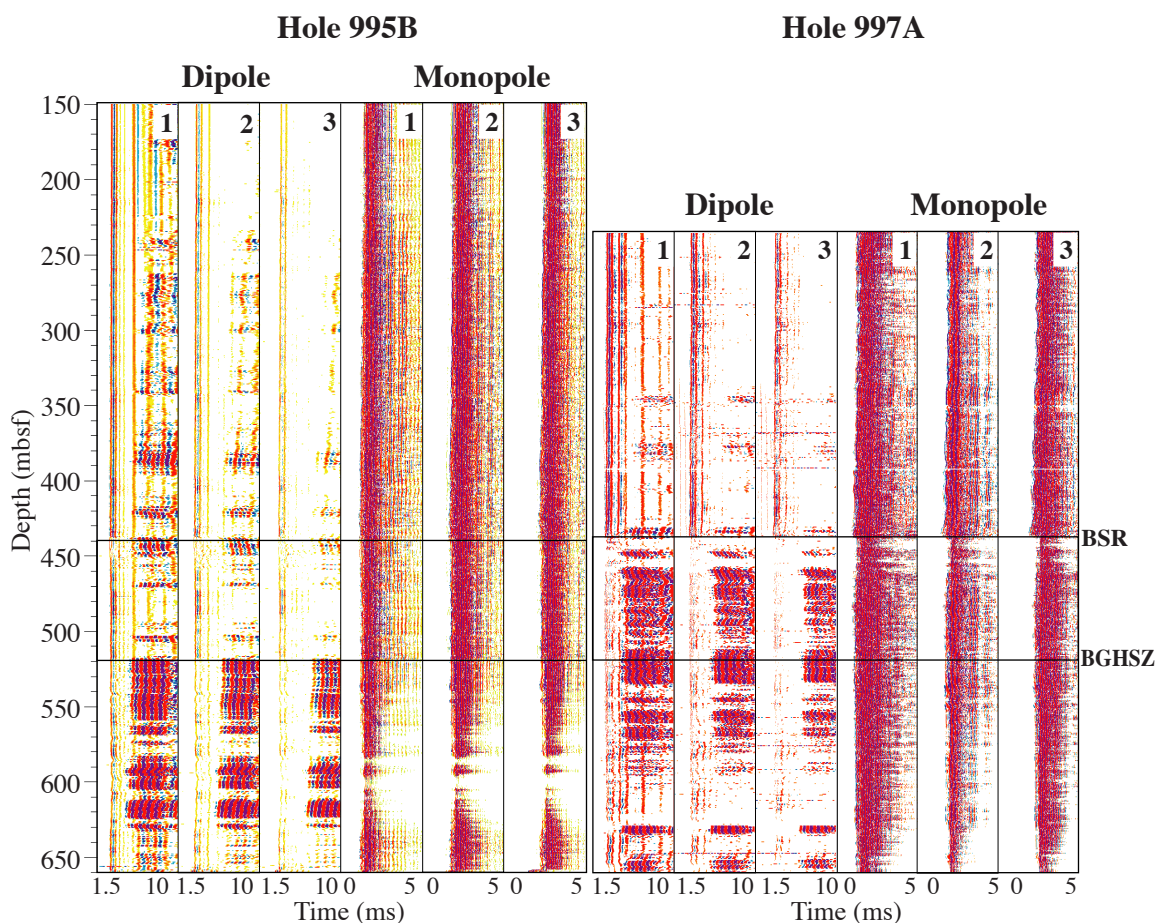


**Figure 2.5:** Sonic waveforms generated by the monopole and the dipole transmitters in Holes 995B and 997A, recorded at three receivers. Near-to-far receivers are represented and numbered from left to right. Red and blue show respectively positive and negative amplitudes. The monopole source has a center frequency of about 13 kHz, and the waveforms are sampled every 5 msec. The dipole has a center frequency of 3 kHz and the waveforms are sampled every 10 msec.

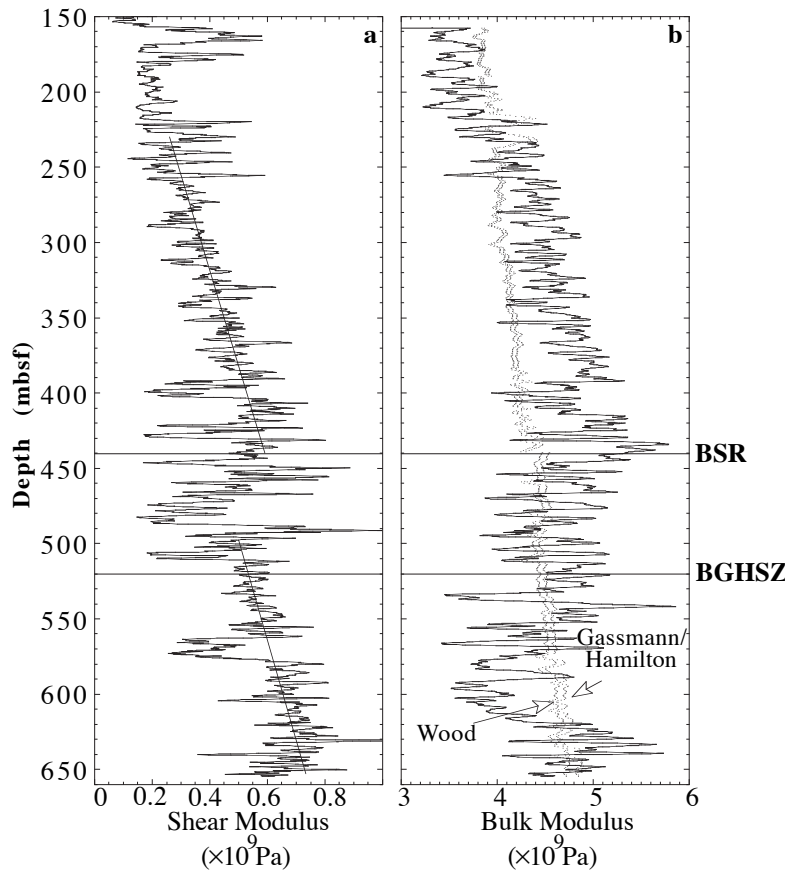


**Figure 2.6.** (a) Shear modulus calculated from the  $V_s$  and density logs. (b) Bulk modulus calculated from  $\rho$ ,  $V_p$  and  $V_s$  logs in Hole 995B. The fine dotted lines show the normal range of consolidation between the Wood model (lower) and the Gassmann/Hamilton (higher). Values higher than the Gassmann/Hamilton model indicate a high level of consolidation, while lower values are likely related to the presence of free gas.

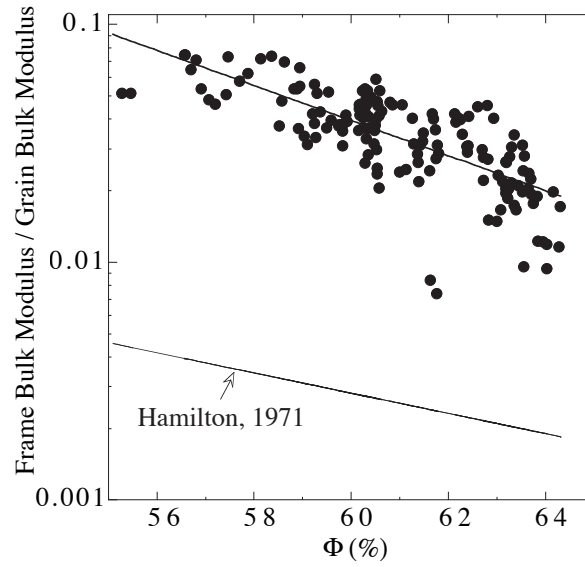


**Figure 2.7.** Crossplot of the ratio of frame modulus to grain bulk modulus as a function of porosity. The least squares fit displayed corresponds to Eq. (11) and can be compared to the relation defined by Hamilton [1971] for the frame bulk modulus of marine clay/silt.

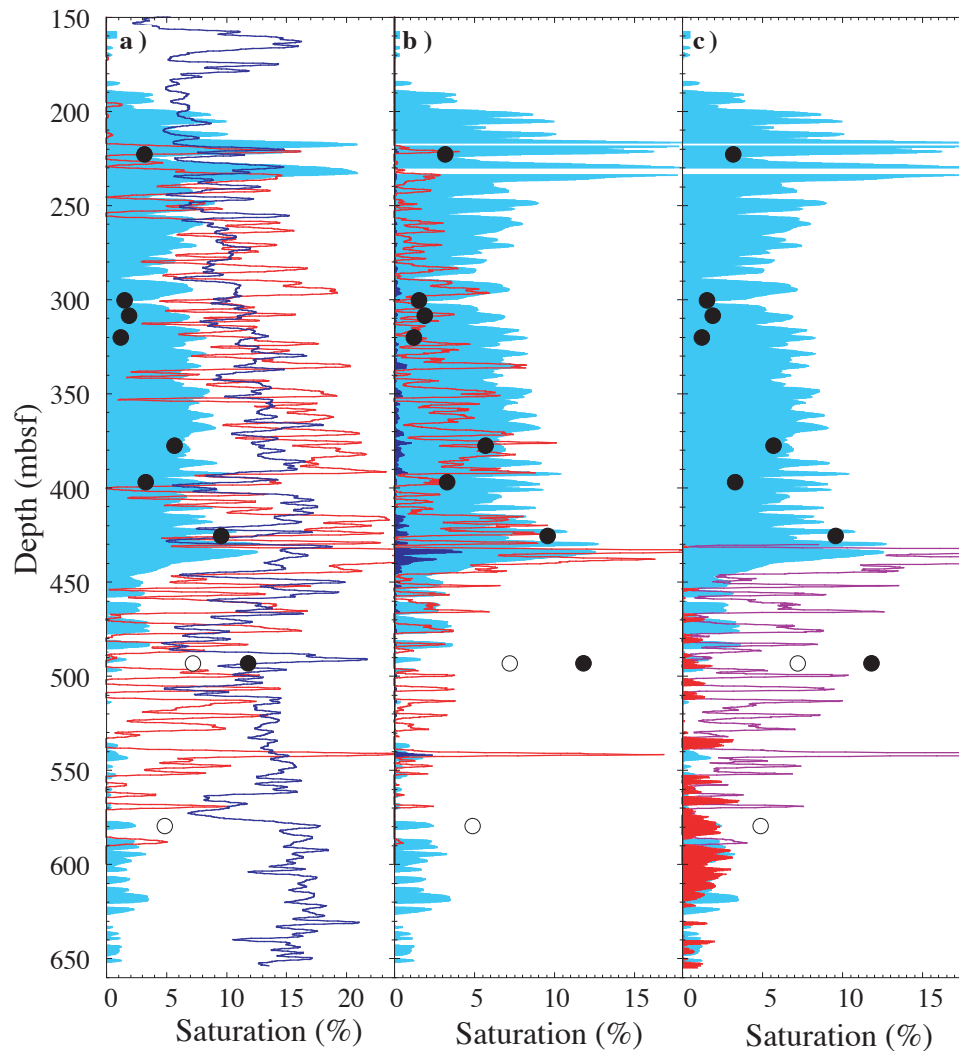


**Figure 2.8.** Estimation of gas hydrate and free gas saturations from the different elastic models. The results are compared to the values estimated from the resistivity log (the light blue area is similar to Figure 2.3j) and to the PCS data (dots). **(a)** Results from the K-T model (see text) using the bulk modulus (red line) or the shear modulus (blue line). **(b)** Results of the cementation model (see text) assuming that the cement is deposited at the contacts (dark blue area, very narrow above the BSR) or uniformly on the grains (red line). **(c)** Saturation of gas hydrate below the BSR calculated using the cementation theory and assuming that 1% of the pore space is free gas (purple line) and percentage of free gas calculated with the Gassmann/Hamilton model (red solid area). Note the different horizontal scale in Figure 2.8a.

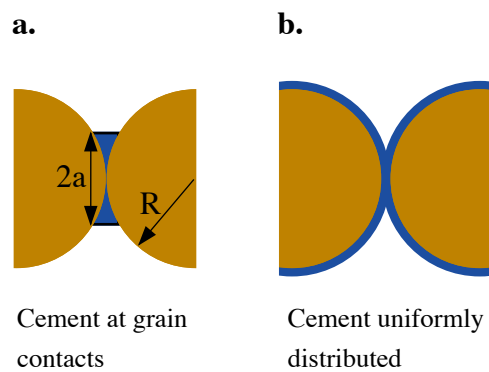


**Figure 2.9** Possible configurations for the cement in the pore space. **(a)** The cement is deposited only at the contact between the grains; **(b)** cement is deposited uniformly on the surface of the grains [after Dvorkin and Nur, 1996].

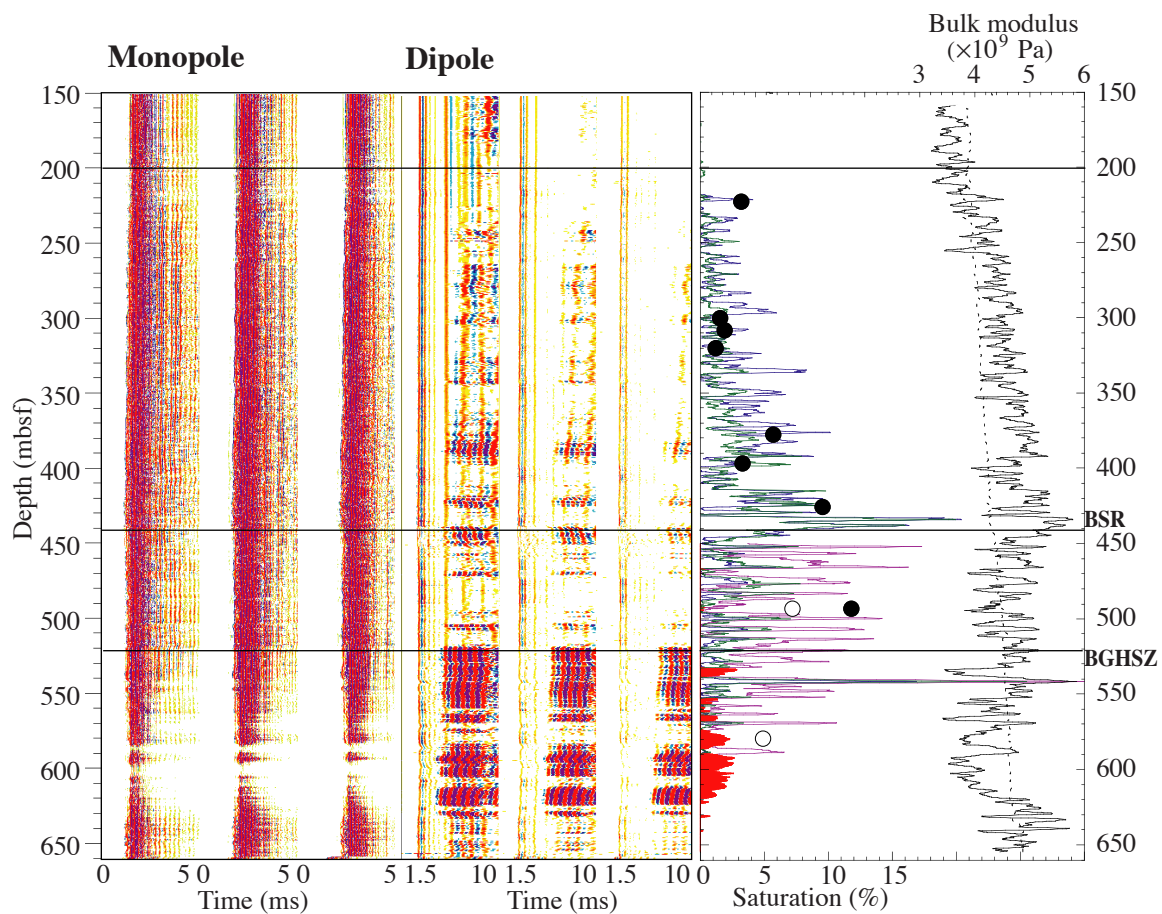


**Figure 2.10** Summary of results from Plate 1 and Figures 5 and 7, linking the sonic logging waveforms and the bulk modulus to the methane saturation estimates of free gas and gas hydrate (see text): methane saturation from cementation theory for hydrates uniformly deposited on the grains (blue line), free gas concentration below the GHSZ (red fill), and hydrate concentration between the BSR and the BGHSZ assuming that 1% of the pore space is occupied by free gas (purple line). The green line gives the result of the cementation theory calculated from density and porosity data measured on cores. Circles are PCS results. Bulk modulus  $K$  (solid black line) and the Gassmann/Hamilton model (dotted line) are also shown. Gas hydrate is present where  $K$  is significantly higher than this model, while free gas is indicated by lower values of  $K$ .

## **Chapter 3:**

### **Simulation of production and elastic properties of reservoirs to validate time-lapse seismics.**

#### **3.1 Introduction**

Time-lapse, or 4-D, seismic monitoring is an integrated reservoir exploitation technique based on the analysis of successive 3-D seismic surveys. Differences over time in seismic attributes are due to changes in pore fluids and pore pressure during the drainage of a reservoir under production. The detection of areas with significant changes or with unaltered hydrocarbon-indicative attributes can help determine drilling targets where hydrocarbons remain after several years of production.

Making sure that seismic differences are related to fluid flows is critical for a complete time-lapse seismic study. Differences in data acquisition, survey orientation, processing and quality of datasets can introduce significant noise in the 4-D analysis. This can be especially true when legacy datasets are used, which were not acquired specifically for 4D interpretation. Also, to quantify the amount of hydrocarbons responsible for the seismic differences, it is necessary to have a complete petrophysical model of the reservoir to establish a direct relationship between seismic attributes and pore fluids. Such a model can be built by stochastic simulations of the lithology and porosity, which are dependant on the availability and spatial distribution of the well data that are used as reference. Both, the 4D seismic analysis and the petrophysical characterization, require an independent validation or calibration.

In this paper, we describe how reservoir simulation can be used to generate independent impedance maps to validate or constrain time-lapse interpretation of legacy data sets. A complete 4D analysis is an iterative loop where the original interpretation can be refined along the way. First, we summarize the steps preceding the reservoir

simulation, including the 3D seismic processing and inversion, and the preliminary time-lapse interpretation. We then describe the elastic models, the properties of reservoir fluids and the reservoir characterization that are used to link the impedance volumes to fluid and lithology distribution in the reservoir. A comparison with impedance maps derived by these equations from simple vertical fluid substitution shows how the observed 4D differences indicate complex migrations that require a realistic reservoir simulation. After description of the reservoir simulator, the results of the simulation are finally used to generate impedance maps that can be compared with seismic inversions. To illustrate the different steps of the entire procedure we use the case study of the K8 reservoir, South Timbalier 295, because of its relative simplicity. In the last section, we present a complete 4D analysis of the Eugene Island 330 field whose complex history is representative of enduring Gulf Coast reservoirs (See location of these two fields offshore Louisiana in Figure 3.1)

## **3.2 The 4D seismic loop**

The first steps of the 4D "loop" are described in great details by *He* [1996] and are only summarized here to define the starting point of the reservoir simulation and lithological model used in the simulation.

### **3.2.1 Registration and normalization of seismic datasets**

Until recently, no seismic survey was shot with the specific purpose of time-lapse analysis. Successive data sets over one location were usually collected with different spacing and orientation. In order to differentiate the seismic attributes (amplitude or impedance) between two surveys, it is first necessary to re-locate them on the same grid. This re-location process uses a 3-D interpolation algorithm, that interpolates between the two grids in travel-time, slice by slice. In addition, in order to be able to compare the

results of the inversion of two datasets, we perform a normalization of the amplitudes of the surveys, globally with respect to each other first, and by rescaling them both to a proper amplitude by using synthetic seismograms generated from velocity and density logs acquired in the same area [He, 1996]

### 3.2.2 Non linear inversion of successive 3D datasets

Standard 3D seismic interpretation uses generally seismic amplitudes to identify reservoirs. Time-lapse analysis performed on seismic amplitudes has also been shown to allow the identification of migration pathways [He, 1996]. However, amplitudes are only proportional to seismic reflectivity, which depends on the relative variability in the elastic properties of the formation, not on the value of these properties. The comparison of 3D amplitude volumes requires wavefield envelope comparison techniques to identify the high-gradient envelop surrounding High Amplitude Regions [He, 1996, Anderson *et al.*, 1994] that have to be identified for time-lapse interpretation.

In contrast, seismic impedance ( $Z$ ) is directly related to the elastic properties of the sediments :

$$Z = \rho V_p \quad (1)$$

where  $\rho$  is the bulk density and  $V_p$  the sonic compressional velocity.  $\rho$  is the volumetric average of the density of the different phases (fluids and solids) and  $V_p$  can be explicitly expressed as a function of their density and compressibility (see later sections). Also, unlike amplitudes, a simple algebraic subtraction between the impedance volumes at two dates can be directly converted into fluid or pressure changes. A 4-D analysis based on impedance volumes allows a direct qualitative interpretation of seismic changes in terms of fluid substitution or migrations [He, 1996].

He [1996] uses a constrained non-linear inversion technique to estimate the acoustic impedance volumes from each 3D survey. After the seismic datasets have been horizontally stacked, migrated and re-located, each seismic trace is considered as a one-

dimensional zero-offset trace. The one-dimensional non-linear inversion uses a forward convolution model to compute seismic traces from impedance functions. The implementation of the inversion is based on a modified Levenberg-Marquardt minimization algorithm [More, 1977]. The procedure has been made fast and robust by using log-derived impedance trends as a priori impedance functions, and by using covariance functions to constrain the objective functions that are minimized during the inversion [He, 1996].

### 3.2.3 Preliminary 4D interpretation of the K8 sand

To illustrate the methodology, we present the results of the successive steps of the 4D analysis of the K8 reservoir in the South Timbalier 295 field, offshore Louisiana (See figure 3.1 for location). It is the uppermost of the three most productive reservoirs in the ST295 field and produced about 350,000 m<sup>3</sup> of oil and 150 millions m<sup>3</sup> of gas between two 3D surveys shot in 1988 and 1994. The K8 sand (Figure 3.2) is a combination of channelled mid-fan sheet sands lapping on a paleo-high in the east and gently dipping to the South West [Hoover, 1997]. It represents a particularly suitable case study in 4D analysis for several reasons: (1) the first 3D seismic survey was shot before production started, providing a reference seismic volume where fluids in place are in hydrostatic equilibrium. (2) The second survey was shot after 5 years of intense production, which should generate profound changes in pore fluid distribution and pressure over the reservoir. (3) Only two wells have been producing between the two seismic surveys (Figure 3.3), which should allow for a relatively simple migration pattern identification in the 4D seismic.

Figures 3.4a and 3.4b show the results of the inversion of the two surveys shot in 1988 and 1994 over K8. The various layers displayed, numbered from top to bottom, follow the structure of the reservoir shown in Figure 3.2b. Each layer has 101×101 data points, distant by 12.5 m and 20 m in the EW direction and NW direction, respectively,

which corresponds to the resolution of the seismic grid after re-location of the two surveys. The difference between the two inversions (Figure 3.4c) shows a global decrease in impedance (red) in most of the shallower layers and updip (NE) from the two producing wells in the deeper layers. Impedance has mostly increased (blue) in the deeper layer of the reservoir between the two surveys. Because the reservoir was originally filled with oil, and the replacement of oil by gas or water respectively decreases or increases the density and the sonic velocity of the formation, Eq. (1) allows a preliminary qualitative interpretation: oil might have been replaced mostly by gas in the shallower layers of the reservoir and by water in the deeper layers. The substitution of oil by gas exsolution updip is controlled by the pressure decrease induced by the producing wells (see pressure drop in Figure 3.3b), while the replacement of oil by water in the deeper layers is assisted by the presence of an aquifer supporting the reservoir [Tucker, 1997, Mason, 1992].

Independently of the nature of the pore fluid, the bulk of the impedance of such medium porosity sediments (40% maximum) is controlled by the porosity and lithology distributions. To relate quantitatively the observed changes in impedance with the nature and the volume of the pore fluids, it is necessary to have a complete representation of the sediment matrix, and to define the relationships between the different component of the system and its elastic properties.

### **3.3 Elastic properties of reservoir sediments**

#### **3.3.1 Elastic models**

Explicit relationships relating pressure, pore fluid, porosity, matrix materials and the elastic properties of marine sediments have been the topic of many studies, some theoretical [Gassmann, 1951, Biot, 1956, or Kuster and Toksöz, 1974], some empirical (Han et al., 1986, Ramamoorthy et al., 1995, Tosaya and Nur, 1982). They are all limited

in application by the infinite number of parameters affecting the elastic properties of sediments and no approach can offer a comprehensive formulation. We reviewed some commonly accepted models and relationships that could be used to link the changes observed in our impedance maps with fluid substitutions in the reservoirs. Most of them define relationships for the elastic moduli of the formation instead of the impedance. The bulk modulus ( $K$ ) is the inverse of compressibility and the shear modulus ( $G$ ) is a measure of the shear strength. Compressional and shear ( $V_s$ ) sonic velocity can be expressed as functions of these moduli and of the density of the sediments:

$$V_p = \sqrt{\frac{1}{\rho} \left( K + \frac{4}{3}G \right)} \quad (2a) \quad \text{and} \quad V_s = \sqrt{\frac{G}{\rho}} \quad (2b)$$

and the impedance can be re-written

$$Z = \rho V_p = \sqrt{\rho \left( K + \frac{4}{3}G \right)} = \sqrt{\rho K + \frac{4}{3} \rho^2 V_s^2} \quad (3)$$

### 3.3.1.1 Theoretical formulations

*Gassmann* [1951] and *Biot* [1956] expressed the bulk modulus of fluid-saturated sediments as a function of the bulk moduli of the dry frame ( $K_f$ ), of the pore fluid ( $K_f$ ) and of the grains ( $K_g$ )

$$K = K_g \frac{K_f + Q}{K_g + Q} \quad \text{with} \quad Q = \frac{K_w (K_g - K_f)}{\Phi (K_g - K_w)}. \quad (4)$$

This formulation requires the knowledge of the dry bulk modulus, for which *Hamilton* [1971, 1982] established empirical relationships as a function of porosity for several types of lithology. Using his results for clay, silts and fine sands, we define a single formula for elastic sediments:

$$\log(K_f) = \log(K_g) - 4.25\Phi \quad \text{or} \quad \log(K_f/K_g) = -4.25\Phi. \quad (5)$$

The grain modulus of a shale/sand mixture can be calculated by a Voigt-Reuss-Hill average of the grain moduli of sand ( $K_s$ ) and clay ( $K_c$ ) [*Hamilton*, 1971]:

$$K_g = \frac{1}{2} \left[ \gamma K_c + (1 - \gamma) K_s + \frac{K_s K_c}{K_s \gamma + K_c (1 - \gamma)} \right] \quad (6)$$

where  $\gamma$  is the shaliness or volumetric shale fraction. We refer to it as the Gassmann/Hamilton model [*Guerin and Goldberg, 1996, Chapter 2*]. Values of the grain moduli are given in Table 1.

*Kuster and Toksöz [1974]* used the theory of sonic waves scattering and propagation to calculate the effective elastic moduli of a two phase medium made of spherical inclusions in a uniform matrix:

$$K = K_m \frac{1 + \left[ 4G_m (K_i - K_m) / ((3K_i + 4G_m)K_m) \right] I_c}{1 - \left[ 3(K_i - K_m) / (3K_i + 4G_m) \right] I_c} \quad (7)$$

$$\text{and } G = G_m \frac{(6K_m + 12G_m)G_i + (9K_m + 8G_m) \left[ (1 - I_c)G_m + I_c G_i \right]}{(9K_m + 8G_m)G_m + (6K_m + 12G_m) \left[ (1 - I_c)G_i + I_c G_m \right]} \quad (8)$$

where the *i* and *m* subscripts refer to the inclusion and the matrix properties, respectively, and  $I_c$  is the volumetric fraction of the inclusion. This formulation can be extended to a three phases medium [*Zimmermann and King, 1986, Chapter 2*]. In the case of shaly sediments, the grain aggregate is considered a shale matrix with spherical sand grain inclusions ( $I_c = 1 - \gamma$ ). The aggregate is then treated as an inclusion within a fluid matrix ( $I_c = 1 - \Phi$ ). This fluid matrix is considered as a single phase, independently of the possible presence of various fluid types in the pore space.

Unlike the Gassmann/Hamilton model, Eqs. (7) and (8) do not require an empirical expression of the dry modulus, and for this reason could seem of a more practical use. This model (KT) also offers a relationship for the shear modulus, which is required to calculate  $V_p$  and the impedance but is not provided by Gassmann/Hamilton. However, it depends on strong assumptions on the shape and arrangement of the grain that can be of limited relevance to describe the grains configuration of the rapidly buried Gulf Coast sediments.

### 3.3.1.2 Experimental relationships

Underlining the practical limits of these theoretical relationships, particularly regarding the specific influence of clays on sonic wave velocities, *Han et al.* [1986] used shaly sandstone core samples presenting a wide range of porosity and shaliness to define in laboratory the following linear relationships between ultrasonic velocities, porosity and clay content:

$$V_p = 5.59 - 6.93\Phi - 2.18\gamma \quad (9)$$

$$V_s = 3.52 - 4.91\Phi - 1.89\gamma \quad (10)$$

They conclude that clay content is, after porosity, the most important parameter affecting the sonic velocity of shaly sediments. In this formulation, both velocities are independent of the pore fluid, and the only effect of pore fluid substitution on impedance is in the density.

*Ramamoorthy et al.* [1995] note that (9) and (10) and other similar empirical linear relationships fail to describe properly the elastic properties of shaly sediments in some standard lithological conditions. They propose to consider independently the effects of porosity and clay. Using *in situ* data from shear sonic and geochemical logs they give the following relationship for the shear modulus of shaly sediments:

$$G = G_{\text{grain}}(1 - 3.48\Phi + 2.19\Phi^2) \quad (11)$$

$$\text{with } G_{\text{grain}} = (0.039\log_{10}(\gamma) + 0.072)^{-1} \quad (12)$$

$G_{\text{grain}}$  is the effective grain shear modulus. Eq (11) was originally derived by *Murphy* [1993] from measurements on clean sandstones where  $G_{\text{grain}}$  was the bulk modulus of pure quartz.

Knowing the limits of any of the above relationships we have to determine which one could be used the most reliably and the most readily for the qualitative interpretation of the time-lapse impedances maps in an integrated 4D analysis. In addition to the properties of the matrix, this requires to formulate also the elastic properties of the pore fluid, which are the primary parameters responsible for changes in impedance during production.

### 3.3.2 Fluid properties

#### 3.3.2.1 Properties of fluid mixtures

The elastic properties of the pore fluid are in fact the properties of a fluid mixture, which is a function of the properties of the various fluid phases. The three primary types of pore fluid in a reservoir are hydrocarbon gas (gas) hydrocarbon liquid (oil), and brine. The density and the compressibility of the mixture are the weighted averages of the three phases:

$$S_{oil} + S_{gas} + S_{brine} = 1 \quad (13)$$

$$\rho_{fluid} = S_{oil}\rho_{oil} + S_{gas}\rho_{gas} + S_{brine}\rho_{brine} \quad (14)$$

$$\frac{1}{K_{fluid}} = \frac{S_{brine}}{K_{brine}} + \frac{S_{gas}}{K_{gas}} + \frac{S_{oil}}{K_{oil}} \quad (15)$$

where  $S_{brine}$ ,  $S_{gas}$  and  $S_{oil}$  are the saturations, or fraction of the pore space, occupied by each phase. Subscripts refer to the attributes of each phase. Equation (13) expresses the presence of only three fluid phases maximum.

#### 3.3.2.2 Elastic properties of reservoir fluids

*Batzle and Wang [1992]* give a detailed description of the properties of reservoir pore fluids and we only summarize the parameters and principal relationships that can be used in time-lapse analysis. Physical properties of reservoir fluids are dependant on composition, pressure and temperature. Unless thermal recovery techniques are used, the variations of temperature in a reservoir are negligible during its production history, and pressure and composition are the dominant parameters affecting the changes observed between two surveys.

**Brine:** Brine physical properties are extremely dependant on its salinity (S). In the Gulf of Mexico, the presence of the buried Jurassic salt generates a significant increase of

salinity with depth. In most reservoirs, brine samples are collected and their salinity measured, but *Batzle and Wang* [1992] offer a relationship to estimate salinity as a function of depth that can be used for gulf coast sediments. They also provide relationships for the velocity and density of brine as a function of salinity, pressure and temperature (See Appendix). Brine density and velocity increase with pressure in standard hydrocarbon reservoir conditions.

**Gas:** The gaseous phase present in the pore space of a reservoir is a mixture of the lightest hydrocarbon fractions. Its composition can vary during production when reservoir pressure decreases and the lightest oil components come out of solution. The properties of the gas mixture can be characterized by the gas specific gravity ( $G$ ) measured at standard temperature and pressure conditions (15.6°C and 1 atm). If a complete PVT (Pressure-Volume-Temperature) analysis of the physical properties of gas samples is not systematically performed, the measure of its gravity is most often available and allows a good estimation of its properties as function of pressure and temperature [*Batzle and Wang*, 1992]. The formulas in the Appendix show that the density and the bulk modulus of gas mixtures increase significantly with pressure.

**Oil:** The elastic properties of the 'Oil' phase, or liquid hydrocarbon, are the most complex of the reservoir fluids, but can also be calculated from a few experimental parameters [*Batzle and Wang*, 1992]. In addition to the crude oil produced at the surface, the oil phase in a reservoir can include dissolved light hydrocarbons that are gaseous at lower pressure. One of the key parameters controlling the properties of oil is the bubble point pressure, which is the maximum pressure where free gas can be present. As long as reservoir pressure is above bubble point, oil is under-saturated with regard to gas, its composition remains fixed and the density and bulk modulus both increase with increasing pressure. If reservoir pressure falls below bubble point during production, the lightest dissolved gas start coming out of solution. As pressure decreases and more light component leave the liquid phase, only the heaviest hydrocarbon remain in this phase,

and the density and bulk modulus of the oil phase increase with decreasing pressure [Batzle and Wang, 1992, England et al., 1987].

The value of the bubble point and the relationships between pressure and elastic properties should be determined from PVT analysis of actual oil samples. If such analysis is not performed, the values of oil and gas density at surface conditions can be used to determine these relationships and the bubble point pressure [Batzle and Wang, 1992, Beggs, 1992 , see equations in Appendix].

One of the standard indicators of fluid properties is the produced Gas-Oil ratio (GOR), which is the ratio of the volumes of gas and oil produced at the surface. The GOR remains constant as long as the reservoir pressure is above bubble point, but increases as soon as pressure falls below this value and free gas saturation exceeds a critical value, at which point it becomes mobile and gets preferably produced [Batzle and Wang, 1992, Steffensen, 1992]. This is shown clearly in K8 (Figure 3.3b) by the rapid increase in gas production in well A22 at the beginning of 1993 when reservoir pressure fell below the bubble point at 51.7 MPa. The evolution of the GOR is one of the key control parameters in monitoring production simulation.

### **3.3.2.3 Original fluids in place**

The last aspect of fluid properties affecting the impedance volume is the distribution of the different phases within the reservoir. While one of the goals of the reservoir simulation is to determine the evolution of these distributions during production, the original fluids in place before production can be totally determined from the fluid PVT properties if we assume the reservoir in hydrostatic equilibrium. The density-pressure relationships provide the pressure gradient within each phase and the entire pressure and fluid distributions can be integrated from the knowledge of the depth of the oil-water contact (OWC) and of one pressure value at one depth within the oil or gas zone.

Additional parameters necessary for the most accurate distribution include capillary pressures between each phase and the connate water fraction, or irreducible water saturation, which depends on matrix properties and is measured on reservoir samples.

In the case of K8, the original oil-water contact in 1988 was detected at 3350 mbsf, downdip from the study area. The Bottom Hole Pressure (BHP) measured in A-12 at the beginning of production was 57.7 MPa. These two data points and the oil gravity (define the pressure distribution at equilibrium shown in Figure 3.5. Because the lowest pressure was higher than the bubble point (51.7 MPa ) no gas was present. Because the OWC was deeper than the lowest point in the study area, water saturation was uniformly equal to the connate water fraction [30%, Hoover, 1997] and oil occupied the rest of the pore space (70%).

### 3.3.3 Stochastic reservoir characterization

The missing link between impedance volumes, fluids properties, saturations and pressure distribution using equations (1)-(15) resides in the characterization of the reservoir porosity and lithology distribution. We use geostatistical simulations for this characterization, assuming that within an individual reservoir petrophysical and acoustic properties are closely related and can be associated with calibrated cross-correlation functions [He, 1996]. Using well logs as “Hard” accurate data and impedance volumes as “Soft” data, this method combines the high vertical resolution and accuracy of logs with the wide aerial coverage of 3D seismics. He [1996] provides a complete description of the Markov-Bayse conditional soft indicator technique used .

The lithology is expressed in terms of shaliness. The hard data are shale fraction values calculated from Gamma Ray (GR) and Spontaneous Potential (SP) logs in wells distributed across the reservoir. The soft “inaccurate” data, which have to be of the same type, are approximate shaliness values ( $\gamma_s$ ) calculated from the impedance volume by a simple weighted average:

$$\gamma_s = \frac{Z - Z_{\text{sand}}}{Z_{\text{shale}} - Z_{\text{sand}}} \quad (16)$$

where  $Z$  is the inverted impedance, and  $Z_{\text{sand}}$  and  $Z_{\text{shale}}$  are impedance values for pure sand and shale formations. For the porosity distribution, the hard data come from porosity logs, and the soft data are calculated from the impedance volume by a modified time-average relationship:

$$\Phi = \left( \frac{Z - Z_{\text{sand}}}{Z_{\text{fluid}} - Z_{\text{sand}}} \right) - \gamma_s \left( \frac{Z_{\text{sand}} - Z_{\text{shale}}}{Z_{\text{fluid}} - Z_{\text{shale}}} \right) \quad (17)$$

where  $Z_{\text{fluid}}$  is an average brine impedance value [He, 1996].

Sixteen wells provided the hard data used to constrain the reservoir characterization of K8 (figure 3.6). Both porosity and shale distributions show a high level of heterogeneity, illustrating the channelled deposition of the reservoir. The bulk of the porosity is located immediately downdip from the two producing wells and in the South East corner of the study area.

### 3.3.4 From saturation to impedance

The reservoir characterization allows to use any of the petrophysical models (Eqs 4-10) to calculate the impedance volumes when pressure and fluid distributions are known. Having previously established the fluid and pressure distribution before production in K8, we can compare the estimations of the different models with the 1988 impedance inversion to determine which formulation offers a better representation of the observed reservoir properties. Since the Gassmann/Hamilton model (Eqs 4-6) does not provide a value for the shear modulus, we combined this bulk modulus estimate with the shear velocity or moduli expressions of *Han et al.* [1986](Eq. 10), *Kuster and Toksöz* [1974] (Eq. 8), and *Ramamoorthy et al.* [1995] (Eq. 11) to estimate three different impedances values. We refer to these values as the Gassmann+Han, Gassmann+KT and Gassmann+Ramamoorthy impedances, respectively. Two additional impedance volumes were calculated with the complete KT model (Eqs. 7-8) and with the expression of  $V_p$  and

$V_s$  given by *Han et al.*, [1986] (Eqs 9-10). We refer to these values as the KT and Han impedances, respectively. All the parameters used for grain and fluid properties are given in Tables 1 and 2.

In Figure 3.7, the crossplots of the different models with the 1988 impedance allow to compare their respective validity. In all these figure, a perfect formulation should result in an identical linear fit with the inverted values. The KT and Gassman+KT impedances (Figs 3.7a and 3.7b) display the highest level of scattering and consequently the poorest agreement with the inversion results. The Han and Gassmann+Han impedances present the best agreement with the inversion, with regression coefficients higher than 0.80. This comparison seems to indicate the better readiness of these two formulations to represent the acoustic properties of the reservoir in hydrostatic equilibrium. The impedance distribution calculated with Gassmann+Han is shown in figure 3.8a and compares very well with the 1988 inversion (Fig 3.4a). It will be necessary, however, to make a similar comparison after simulation to evaluate how fluid substitution affects the comparison between the calculated and the inverted impedance.

### 3.3.5 Comparison with vertical sweep

This preliminary validation of the elastic formulations can be used to illustrate the need for an accurate understanding of the reservoir dynamics that time-lapse seismic can provide. A traditional view of the fluid movements within a producing reservoir is of a uniform buoyancy-driven movement of the different phases, the contact surfaces between adjacent phases remaining horizontal. In the case of K8, where the driving mechanisms are gas ex-solution and a weak aquifer support [*Mason*, 1992], this would mean that the gas/oil contact (GOC) migrates uniformly downdip, as the gas cap expands and more gas come out of solution, while the WOC progresses upwards. Because the BHPs measured in the two wells after 1992 were below the bubble point, this indicates that the GOC has migrated down to at least these depths (3250 mbsf). Assuming that the GOC and WOC

have been simply sweeping uniformly along dip, and that the reservoir is still globally in hydrostatic equilibrium at any time, we have calculated as previously the pressure and fluid distribution that would exist in 1994 if an horizontal gas cap had formed down to 3280 mbsf and the WOC had moved up to 3320 mbsf. The impedances calculated from these values using the Gassmann+Han formulation are shown in Figure 3.8b. Comparison with Figure 3.4b shows that the impedances calculated present strong similarities with the 1994 inversion results. The impedance changes over time (Figures 3.4c and 3.8c) also display some global similarities: decrease in impedance updip from the wells, and increase downdip. However, the pattern and the absolute values of the observed impedance changes are much more heterogeneous in Fig 3.4c than in this simple ‘gravitational sweep’. The bright areas in the observed impedance changes correspond to isolated impedance decreases, that could indicate areas with low connectivity where hydrocarbon, mostly gas, would remain trapped as the reservoir pressure decreases. The comparison of Figs 3.4c and 3.8c shows that after a few years of intense production, the representation of a GOC as a continuous horizontal surface is merely irrelevant. The fact that the impedances calculated after the reservoir sweep (Fig 3.8b) compare reasonably well with the inversion results in 1994, despite the major differences in the changes over time (Fig 3.4c vs. Fig 3.8c), shows how crucial it is for each inversion to be the most accurate, as differentiating between the inversions of successive surveys is much more sensitive to errors than either inversion.

### **3.4 Reservoir Simulation**

The entrapment of hydrocarbons is mostly the result of the heterogeneity in the reservoir and in the permeability distribution. Assuming that our inversion results are correct, the heterogeneity observed in the impedance difference over time suggests a migration process more complex than the simple gravitational sweep. Numerical

simulation of the migration of the different phases can be used to identify the actual behavior of the reservoir under production.

### 3.4.1 Permeability distribution

In addition to porosity, the primary control on the reservoir drainage is the permeability distribution. While permeability is directly related to porosity, it can also be affected considerably by the presence of shales [Audet, 1992, McCarthy, 1991]. In clean sands, permeability has been found to be an exponential function of porosity

$$k_{ss} = \alpha \exp(\beta \Phi) \quad (18)$$

where the coefficients  $\alpha$  and  $\beta$  can be measured experimentally on core samples. Figure 3.9a shows the exponential regression derived from sidewall core samples collected in K8. The samples used were almost pure sandstone. McCarthy [1991] showed that the effects of porosity and shaliness ( $\gamma$ ) on the permeability of sand/shale mixtures are independent and that the effective permeability of shaly sandstones is:

$$k = k_{ss} \cdot (1 - \gamma)^m = \alpha \exp(\beta \Phi) \cdot (1 - \gamma)^m \quad (19)$$

where  $m$  is an exponent dependant on the aspect ratio of the clay minerals. If  $m = 5$ , which is a lower bound for the values calculated by McCarthy [1991], the presence of only 30% of shale would decrease the permeability by 85%, almost an order of magnitude. The permeability distribution in K8, calculated with  $m = 5$ , with the coefficients  $\alpha$  and  $\beta$  from Fig 3.9a, and using the porosity and shaliness of Figure 3.6, is shown in Figure 3.10.

### 3.4.2 Multiple-phase fluid flows in porous media

Reservoir simulation is based on solving the mass conservation equation of multiple-phase fluids in porous media, which can be expressed for a finite volume  $V$  within a surface  $A$  by:

$$\int_V \frac{\partial}{\partial t} (\rho_f \phi) = - \int_A \bar{q} \cdot d\bar{A} + G_V. \quad (20)$$

$G_V$  is a source term that can encompass the effect of injecting or producing wells.  $\bar{q}$  represents the fluid flow per surface unit, according to Darcy's law for multi-phase fluid flows in porous media:

$$\bar{q} = -k \cdot \sum_{\varphi=o,g,w} S_\varphi \rho_\varphi \frac{k_{r\varphi}}{\mu_\varphi} [\bar{\nabla} P_\varphi - \rho_\varphi \bar{g}] \quad (21)$$

where the subscript  $\varphi$  refers to the attributes of each phase (oil, gas, water): saturation ( $S_\varphi$ ), pressure ( $P_\varphi$ ), density ( $\rho_\varphi$ ), viscosity ( $\mu_\varphi$ ) and relative permeability ( $k_{r\varphi}$ ).  $k$  is the absolute permeability of the formation and  $\bar{g}$  the gravity acceleration.

The relative permeability of each phase increases with its saturation and can be calculated in three phases fluid as a combination of the relative permeabilities of two-phases fluid mixtures:

$$k_{ro} = \frac{S_g k_{rog} + (S_w - S_{wco}) k_{row}}{S_g + S_w - S_{wco}} \quad (22)$$

where  $k_{rog}$  and  $k_{row}$  are the oil relative permeability for systems with oil and gas only and oil and water only, respectively.  $S_{wco}$  is the connate, or irreducible, water saturation. The variations of  $k_{rg}$  and  $k_{rog}$  as a function of gas saturation and of  $k_{rw}$  and  $k_{row}$  as a function of water saturation, called saturation functions, have to be explicitly provided to the simulator. The lower end member of each saturation function is the critical saturation, which is the minimum saturation value for each phase to become mobile. Because of their dependance on the fluid compositions and on the pore structure, saturation functions should be measured in laboratory for every reservoir. However, relative permeability measurements are rarely performed, in part because the experimental procedures to measure them are not universally established [Rose, 1992]. No relative permeability measurements were available for either K8 or the Eugene Island LF330 field, and since this absence has to be expected in most reservoirs, saturation functions are among the

prime parameters to adjust within the 4D loop. The saturation functions used in K8 are shown in Figure 3.9.

### 3.4.3 Simulator description

The code used to solve Eq (20) is ECLIPSE, a commercial three phase, three dimensional finite differences simulator using a corner point geometry grid that allows to define highly distorted nodes to represent the reservoir geometry [Ponting, 1989]. The position and the shape of each grid block is defined by the coordinates of its eight “corners”. The coordinates and the attributes of the grid blocks (porosity and permeability) are directly imported from the reservoir characterization grid. The numerical formulation of Eq. (20) in finite differences for a grid block n connected to a number of blocks m is:

$$\frac{V\Phi}{\Delta t} \sum_{\varphi=o,w,g} \Delta(\rho_{\varphi} S_{\varphi}) = \sum_{\varphi=o,w,g} \left( \frac{\rho_{\varphi} T k_{r\varphi}}{\mu_{\varphi}} \right)_{n,m} \left[ P_{\varphi m} - P_{\varphi n} - \eta_{n,m} D_{n,m} \rho_{\varphi} g \right] + (GV)_n \quad (23)$$

where the transmissibility  $T_{n,m}$  between n and m is calculated by:

$$\frac{1}{T_{n,m}} = \frac{1}{T_n} + \frac{1}{T_m} \quad (24)$$

$$T_n = k_n \frac{\bar{A}_{n,m} \cdot \bar{D}_{n,m}}{\bar{D}_{n,m}^2} = k_n \frac{A_{n,m_x} D_{n,m_x} + A_{n,m_y} D_{n,m_y} + A_{n,m_z} D_{n,m_z}}{D_{n,m_x}^2 + D_{n,m_y}^2 + D_{n,m_z}^2} \quad (25)$$

$\bar{A}_{n,m}$  is the outbond surface vector for the interface between n and m and  $\bar{D}_{n,m}$  is the vector connecting the center of block n to the centre of the interface.

Since the only actual measurable effects of the reservoir drainage are the volumes of hydrocarbons collected at the surface, the production history recorded on the rig floor is the principal constraint on the simulator. It is expressed in terms of daily production rate of oil or gas for each well, and averaged monthly. This imposed production is translated into pressure gradients between the wellbores and the formation, which are echoed in the

reservoir at each time step of the simulation. The flow rate of phase  $\varphi$  across an open wellbore interval is

$$Q = TM_{\varphi}(P_{\varphi} - P_{\text{well}}) \quad (26)$$

with  $T$  = Connection transmissibility factor =  $2\pi kh/\ln((r_o/r_w) + S)$

$r_o$  = pressure equivalent radius of the grid block =  $0.14 (D_x^2 + D_y^2)^{1/2}$

$M_{\varphi}$  = phase mobility =  $k_{r\varphi}/\mu_{\varphi}B_{\varphi}$

where  $P_{\varphi}$  is the pressure of phase  $\varphi$  in the node containing the connection,  $P_{\text{well}}$  the pressure in the well at the depth of the connection,  $k$  the absolute permeability of the node,  $r_w$  the well bore radius,  $S$  the skin factor representing the effect of formation damage, partial penetration or well deviation,  $D_x$  and  $D_y$  are the horizontal dimensions of the grid block and  $B_{\varphi}$  is the formation volume factor of phase  $\varphi$ , or its volumetric change from surface to reservoir conditions.

In addition to the perforated well intervals, the only flows allowed in and out the reservoir model are from eventual aquifers. The strength of the aquifer support is defined in water influx per unit pressure difference. All other model boundaries are considered impermeable, either lithologically (shaled out) or structurally (sealing faults).

By default, ECLIPSE uses a fully implicit solution procedure to solve Eq. (23), but in the case of regular grids and short time steps, the IMPES method (Implicit Pressure, Explicit Saturation) can be used for faster and less dispersive simulation but is more unstable than the default fully implicit formulation [Coats, 1992].

### 3.4.4 Simulation of K8

#### 3.4.4.1 Constraint on the simulation: production history analysis

The production history imposed on K8 during the simulation was the oil simulation shown in Figure 3.3a. A-12 was the only producing well from September 89 to June 1992. The primary control of the success of the simulation was to reproduce the gas production and pressure evolution histories (Figures 3.3b). The parallelism between oil

and gas production before 1993 shows that during this period reservoir pressure was above bubble point and reservoir oil was undersaturated with a constant GOR. At the beginning of 1993 the increase in gas production relative to oil production indicates that gas started coming out of solution and that the reservoir pressure in the vicinity of the wells was below the bubble point (51.7 MPa). This gas exsolution is most likely responsible for the decrease in impedance observed between the two seismic surveys in most of the upper layers of the reservoir and updip from the wells .

#### **3.4.4.2 Simulation results**

##### **3.4.4.2.1 History match**

Figure 3.11 shows how the simulator was able to reproduce the production history of K8, starting from the initial conditions determined in 1988. Dots represent observed production data (from Fig 3.3) and the lines the simulation results. Because oil production was the imposed control mechanism, the perfect match for this production was expected. The poorer match in gas production (Fig 3.11b) indicates that we were not able to reproduce the exact evolution of K8, despite the good agreement of the simulated reservoir pressure (black line in Fig 3.11c) with the few pressure measurements available (black dots). The significant difference in the simulated pressures between the average field pressure and the BHPs of the producing wells shows the artificial pressure drawdown in the wells generated by intense production. The spikes in the simulated A12 BHP correspond to short periods where this well was shut down and the borehole started re-equilibrating with the surrounding reservoir conditions.

Even without matching the exact production history, the simulation helps to understand the dynamics in the reservoir. Figure 3.12 shows the simulated oil streamlines at various times in the simulation. In May 1992, A-12 is the only well producing, and all

streamlines converge towards this well. In January 1993, shortly after the beginning of production in A22, some of the streamlines are heading for this well, but the main flow is still bypassing A22 downdip, towards A12. At the two later time steps, the streamlines become equally focussed on the two wells. As long as A12 was the only producing well, migrations occurred mostly in the center of the reservoir. The activation of A22 drove the oil in the western part of the reservoir to flow downdip (to the south) before heading west across the bulk of the reservoir towards the wells. This counter-buoyancy drive requires a consequent pressure drawdown in the south, confirmed by the evolution of the pressure field in Figure 3.13.

#### **3.4.4.2.2 Fluid saturations and impedance**

Figure 3.14 shows the oil and gas distributions at the end of the simulation, which have to be compared with the uniform values of 70% oil and no gas at the origin of the simulation. Figure 3.15 shows the impedance volumes and changes over time calculated with these values using the Gassmann+Han formulation. The simulated impedance distribution in 1994 (Figure 3.15b) seems very similar to the inversion results at this date (Fig 3.4b), but to confirm that this relationship still offers the best representation of the reservoir properties after fluid substitutions, we also calculated the impedances after the simulation with the other petrophysical formulations. Figure 3.16 shows the crossplots comparing the different model predictions to the 1994 inversion. As before production, the KT and Gassmann+KT results display the poorest agreement with the inverted impedance, showing even a lower correlation in 1994 than at the origin of the simulation. Figs 3.16c and 3.16d confirm that the impedances calculated with Han and Gassmann+Han still present the best comparison with the inverted impedance after fluid substitutions. A crossplot between the two inversion results (Figure 3.16f) shows that the regressions between the 1994 impedance and the Han and Gassmann+Han models at this date are better than the comparison between the two impedance volumes. This indicates

that the errors in the elastic formulations are lower than the changes that they are supposed to quantify, which is a prerequisite for any meaningful quantification. As a step of the 4-D analysis loop, similar comparison between various models should be performed for any reservoir, because some formulations might be more appropriate for different depths, pressures or lithologies. For the K8 sand, and for the LF330 reservoir which has a very similar lithology, the combination of Gassmann/Hamilton and Han were the most suitable.

The comparison of the observed impedances changes over time (Figure 3.4c) with the simulated gas saturation and impedances changes (Figures 3.14b and 3.15c) confirms that the impedance decrease observed directly updip from the wells corresponds to an increase in gas saturation. The impedance decrease in the simulation results does not extend as broadly in the NE part of the reservoir as in the inversion differences. The decrease indicated by the inversions in this area can actually be caused by the production and the gas exsolution in the underlying K16 reservoir which merges with K8 at the crest of the structure. In the SW of the reservoir, downdip from the wells, the results of the simulation indicate a stronger decrease in impedance than observed from the inversion. This simulated decrease is generated by 10 to 15% free gas that came out of solution in this low-porosity part of the model (Fig 3.14b). This could show that the connectivity is higher in this area downdip from the bulk of the reservoir than in our reservoir characterization. Instead of remaining trapped in this corner most of the ex-solved gas should migrate updip to the wells. A higher gas relative permeability could also allow a more efficient mobilization of the gas. In any case, the considerable gas exsolution prevents the oil from being effectively drained in the deeper layers (Fig 3.14a), and a possible way to recover this oil would be to increase the pressure to re-dissolve the free gas. A program was initiated in 1997 for this purpose by injecting water downdip from the oil-water contact [Anderson *et al.*, 1998]. To recover hydrocarbon which are bypassed in the migration shown in Fig 3.12, both simulation results and inversions indicate that

the eastern flank of the reservoir could still contain large amounts of unproduced hydrocarbons.

### **3.5 LF sand, Eugene Island 330**

The production history match is not perfect and the differences between simulated and inverted impedances changes show that our analysis of K8 needs refinement, but such discrepancies have to be expected when putting together so many types of data and disciplines in an integrated interpretation. Reducing or explaining the discrepancies is the object of the following steps of the 4D interpretation before spudding a new well.

The case of the LF reservoir, Eugene Island Block 330, is more complex, because of a much longer production history (more than 20 years), and more producing wells (14). It will underline the difficulties in time-lapse analysis and the need for an integrated multidisciplinary iterative loop to optimize the 4D interpretation.

#### **3.5.1 Geological setting and history**

The LF sand is one of the most productive reservoirs in the Eugene Island 330 (EI330) field, the world's most prolific Pleistocene oil field [*Anderson et al.*, 1993], 200 km South-West of New Orleans (Figure 3.1). Because of its exemplary longevity, EI330 has been one of the most thoroughly studied fields in the Gulf of Mexico since its discovery in 1971. It has been the object of multiple seismic surveys and provided a large amount of core and log data, making it a typical case for petrophysical characterization and time-lapse interpretation. The more than 25 sands that constitute the field are stacked under rollover anticlines within an active growth fault system. Down-to-the-basin and antithetic faults have divided the field into several fault blocks, sealing laterally individual sand compartment to form a total of more than 100 separate reservoirs [*Holland*, 1991]. The LF sand is a Pleistocene distributary-mouth bar deposit, thickening

progressively from the shaled out crest of the anticline on the East to about 40 meters to the West. The top of the reservoir dips gently 10-20° to the west, from 1900 mbsf at the crest to 2300 mbsf (See Figure 3.17).

The 3 x 2 km study area is centered on the boundary between Blocks 330 and 331 within the fault block B of the Red Fault system [He, 1996]. In this compartment alone, 14 wells have produced 2.75 million m<sup>3</sup> of oil and 550 million m<sup>3</sup> of gas since 1972. While production has been slowing down over the years, the depletion rate has been particularly slow (Anderson et al, 1993), and the four wells still producing after 1985 recovered 130,000 m<sup>3</sup> of oil and 40 million m<sup>3</sup> of gas between the two 3D surveys of 1985 and 1992 ( Figure 3.18)

### **3.5.2 Preliminary 4-D impedance analysis**

The results of the seismic impedance inversions in 1985 and 1992 are shown in Figure 3.19. Because of its greater quality, the 1992 survey was used as the base for the re-bining before inversion, resulting in a spacing of 23 m along the dip direction, 15 m along strike and 1.0 m vertically, for a total grid dimension of 134×125×61 nodes. In the two inversions, the lowest impedances are found in the bulk of the reservoir (layer 24 in Fig 3.19), where the higher porosity reinforces the influence of fluid distribution on the elastic properties.

The subtraction of the two impedance volumes in figure 3.19c shows the changes that occurred during the seven years between the surveys. In the upper layers, impedance has decreased almost uniformly, likely because of continuous pressure decrease and gas exsolution. In the deeper layers, impedance generally increased as water was replacing oil, except in two locations: on the northern edge of Block 330, where A-12 was re-activated in 1991 to produce mostly gas and where A-6 and A-8 were active until 1988,

and in a large area centered on the block line downdip from well B4, which was the most productive well during this period. The lateral extent of this “brighter” area decreases with depth, but it extends surprisingly far downdip in Block 331, where no well was active between the two surveys.

### **3.5.3 Reservoir characterization of LF330**

*He* [1996] used GR and SP logs from 20 wells to calibrate the geostatistical characterization of the lithology, using the 1992 impedance volume as soft data. Because only a few porosity logs were available in Block 330, it was not possible to use an independent geostatistical simulation to determine porosity distribution. Instead, porosity was calculated with the time average relationship (Eq. 17) and the results of the lithology characterization. The resulting lithology and porosity distributions are shown in Figure 3.20. Because of the absence of log-derived correlation functions, the porosity distribution inherits the low spatial correlation of the impedance volume, which prevents from identifying eventual high porosity channels and results in a porosity generally lower than the actual reservoir values (see porosity values of clean samples in Fig 3.21). Permeability measurements on 250 core samples (Fig 3.21) were used to establish the permeability-porosity relationship in the LF sand. The effective permeability distribution (Figure 3.20c) was calculated with an exponent  $m = 2$  for the shale fraction in Eq. (19).

The resolution of the impedance volume was upscaled by 3 in the reservoir simulator, resulting in a grid of  $33 \times 33 \times 20 = 21780$  nodes, with dimensions 69 m  $\times$  45 m  $\times$  3 m. In the upscaling process, both porosity and shaliness were calculated by volumetric average, and the permeability of each node in the model was calculated with the averaged attributes in Eq. (19).

### **3.5.4 Fluid properties and initial conditions**

Because at the time of the first 3D survey (1985), the reservoir had already been producing for 13 years from 14 wells, the distribution of the fluids in place was too complex to assume proper initial conditions for the reservoir simulation at this time. Eventhough the period of interest was within the last seven years, it was necessary to start the simulation from the only fluid distribution that could be determined reliably, which was the hydrostatic equilibrium before production. The OWC and GOC were identified in 1972 at 2320 m and 2050 m respectively [*Holland, 1991*]. The location of the GOC at the crest of the anticline indicates that the upper part of the reservoir was at bubble point pressure (28.5 MPa) before the beginning of production. The other PVT parameters measured on LF hydrocarbon samples and used to calculate reservoir fluid properties are in Table 2. From these data we integrated the initial pressure and fluid distribution in 1972 in the same manner as for K8.

### **3.5.5 Simulation results**

The results of the production and pressure history match in blocks 331 and 330 are shown in Fig 3.22. In block 331 (Figs 3.22a and 3.22b), where most wells produced only until 1977, the simulated productions (lines) match almost perfectly the recorded data (diamonds). The good oil production match was forced as the engine of the simulation. Because of the greater depth in this part of the reservoir and of its short production activity, the pressure remained close to bubble point in most of Block 331 during its producing history. Consequently, gas saturation never exceeded the critical gas saturation value and gas production remained almost proportional to the oil production with constant GOR. The most significant mismatches in block 331 occur with wells A3 and A5, where the simulation does not reproduce the gas production increases observed in 1975. This increase indicates that at this time the gas cap must have reached A3 and A5,

the most updip producing wells of Block 331. The simulation is therefore lagging reality in the extension of the gas cap. However, the good reproduction of the pressure evolution in the field (Fig 3.22e) shows that the mismatch could be related to errors in connectivity in the vicinity of the wells, while the reservoir is behaving properly overall.

In Block 330 (Figs 3.22c and 3.22d), the presence of the gas cap at the onset of production makes the relative productions of oil and gas depend intimately on the correct evolutions of the local pressure fields and of the saturations of the different phases which controls the relative permeabilities. Volumes of oil produced are usually more accurately recorded than gas production, and are consequently more reliable constraints for the reservoir simulation. However, we were able to get a better cumulative oil and gas match by forcing gas production instead of oil in two wells: A-12 and A-6. Forcing oil production in these wells resulted in gas production much lower than observed, the oil and gas production remaining proportional to each other. This could show that porosity, and permeability, are lower in the vicinity of these wells than estimated from our time-average relationship. With lower formation permeabilities, the pressure gradients required to produce the same amount of hydrocarbon would be higher, generating lower pressures around the wells, and therefore higher produced gas/oil ratio. The uncertainty in the porosity estimation is a direct consequence of the lack of reliable well data in the northern part of Block 330 where A-6 and A8 are located [He, 1996]. However, the good reproduction of the pressure evolution (Fig 3.22e) and the overall good match of the most of the wells production suggest that we reproduced reasonably well the volumes of the different phase migrations. In particular, the very good match for Block 331 and the good match in Block 330 in the first years of the simulation indicate that the conditions in the field at the time of the first survey should be similar to the results of our simulation in 1985.

The results of the simulation in terms of oil and gas saturations at the time of the two surveys are shown in Figure 3.23 and 3.24. The comparison of gas saturation and

inverted impedance changes shows that the impedance decrease observed in the shallower part of the reservoir between the two surveys can be associated with an increase in gas saturation. Figure 3.24c shows that, despite the absence of production activity in Block 331 between the two surveys, the gas cap kept extending downward in this block, confirming our preliminary impedance interpretation. However, this qualitative association between gas increase and impedance decrease does not translate quantitatively in the impedance distribution and impedance changes calculated from the simulation results (Fig 3.25). Both impedance volumes calculated in 1985 and 1992 appear generally similar to the inversion results, but the discrepancies between simulation and inversion are apparent when comparing the simulated and inverted impedance changes over time (Fig 3.19c vs. 3.25c). By removing most of the contribution of the matrix materials to the impedance, the differentiation between successive results is much more sensitive to possible disagreements between simulation and inversion. In particular, while the inversion results indicate a decrease in impedance at all depths in the central part of the reservoir (Fig 3.19c), this decrease is limited to the upper layers and the deeper layers in the simulation, where porosity and permeability are low and free gas coming out of solution remains trapped. In the bulk of the reservoir (see layer 8), the simulation results show an increase in impedance associated with oil replacing some of the free gas. Because of the relatively low production between the two surveys, the pressure decrease generated by production is balanced by the return to normal pressure in the reservoir after years of intense production. Figure 3.22e shows that between 1985 and 1992, the average field pressure decreased only slightly, while BHPs across the field increased after having been drawn to values much lower than formation pressures. Although the impedance decrease interpreted from the inversion results at the center of the reservoir is clearly identifiable in Fig 3.19c, its amplitude is difficult to explain with only one well producing in the area (B4) at a rather slow rate (about 25 m<sup>3</sup>/day). Such inconsistencies between

seismic inversion, reservoir simulation and actual production data are at the core of the 4-D optimization loop.

### **3.6 Discussion - End of the 4D loop**

#### **3.6.1 Discussion of the LF sand results**

Some of imperfections of the LF simulation have to be attributed to the simplified porosity determination. A close look at the two survey times indicates that the agreement between inversion and simulation is better in 1992 than in 1985. This is due to the fact that the porosity distribution was explicitly derived from the 1992 inversion by a simple time average formulation. A qualitative comparison of the 1992 impedance inversion (Fig 3.19b) with the porosity distribution (Fig 3.20a) shows that the porosity pattern can be directly mapped on the 1992 impedance. Such direct relationship between reservoir characteristics and seismic attributes introduces a clear bias in the ability of the simulation to provide an independent validation of the 4D interpretation. For comparison, the porosity distribution in K8 (Fig 3.6a), which was calculated by a complete log-constrained stochastic characterization, cannot be directly mapped on any of the two impedance inversions (Fig 3.4).

Independently from this clear bias in the 1992 impedance match, the poor reproduction of the impedance changes in the LF sand underline the difficulties of time-lapse analysis. The only actual constraints on the progress of the simulation are the well production histories and the few pressures recorded, which are very localized data. It is therefore crucial to have reliable inversion results and a complete stochastic reservoir characterization for a precise volumetric reference at the time of the surveys. In the case of the LF sand, because the 1985 survey was acquired a time when 3D seismics were still in their infancy, it does not provide such dependable reference. The original time-lapse analysis of the LF sand was performed through the comparison of region-grown volumes

[He, 1996]. This technique allowed the identification of migration patterns and a preliminary interpretation of the reservoir dynamics but can not be used for a quantitative estimation of the changes in the reservoir fluids distribution. The subtraction of the two impedance volumes that we use for our qualitative evaluation is much more sensitive than region-growing algorithms to the effects of differences in the acquisition of the two surveys. The low level of confidence in the 1985 impedance added to the inability to constrain the stochastic porosity simulation and to the recurrent absence of parameters such as relative permeabilities make the problem become clearly under-determined in this reservoir.

### **3.6.2 Closing the 4D analysis loop - optimization**

Improving the present results and, more generally, the optimization of the 4D interpretation loop can take several forms. Different sources of uncertainty have been identified, in particular: (1) various numerical parameters and missing reservoir properties, (2) the numerical formulation of reservoir petrophysical properties and (3) results from steps preceding the reservoir simulation, such as seismic inversion and reservoir characterization.

Recurrently missing properties and numerical parameters such as relative permeability functions, critical saturations, capillary pressures, aquifer strength or the shale exponent in the effective permeability calculation can be varied between successive simulations in order to find a better history match. Upscaling the reservoir model dimensions for shorter computation times, it is possible to automate the variation of some of these arbitrary numerical parameters or loosely constrained properties to minimize the difference between measured and simulated production history.

The choice of the most representative petrophysical formulation (Han, Gassmann, KT or others) is crucial to establish the correspondence between impedance inversion and fluids in place. In addition to the formulation themselves, the elastic parameters of the

grain matrix in these formulations can be varied to represent different lithologies and grain arrangements. The simple comparison between various formulations such as the crossplots used for K8 (Figures 3.7 and 3.16) can be improved by iteratively varying grain elastic parameters in order to improve the regressions. The relatively limited number of parameters in these formulations can allow simple automated optimization routines to identify the most appropriate model and the proper matrix properties.

Limiting the optimization to the identification of these parameters or to the choice of the petrophysical representation requires that more fundamental components of the 4D interpretation are dependable, in particular the impedance inversions and the reservoir characterization. Reservoir simulation can be used either to validate these prior results, or to constrain their re-evaluation. In the case of LF330, a major source of inaccuracy is the porosity distribution. In the absence of additional logs, a possible way to improve the porosity distribution is to use the simulation results to re-estimate the porosity from the 1992 inversion with the time-average relationship (Eq. 17) and the fluid distribution resulting from the simulation [He et al., 1998]. For all the imprecisions still resulting from the absence of stochastic parametrization and from possible errors in the simulation, the porosity calculated with these simulated saturations should be more appropriate than the uniform average “brine impedance” originally used. This procedure can be used more generally when no survey was shot before production and no reference survey with known hydrostatic fluid distribution provides a reliable reference such as in K8. This would provide a more accurate “soft” porosity distribution for the reservoir characterization.

In addition to the uncertainties in porosity distribution, the analysis of the LF sand is also impaired by the limited confidence in the 1985 seismic dataset. While the steady improvement of 3D acquisition techniques over the last few years has greatly reduced this source of concern for recently acquired datasets, it remains a primordial issue when using legacy datasets which were not acquired along the rigorous guidelines required by

time-lapse seismic. The assessment of this uncertainty and of possible remedies requires to go beyond the parameters directly associated with the reservoir simulation. It requires to complete the 4-D analysis by returning to the initial steps of the interpretation loop and to the original data: seismic amplitude volumes.

To complete the loop, the impedance volumes calculated from the results of the reservoir simulation have to be fed into a 3D seismic waves propagation elastic model to try to reproduce the observed datasets. For this purpose, we have built tools allowing to remesh the simulation grid within the original data volume [Mello *et al.*, 1998] and developed a full elastic 3D finite difference model to simulate the propagation of seismic waves and generate a synthetic seismic amplitude volume. The comparison of the simulated amplitudes with the original datasets can be used as a simple validation of the reservoir simulation, but it can also be used to re-evaluate the inversion or the reservoir characterization results when data are missing or unreliable. In the case of the LF sand, the impedance changes calculated from the reservoir simulation are much smaller than indicated by the subtraction of the two inversions. The reservoir simulation and the impedances calculated from its results might be only partially accurate, but since the simulated production volumes and pressure variations were equivalent to the actual production data, the range of the simulated impedance changes should be representative of the actual changes between the two surveys. If we assume that the 1992 inversion is the most accurate, this shows that the 1985 inversion has to be re-estimated. This can be done by applying the 3D elastic model to the 1985 simulated impedances. If the resulting seismic amplitudes volume compares well with the original 3D survey, the simulated impedances can be used as a new *a priori* impedance distribution for the re-evaluation of the inversion of the 1985 survey. Because most of the production occurred before the first 3D survey, the few wells producing after 1985 have merely been developing features of the earlier production phase. Therefore, properly simulating the reservoir before 1985 is as crucial to our time-lapse analysis as the simulation between the two surveys. This can

only be completed by a good agreement between seismic inversion, reservoir simulation and elastic simulation at the time of this first survey.

### **3.7 Conclusion**

These are mere possibilities for the 4D interpretation to proceed from reservoir simulation to get an exact understanding of the reservoir dynamics. Because the exploration, production history and the configuration of each reservoir are unique, there is no exhaustive procedure for time-lapse monitoring. We have tried to develop an integrated series of tools allowing to apply our general methodology to any reservoir, but its flexibility requires a clear understanding of the possible sources of errors in order to use the iterative procedure to minimize them.

At the junction between complex theoretical methods (non-linear seismic inversion, 3D elastic modelling or stochastic simulation) and the most primary field data, reservoir simulation provides the link between the observed changes in seismic attributes, the hydrocarbons produced on the rig floor and the actual fluid dynamics within a reservoir. Because it should ultimately indicate where to drill to recover trapped hydrocarbon, and the volumes to expect, it can help understand the passed history of a reservoir, but more importantly, how to make the best of its future. In the case of the K8 sand, the good agreement between simulation and inversion indicate that the final optimization should be only a refinement of the present results. Because of its more complex history and of the lesser quality of the available data, the complete assessment of the future of the LF sand requires a more profound overhaul of our original assumptions.

Completing our conclusions of chapters 1 and 2, we have shown how different types of elastic formulations can be used to quantify transformations of the pore space and of the pore materials in marine sediments. In the case of silica diagenesis and gas hydrate

formation, these models allowed to describe the nature of the transformation of the pore space and understand very distinct seismic signatures of long-range processes. Their application to fluid substitutions in a producing reservoir can have direct short term implications: the spudding of a new well. In the last chapter, we describe how temperature and heat flow measurements can be used to identify the long term migrations in active fault zones feeding the LF sand and similar reservoir as we exploit them.

## References:

- Anderson, R.N., 1993, Recovering dynamic Gulf of Mexico reserves and the U.S. energy future, *Oil & Gas Journal* , April 26, 85-91.
- Anderson, R.N., G. Guerin, W. He, A. Boulanger and U. Mello, 4-D, 1998, Seismic reservoir simulation in a South Timbalier 295 turbidite reservoir, *The Leading Edge*, 17(10),1416-1418.
- Batzle, M., and Z. Wang, 1992, Seismic properties of pore fluids, *Geophysics*, 57(11):1396-1408.
- Beggs, H.D., 1992, Oil system correlations, *in* Petroleum Engineering Handbook, Bradley, Ed, Third printing, part 22, SPE, Richardson, TX.
- Coats, K.H., 1992, Reservoir Simulation, *in* Petroleum Engineering Handbook, Bradley, Ed, Third printing, part 48, SPE, Richardson, TX.
- England, W.A., A.S. Mackenzie, D.M. Mann and T.M. Quigley, 1987, The movement and entrapment of petroleum fluids in the subsurface, *J. of the Geol. Soc.*, London, 144, 327-347.
- Gassmann, F., 1951, Elastic waves through a packing of spheres, *Geophysics*, 16, 673-685.
- Guerin, G., and D. Goldberg, 1996, Acoustic and elastic properties of calcareous sediments across a siliceous diagenetic front on the eastern U.S. continental slope, *Geophys. Res. Lett.*, 23(19), 2697-2700.
- He, W., 1996, 4-D Seismic Analysis and Geopressure Prediction in the Offshore Louisiana, Gulf of Mexico. Ph.D. Thesis, Columbia University.
- He, W, G. Guerin, R.N. Anderson, and U.T. Mello, 1998, Time-dependent reservoir characterization of the LF sand in the South Eugene Island 330 Field, Gulf of Mexico, *The Leading Edge*, 17(10).
- Hamilton, E.L., 1971, Elastic properties of marine sediments, *J. Geophys. Res.*, 76, 579-601.

- Hamilton, E.L., Bachman, R. T., Berger, W. H., Johnson, T. C., and Mayer, L. A., 1982, Acoustic and related properties of Calcareous deep-sea sediments, *J. Sed. Pet.*, 52(3), 733-753.
- Han, D-H., A. Nur and D. Morgan, 1986, Effects of porosity and clay content on wave velocities in sandstones, *Geophysics*, 51(11), 2093-2107.
- He, W., Holland, D. S., Leedy, J. B., and Lammlein, D. R., 1990, Eugene Island Block 330 field-U.S.A., offshore Louisiana, in Beaumont, E.A., and Foster, N. H., compilers, *Structural traps III, tectonic fold and fault traps: AAPG Treatise of Petroleum Geology Atlas of Oil and Gas Fields*: 103-143.
- Hoover, A., 1997 Reservoir and production characteristics of the South Timbalier 295 field, offshore Louisiana, with comparison to outcrop analogue and 4-D seismic results, M.S. Thesis, Pennsylvania state university.
- Kuster, G.T., and M.N. Toksöz, 1974, Velocity and attenuation of seismic waves in two-phase media, 1, Theoretical formulation, *Geophysics*, 39, 587-606.
- Mason, E.P., 1992, Reservoir geology and production performance of turbidite sands at South Timbalier 295 field, offshore Louisiana, in transactions of the Gulf Coast Association of Geological Societies, Vol XLII, 267-278.
- McCarthy, J.F., 1991, Analytical models of the effective permeability of sand-shale reservoirs, *Geophys. J. Int.*, 105, 513-527.
- Mello, U.T., P.R. Cavalcanti, A. Moraes and A. Bender, 1998, New developments in the 3D simulation of evolving petroleum systems with complex geological structures, AAPG international conference and exhibition abstracts, AAPG Bulletin, 82(10), p. 1942.
- More, J., 1977, The Levenberg-Marquardt algorithm, implementation and theory: numerical analysis, G.A. Watson, Ed., Lecture notes in Mathematics, 630, Springer-Verlag.

- Murphy, W.F, A. Reischer, A., and K. Hsu, 1993, Modulus decomposition of compressional and shear velocities in sand bodies, *Geophysics*, 58(2), 227-239.
- Ponting, D.K., 1989, Corner Point Geometry in Reservoir Simulation, proc. Joint IMA/SPE European Conference on the Mathematics of Oil Recovery, Cambridge.
- Ramamoorthy, R., W.F. Murphy and C. Croll, 1995, Total porosity estimation in shaly sands from shear modulus, Trans. SPWLA 36th Logging Symposium, paper H.
- Rose, W., 1992, Relative Permeability, *in* Petroleum Engineering Handbook, Bradley, Ed, Third printing, part 28, SPE, Richardson, TX.
- Steffensen, R.J., 1992, Solution-Gas-Drive reservoirs, *in* Petroleum Engineering Handbook, Bradley, Ed, Third printing, part 37, SPE, Richardson, TX.
- Tucker, B., 1997, Time-lapse seismic monitoring of the South Timbalier Block 295 field, offshore Louisiana, M.S. Thesis, Pennsylvania state university.
- Tosaya, M.N., and A. Nur, 1982, Effects of diagenesis and clays on compressional velocities in rocks, *Geophys. res. lett.*, 9, 5-8.
- Zimmerman, R.W., and M.S. King, 1986, The effect of the extent of freezing on seismic velocities in unconsolidated permafrost, *Geophysics*, 51, 1285-1290.

**Table 1:** Elastic properties of matrix materials.

Grain type	$\rho$ (g/cc)	$V_p$ (m/s)	$V_s$ (m/s)	K ( $.10^9$ Pa)	G ( $.10^9$ Pa)
Clay	2.6	3400	1600	21.2	6.666
Sand	2.7	5980	4040	38.0	44.0

**Table 2 :** Properties of the reservoir fluids used in the simulation and in the elastic models

Parameter	K8 (ST295)	LF (EI330)
Temperature	88.9°C	71°C
Bubble point pressure	51.7 MPa	28.5 MPa
Gas Gravity (relative to air)	0.6112	0.6953
Oil density )	0.855 g/cc (34.0 API)	0.839 g/cc (37.2 API)
Original OWC	3350 mbsf	2320 mbsf
Original GOC	N/A	2050 mbsf
Connate water saturation	30%	40%
Critical gas saturation	5 %	20 %
Critical Oil saturation	20 %	20%

## Appendix: Reservoir fluids properties

In an ideal time lapse analysis, a complete PVT analysis of reservoir fluid samples should provide the exact relationships between reservoir fluid properties, pressure and saturation. The main parameters required for the simulation and for calculating impedances are mostly compressibility, density, viscosity. In a typical case only some of these relationships are actually measured, and only a few parameters are systematically measured. *Batzle and Wang* [1992] provide a very complete description of the elastic properties of reservoir fluids. We summarize here the few relationships that can be readily used in a typical 4D analysis using only the few parameters that are systematically measured: the oil and gas gravities, reservoir temperature and pressure. In all the following relationships, Temperature is in °C, Pressure in MPa, density in g.cc<sup>-1</sup> and bulk modulus in MPa.

### Brine properties:

In most reservoirs, brine samples are analysed for such purposes as logs calibration or reservoir evaluation. In the absence of brine samples, a linear fit to the data compiled by *Batzle and Wang* [1992] provides a way to estimate salinity (S) vs. depth (z, in m):

$$S = 1.4 \times 10^{-4} z - 0.2 \quad (22)$$

where S is in weight fraction of Sodium Chloride.

The density of water  $\rho_w$  can be approximated by a polynomial function of pressure and temperature:

$$\begin{aligned} \rho_w = & 1 + 10^{-6} (-80T - 3.3T^2 + 0.00175T^3 \\ & + 489P - 2TP + 0.016T^2P - 1.3 \cdot 10^{-5}T^3P - 0.333P^2 - 0.002TP^2) \end{aligned} \quad (23)$$

and the brine density is:

$$\begin{aligned} \rho_{\text{brine}} = & \rho_w + \\ & S[0.668 + 0.44S + 10^{-6}(300P - 2400PS + T(80 + 3T - 3300S - 13P + 47PS))] \end{aligned} \quad (24)$$

The sonic velocity in pure water has been studied by *Wilson* [1959], who provided the following relationship:

$$V_w = \sum_{i=0,4} \sum_{j=0,3} w_{ij} T^i P^j \quad (25)$$

where the parameters  $w_{ij}$  are given in the following table:

	i = 0	1	2	3	4
j = 0	1402.85	4.871	-0.04783	$1.487 \times 10^{-4}$	$-2.197 \times 10^{-7}$
1	1.524	-0.0111	$2.747 \times 10^{-4}$	$-6.503 \times 10^{-7}$	$7.987 \times 10^{-10}$
2	$3.437 \times 10^{-3}$	$1.739 \times 10^{-4}$	$-2.135 \times 10^{-6}$	$-1.455 \times 10^{-8}$	$5.230 \times 10^{-11}$
3	$-1.197 \times 10^{-5}$	$-1.628 \times 10^{-6}$	$1.237 \times 10^{-8}$	$1.327 \times 10^{-10}$	$-4.614 \times 10^{-13}$

### Gas properties:

Gas mixture properties can be characterized by their specific gravity,  $G$ , which is the ratio of the gas density to air density at standard conditions.

For temperatures and pressures typically encountered in oil fields, the gas density ( $\rho_g$ ) and bulk modulus ( $K_g$ ) can be calculated by:

$$\rho_g = \frac{28.8GP}{ZR(T + 273.15)} \quad (26)$$

$$K_g = \frac{P}{\left(1 - \frac{P_{pr}}{Z} \frac{\partial Z}{\partial P_{pr}}\right)} \gamma_o \quad (27)$$

where  $R$  is the ideal gas constant ( $R = 8.31$  SI) and  $Z$  is the compressibility factor, which is a measure of the departure from the ideal gas law that can be measured on samples or approximated by:

$$Z = [0.03 + 0.00527(3.5 - T_{pr})^3]P_{pr} + (0.642T_{pr} - 0.007T_{pr}^4 - 0.52) + E \quad (27)$$

$$\text{with } E = 0.109(3.85 - T_{pr})^2 \exp\left\{-\left[0.45 + 8\left(0.56 - \frac{1}{T_{pr}}\right)^2\right] \frac{P_{pr}^{1.2}}{T_{pr}}\right\} \quad (28)$$

$$P_{pr} = \frac{P}{(4.892 - 0.4048G)} \quad \text{and} \quad T_{pr} = \frac{(T + 273.15)}{(94.72 + 170.75G)} \quad (29)$$

$$\text{and } \gamma_o = 0.85 + \frac{5.6}{(P_{pr} + 2)} + \frac{27.1}{(P_{pr} + 3.5)^2} - 8.7e^{-0.65(P_{pr} + 1)} \quad (30)$$

### Oil properties

The properties of oil vary differently whether pressure is higher or lower than the bubble point. In any case, if PVT analysis results are not available, elastic properties can be calculated from its density  $\rho_o$  at standard surface condition, the gas gravity  $G$  and the bubble point pressure. Oil gravity is usually expressed by its American Petroleum Institute (API) gravity:

$$\text{API} = \frac{141.5}{\rho_o} - 131.5 \quad (31)$$

Above bubble point, the composition of the oil phase remains constant with varying pressure, and the density and velocity can be expressed by:

$$\rho_{oil} = \frac{\rho_o + (0.00277P - 1.71 \times 10^{-7}P^3)(\rho_o - 1.15)^2 + 3.49 \times 10^{-4}P}{(0.972 + 3.81 \times 10^{-4}(T + 17.78)^{1.175})} \quad (32)$$

$$V_{oil} = 2096 \sqrt{\frac{\rho_o}{2.6 - \rho_o}} - 3.7T + 4.64P + 0.0115(4.12 \sqrt{\frac{1.08}{\rho_o}} - 1 - 1)TP \quad (33)$$

Below bubble point, the 'oil' phase is saturated with dissolved gas and its composition varies as pressure decreases and more light hydrocarbon come out of solution. The density of this 'live' oil is given by:

$$\rho_{oil} = \frac{(\rho_o + 0.0012GR_G)}{B_o} \quad (34)$$

$$\text{where } R_G = 2.03[Pe^{(0.02878API - 0.00377T)}]^{1.205}$$

(35)

and

$$B_o = 0.972 + 0.00038 \left[ 2.4R_G \sqrt{\frac{G}{\rho_o}} + T + 17.8 \right]^{1.175}$$

(36)

The velocity can be calculated by replacing  $\rho_o$  in (33) with a pseudo density  $\rho'$  representing the expansion caused by gas intake:

$$\rho' = \frac{\rho_o}{B_o(1 + 0.001R_G)}$$

(37)

in both cases, the bulk modulus is calculated from density and velocity by

$$K_{oil} = \rho_{oil} V_{oil}^2$$

(38)

which is equivalent to Eq (2a) because fluids do not have any shear strength.

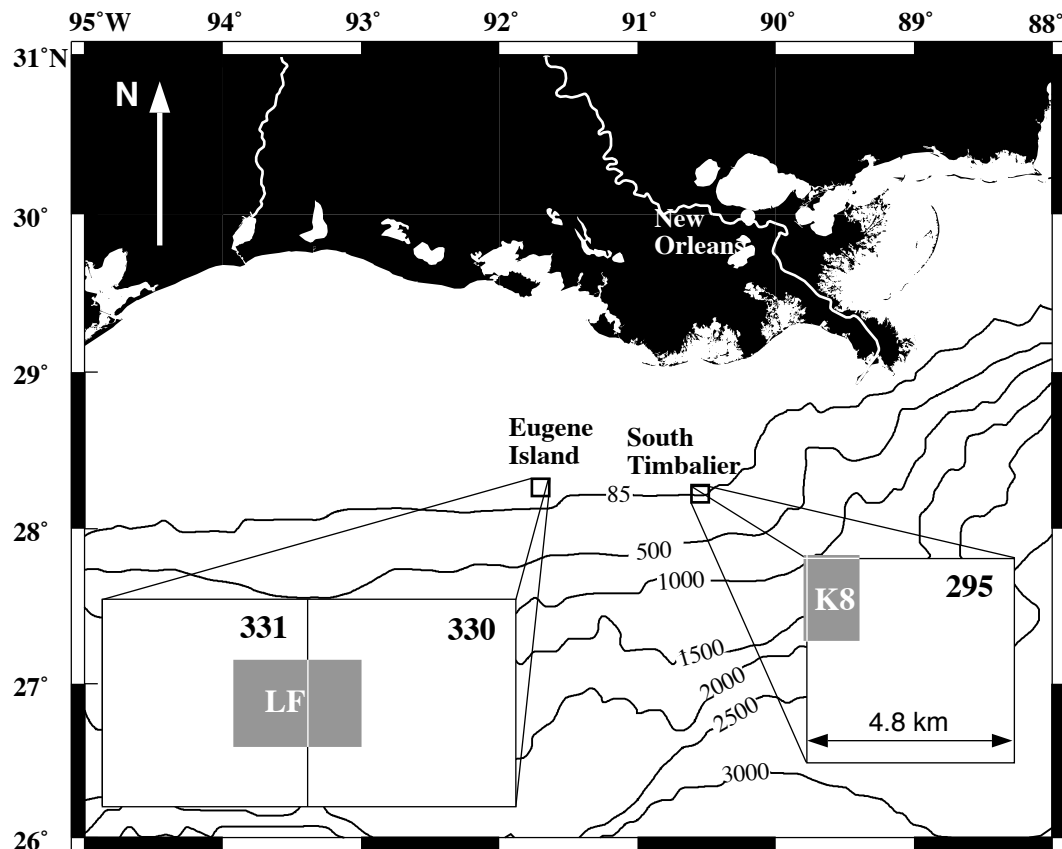


**Figure 3.1** Location map of the two oil fields off-shore Louisiana presented in this paper. The LF sand, Eugene Island Block 330, produced 130,000 m<sup>3</sup> of oil and 40 million m<sup>3</sup> of gas between two 3D surveys shot in 1985 and 1992. The K8 sand, South Timbalier Block 295, produced 350,000 m<sup>3</sup> of oil and 150 millions m<sup>3</sup> of gas between surveys in 1988 and 1994. The grey areas show the actual overlap between successive surveys that were used in the 4D analysis.

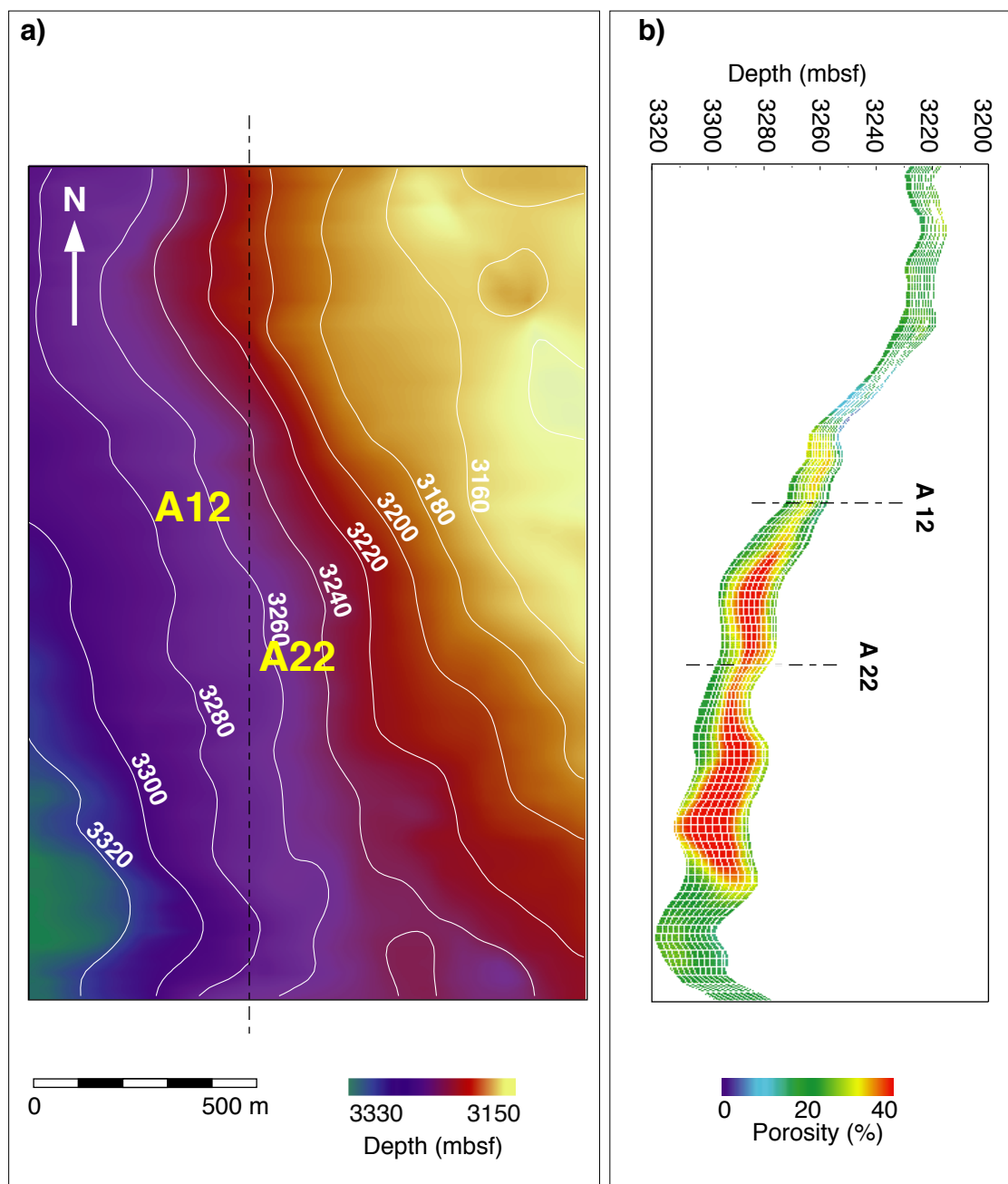


**Figure 3.2** (a) Structure of the top of the K8 reservoir, South Timbalier 295. The reservoir dips slightly to the South West and leans on a paleohigh to the east. A12 and A22 are the two wells producing between the 1988 and 1994 surveys (b) North South cross-section of the K8 reservoir. The grid represents the grid used in the simulation. Colors show the porosity, estimated by stochastic simulation.

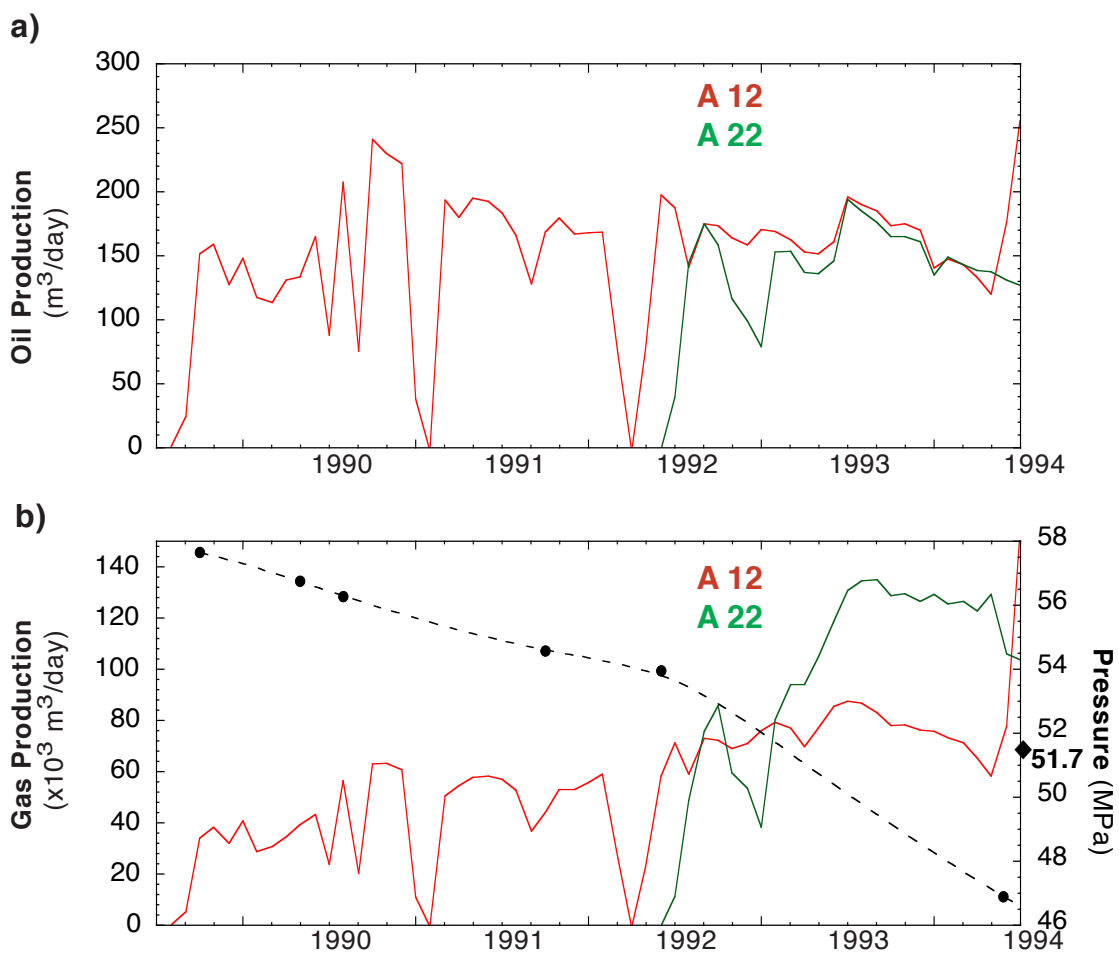


**Figure 3.3:** (a) Oil and (b) gas production history of the two wells producing from the K8 reservoir. The Bottom Hole Pressures (BHP) measured in A12 illustrates the increase in GOR and in gas production when reservoir pressure falls below bubble point at the beginning of 1993.

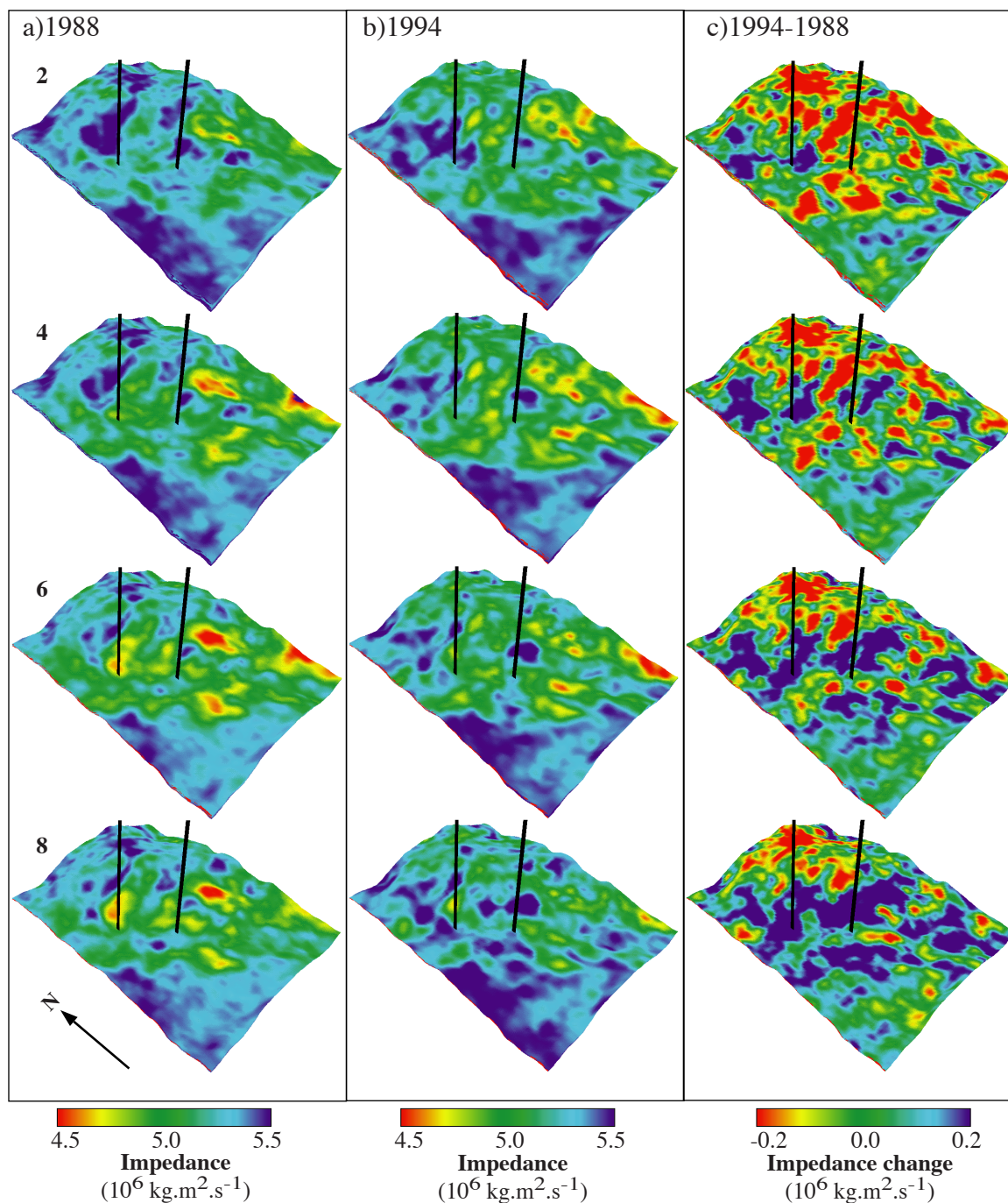


**Figure 3.4:** Results of the impedance inversion of 3D seismic surveys of K8 in 1988 (a) and 1994 (b). The layers are numbered from bottom to top, referring to the grid shown in Figure 3.2b. By convention, for consistency with the seismic ‘brightening’ usually associated with free gas, low impedance values are in red and high impedance in blue. (c) Difference between the two impedance inversions. Impedance decrease between 1988 and 1994 is in red. In this figure, as in all the following representations of the reservoir, the two producing wells are indicated by the black lines.

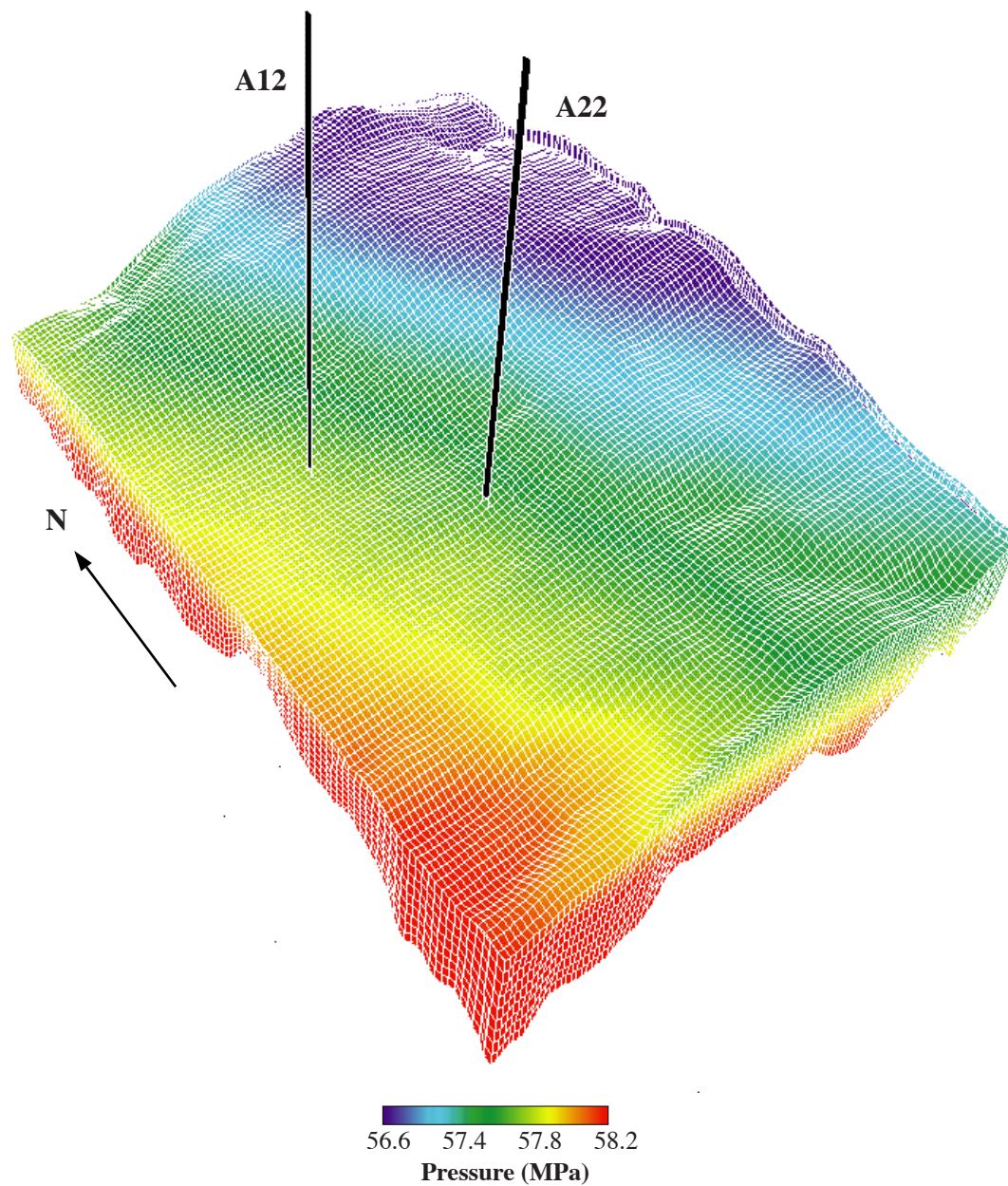


**Figure 3.5:** Pressure distribution estimated in K8 before the beginning of production in 1989, assuming that the reservoir was in hydrostatic equilibrium. The vertical dimension of the elements is exaggerated in this figure to enhance configuration of the grid used in the simulation.

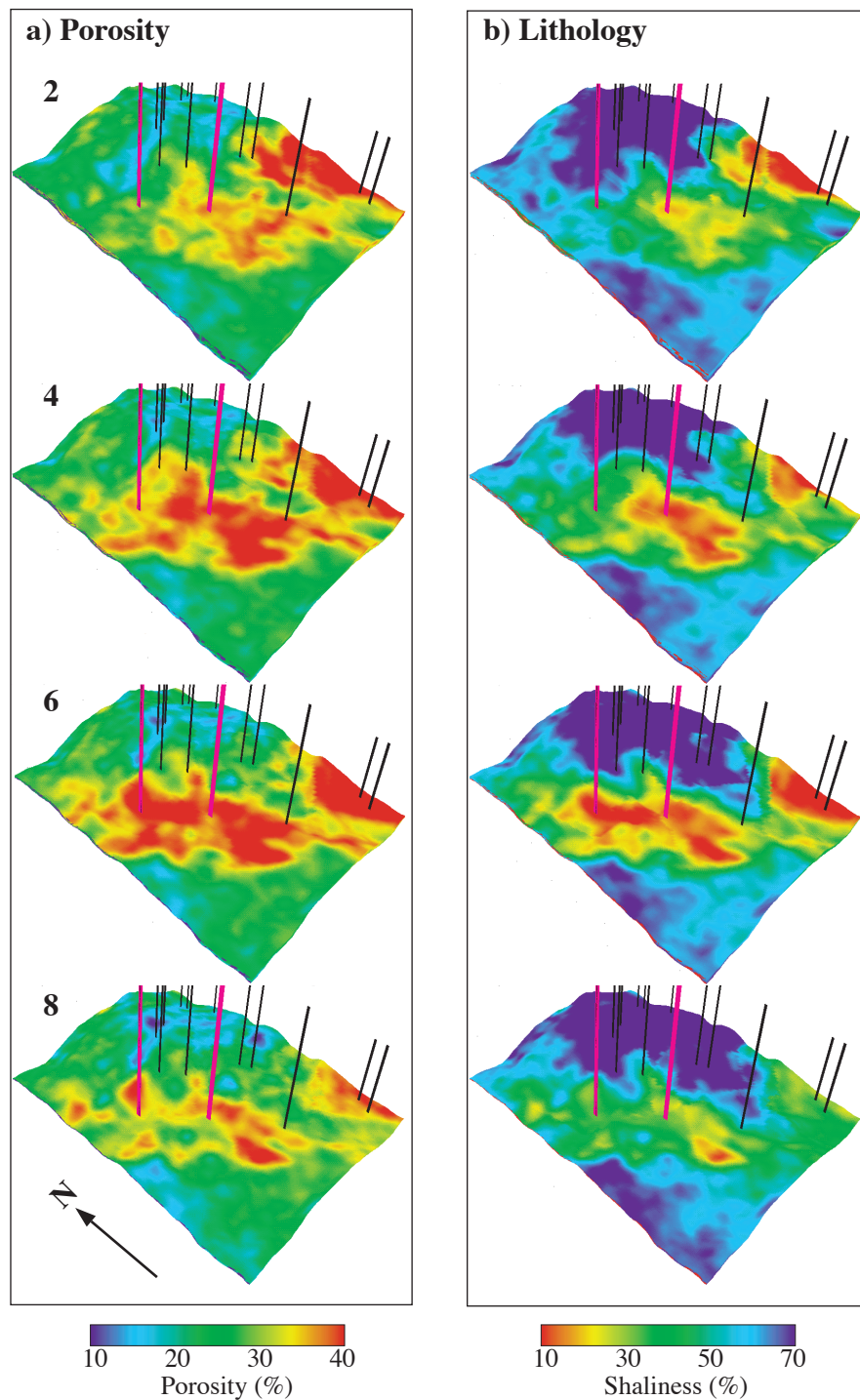


**Figure 3.6:** Results of the stochastic reservoir characterization of K8: (a) porosity (b) shaliness. For visual coherence between the two figures, high shaliness (low sand content and low porosity) is in blue. In addition to the two producing wells (purple), the other wells used for the calibration of the reservoir characterization are shown (black).

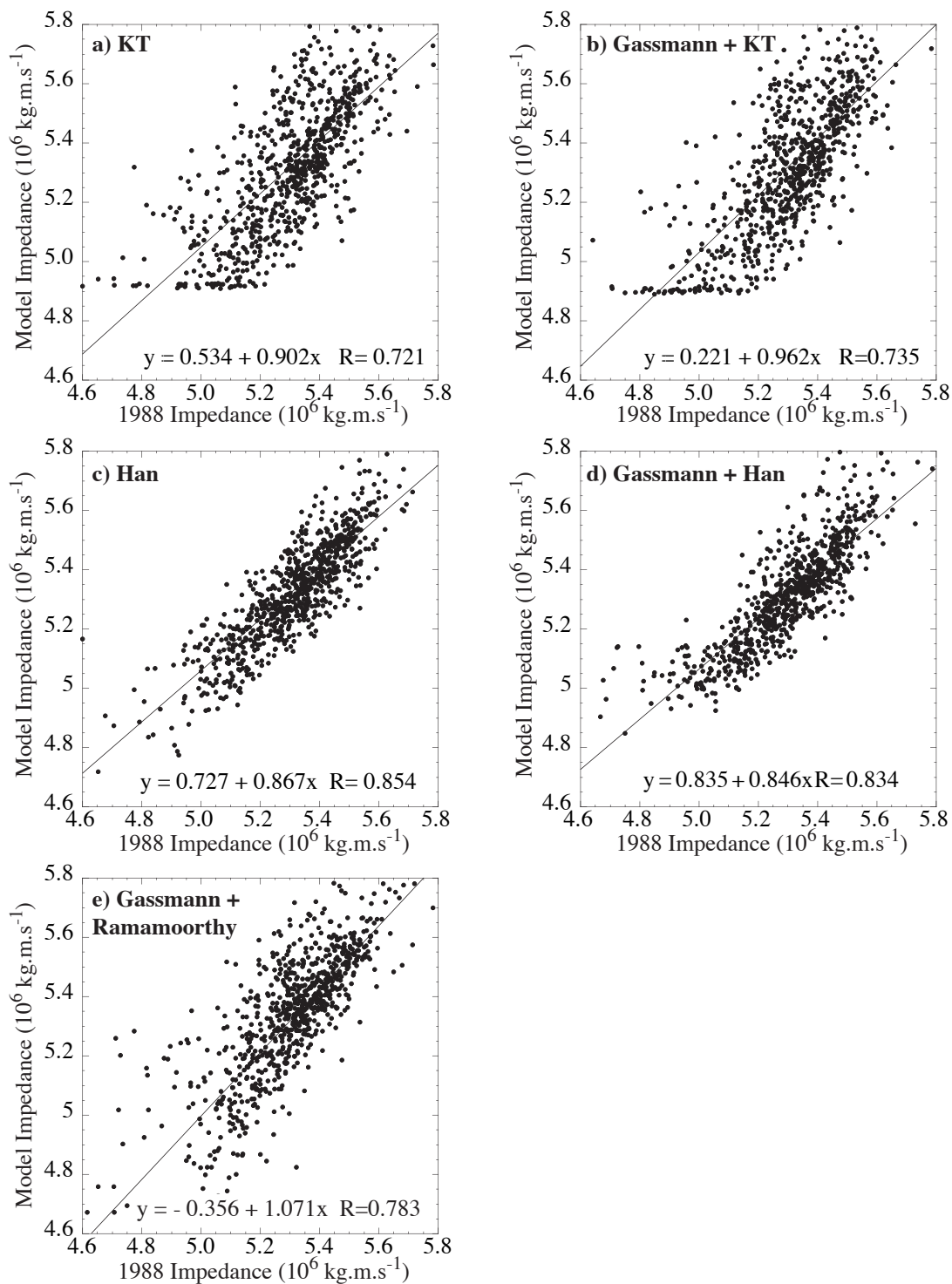


**Figure 3.7:** Comparison of the predictions of the various petrophysic models with the impedance inversion of 1988, before production. (a) KT, (b) Gassmann+KT, (c) Han, (d) Gassmann+Han and (e) Gassmann+Ramamoorthy. Equations of the linear fits and regression coefficients (R) are given in each figure.

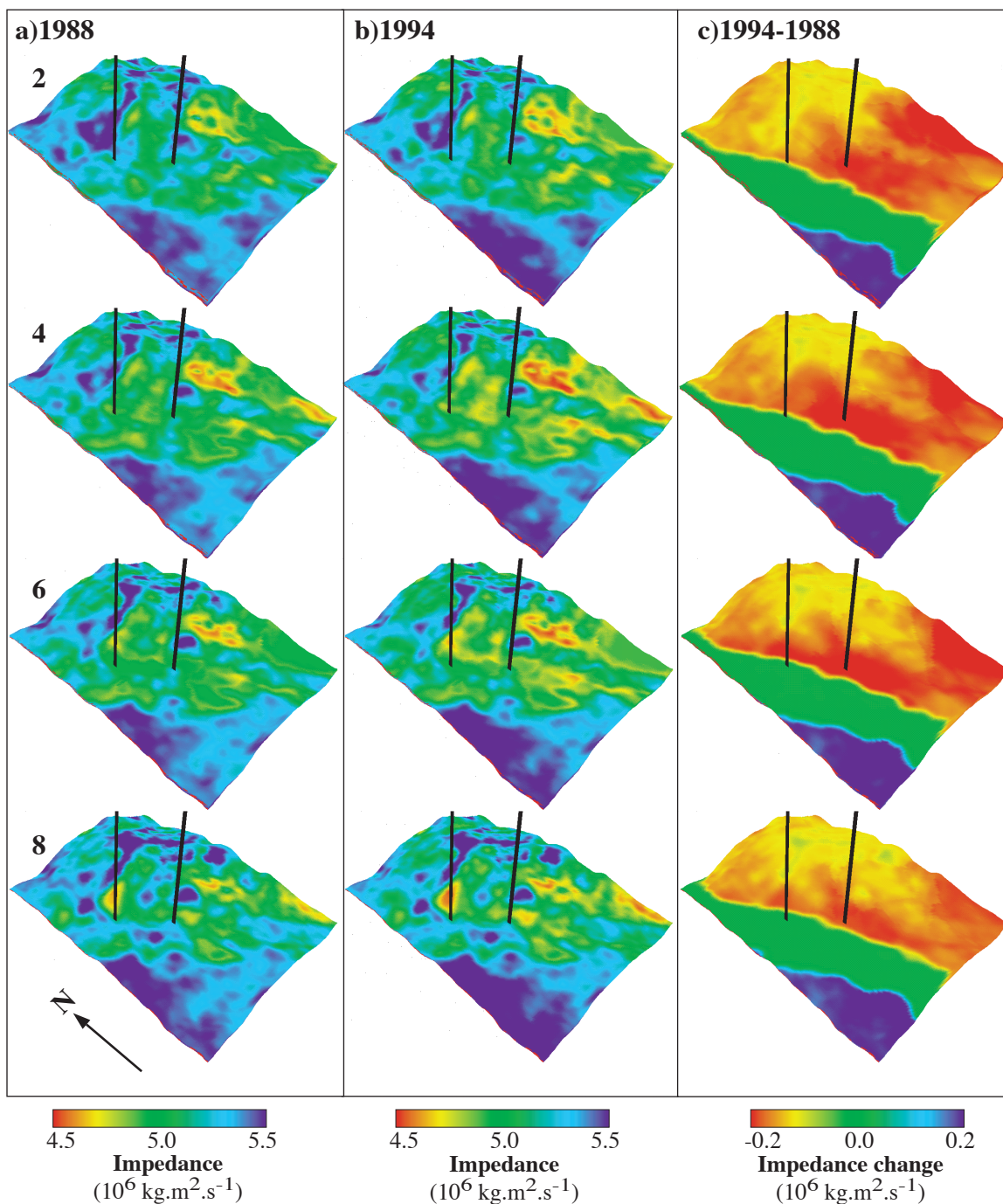


**Figure 3.8:** Evolution of the reservoir impedance distribution in the case of a uniform sweep of the reservoir. (a) Impedances calculated before production, when the reservoir fluids are in hydrostatic equilibrium. Oil saturation is uniformly 70%, the rest of the pore space corresponds to connate water. (b) Impedance distribution if the gas cap had migrated uniformly downdip to 3280 mbsf between 1989 and 1994. (c) Change in impedance that would be observed in this simple case. The comparison with the inversion results (Fig 3.4c) shows that the reservoir behavior is more complex.

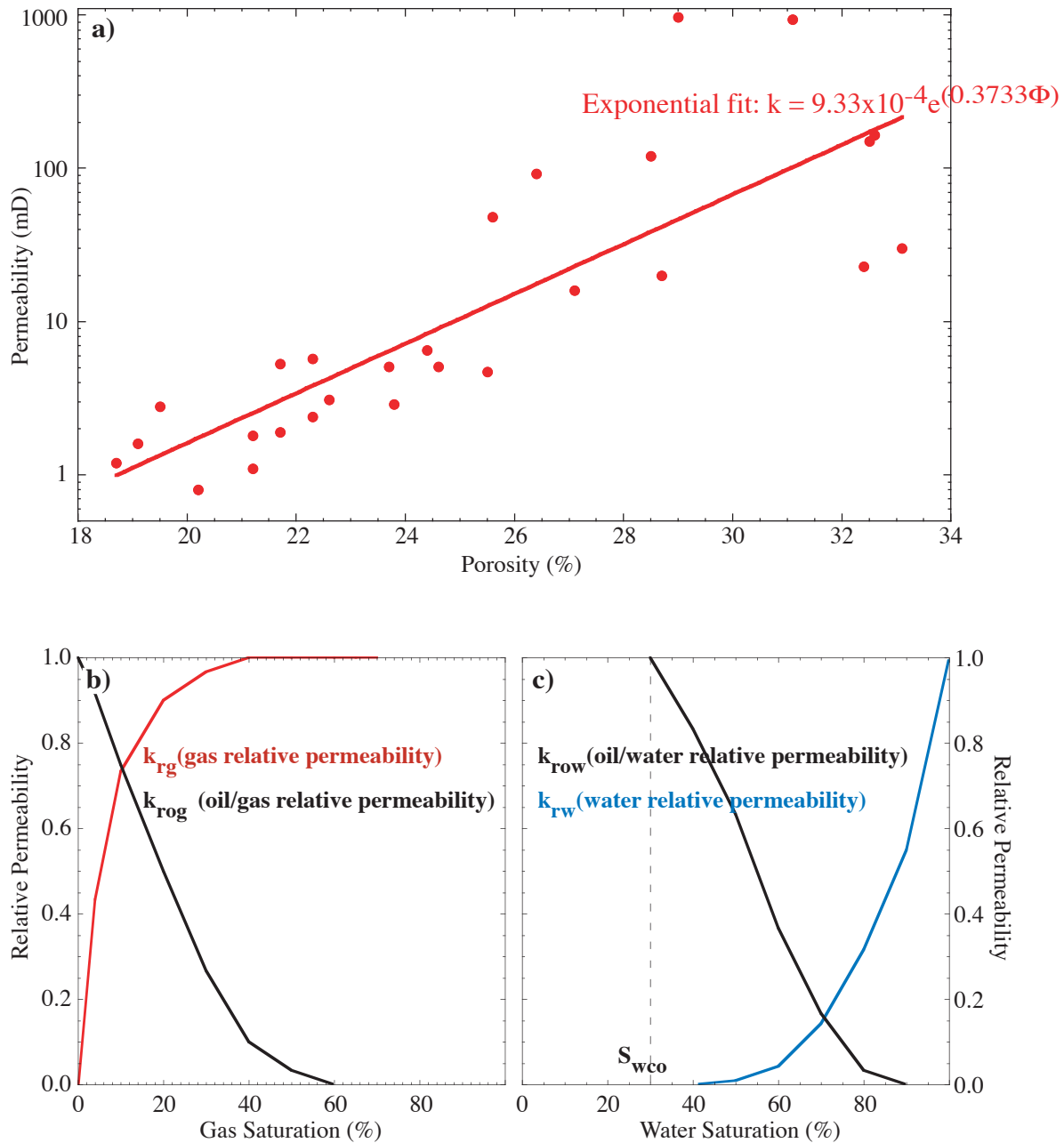


**Figure 3.9:** (a) Relationship between permeability and porosity measured on 26 sidewall cores collected in K8. The equation of the exponential fit is used to define the permeability distribution in K8. (b) Gas/Oil saturation function. (c) Oil/Water saturation function

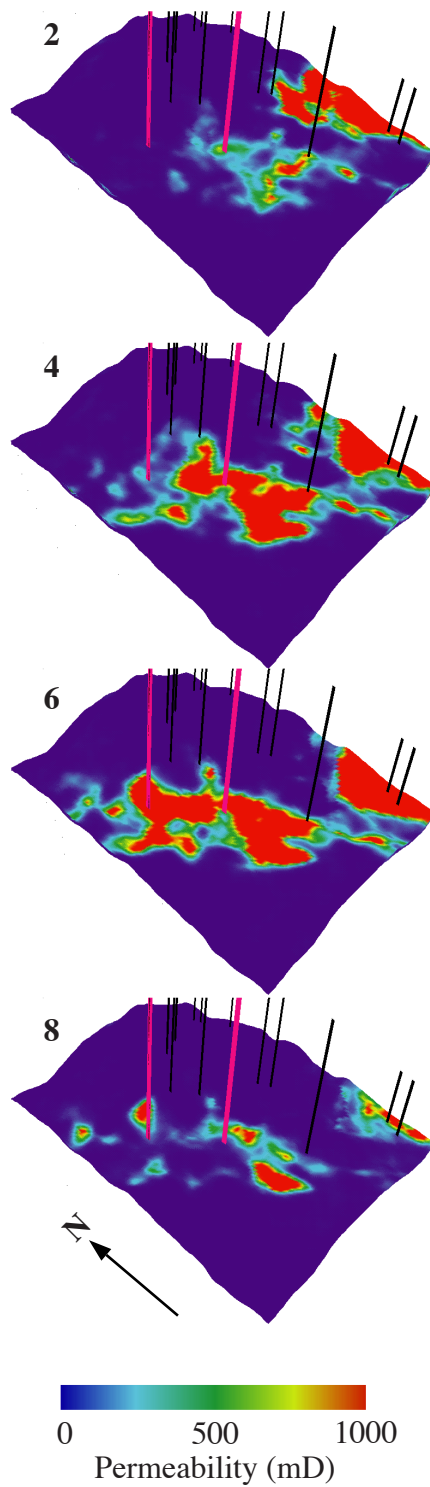


**Figure 3.10:** Permeability distribution in K8, calculated from the results of the reservoir characterization and the permeability/porosity relationship derived from K8 core samples. All the wells used for the reservoir characterization are shown.

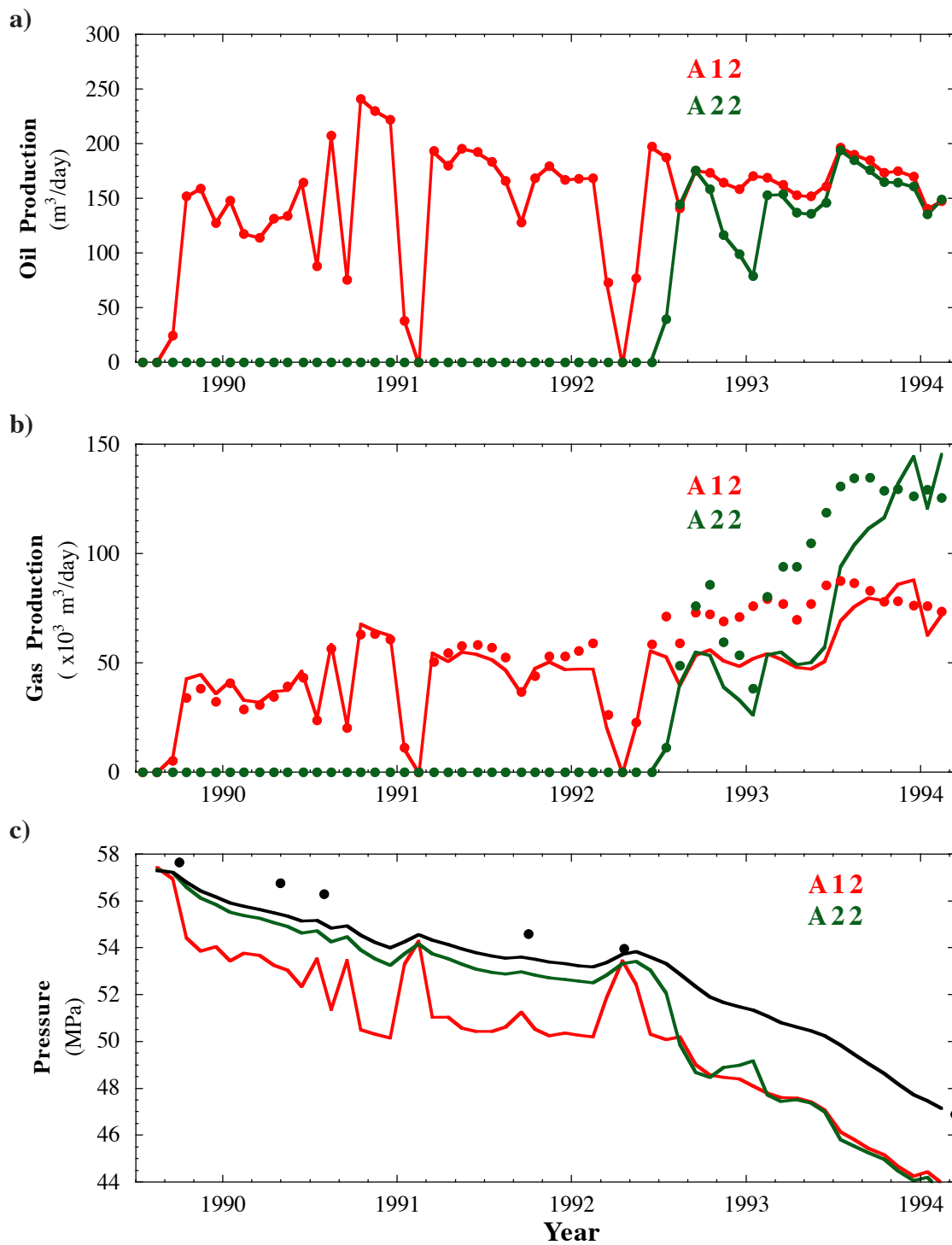


**Figure 3.11:** Comparison between observed and simulated (a) oil and (b) gas productions in K8. Filled circles represent the observed data shown in Figure 3.3, and lines are simulation results. In (c) evolution of the field pressure (Black line) can be compared with the few BHPs available.

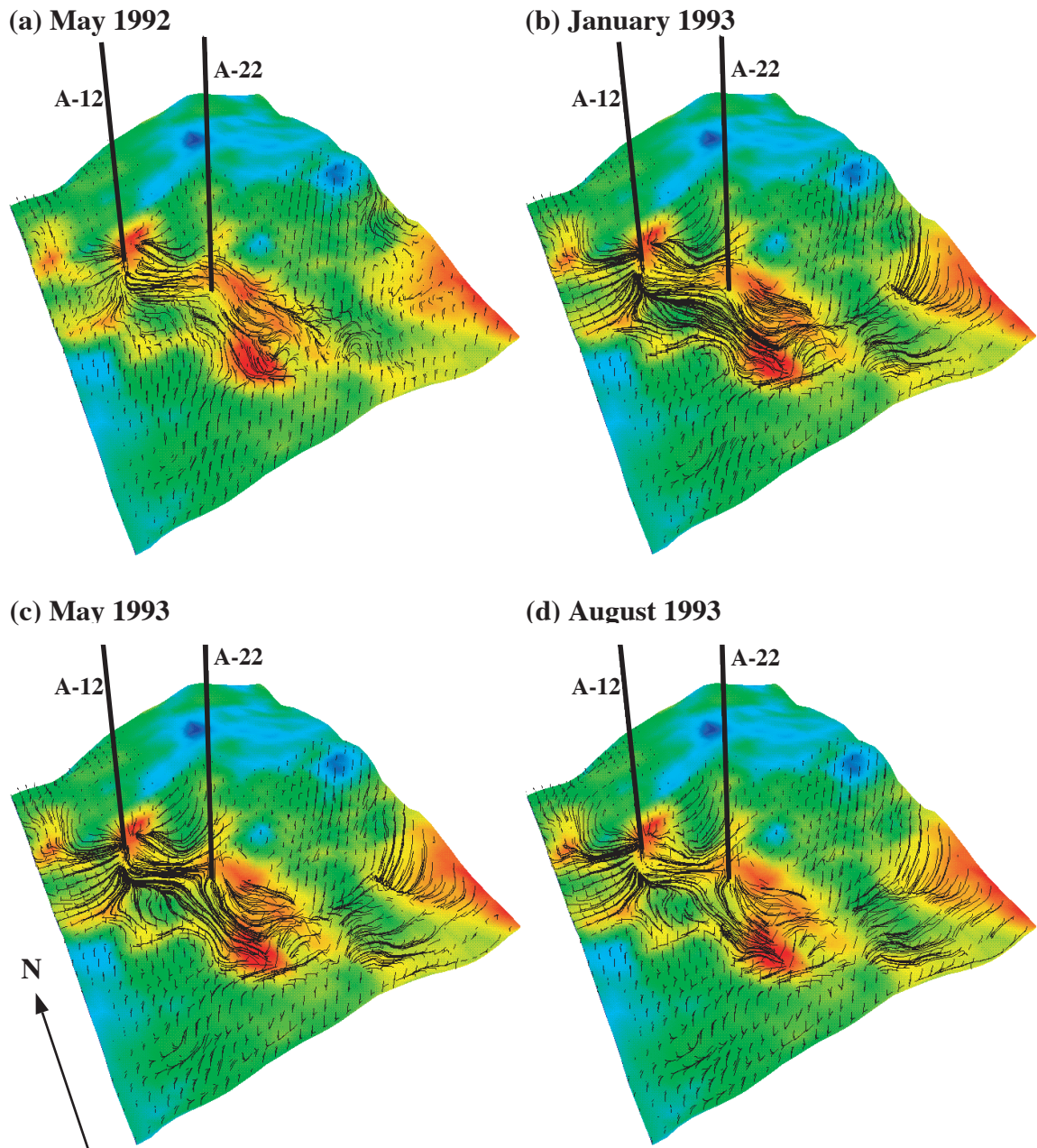


**Figure 3.12:** Oil migration stream line in K8 at various dates (a) 05/92, (b) 01/93, (c) 05/93, (d) 08/92. The lines are not actual particle trajectories, but represent the velocity field at each time. The background color pattern is the porosity distribution at the bottom of the reservoir.

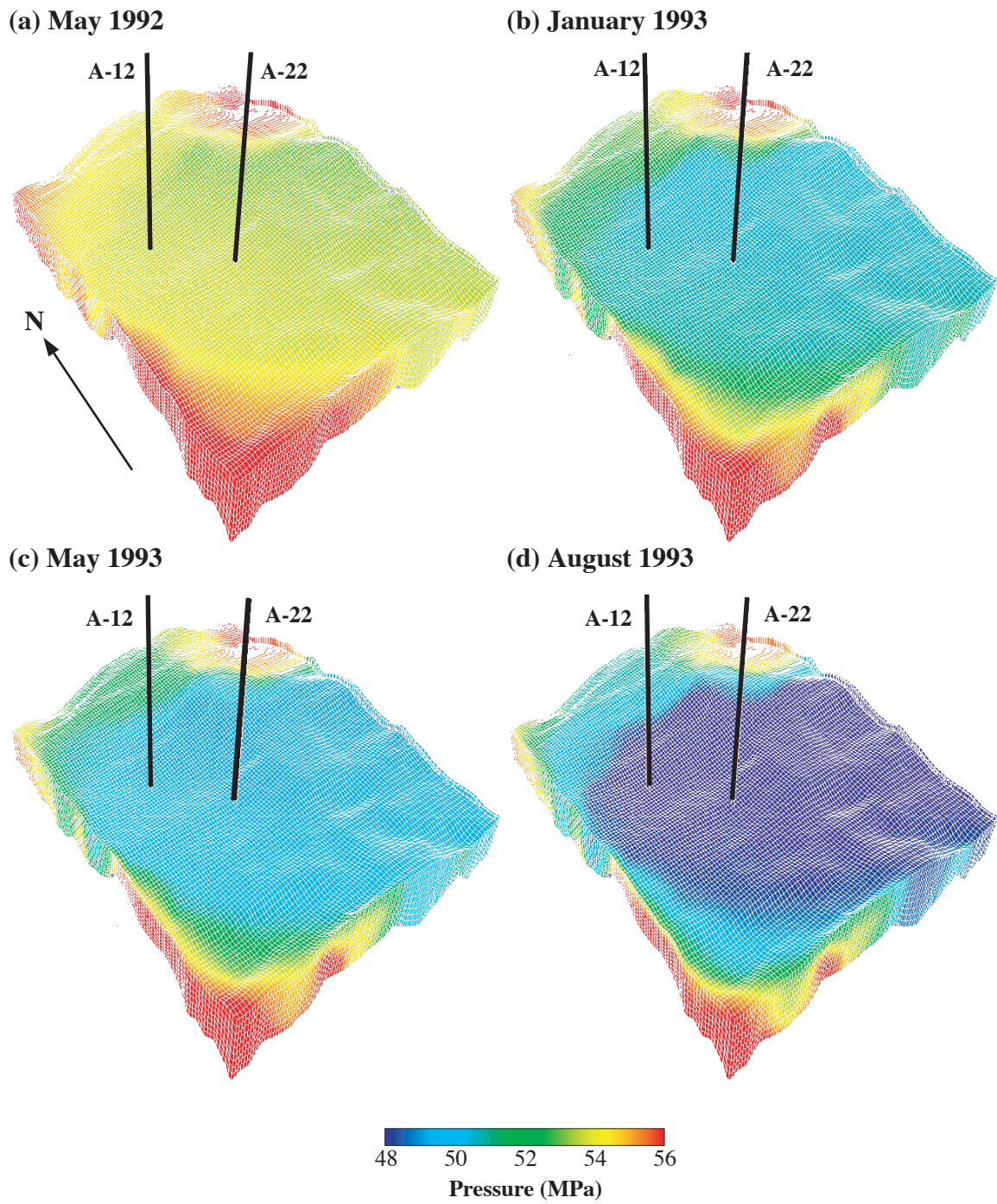


**Figure 3.13:** Pressure distribution in the reservoir at the same times as in figure 3.12.

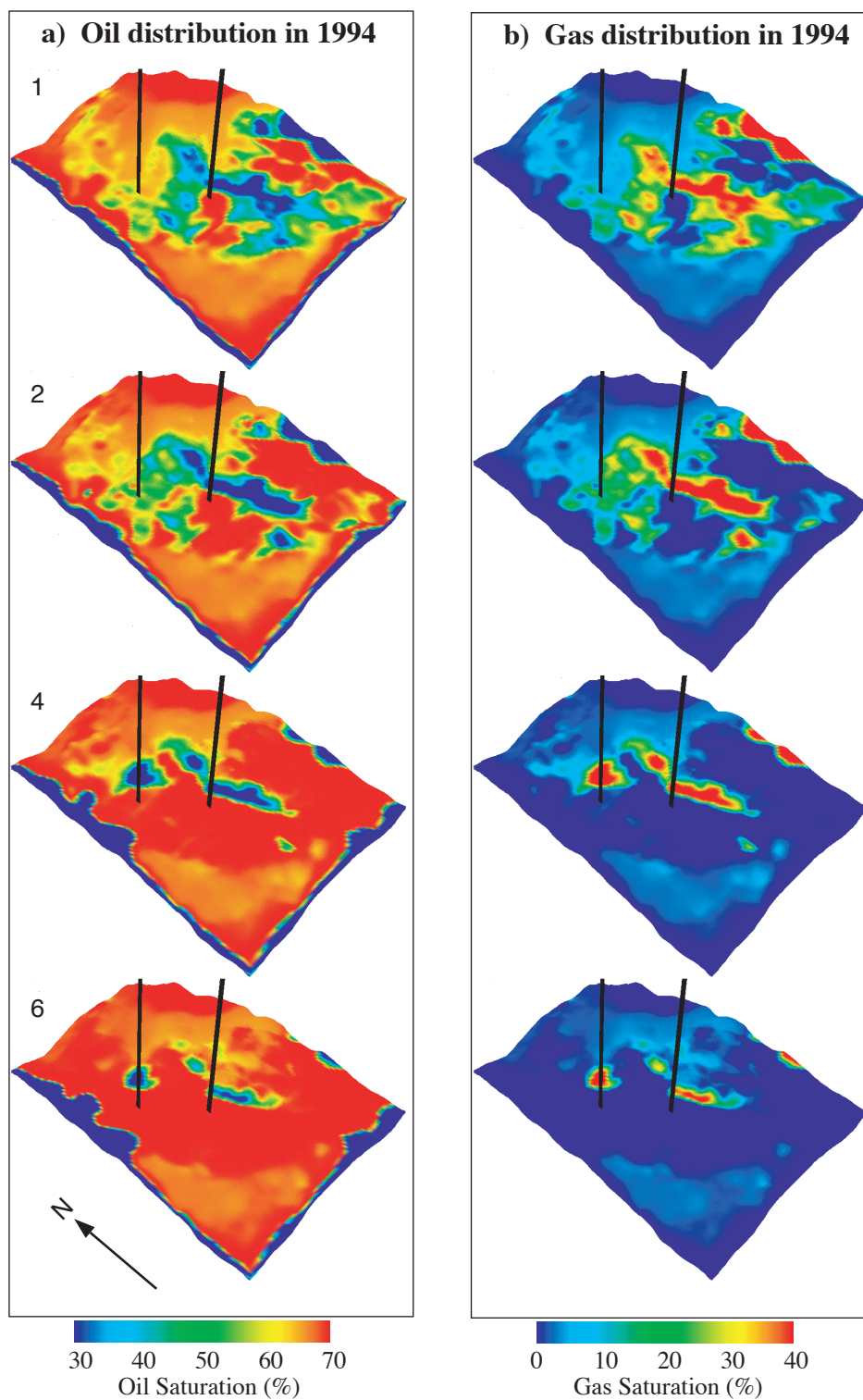


**Figure 3.14:** (a) Oil and (b) gas saturation at the end of the simulation of K8 in 1994. At the beginning of the simulation, they were uniformly 70% and 0%, respectively.

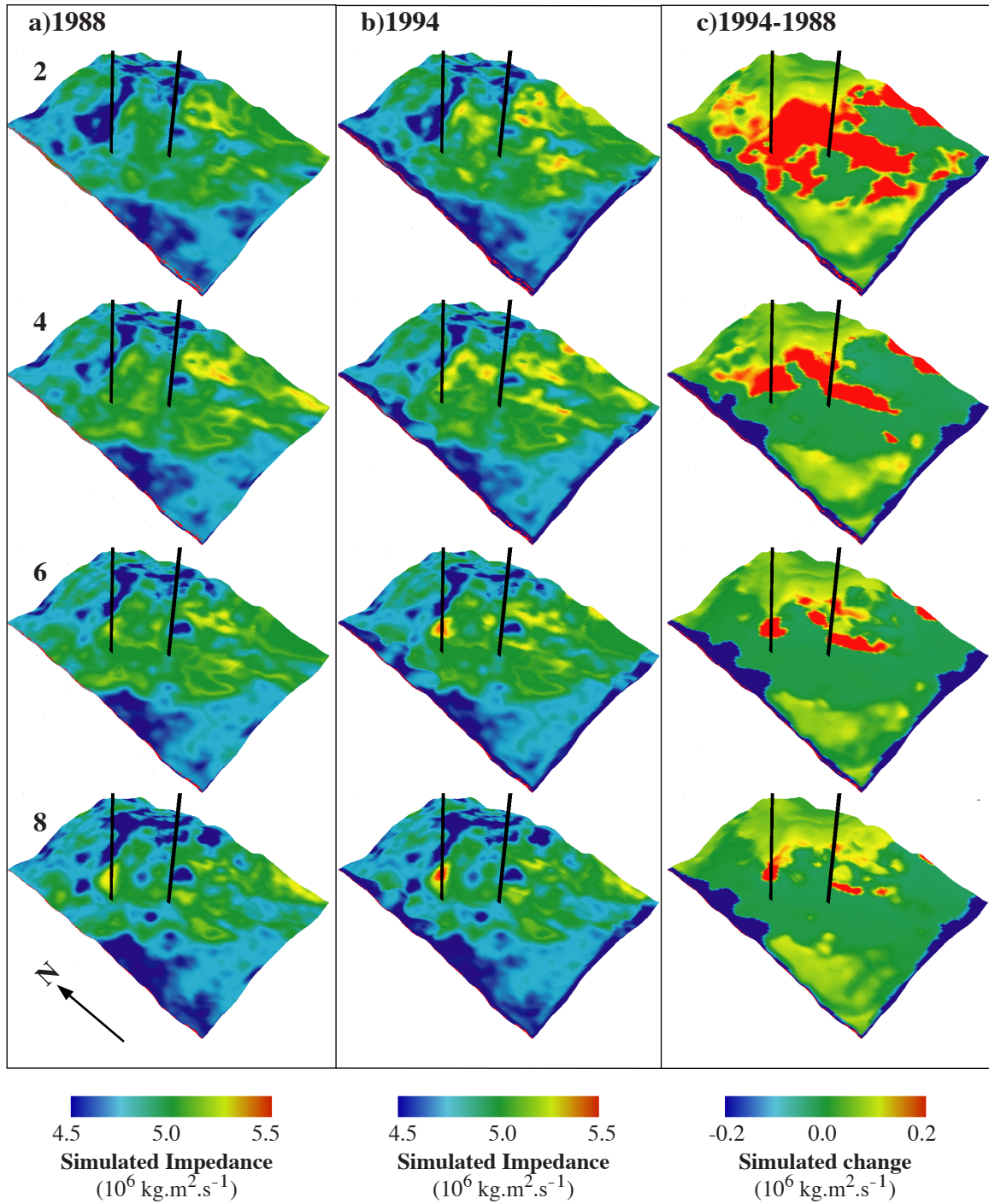


**Figure 3.15:** Impedances calculated from the simulation results in K8 in 1988 (a), and in 1994 (b). (c) Difference between the two time steps.

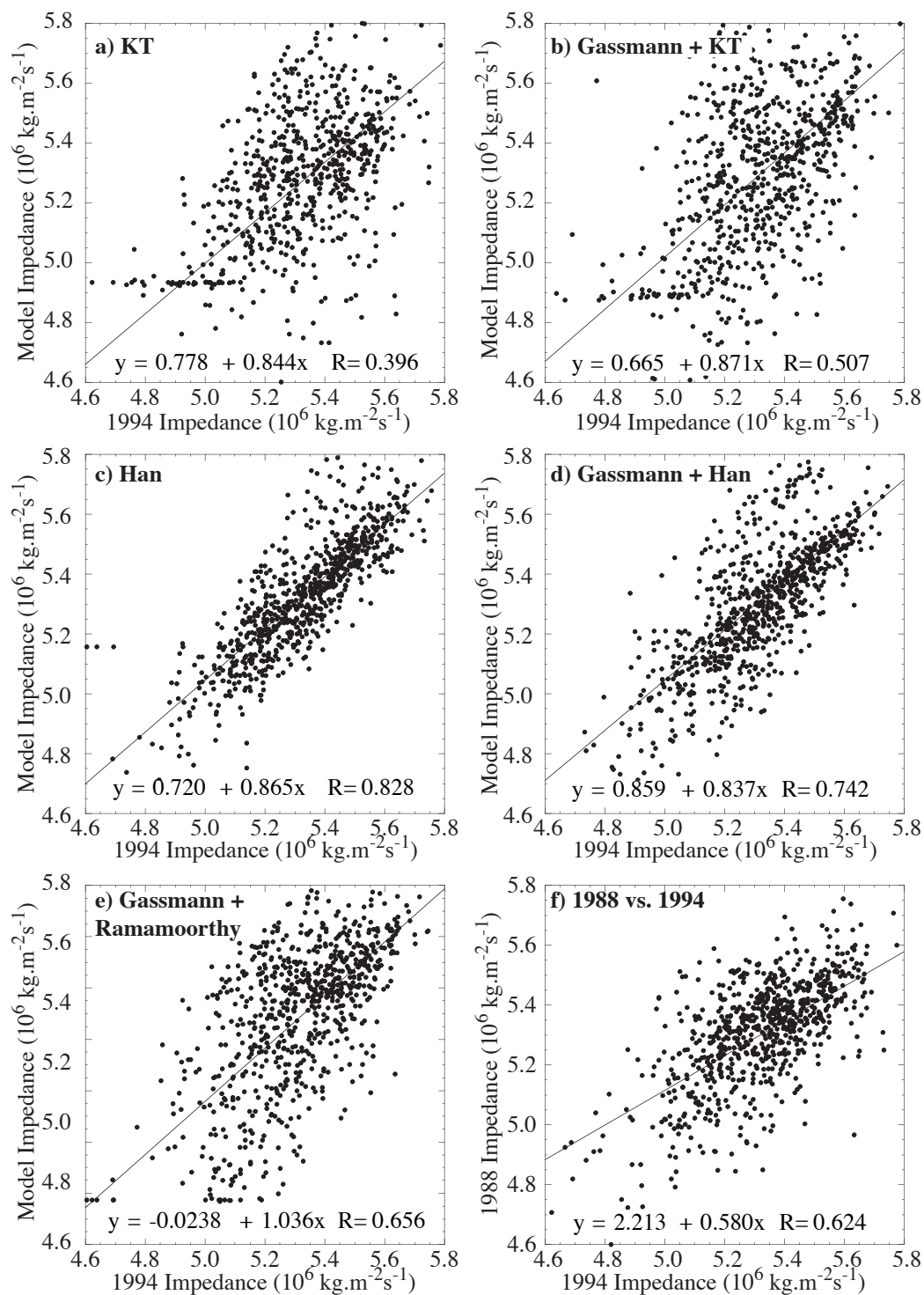


**Figure 3.16:** Comparison of impedances calculated with the various elastic models at the end of the simulation with the impedance inversion of 1994 (a) KT (b) Gassmann+KT, (c) Han, (d) Gassmann+Han and (e) Gassmann+Ramamoorthy. (f) Crossplot of the two inversion results. Equations of the linear fits and regression coefficients (R) are indicated in each figure.

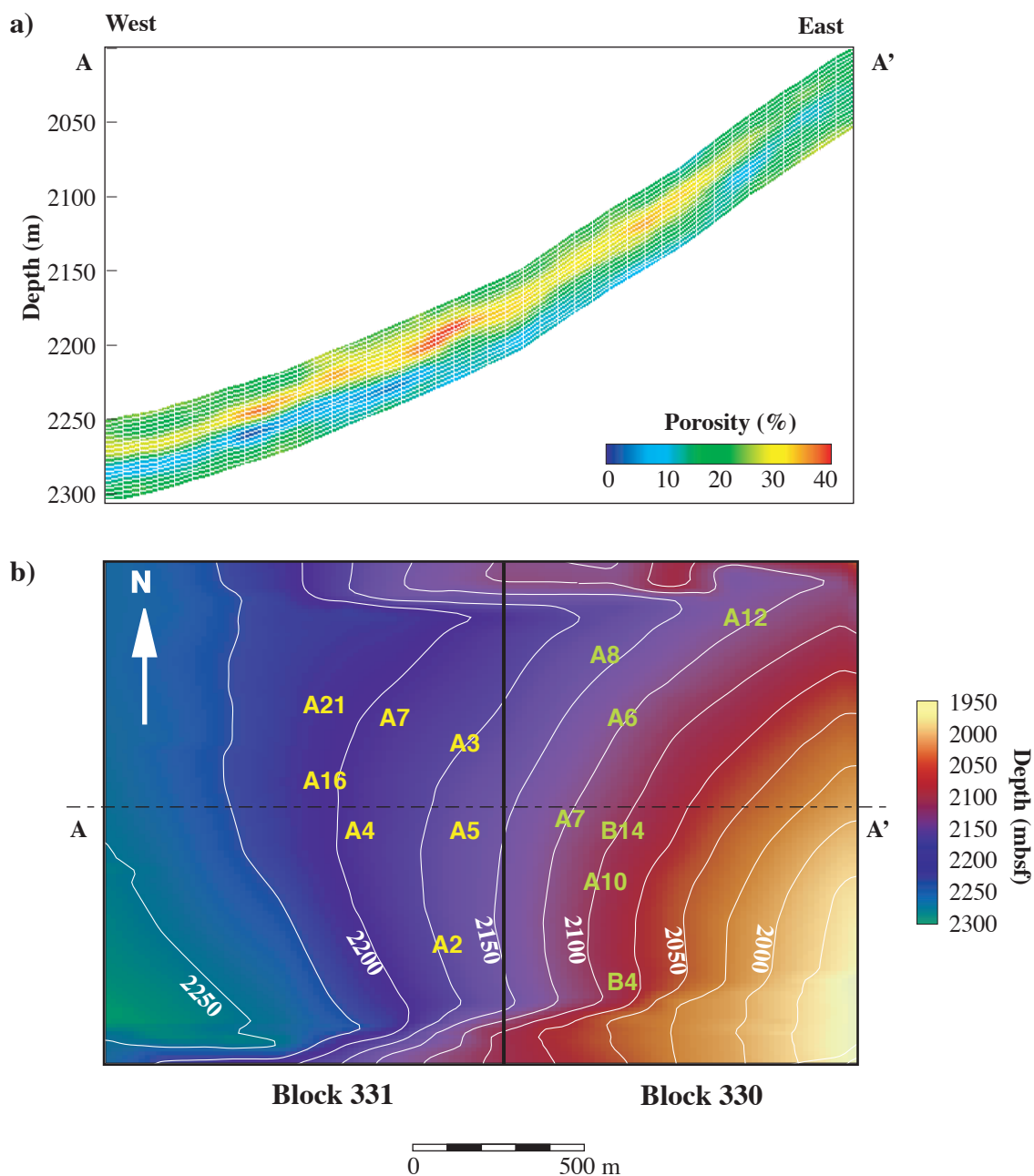


**Figure 3.17:** (a) East-West cross section of the LF sand, showing the grid used in the simulation and the porosity distribution. Layers in the grid have all the same thickness (3 m) and are numbered from top to bottom. (b) Structure of the top of the LF sand within the fault block B and location of the 14 wells that have been producing from this part of the reservoir between 1972 and 1992.

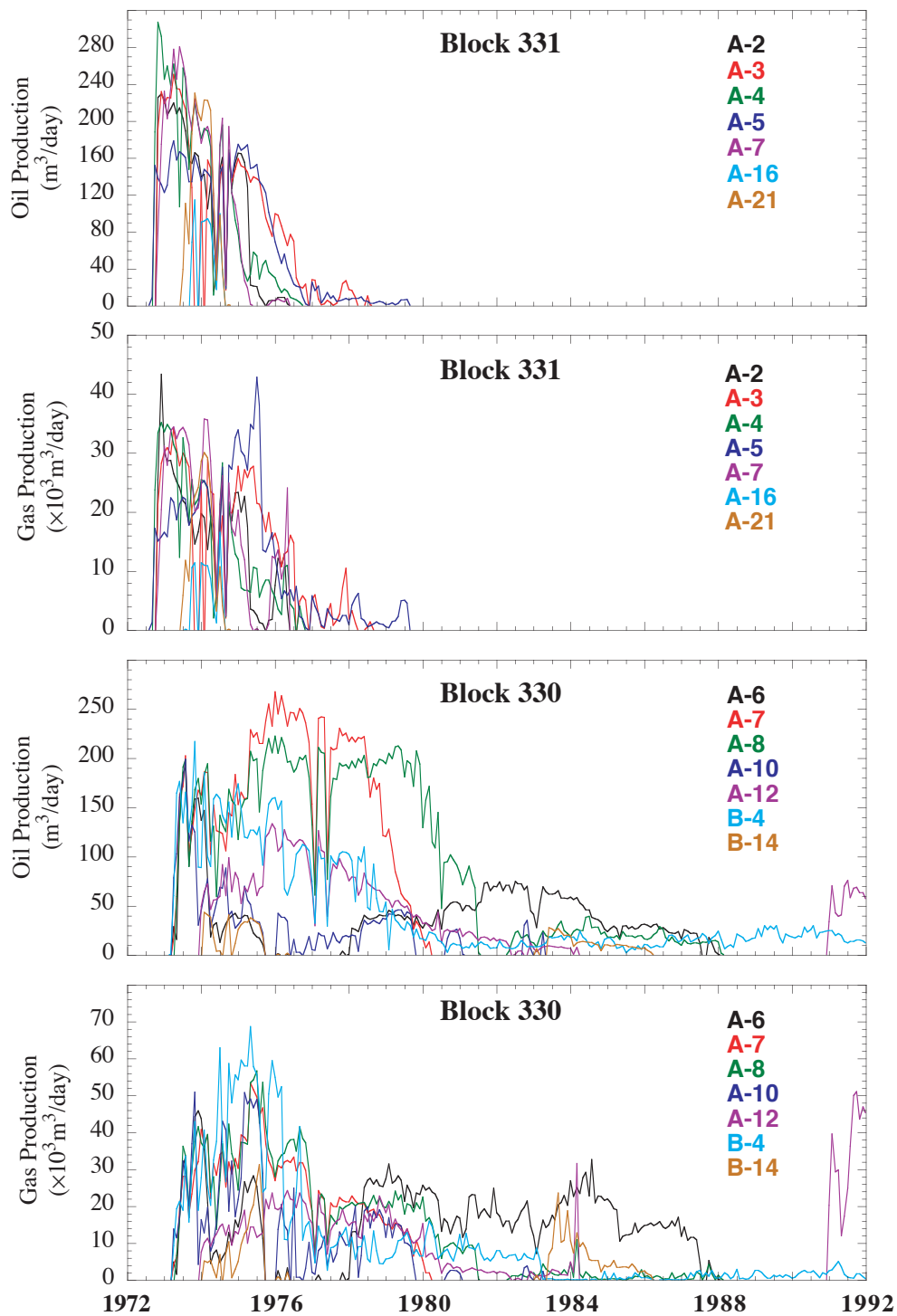


**Figure 3.18:** Production history from the fault block B in the LF sand. (a) Oil and (b) gas production rates in the downdip block 331. Production in this Block stopped in 1980. (c) Oil and (d) Gas production in Block 330. Seven wells were producing from each block.

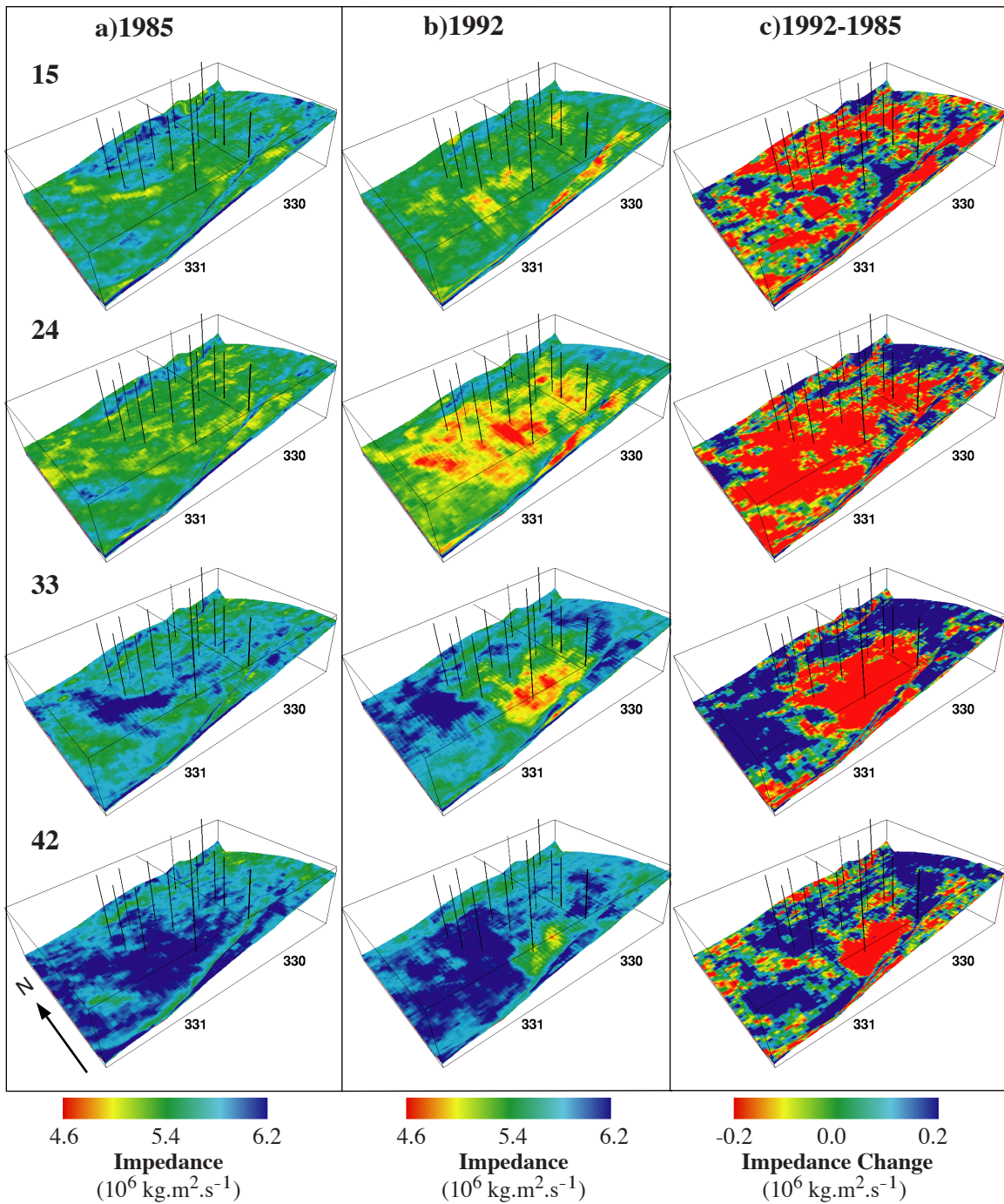


**Figure 3.19:** Impedance inversion results in the LF sand in 1985 (a) and 1992 (b). (c) Difference between the two inversions. Color convention are the same as in Fig. 3.4, red indicating low impedance in (a) and (b) and decrease in impedance in (c).

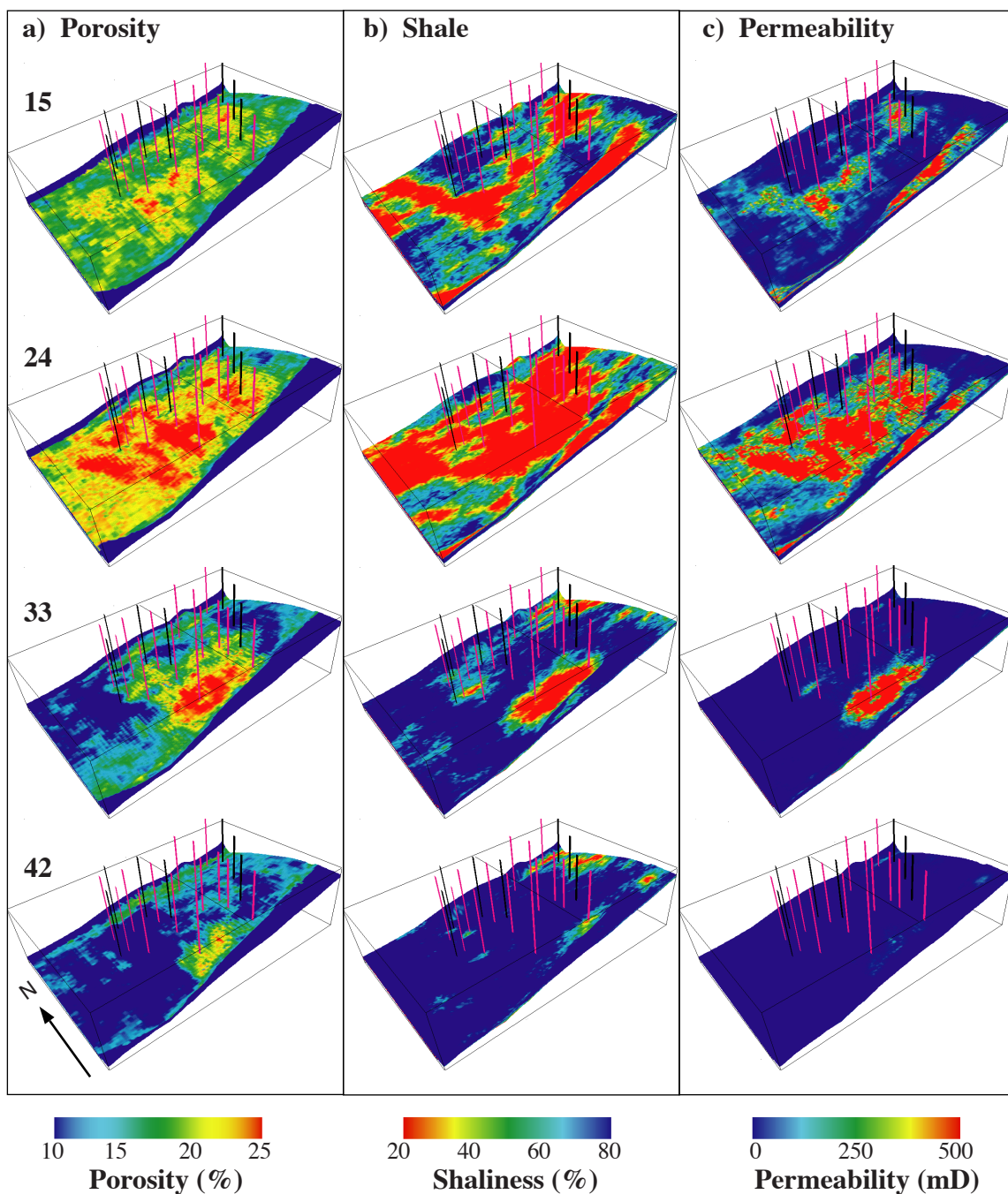


**Figure 3.20:** (a) Porosity, (b) shaliness and (c) permeability distributions in the LF sand. The shaliness was determined by geostatistical simulation. Porosity was calculated by a time-average relationship using the 1992 impedance and the shaliness. The blue areas in the porosity distribution indicate the actual limits of the fault block B, bounded by two sealing faults to the north and to the south. The producing wells are purple. Additional wells used to constrain the reservoir characterization are also shown in black.

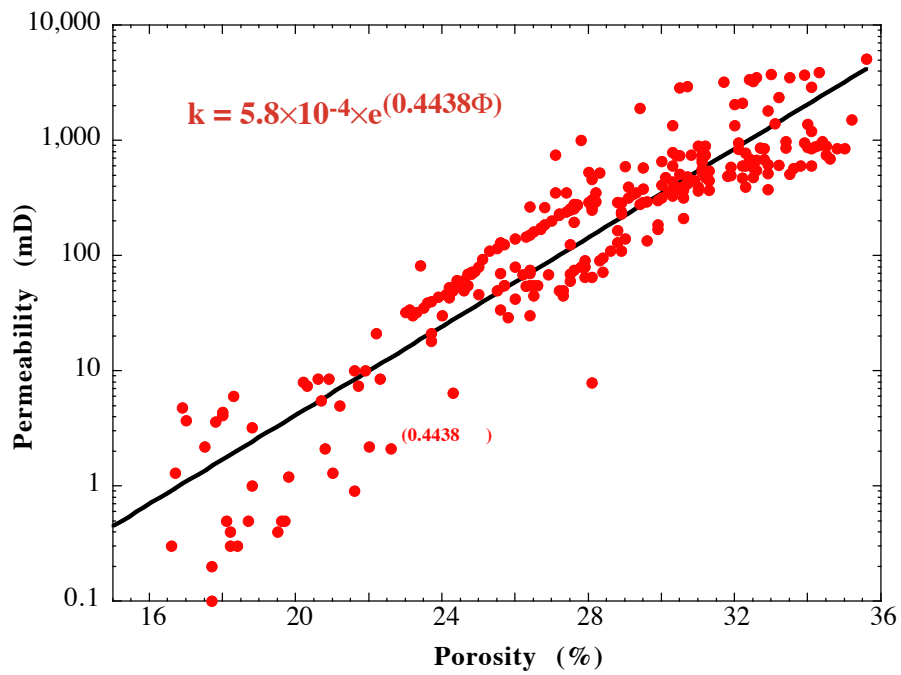


**Figure 3.21:** Permeability/Porosity relationship measured on 250 core samples from the LF sand. The equation of the least square exponential fit was used to calculate the permeability distribution in the reservoir model.

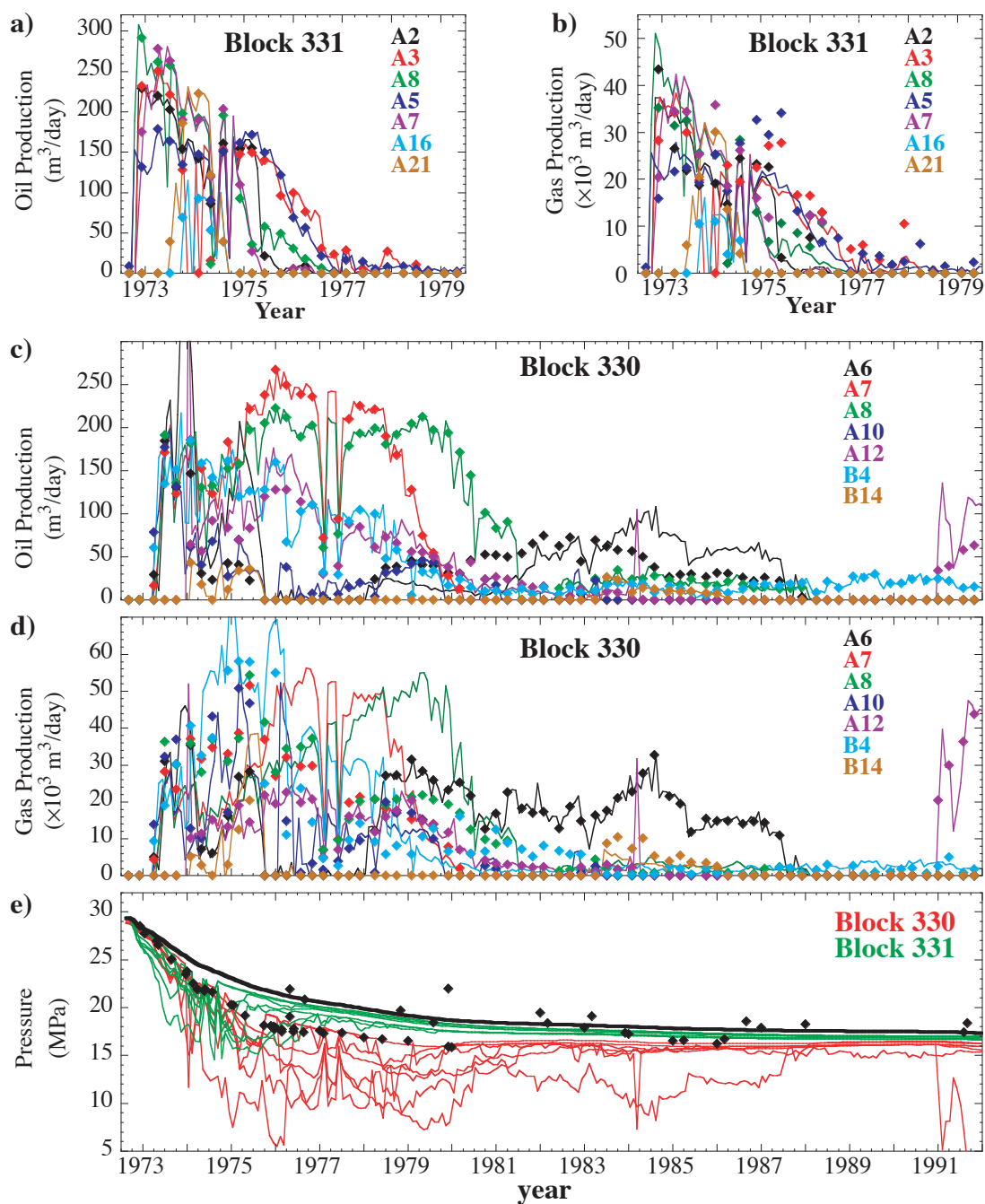


**Figure 3.22:** Results of the production history match in the LF sand. (a) Oil and (b) gas history match in Block 331. (c) Oil and (d) gas history match in Block 330. Diamonds are the observed data shown in Figure 3.18. Lines are simulated production. (e) Comparison of the simulated BHPs with the BHPs collected during the history of the reservoir. Because the location of most data (diamonds) were not available, they are only indicators of the global reservoir pressure evolution. Green and red lines indicate simulated pressures from the wells in Blocks 331 and 330 respectively. The thick black line shows the evolution of the average reservoir pressure.

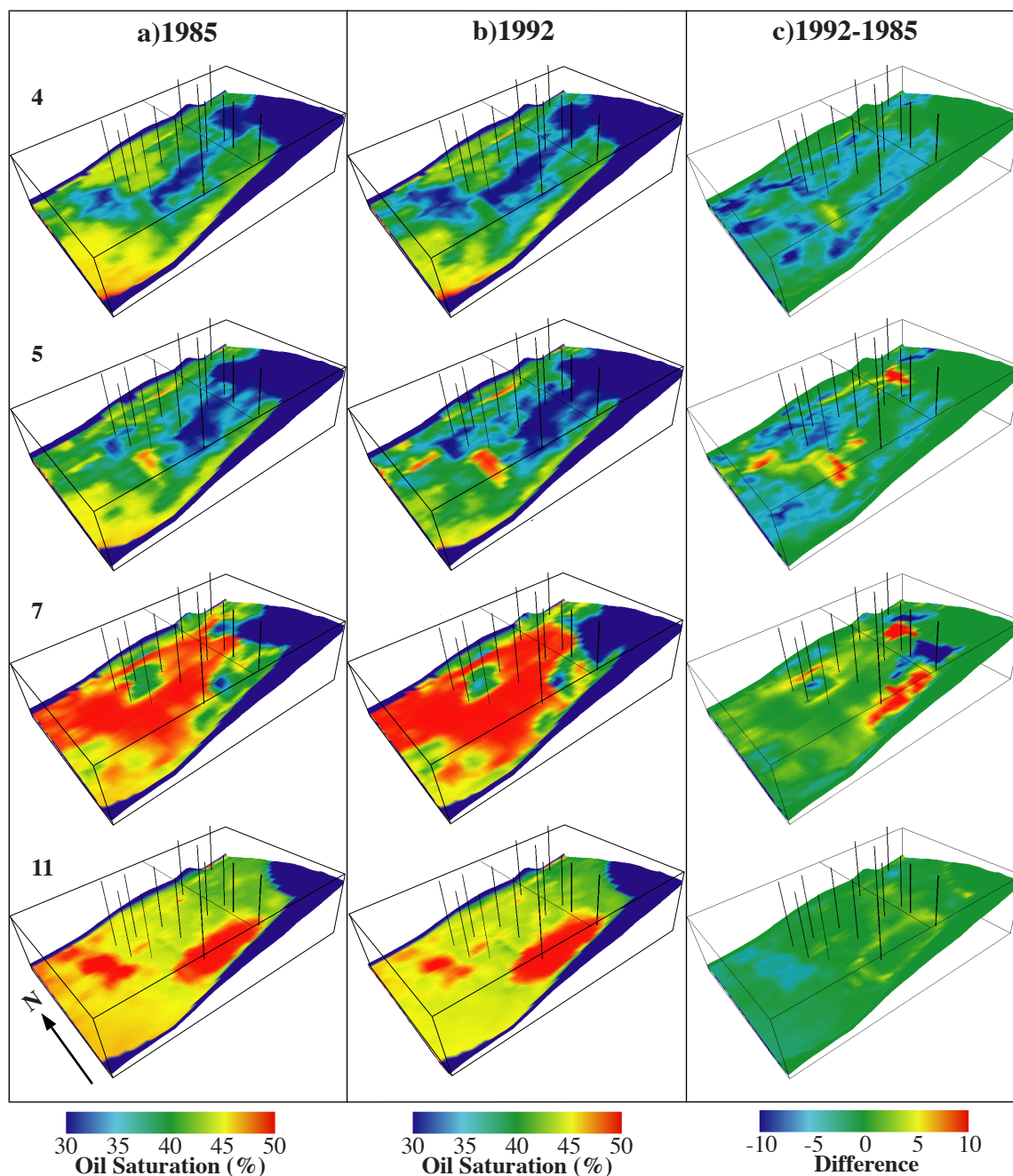


**Figure 3.23:** Simulated oil saturation in the LF sand in (a) 1985 and (b) 1992. (c) Difference between (a) and (b), indicating the changes in oil saturation between the two 3D seismic surveys. In this figure and the following ones, the resolution of the original volume has been upscaled by 3, corresponding to the actual resolution of the simulator. The layer numbers refer to the upscaled model layers.

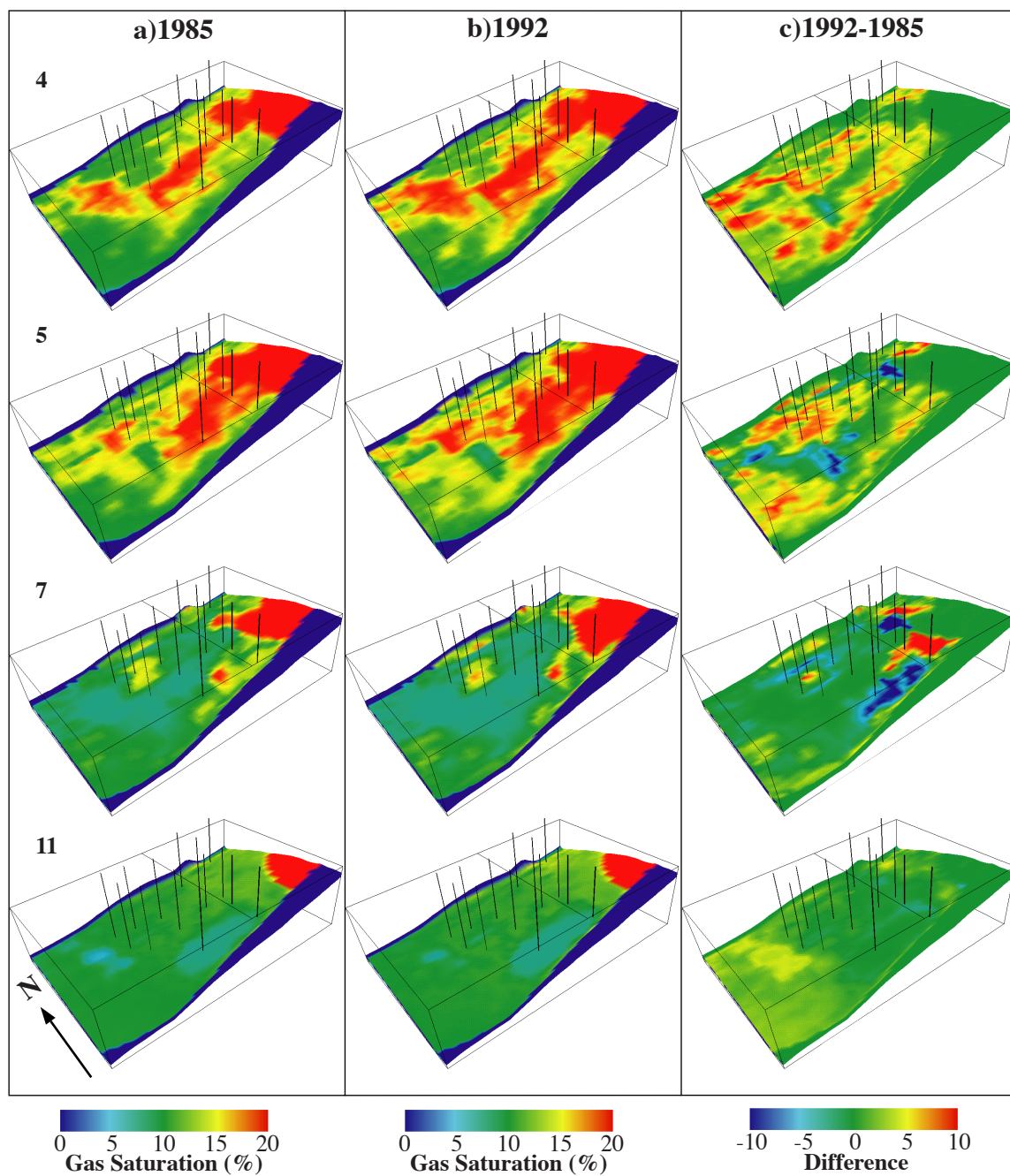


**Figure 3.24:** Simulated gas saturation in the LF sand in 1985 (a) and 1992 (b).  
 (c) Difference between (a) and (b), indicating the changes in gas saturation between the two 3D surveys.

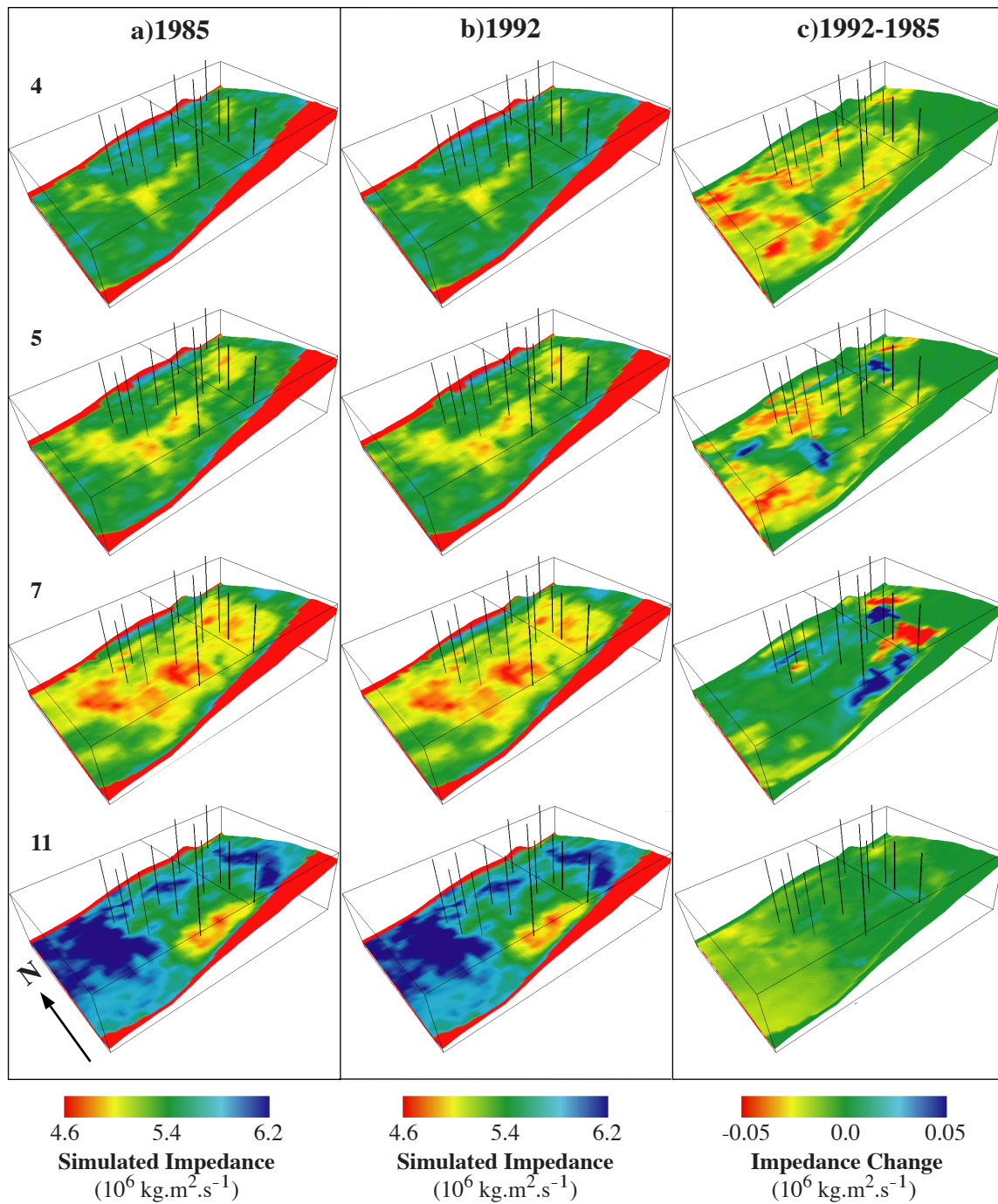


**Figure 3.25:** Impedances calculated from the simulation results in LF at the time of the 3D seismic surveys in 1985 (a) and in 1992 (b). (c) Simulated impedance difference between the two surveys.

## **Chapter 4:**

### **3D Temperature distribution and numerical modeling of heat transfers in an active fault zone: Eugene Island 330, Offshore Louisiana.**

#### **4.1 Abstract**

At the center of an active growth fault system underlain by high-relief salt diapirs, the Eugene Island 330 field is a case study for the dynamics of active oil fields. Here, Plio-Pleistocene sandstone reservoirs are supplied with mature hydrocarbons by migration of fluids from overpressured shales upwards along the active fault system. The heat carried by the ascending fluids and the presence of highly conductive salt diapirs create strong temperature anomalies affecting the entire mini-basin. We present a method to interpret such complex temperature distributions by using some of the most commonly recorded data in modern oil field exploration: Bottom Hole Temperatures (BHT) and 3D seismic interpretation. More than 600 BHT from 200 wells allowed us to determine the present-day temperature field in a  $15 \times 15 \times 6$  km datacube. Using a lithological model built from the main seismic reflectors interpreted from 3D surveys, we perform a 3D numerical simulation of the conductive regime in the mini-basin. The results identify a 5-8°C temperature anomaly over the main salt diapirs. After subtraction of these results from the observed temperature field, we isolate a residual 5-10°C temperature anomaly potentially created by the upward migration of warm fluids along the multiple fault systems. Finally, using the fault surfaces interpreted from the 3D seismic survey to define the migration pathways, we build a 3D numerical model of the heat and fluid transfers required to reproduce these anomalies. Our simulations show that they could be created by periods of fluid expulsions lasting 1,000 to 5,000 years within the fault system. Such fluid expulsion activity is likely to have filled the most productive reservoirs of the EI330 oil field.

## 4.2 Introduction

The Eugene Island 330 (EI330) oil field in the Northern Gulf of Mexico (Figure 4.1) has been the focus of an unprecedented interdisciplinary effort to understand the dynamics of an active oil field. The largest Pleistocene oil field in the world [Anderson *et al.*, 1994], EI330 is at the core of an active growth fault system. Over the 30 years since discovery, multiple evidences have shown that hydrocarbons have been actively migrating along the fault during the recent history of the field and are still flowing: 1) the presence of hydrocarbon seeps at the sea floor, 2) discrepancies between oil maturity in the multiple reservoirs, and 3) temporal changes in the composition of oils produced over the last 20 years [Anderson *et al.*, 1994, Holland *et al.*, 1990]. Identifying the mechanisms and pathways of the hydrocarbon migration could indicate where to drill to take advantage of natural expulsion processes.

To study this oil field, a 15 km × 15 km × 6 km ‘data cube’ was assembled, combining multiple 3D seismic surveys, fluid samples, core, log and production data from over 600 wells. Region growing techniques were applied to High seismic Amplitude Events (HAE) in the 3D seismic data to identify the trails left by hydrocarbons moving along migration pathways [Anderson *et al.*, 1994]. However, seismic imaging alone cannot be used to determine the volumes, duration and timing of hydrocarbon migrations. The comparison of successive 3D surveys indicates changes in seismic attributes within reservoirs under production, but this 4D analysis detects changes in seismic attributes due to forced fluid substitution and pressure depletion during the production of reservoirs [He, 1996, Chapter 3]. It is mostly sensitive to the movement of strong seismic events such as oil/water and gas/oil contacts on the scale of a reservoir [Anderson *et al.*, 1994]. It cannot be used for the much slower migrations within the fault that feed the reservoirs over thousands of years.

Unlike seismic attributes, formation temperature can be an indicator of long term fluid circulation. The upward migration of large volumes of fluid coming from deeper and warmer formations along localized conduits can create significant thermal anomalies [Hopper, 1990, Borner and Sharp, 1988]. The amplitude and the extent of the anomaly is dependant on both velocity and duration of the fluid migration, and it can remain detectable well after the end of the migration because of the low thermal diffusivity of most sediments. However, in addition to possible fluid migration along the fault, the presence of heterogeneous structures such as salt diapirs common in the Gulf of Mexico can also create strong thermal anomalies. Therefore, the interpretation of the temperature distribution requires to identify and quantify the various components of the thermal regime in order to isolate the specific contribution of fluid migrations.

More than 600 Bottom Hole Temperatures (BHT) have been recorded in 200 wells penetrating the EI330 field. After correcting the data for drilling disturbances, we present the current 3-D temperature distribution in EI330, which displays several anomalies indicative of a complex thermal regime. To identify its various components, we numerically simulate first the 3D conductive regime to determine the temperature anomalies produced by the salt diapirs underneath the mini-basin. Assuming that the differences between this model and the measured temperatures result from advective heat flow through the fault, we reproduce these differences by a complete 3D numerical modeling of heat and fluid flows in the fault. Our results indicate the fluid migration history and mechanisms that could be at the origin of the observed temperature distribution.

### **4.3 Geological Setting**

The Eugene Island Block 330 field lies under 85 m of water, approximately 270 km southwest of New Orleans, near the southern edge of the Louisiana Outer Continental

Shelf (Figure 4.1). The extremely rapid influx of Upper Cretaceous and Lower Tertiary terrigenous sediments from the ancestral Mississippi delta has mobilized the Jurassic Louann salt, which left a trail of isolated diapirs across the shelf, and formed semi-continuous salt uplifts under the slope of the Gulf Coast margin [Woodbury *et al.*, 1973]. The study area is made of nine property blocks located at the transition between these two salt provinces [Holland *et al.*, 1990], with two salt diapirs underneath the South-East and the North-West corners of the study area (Figure 4.2).

The Tertiary and Quaternary sediments overlying the salt define three main facies representative of the normal evolution of a deltaic system prograding across a continental margin [Selley, 1988; Holland *et al.*, 1990, Alexander and Flemings, 1995]: 1) directly over the salt, massive shales and turbidites were deposited in a prodelta environment. 2) They are overlain by a sequence of proximal deltaic sands and transgressive shales deposited during sea-level fluctuations when the delta slope was located nearby. The most productive reservoirs of the field are in this interval [Holland *et al.*, 1990]. 3) The uppermost section was deposited after the delta had prograded southward, and is composed of fluvial massive sands. The transitions between the different sedimentation phases were identified in the 3D seismic data by reflectors corresponding to transgressive episodes. Biostratigraphic markers *Cristellaria* "S" (*Cris S*) and *Small Gephyrocapsa* (2) (*Sm. Gep(2)*) [Alexander and Flemings, 1995] define the bottom and the top of the proximal deltaic phase, respectively (Figure 4.3).

Structurally, the EI330 field is a classic salt-withdrawal shelf minibasin [Alexander and Flemings, 1995]. It is bounded by two main fault zones (see Figure 4.3). The northern and eastern boundaries are defined by the listric, normal, "Red" Fault, while the south and west borders are defined by the counter-regional "Blue" Fault that developed as extensional compensation during the salt withdrawal to the south. Oil and gas reservoirs are trapped under two rollover anticlines on the downthrown side of the Red Fault.

## 4.4 The Temperature distribution in Eugene Island 330

### 4.4.1 Data Correction

As one of the most productive oil fields in the Gulf of Mexico, EI330 has been extensively studied and sampled. Over 600 Bottom Hole Temperatures were collected from about 200 wells in the 9 blocks study area. During the drilling of a well, large quantities of “mud” are circulated in the borehole to facilitate the drilling, evacuate the cuttings and stabilize the hole. The influence of this circulation on the borehole temperature was first discussed by *Bullard* [1947]. Typically, the temperature of the mud flowing down the drill-pipe is close to sea surface temperature and lower than the formation temperature at depth. Therefore the deepest part of the well gets cooled, while the mud ascending outside the pipe carries some of the heat from the deep formation and increases the temperature in the upper section of the well. The time elapsed between the end of the mud circulations and the BHT measurement is usually not long enough for the borehole temperature to return to the formation temperature [*Bullard*, 1947]. It is however possible to estimate the influence of mud circulation on the borehole temperature and to determine the actual formation temperature from these data.

*Brigaud* [1989] reviewed various methods to estimate the equilibrium temperature from BHT's. The most commonly used, often referred as the ‘Horner Plot’, was originally theorized by *Bullard* [1947], and later developed by *Horner* [1951] and *Lachenbruch and Brewer* [1959]. It assumes that the effect of drilling and mud circulation is equivalent to the effect of a linear heat source in the formation, whose strength ( $S$ ) is independent of depth and time. It also assumes that the formation is homogeneous and infinite. With these hypotheses, the formation temperature ( $T_{eq}$ ) can be expressed as a function of the measured temperature ( $T_{BHT}$ ), of the time elapsed since the end of the circulation ( $t$ ), and of the duration of the circulation ( $t_c$ ):

$$T_{\text{BHT}} = T_{\text{eq}} + S \ln\left(1 + \frac{t_c}{t}\right) = T_{\text{eq}} + \frac{Q}{4\pi K} \ln\left(1 + \frac{t_c}{t}\right) \quad (1)$$

where  $Q$  is the heat influx per unit time and unit length of borehole wall during drilling and circulation and  $K$  the thermal diffusivity of the formation. In this form, Eq. (1) is difficult to use because the strength of the source ( $S = Q/4\pi K$ ) depends on poorly constrained parameters, including pumping rate, mud temperature and thermal properties of the mud and formation. Two temperatures recorded in a well at the same depth but at different times with no thermal disturbances in between can help overcome this difficulty, by providing two equations for the two unknowns  $S$  and  $T$ . By reworking (1) for two BHT's  $T_1$  and  $T_2$  measured at times  $t_1$  and  $t_2$ , the formation temperature at thermal equilibrium can be estimated by:

$$T_{\text{eq}} = \frac{T_1 \ln(1 + t_d/t_2) - T_2 \ln(1 + t_d/t_1)}{\ln(1 + t_d/t_2) - \ln(1 + t_d/t_1)}. \quad (2)$$

Even if the assumptions made are extreme simplifications of the influence of the drilling process, *Lachenbruch and Brewer* [1959] show that the maximum relative error is less than  $t_c/[6(t_c + t)]$ , which for typical values of  $t_c = 2$  hours and  $t = 6$  hours is about 4%.

This method was used to correct about 25% of the measurements. For the other data where only one measurement was available at each depth, the impossibility to determine  $S$  in (1) required an other approach. We used a method described by *Gable* [1977, 1986], who shows that within a confined area, the single-measurement BHT's can be corrected by a polynomial function of depth  $T_{\text{corr}}(z)$  defined from the actual Horner corrections made in this area:

$$T_{\text{eq}} = T_{\text{BHT}} + T_{\text{corr}}(z). \quad (3)$$

To determine  $T_{\text{corr}}(z)$  for the study area, we calculated a 2<sup>nd</sup> order polynomial fit for the data already corrected by the Horner Plot method ( $\tau(z) = 26.94 + 0.0249z - 1.748 \times 10^{-07} z^2$ ), and for the entire set of uncorrected BHT's ( $\tau_{\text{BHT}}(z) = 29.49 + 0.0171z - 3.714 \times 10^{-08} z^2$ ). The correction law  $T_{\text{corr}}(z)$  is the difference between these two functions:

$$T_{\text{corr}}(z) = \tau(z) - \tau_{\text{BHT}}(z) = -3.45 + 0.0078z - 1.377 \times 10^{-07} z^2. \quad (4)$$

The negative constant coefficient (-3.45) illustrates the warming of the upper section of the hole because of the mud circulation.

This method does not take into account differences between separate wells in the duration of the mud circulation, or in the time elapsed between the end of the circulation and the measurement. It implicitly assumes that the drilling conditions, the timing of operations and the drilling mud were comparable for all the wells in the area, and that the thermal diffusivity of the formations surrounding the different wells were also similar. These assumptions are difficult to verify but reasonable since all the wells in this small area encountered the same type of lithology and were drilled with the same techniques.

Figure 4.4 shows the entire set of BHT's before and after correction and the two polynomial fits  $\tau(z)$  and  $\tau_{\text{BHT}}(z)$ . Two temperature logs measured in separate wells (A-20 and C-19) in this area are also shown for comparison and illustrate the evolution of the temperature in a borehole. Both logs were recorded a short time after the end of circulations. The log in C-19 was recorded after a shorter time than in A-20, and displays lower temperatures at depth, but both logs are close to the polynomial fit for the uncorrected BHT's and within the range of these data.

In the interval with the highest density of data (1750m-3000m, see Figure 4.4), BHT's were available at several depths in most wells. We calculated the temperature at specific depths in these wells (i.e. 1750, 2000, 2500 and 2750 m) by linear interpolation or extrapolation between the two most closely located corrected measurements. The calculated temperature distribution is shown in Figure 4.5. Using a regular mesh of  $50 \times 50$  elements for consistency with the following modeling, these surfaces were produced by a gaussian kernel smoothing of bandwidth 5.

#### **4.4.2 Heat transfer in sedimentary basins**

In order to interpret the temperature distribution in Figure 4.5, we will summarize the constituents of the thermal regime in sedimentary basins, before considering the specific

features of EI330. The thermal regime in sedimentary formations can be described by a general expression of the conservation of energy in porous media :

$$\int_V \frac{\partial(\rho CT)}{\partial t} dV = \int_S \lambda \vec{\nabla} T d\vec{S} - \int_S \rho_f C_f T \vec{\nabla}_d d\vec{S} + \int_V H dV \quad (5)$$

where  $V$  and  $S$  are respectively the volume and the external surface of an arbitrary unit of sediments and  $d\vec{S}$  is the outbond normal to  $S$ . The left side is the variation of internal energy, a function of the bulk density ( $\rho$ ) and specific heat ( $C$ ) of the materials and of the temperature ( $T$ ). The first term on the right represents the heat transfer by conduction defined by Fourier's law and proportional to the thermal conductivity  $\lambda$  of the material and to the temperature gradient ( $\vec{\nabla}T$ ) across its surface  $S$ . This term is usually the dominant heat transfer component in sedimentary basins [Rybach, 1981] and can generate strong anomalies in the presence of geological bodies of high thermal conductivity, such as salt diapirs [Mello *et al.*, 1994] or ore deposits [Castoviejo *et al.*, 1997]. The second term represents the heat carried by fluids of specific heat  $C_f$  and density  $\rho_f$  flowing with Darcy velocity  $\vec{\nabla}_d$ . We assume here that the pore space is fluid-saturated, and that the volumetric flow rate can be expressed by Darcy's law for single phase fluid flows  $\vec{\nabla}_d = -k/\mu[\vec{\nabla}P - \rho_f \vec{g}]$ , where  $\vec{\nabla}P$  is the pressure gradient,  $k$  the permeability of the sediments,  $\mu$  the dynamic viscosity of the fluid and  $\vec{g}$  the acceleration of gravity. The last term in Eq. (5) is the heat generated by eventual sources of volumetric strength  $H$ .

For the numerical formulation, assuming that the temperature distribution is continuous and varies smoothly on the scale of the grid blocks, it is more convenient to rewrite (5) as a local partial differential equation:

$$\frac{\partial(\rho CT)}{\partial t} = \vec{\nabla}(\lambda \vec{\nabla} T) - \vec{\nabla}(\rho_f C_f T \vec{\nabla}_d) + H \quad (6)$$

### 4.4.3 Heat sources

In most sedimentary formations, possible heat sources are the radiogenic heat produced by the decay of radioactive isotopes of Potassium, Thorium and Uranium, and the heat produced by chemical reactions such as diagenesis or hydrocarbon generation.

#### 4.4.3.1 Radiogenic heat

Values collected by *Rybach* [1981] show that in clastic sediments the volumetric heat production due to radioactive decay is about  $1.0 \mu\text{W}/\text{m}^3$ . If the specific heat and the bulk density of sediments are respectively  $2000 \text{ Jkg}^{-1}\text{K}^{-1}$  and  $2500 \text{ kg}/\text{m}^3$ , the time required to increase the temperature of a unit mass of sediments by  $1^\circ\text{C}$  would be 150,000 years, which is much longer than the periods of activity in the Red Fault, lasting a few thousand years [*Roberts et al.*, 1996, *Anderson et al.*, 1994]. Moreover the globally uniform lithology of EI330 makes radiogenic heat a practically uniform process over the entire area, that cannot be associated with significant localized anomalies such as seen in Figure 4.5. Because of its numerical simplicity, this term is however included in the following simulations to remain as close as possible to the actual thermal regime.

#### 4.4.3.2 Heat generation from oil maturation

Most thermal regime studies do not consider the generation of hydrocarbons as a possible source of heat [*Rybach*, 1981, *Bachu et al.*, 1995]. Studies using BHTs to constrain temperature distributions are usually devoted to larger areas and longer histories, and use more sparsely distributed data sets [*Bodner and Sharp*, 1988, *Bachu et al.*, 1995, *Armstrong et al.*, 1996]. This limit their scope to the large scale dominant components: conduction and advection, as well as radiogenic heat for large time scales. By contrast, our goal was a comprehensive understanding of the temperature distribution in a relatively smaller area using a higher density temperature data set so that we could study short-lived time-dependent processes. Therefore, before discarding any possible

component to simplify the formulation, we have to estimate the strength of most possible components, including the heat generated by the transformation of kerogen, which is mostly exothermic. While a complete account of the thermochemistry within the source rocks is beyond the scope of this study, we can estimate an order of magnitude of the heat released in the source rocks. Since the reactions are multiple and complex, we use two different estimations of this process: an average value over time, and its intensity at its peak productivity.

*England et al.* [1987] estimates that a typical source rock will yield about 20g of hydrocarbon per kg of sediments or  $48 \text{ kg/m}^3$  for an average sediment density of  $2400 \text{ kg/m}^3$ . This release occurs mostly between 120 and  $150^\circ\text{C}$  [*England et al.*, 1987], which in reasonable heating conditions (1 to  $10^\circ\text{C}/\text{Ma}$ ) corresponds to an average generation rate of  $5.0 \cdot 10^{-11}$  to  $5.0 \cdot 10^{-10} \text{ g/m}^3/\text{s}$ . Assuming an average molecular weight of  $150 \text{ g/mol}$  ( $\sim \text{C}_{15}\text{H}_{32}$ , which is the median component of the chromatogram measured by *Wheelan et al.* [1994]), and an enthalpy of reaction of  $200 \text{ kJ/mol}$  (based on *Mallard and Linstrom*, [1998]) the heat generation rate is  $6.7 \cdot 10^{-2}$  to  $6.7 \cdot 10^{-1} \mu\text{W/m}^3$ , lower than the radiogenic heat that we already discarded.

But this value represents an average over several million years, underestimating the heat generated at the peak of hydrocarbon productivity [*Tissot et al.*, 1987]. From the description of oil generation by *Burnham* [1995], it is possible to use chemical kinetics to estimate the heat generated at the peak of kerogen transformation. Oil generation from kerogen obeys an Arrhenius-type of law:

$$\frac{dC}{dt} = -AC \exp(-E/RT) \quad (7)$$

where  $C$  is the oil concentration in the source rock,  $T$  the temperature (in K),  $R$  the perfect gas constant,  $A$  is the frequency factor in  $\text{s}^{-1}$ , and  $E$  the activation energy of the reaction, in  $\text{J/mol}$ . *Burnham* [1995] gives values of  $3.0 \cdot 10^{13} \text{ s}^{-1}$  for  $A$  and  $200 \text{ kJ/mol}$  for the activation energy for type II oils (marine sediments). For the same concentration of

organic matter as used previously (20g/kg of rock, or 320 mol/m<sup>3</sup> using the same values for the density and molecular weights as before), and at temperatures of maximum generation (T = 130°C, from *Tissot et al.*, [1987]), the rate of kerogen transformation is  $dC/dt = 7.010^{-11}$  mol/s. With the same enthalpy of reaction used earlier (200 kJ/mol) the heat generation rate is of the order of 14μW/m<sup>3</sup> at its peak.

Both estimates are of the order of the radiogenic heat (1 μW/m<sup>3</sup>), already discussed and discarded. Moreover, the most productive source rocks are located in strata at 120 to 150°C, which are the deepest layers of our model. We will therefore ignore the influence of oil generation on the shallower anomalies of Figure 4.5.

#### 4.4.4 The effect of sedimentation

In the following interpretation and modeling, we will assume that the conductive regime is permanent. This simplification neglects the effect of sedimentation and salt movement on the temperature distribution. While the salt movement beneath EI330 stopped about 1.5 Ma ago, sedimentation is an active process occurring at an approximate rate of 1.0 mm/year, or 1km/Ma [*Alexander and Flemings*, 1995]. We have to estimate the magnitude of its influence on the thermal regime before any further simplification. A crude comparison of the sedimentation and heat diffusion time scales can be derived from Eq. (6). The time Δt required for heat to diffuse through a thickness D of newly deposited sediments can be estimated by the following approximation:

$$\frac{\rho C \Delta T}{\Delta t} \approx \lambda \frac{\Delta T}{D^2} \quad \text{or} \quad \Delta t \approx D^2 \frac{\rho C}{\lambda} = \frac{D^2}{\kappa} \quad (8)$$

where  $\kappa (= \lambda/\rho C)$  is called the thermal diffusivity of the sediments. For 1 km of newly deposited sediments of typical diffusivity 10<sup>-6</sup>-10<sup>-7</sup> m<sup>2</sup>/s, the time required for heat diffusion through the layer is 10<sup>12</sup> - 10<sup>13</sup> s or 0.03 - 0.3 Ma, which is comparable with the deposition time (1 Ma at 1mm/year). Because sediments are deposited continuously over time, this estimation exaggerates the slowness of heat diffusion, whose reach increases only with the square root of time ( $D \propto (\Delta t)^{1/2}$ ). While one meter of sediments gets

deposited in 1,000 years, Eq. (8) shows that it takes less than a year for heat to diffuse across this distance. These values mostly underline how each process has to be weighted in terms of time scale and distance for a correct interpretation.

To estimate more accurately the effect of sedimentation on the conductive regime we can solve the 1D equation of heat conduction in a homogeneous medium moving with a velocity  $U$  equal to the sedimentation rate [Jaeger, 1965]:

$$\frac{\partial T}{\partial t} = \kappa \frac{\partial^2 T}{\partial z^2} - U \frac{\partial T}{\partial z}. \quad (9)$$

*Carslaw and Jaeger* [1959] and *Jaeger* [1965] use Laplace transform to solve (9). In an infinite medium with a constant sedimentation rate, a linear temperature profile at the origin and a constant temperature at the surface, the solution is:

$$T(z, t) = T_0 + g_0(z - Ut) + \frac{g_0}{2} \left[ (z + Ut) e^{Uz/\kappa} \operatorname{erfc}\left(\frac{z + Ut}{2\sqrt{\kappa t}}\right) + (Ut - z) \operatorname{erfc}\left(\frac{z - Ut}{2\sqrt{\kappa t}}\right) \right] \quad (10)$$

where  $\operatorname{erfc}$  is the complementary error function:  $\operatorname{erfc}(x) = 1 - (2/\sqrt{\pi}) \int_0^x e^{-u^2} du$ ,  $g_0$  is the initial temperature gradient and  $T_0$  the temperature at the surface. Figure 4.6a shows the evolution of the temperature profile vs. depth (dotted lines) through time over 6 Million years, equivalent to the deposition of our data cube, and Figure 4.6b shows the evolution of the temperature at the same depths as the surfaces of Figure 4.5. Both figures indicate a steady decrease of temperature with time, at a rate of about 2.0 °C/Ma at the end, corresponding to the present day. This analytical solution overestimates the cooling effect of sedimentation because the infinite medium hypothesis does not allow the heat support provided by the regional basement heat flow. As a result, at any depth, (10) converges to the surface temperature  $T_0$ , which is much more dramatic than the actual effect of sedimentation. However, Figure 4.6b shows that even in such extreme model, the temperature change over the last 100,000 years is less than 0.2°C. Without an exact analytical solution, a likely more reasonable estimate of the 1-D effect of sedimentation can be calculated by numerical method. A Forward-time Centered-Space discretization of (9) is:

$$\frac{T_i^{n+1} - T_i^n}{\Delta t} = \kappa \frac{T_{i+1}^n + T_{i-1}^n - 2T_i^n}{\Delta z^2} - U \frac{T_{i+1}^n - T_{i-1}^n}{2\Delta z} \quad (11)$$

where  $T_i^n$  indicates the temperature at time step  $n$  at the node  $i$  of the discretized vertical column.  $\Delta t$  and  $\Delta z$  are the constant time step and uniform node spacing, respectively. An implicit Crank-Nicholson formulation of (11) expresses the temperature increment between successive time steps as the average of the increments at the two time steps. If (11) can be written by  $T_i^{n+1} = T_i^n + f(T_i^n)$ , this algorithm can be expressed as  $T_i^{n+1} = 1/2.[f(T_i^n)+f(T_i^{n+1})]$ . If we note  $\alpha = U\Delta t/2\Delta z$  and  $\beta = \kappa\Delta t/\Delta z^2$ , the matrix form of this formulation is:

$$\begin{bmatrix} -0.5(\alpha + \beta) & (1 + \beta) & 0.5(\alpha - \beta) \end{bmatrix} \begin{bmatrix} T_{i-1}^{n+1} \\ T_i^{n+1} \\ T_{i+1}^{n+1} \end{bmatrix} = \begin{bmatrix} 0.5(\alpha + \beta) & (1 - \beta) & 0.5(\beta - \alpha) \end{bmatrix} \begin{bmatrix} T_{i-1}^n \\ T_i^n \\ T_{i+1}^n \end{bmatrix} \quad (12)$$

which comes to invert a tri-diagonal system of equations while imposing the following boundary conditions: constant seafloor temperature at the top and constant temperature gradient at the base of the sediment column. The results are also shown in Figure 4.6a and 4.6b (continuous lines) for a 6 km-thick sedimentary sequence deposited at 1mm/year with a 30°C/km linear temperature profile at the origin. They show in particular that the temperature is almost in steady state after about 1.5 Ma, and practically constant at the present time. The equation of the steady state profile can be derived by solving (9) without the time dependent component:

$$k\partial^2 T/\partial z^2 = U\partial T/\partial z \quad (13)$$

The solution of this linear differential equation is:

$$T(z, t) = T_o + \frac{\kappa}{U} \frac{g_b}{e^{UD/\kappa}} (e^{Uz/\kappa} - 1) \quad (14)$$

where  $D$  is the thickness of the sedimentary sequence and  $g_b$  the temperature gradient at this depth, assuming a constant purely conductive heat flux. This solution, shown in green in Figure 4.6a with a 1 mm/year sedimentation rate and 30 °C/km gradient at depth, is barely distinguishable from the Crank-Nicholson solution after 1.5 Ma.

These 1-D estimations of the influence of sedimentation can not be representative of the actual processes in EI 330 where sedimentation rates have varied in space and time and where sediment properties are not uniform, but they show that for periods of time of the order of 10,000 to 100,000 years the present conductive regime can be considered stationary.

#### **4.4.5 Analysis of the present-day temperature distribution**

The most distinct features present at all depths in Figure 4.5 are the lower temperatures on the downthrown block in the South-West (Block 337), and the high temperature zone extending from the South-East corner (Block 339) to the North-West (Blocks 331, 314), across Block 330.

In Figure 4.6a we also display the result of Eq. (14) at two different sedimentation rates, 1mm/year (green) and 2 mm/year (red) showing that faster sedimentation rates can decrease considerably temperature at depth. Therefore, the faster sedimentation rate in the down-thrown block [*Alexander and Flemings, 1995*] can contribute to the lower temperature observed in the SW in Figure 4.5. An other reason for these lower temperatures is the difference between the relative thickness of the sand-rich and shale-rich formations across the fault (see Figure 4.3). The proximal deltaic and fluvial sections are sand-rich and have a higher thermal conductivity than the underlying shale. Assuming a uniform vertical heat flow from the basement, the thick sands maintain a lower temperature gradient over a greater depth in the downthrown block (~4000 mbsf) than in the upthrown section where shale becomes dominant below only 2000 m.

The higher temperatures along the SE-NW trend can be visually correlated in Figures 4.2 and 4.3 with the salt diapir system and with the general pattern of the Red Fault system. The high thermal conductivity of the salt compared to the surrounding sediments ( $4-6 \text{ Wm}^{-1}\text{K}^{-1}$  vs.  $1-3 \text{ Wm}^{-1}\text{K}^{-1}$ , [*Mello et al., 1994*]) and the high amplitude of salt topography, described by *Anderson et al. [1994]* as the most rugged topography on earth

(see Figure 4.2), can generate significant temperature anomalies [Mello *et al.*, 1994]. So could warm fluid ascending along the fault [Roberts *et al.*, 1996]. The respective contributions of these two regimes have to be differentiated.

Coelho *et al.* [1996] show that the presence of oil and gas decreases the thermal conductivity of reservoir sediments and generates a thermal blanketing that increases temperature underneath the reservoirs. They argue that this influence of hydrocarbons could create a positive temperature anomaly as high as 15°C below the main reservoirs and could explain by itself the observed anomalies. However, using their equations, we find that such blanketing would require about 60% of gas distributed uniformly in the pore space with an average porosity of 40 % between 1,000 and 2,000 mbsf. This is hardly representative of the stack of mostly oil-saturated low-porosity reservoirs constituting the Block 330 field, and could not explain the shallower anomalies. This blanketing must contribute to some of the observed anomalies, particularly in the deeper layers, but we choose to take it into account in the following models only by attributing lower conductivity to the sands of the downthrown block.

#### 4.4.6 One dimensional analysis of heat advection

The dominant terms in Eq. (5) are the conductive and the advective components, whose relative strength define the nature of the thermal system [Rybach, 1981]. The differentiation between the strength of these two terms can be performed on a first order by calculating the Peclet number of the system, a dimensionless number that can be calculated from (6) by

$$Pe = \rho_f C_f VD / \lambda \quad (15)$$

where D is a characteristic length for fluid migrations. For large values of Pe ( $Pe \gg 1$ ) heat advection dominates, for low values ( $Pe \ll 1$ ), conduction is preponderant, and for intermediate values the two modes have comparable influences. To determine the strength of migrations in the Red fault that could produce anomalies comparable to the

influence of the salt, we can calculate the velocity required for the Peclet number to be equal to 1. A value for  $D$  can be found in *Holland et al.* [1991] who observe that migration must have occurred over more than 3650 m vertically in the recent history of the EI330 field. For this comparison, the strength of the advective regime has to be compared to the strongest conductive regime in the area, within the salt. Reasonable values for the salt conductivity and for the density and specific heat of the fluids are, respectively  $\lambda = 6 \text{ Wm}^{-1}\text{K}^{-1}$ ,  $\rho_f = 1000 \text{ kg/m}^3$  and  $C_f = 4.185 \cdot 10^3 \text{ JK}^{-1}\text{kg}^{-3}$ . Therefore, the velocity of the fluid migration necessary for heat advection to compete with the heat drainage through the salt is  $V = \lambda / \rho_f C_f D \approx 4 \cdot 10^{-10} \text{ m/s}$ , or  $\approx 1.2 \text{ cm/year}$ . Even though this is a crude one-dimensional comparison of complex processes, this value is not exceptional in an area of significant geopressures and high pressure gradients, and is considerably smaller than the maximum velocities (up to 100 m/yr) considered by *Roberts et al.* [1996], who modeled the expulsion mechanisms in the same area. It shows that the influence of the salt and of ascending fluids have to be both considered in the interpretation of Figure 4.5.

## 4.5 Numerical modeling of the conductive regime

### 4.5.1 Model description

Assuming that sedimentation is uniform and at a constant rate, it is possible to model the combined effects of sedimentation and heat conduction in permanent regime. Using control volumes fixed with regard to the seafloor (the top of the sediments), sedimentation can be considered as a particular form of heat advection. In permanent regime, this can be written:

$$\int_S \lambda \vec{\nabla} T d\vec{S} - \int_S \rho C T \vec{U} d\vec{S} = 0 \quad (16)$$

where  $\bar{U}$  represents the sedimentation, assumed vertical and downward, and  $\rho$  and  $C$  are the density and specific heat of the sediments. For simplification, we consider here that all sediments have the same heat capacity ( $\rho C$ ). We use a finite difference formulation to rewrite this equation in finite difference within a regular rectangular grid. For an element  $n$  of dimensions  $\Delta x, \Delta y, \Delta z$ , it can be rewritten

$$\sum_{\substack{m=B,T,E, \\ W,N,S}} k_m S_m \frac{(T_m - T_n)}{d_m} + \rho C U \Delta x \Delta y \left[ \frac{(T_T + T_n)}{2} - \frac{(T_B + T_n)}{2} \right] = 0 \quad (17)$$

where the subscripts refer to the six elements connected: (T)op, (B)ottom, (W)est, (E)ast, (N)orth, (S)outh, and  $d_m$  and  $S_m$  are respectively the grid dimension along and the surface orthogonal to the  $m$  direction. The thermal conductivity between two adjacent elements is the harmonic “in series” average of the thermal conductivity of  $n$  and  $m$  :

$$k_m = \frac{2\lambda_n \lambda_m}{\lambda_n + \lambda_m} \quad (18)$$

The centered space over-relaxation method [Press, 1994] used to solve (17) is an iterative algorithm where an initial value for the temperature is attributed to all the nodes at the initial step ( $T^0$ ), and the temperature  $T^{i+1}$  at step  $(i+1)$  for any node is calculated from the values of the previous step  $(i)$  at the adjacent nodes, until reaching a convergence threshold. In our rectangular uniform grid, where the node dimensions are  $h \times h \times v$  the recurrent formula is :

$$T_n^{i+1} = (1 - \alpha) T_n^i + \beta [h^2(T_T^i k_T + T_B^i k_B + \gamma(T_T^i - T_B^i)) + v^2(T_N^i k_N + T_S^i k_S + T_W^i k_W + T_E^i k_E)] \quad (19)$$

with 
$$\beta = \frac{\alpha}{h^2(k_T + k_B) + v^2(k_N + k_S + k_E + k_W)} \quad \text{and} \quad \gamma = \frac{U v \rho C}{2}$$

where  $\alpha$  is the over-relaxation coefficient, between 1.0 and 2.0 for unconditional convergence [Press, 1994].

If the heat capacity of the sediments is uniform, the construction of this model requires only to specify the thermal conductivity. We use four different types of

formation with specific attributes in our model, corresponding to the main facies associated with the development of the minibasin: the salt (1) is overlain by massive shales (2), underlying interbedded sands and shales (3), and the uppermost section is composed of massive sands (4). The salt topography and the transgressive surfaces *Cris S* and *Sm. Gep* (see Figure 4.3) used to delineate these units were directly imported and gridded from the 3D seismic interpretation. Reproducing each individual sand between these two surfaces would require a much finer grid and would not change significantly the results because of the limited difference in conductivity between sands and shales compared to the salt. Therefore, only a few representative sand units were used in the interbedded sand/shales sequence. This simplified lithology and structure are shown in Figure 4.7. Thermal conductivity values are given in Table 1.

The boundary conditions are chosen to be representative of a passive margin environment: 1) uniform temperature at the seafloor (18°C), 2) null heat flux across the lateral boundaries (null horizontal gradients) and 3) a uniform vertical heat flow at the bottom boundary (60 mW/m<sup>2</sup>, from *Anderson et al* [1991]). The over-relaxation algorithm was implemented on a regular 50 × 50 × 50 elements mesh, of dimensions 300m × 300m × 120m. The initial temperature distribution ( $T^0$ ) is defined by the seafloor temperature (18°C) and an uniform linear temperature gradient of 30°C/km. The convergence was considered attained when the actual heat influx in any element (the left side of Eq.(17)) was less than 100 W, or about 10 μW/m<sup>3</sup>.

#### 4.5.2 Results

The results in Figure 4.8 indicate a ~10°C temperature anomaly following the SE-NW pattern of the salt (see Figure 4.2). The influence of salt domes in Block 314, 330-329 and 339 can be identified and correlated with similar features in Figure 4.5. Since we do not include in this simulation the effects of the differences in sedimentation rates between the two sides of the fault, nor the effect of the presence of oil and gas in the

sediments of the hanging wall, we could not reproduce the generally lower temperatures on the downthrown side of the fault. Therefore, the features apparent in Figure 4.8 are mostly associated with the salt. The difference between these results and the observed temperatures (Figure 4.5) is shown in Figure 4.9 where a substantial  $\sim 10^{\circ}\text{C}$  residual anomaly remains at all depths in the center of the study area. The superimposition of the fault pattern on this figure (white lines) shows that this residual anomaly follows roughly the SE-NW arc of the "Red" fault, from Block 339 to Blocks 331-314, through Block 330. In the deepest section, the anomaly is mainly located in the southern oil field (Blocks 338-339), while in the shallower surfaces, it is distributed along the arc of the fault zone and centered on the block 330 and 331 oil fields. The general coincidence of these residual anomalies with the regional fault pattern suggests that they could be produced by heat advection through fluid migrations along the active faults.

## **4.6 Numerical simulation of fluid migration**

### **4.6.1 Indications for fluid circulation within the Red Fault**

The temperature anomalies along the Red Fault are only one manifestation of the fluid migration in the recent history of the Eugene Island area. Hydrocarbon seepages at the seafloor and discrepancies between the respective maturity of the oil and of the reservoirs [Holland *et al.*, 1991], temporal changes in the composition of the oil produced over the 20-years history of the field [Wheelan *et al.*, 1994] and the slow depletion rate of the production during this period [Anderson *et al.*, 1993] were among the factors that indicated the ongoing migration and initiated the Global Basins Research Network interest in EI330. Region growing techniques applied to 3-D seismic amplitudes were used to identify the migration paths characterized by High Amplitude Events [Anderson *et al.*, 1994] left by trapped migrating hydrocarbons. These results were used to determine the trajectory of the Pathfinder and A-10 wells within the fault zone, in which successive

Thermal Decay Time (TDT) logs detected migration of fluids that were occurring at the time of the measurements [*Losh et al.*, 1999, *Anderson et al.*, 1994].

Fluid migrations in EI330 are directly related to the presence of anomalously high pressures that are common to many areas of the Gulf Coast. While various mechanisms can generate geopressures, *Hart et al.* [1995], and *Mello et al.* [1994] show that compaction disequilibrium is the principal factor for their development in Eugene Island. Pore pressure increases anomalously when the deposition of low-permeability clay-rich sediments is too fast for the pore fluid to be expelled while the sediments get buried [*Hart et al.*, 1995, *Bredehoeft and Hanshaw*, 1968]. The location and the depth of the geopressures in the Eugene Island area have been discussed by *He* [1996], *Hart et al.*, [1995], and *Mello et al.* [1994]. *Roberts et al.* [1996] have shown that the periodic release of overpressured fluids could be at the origin of significant temperature anomalies.

#### **4.6.2 3D Numerical simulation of the pressure and temperature**

If the residual anomalies in Figure 4.9 are produced by fluid migration along the fault, the numerical simulation of these anomalies can give an estimate of the duration, fluid volumes and velocities necessary to create them. *Roberts et al.* [1996] used a two dimensional finite element model to reproduce the observed temperatures. Their results give an indication of the duration and of the strength of the migration, but they are only based on a representative two dimensional cross section of the area. This does not account for the actual three-dimensional nature of the system shown by the distribution of anomalies in Figure 4.9. This figure suggests that the deepest part of the fault is most active in its southern extension (Blocks 338 and 339), and that while migrating upwards, the fluids simultaneously propagate to the North-West in the fault, and spill into the downthrown block, filling the reservoirs in Blocks 330, 331 and 314. That is, if the anomalies are actually generated by fluid migration, this figure shows that the migration is not only ascendant, but also lateral, and intrinsically three dimensional. Therefore, a

realistic simulation has to consider all the spatial dimensions of this system, as well as the 4<sup>th</sup> dimension, time.

#### 4.6.2.1 Numerical formulation

To simulate time-dependent heat advection requires consideration of pressures in the data cube, in addition to temperature. The additional equation necessary is given by the law for the conservation of pore fluid mass in saturated porous media:

$$\int_V \frac{\partial}{\partial t} (\rho_f \phi) dV = - \int_S \rho_f \vec{V}_d \cdot \vec{dS} + \int_V G dV \quad (20)$$

with notations similar to (5). The term on the left represents the change of pore fluid mass over time, the first term on the right is the fluid transport through the control surface  $S$ , and the last term is an eventual fluid source of volumetric strength  $G$ . Once more, the local partial differential equation is the formulation actually used in the numerical discretization:

$$\frac{\partial(\rho_f \phi)}{\partial t} = - \vec{\nabla} \cdot (\rho_f \vec{V}_d) + G \quad (21)$$

We use an Integrated Finite Differences Method (IFDM) for this discretization [Narasimhan and Witherspoon, 1976]. Our model was adapted from the code ‘‘PT’’ originally developed and described by Bodvarsson [1982]. Equations (5) and (21) are formulated as follows for a node  $n$  connected to an arbitrary number of nodes  $m$  :

$$(\rho CV)_n \frac{\Delta T_n}{\Delta t} = \sum_m \left\{ \left[ \frac{(\lambda S)_{n,m}}{D_{n,m} + D_{m,n}} (T_m - T_n) \right] + (\rho_f C_f V_d S T)_{n,m} + (HV)_n \right\} \quad (22)$$

$$(\rho_f \Phi V \beta)_n \frac{\Delta P_n}{\Delta t} = \sum_m (\rho V_d S)_{n,m} + (GV)_n \quad (23)$$

$$V_{d_{n,m}} = \left( \frac{k}{\mu} \right)_{n,m} \left[ \frac{P_m - P_n}{D_{n,m} + D_{m,n}} - \eta_{n,m} \rho_{n,m} g \right] \quad (24)$$

where  $\beta$  is the fluid compressibility ( $\beta = -1/V \cdot \partial V / \partial P$ ),  $V_{d_{n,m}}$  is Darcy’s velocity at the interface between nodes  $n$  and  $m$ ,  $T_{n,m}$  is the temperature at this interface,  $\eta_{n,m}$  the direction cosine of its outward normal (for a vertical surface,  $\eta_{n,m} = 0$ ), and  $D_{n,m}$  and  $D_{m,n}$

are respectively the distances from the nodal points in  $n$  and  $m$  to their shared surface of area  $S_{n,m}$ .

#### 4.6.2.2 Properties at the interface

$\rho_{n,m}$  and  $\mu_{n,m}$  are respectively the fluid density and viscosity at the interface. Both are calculated as a weighted average of the values for each nodes. At each time step, fluid viscosity, density and compressibility are calculated for each node as a function of temperature and pressure after *Batzle and Wang* [1992].

$T_{n,m}$  is calculated by an upstream weighting formulation :

$$T_{n,m} = vT_u + (1-v)T_d \quad (25)$$

where  $u$  and  $d$  designate the upstream and downstream nodes and  $v$  is the upstream weighting coefficient, restricted in values to the range 0.5 to 1 for unconditional stability. We use  $v = 0.7$ .

The permeability and the thermal conductivity between nodes are calculated with an harmonic mean, to insure continuity of fluxes at the interface:

$$k_{m,n} = k_m k_n \frac{D_{n,m} + D_{m,n}}{k_m D_{n,m} + k_n D_{m,n}} \quad \text{and} \quad \lambda_{m,n} = \lambda_m \lambda_n \frac{D_{n,m} + D_{m,n}}{\lambda_m D_{n,m} + \lambda_n D_{m,n}} \quad (26)$$

#### 4.6.2.3 Sources

In Equations (22) and (23),  $H_n$  and  $G_n$  are respectively the volumetric heat and mass generation rates of eventual sources in element  $n$ .

$H_n$  was discussed and discarded earlier.

The possible volumetric mass generation rate  $G_n$  could include the generation of hydrocarbon, clay dehydration, and fluid expulsion by compaction. *England et al.* [1987] estimate that in a typical oil producing environment, the velocity of fluids expelled by a source rock containing an average potential of 0.02kg of oil per kg of rock is of the order of  $10^{-14}$  m/s or  $3.2 \cdot 10^{-7}$  m/year. This value is several orders of magnitude

lower than the velocities estimated by *Roberts et al.* [1996] in EI330, and proves to be also much smaller than velocities in our own models. Therefore we do not account for this potential source or for similarly slow fluid generation processes (clay dehydration) and we do not include any mass generation term in our simulations.

#### 4.6.2.4 Lithology description

The model grid was built from the same surfaces used in the conductive model: the top of the salt, and the *Cris S* and *Sm. Gep 2* transgressive surfaces [*Alexander and Flemings, 1995*]. For the same reason as in the conductive regime simulation, only four representative sand units were defined in the sand/shale sequence, and the representation of the lithology was similar to the conductive model in Figure 4.7 (see Figure 4.10). Because the calculation of time-dependent pressure and temperature over the entire datacube requires the resolution of large, sparse linear equation systems at every time step, the computational constraints are higher than for the conductive regime simulation. The largest model for the entire data cube had 20 (EW)  $\times$  20 (NS)  $\times$  25 (vertical) = 10,000 elements, ranging in size from 1000 $\times$ 1000 $\times$ 1000 m to 500 $\times$ 500 $\times$ 100 m. Thermal conductivity values were the same as in the conductive model, and the permeability ranges are given in Table 1. The grid is shown in Figure 4.10.

#### 4.6.2.5 Numerical controls

For stability purposes, the linear equations are solved implicitly. This means that at every time step, the values used for pressure and temperature in (22) and (23) are the values at the end of the time step. If  $T_n^{i-1}$  and  $P_n^{i-1}$  are the temperature and pressure at the beginning of step (i), the values used for  $T_n^i$  and  $P_n^i$  at step (i) in (22) and (23) are  $T_n^i = T_n^{i-1} + \Delta T_n$  and  $P_n^i = P_n^{i-1} + \Delta P_n$ . The actual unknown in the equations are  $\Delta T_n$  and  $\Delta P_n$ . A sparse matrix solver, MA28 from the Harwell Subroutines Library, is used to solve the linear equations resulting from this formulation.

While the implicit formulation is unconditionally stable, it is only first order accurate in time and requires time steps to be short enough to reproduce short-lived events. To limit this effect on our results, we limit the length of each time step so that the fluid displacement during one time step doesn't exceed the minimum dimension of any of the elements. From the previous 1-D analysis, velocities of the order of  $4 \times 10^{-10}$  m/s  $\sim$  1.2 cm/yr must exist to generate anomalies competing with the salt. *Roberts et al.* [1996] simulate velocities of more than 100 m/yr, but create anomalies much stronger and more focused than what we observe in Figure 4.9. This suggests that intermediate values on the order of 1 m/yr can be used as a reasonable order of magnitude. The smallest element dimension in our grid being 100 m this limits the simulation time steps to less than  $\Delta t_{\max} \sim 100$  years, which we used as the maximum time increment. Since the maximum velocity is actually not constant, it is calculated after each time step and the time increment is reduced if any "overshoot" was possible over any node. Tests made consequently by allowing longer time steps (up to 5,000 years) provided results similar to the results that we present.

Initial temperature conditions are the results of the conductive model run on the same grid. Initial pressures are defined as a linear profile from seafloor pressure ( $1.1 \times 10^6$  Pa) to a pressure at the bottom boundary equivalent to 90 % of the average lithostatic pressure, similar to the values measured in the Pathfinder well in the overpressured shales [*Anderson et al.*, 1994].

The boundary conditions are defined by (1) constant and uniform pressure and temperature at the seafloor, (2) constant pressure and steady, uniform vertical heat flow at the bottom, and (3) no heat or fluid flux at the lateral model boundaries, maintained by null horizontal temperature and pressure gradients. Values are given in Table 2.

The fluid present in the pore space and migrating is assumed to be brine. Salinity is calculated as a linear function of depth derived from the compilation of Gulf Coast data

of *Batzle and Wang* [1992]. The density, viscosity and compressibility of the fluid are calculated from salinity, pressure and temperature after *Batzle and Wang* [1992].

#### **4.6.2.6 Fault simulation**

The fault zone is defined in the model by importing the main fault surfaces interpreted from 3D seismic: the down to the south “Red Fault”, and the counter-regional down-to-the-north “Blue” and “F” faults [*Alexander and Handschy*, 1998, *Rowan et al.*, 1998]. The fault zone is represented by a subset of variable-permeability “fault nodes”, which are the elements of the grid that are crossed by the imported fault surfaces, and the elements directly adjacent in order to assure connectivity between diagonally connected nodes in the rectangular mesh (See Figure 4.10b). These nodes are given the same attributes (conductivity, density, specific heat, porosity, permeability) as the lithological unit (shale/sand) within which they are defined. The fault opening is simulated by increasing their permeability. *Roberts et al.* [1996] show that the fault must have increased permeability as deep as 2,000 meters below the top of overpressure to reproduce temperature anomalies of amplitudes equivalent to that observed in Eugene Island. Therefore the deepest nodes allowed to open in our models are located at about 5,000 mbsf.

*Wang and Xie* [1998] provide a complete discussion on the criteria that can be used to open the fault by compaction-induced hydrofracturing, and on the permeability increase due to the fault opening. The most commonly accepted condition for fault opening in sediments, which we use in our model, is when the pore pressure exceeds the lowest compressive strength of the sediments, roughly 85% of the lithostatic pressure [*Wang and Xie*, 1998, *Roberts et al.*, 1996, *Hart et al.*, 1995]. When the pore pressure reaches this value in a fault node, its bulk permeability is increased by a factor of  $10^2$  to  $10^3$  [*Wang and Xie*, 1998].

Without simulating the sedimentation and compaction disequilibrium that generate and maintain the overpressure, we could not reproduce the actual cycle of activity of the fault. However, by extending the results of *Wang and Xie* [1998] to the sedimentation rates of EI330, we can estimate that the shortest time between successive hydrofracturing events should be over 200,000 years, which leaves enough time for the 8 to 10°C anomalies to dissipate almost entirely between two events. Therefore we assume that the observed anomalies are the result of a single expulsion event and we monitor only the temperature produced by the event triggered by the overpressures defined in the initial conditions. The duration of the enhanced permeability within the fault is not imposed, but implicitly controlled by two parameters: 1) the value of the permeability increase in the fault nodes when the fault opens, which determines the time taken for the overpressured fluids to be expelled, and 2) the closing pressure, which is the pressure below which fault nodes are re-assigned their original permeability, simulating the end of the activity period. By introducing a ‘closing pressure’, lower than the opening pressure, we try to reproduce the observation of *Wang and Xie* [1998] that the permeability within the fault remains high even after the pore pressure has fallen below the opening pressure. They suggest that this could be due to microscopic roughness on the fracture surfaces that would keep some space open along the closed fracture, called ‘fault smear’. Our closing pressure can be understood as a minimum pore pressure required to support this remaining open space in the fractures. It is expressed as a fraction of the lithostatic pressure, arbitrarily set between 75 and 80%.

#### **4.6.3 Results**

In addition to the permeability in the fault zone and to the value of the closing pressure, another parameter essential to the evolution of the temperature field is the horizontal permeability in the sands, which controls the ease for the ascending fluids to spill into the reservoirs. Otherwise, fluids continue to the seafloor and appear as seeps,

which have been observed in abundance in the area [Roberts, 1998]. This variable is defined by the permeability anisotropy in the sands (the ratio of the horizontal to vertical permeability).

The results of different simulations for various values of these parameters are shown in Figures 4.11, 4.12, 4.13 and 4.14. In Figure 4.11 the closing pressure is 80% of the lithostatic pressure, the permeability enhancement in the fault is  $10^2$ , and the permeability anisotropy in the sands is  $10^2$ . In Figure 4.12, the parameters are the same except the permeability enhancement in the fault, which is set to  $10^3$  in the shales,  $10^2$  in the proximal deltaic sands and  $10^1$  in the fluvial sands. In Figure 4.13 parameters are the same as in Fig. 4.12, except for a  $10^3$  permeability anisotropy in the sands. Finally, the model in Fig. 4.14 is similar to Fig. 13 except for the closing pressure ratio at 75%. In all the figures, (a) shows the evolution through time of the entire temperature field and (b) shows the evolution of the anomaly created by the fluid migration after removal of the salt influence, and therefore should be compared to Figure 4.9.

In all cases, the migration was mostly confined within the fault at the beginning of the simulation for at least 1,000 years, generating the distinct anomalies in the first steps (left) in figures 4.12b, 4.13b and 4.14b. Maximum calculated velocities during this initial phase are up to  $1.0 \cdot 10^{-6}$  m/s, or 30m/year. In these first stages, the temperature anomalies are localized only in the fault nodes. As upgoing fluids reach the interbedded sand/shales, they start flowing into the sands and the reservoirs, broadening the temperature anomaly significantly in the cases with high horizontal permeability (Figs 4.13b and 4.14b). After the fault closes, migration is mostly sub-horizontal, filling the reservoirs, and diffusing rapidly the temperature anomaly which becomes a low-amplitude, broader feature after 10,000 years. The exception is in Figure 4.12b where the anomaly remains focused because the sand permeability is lower. Another observation common to the different simulations is that the amplitude of the anomalies is generally higher at shallower depths

(1750, 2000 mbsf), because the contrast in temperature between the ascending fluids and the formation temperature is higher in the shallower, colder, formation.

#### 4.6.4 Discussion

The significant differences between Figures 4.11b, 4.12b, 4.13b and 4.14b show that the three parameters varied between the models all have an influence on the duration, the amplitude and the distribution of the temperature anomalies.

Figure 4.11 shows the only case where the permeability enhancement at the opening of the fault is  $10^2$  in all the formations. In this case, most of the fault nodes remained open to flow during the 10,000 years of the simulation. The anomaly develops progressively to its maximum ( $6^\circ\text{C}$ ) at the end of the simulation, which is lower than after only 1,000 years of any of the other simulations and smaller than the anomalies observed (Figure 4.9). This shows that in this case, the migration is too slow to carry enough heat in the shallower formations to reproduce the anomalies observed in EI330.

By comparison, Figure 4.12 shows that anomalies of the same amplitude as what is observed in EI330 (i.e.  $\sim 10^\circ\text{C}$ ) can develop in about 1,000 years of activity in the fault if the permeability in the shales is increased by three orders of magnitude ( $10^3$ ) when the fault opens. However, due to the low horizontal permeability in the sands, the ascending fluids are not deviated in the reservoirs and keep migrating upwards to the shallower fluvial sands. After the fault has closed, which is complete after about 5,000 years, the absence of lateral migration maintains the anomalies strong and localized in the fault nodes, because the only dissipation of this heat occurs through diffusion. The amplitude of the anomalies in this figure suggests that the  $10^3$  permeability enhancement in the faulted shales could be representative of the processes in EI330, showing that the fault opening has to increase the permeability of the shales by at least three orders of magnitude to allow the overpressured fluids to be released. However the anomalies

observed in Figure 4.9 are broader and less focused than in any stage of Figure 4.12b, indicating that some of the heat gets carried into the formations adjacent to the fault.

In Figures 4.13 and 4.14, where fault permeability is the same as Fig. 4.12, but horizontal permeability in the sands is higher, the anomaly is also mostly limited to the fault nodes until about 2,000 years of simulation. When the fault closes after this time, the anomalies become wider than in Figure 4.12, and more similar to Figure 4.9. In these two cases, the fault closes earlier than in Figure 4.12 because the fluids flowing into the adjacent formation release some of the pressure in the fault nodes. The only difference between Figures 4.13 and 4.14 is in the deeper part of the model (2500 and 2750 m) where the anomaly is slightly higher in Fig. 4.13b (where the closing pressure ratio is 80%) than in Figure 4.14b (where it is 75%). The small difference between the opening and closing pressures in the first case allows the pressure to build up rapidly after the closing of the fault and to reach the opening pressure in a short time, maintaining some semi-continuous activity in the deeper part of the fault for almost 5,000 years before closing definitely. In the case of Figure 4.14, where the closing pressure is 75% of the overburden, the pressure is too far below the opening pressure when it closes after 1,000 years to rebuild to this value.

For a finer comparison with the observed data, Figures 4.15 and 4.16 show the simulated temperature distribution and advective anomaly in the case corresponding to the model in Fig. 4.13 after 5,000 years (These figures have the same format as Figures 5 and 9). Among the different simulations, this case reproduces most closely the field observations. Comparison between Figures 4.15 and 4.5 shows that the main features of the present-day temperature distribution are reproduced by our simulation, including the influence of the salt, the higher temperatures in Block 338 (South, center) in the deepest layers (2,500 and 2,750 mbsf), and in the West part of the field (Blocks 331, and 314) at shallower depths. These two separate domains of activity are emphasized in Figure 4.16 (to compare with Fig. 4.9) where the highest anomaly at depth is in the south of the field,

and the anomaly becomes stronger in the western part at 1750 and 2000 mbsf. These two domains correspond respectively to the “Blue” Fault, which seems to be more active at depth, and to the “Red” fault (see Figure 4.3a) which is the dominant migration path to the shallower reservoirs.

#### **4.6.5 Limitations of the results**

Even if the temperatures simulated in Figure 4.15 and 4.16 were reproducing more closely the data in Figure 4.5 and 4.9, it would be unreasonable to assume that these models indicate the exact origin of the observed anomalies. The necessary reservations about the accuracy of these results come mostly from (1) the limited quality of the temperature data and (2) the simplifications of the numerical modeling, and particularly (3) the coarseness of the model grid, especially around the fault.

Despite the care taken in processing the BHT's, the possible error in the data is on the order of the anomaly amplitudes that we try to explain (4% or about 5°C, *Lachenbruch and Brewer*, [1956]). The only assurance of the reality of the interpreted temperatures comes from the clarity of some unquestionable features such as the influence of the salt diapirs. Figure 4.9 shows that the anomalies that we attribute to heat advection are indeed located around the faults, but the pattern of these anomalies is far from being as clearly related to the faults as the simulated anomalies in Figures 4.11b, 4.12b, 4.13b and 4.14b or 4.16. Part of this discrepancy must come from the quality of the temperature data. It is unfortunately impossible to do any more with the present data set because it was never collected for such purposes. If our results are valid, the simplicity of our methodology should encourage a systematic record and registration of such data sets in the future, including multiple measurements at the same depth when possible. While it doesn't require any expensive or time consuming procedure, it can provide a comprehensive representation of the hydrologic activity in similar, extensively drilled areas.

Among the most flagrant simplifications of our model, the uniform permeability attributed to elements not smaller than  $500 \times 500 \times 100\text{m}$  can not account for the heterogeneity in shale distribution and permeability on the scale observed in individual reservoirs [Chapter 3; *He*, 1996], or for the intricate distribution of individual faults and fractures in the fault zone [*Losh et al.*, 1999, *Losh*, 1998]. The heterogeneity in shaliness within a reservoir is an important factor in reservoir simulations over short periods (10 to 20 years of production), and it controls the path of the forced migration and the distribution of the various fluid phases [Chapter 3]. However, the influence of this heterogeneity on the temperature distribution is more limited. The diffusion into adjacent formations of the heat carried by centuries-long advection prevents small scale heterogeneity in the temperature distribution. In any case none that could be detected by the low spatial resolution of our temperature field reconstruction. An effective permeability value that takes into account the average sand and shale content and the horizontal anisotropy due to the sediments layering can actually be representative of such large scale permeability [*McCarthy*, 1991]. More concern regarding the numerical simplifications can come from the choice of a rectangular grid. *Narasimhan and Witherspoon* [1976] report that for maximum accuracy of the Integrated Finite Difference Method (IFDM) used in the model, interfaces between elements should be perpendicular to the line joining the two center points and intersect that line at a mean position. For all practical purposes, this limits us to rectangular elements, unless we use advanced mesh generators. It forces flow to occur only across vertical and horizontal boundaries and follow step-like paths instead of running along the actual dip of the bedding or of the fault. Practically, this increases the volume of rock interacting with the fluids [*Fisher et al.*, 1994], and dissipates artificially some of the heat carried by the fluids. It eventually leads to a reduction of the amplitude of the thermal anomalies simulated at shallower depth.

Finally, regarding the coarseness of the grid, *Roberts et al.* [1996] give a fine scale description of the fault activity by using much narrower elements to define the fault (10 m wide, with fault apertures of the orders of microns), and successfully reproduce in 2D some of the temperature anomalies in Eugene Island. However, similar refinements in the vicinity of the fault planes for a rectangular grid in 3D would multiply the number of nodes and expand to unpractical dimensions the size of the linear equation systems to solve. Moreover, *Losh* [1998] shows that the fault zone crossed by the Pathfinder well is more than 100 m thick, and the various interpretations of adjacent fault splays [*Rowan et al.* 1998, *Alexander and Handschy*, 1998, *Holland*, 1991] suggest that migration could occur along wide paths, flowing along several fault segments which are only partially constrained [*Rowan et al.*, 1998], or flowing across faults [*Alexander and Handshy*, 1998]. Therefore, while the results of *Roberts et al.* [1996] provide the explanation for the expulsion mechanisms along a single fault, the uncertainties in picking individual faults in 3D seismic and the large number of faults in the data-cube could barely justify such high resolution to realistically represent the Eugene Island fault zone in 3D. We assume that the permeability of our fault nodes represents an average bulk permeability, similar to the 1D model of *Wang and Xie* [1998], which distributes over the entire node the same amount of fluid that is actually confined within the individual fault planes crossing the node.

## 4.7 Conclusion

The purpose of these models is to offer a method, relatively simple in its assumptions and realization, for analyzing in 3D the processes occurring in an active basin. Despite all the care that can be taken in processing the BHTs, the way they are collected precludes the possibility of establishing reliably an exact fine-scale temperature distribution. Therefore, even the most legitimate interpretation can be only qualitative. However, the

high density of the data in EI330 and in similar densely sampled oil fields can somewhat compensate for the lack in quantitative accuracy of individual measurements. 3D models built on a well-constrained lithology defined by 3D seismic interpretation can provide a complete, semi-quantitative description of the fluid migration activity within the basin. Our results show that the temperatures observed today in the Eugene Island 330 field could be the result of 1,000- to 5,000-years long pulses of fluid expulsion activity within the fault. Our most important conclusions from this modeling is that fluids expelled from the overpressured shales migrate predominantly upwards within the fault during the period of activity, and then flow into the adjacent formation after the fault closes, carrying their heat, and hydrocarbons, into the most productive reservoirs of the field.

## References

- Alexander, L.L., and Flemings, P. B., 1995, Geologic evolution of a Plio-Pleistocene salt withdrawal Mini-Basin: Block 330, Eugene Island, South Addition, Offshore Louisiana, *AAPG Bull.*, 79(12), 1737-1756.
- Alexander, L.L., and J.W. Handschy, 1998, Fluid flow in a faulted reservoir system: Fault trap analysis for the Block 330 field in Eugene Island, South Addition, Offshore Louisiana, *AAPG Bull.*, 82(3), 387-411.
- Anderson, R.N., He, W., Hobart, M.A., Wilkinson, C.R., and Nelson, H.R. Jr., 1991, Active fluid flow in the Eugene Island Area, offshore Louisiana, *Geophysics: The Leading Edge*, 10(4),12-17.
- Anderson, R.N., 1993, Recovering dynamic Gulf of Mexico reserves and the U.S. energy future, *Oil & Gas Journal* , April 26, 85-91.
- Anderson, R.N., Flemings, P.B., Losh, S., Austin, J., Woodhams, R., and the Global Basins Research Network Team, 1994, Gulf of Mexico Growth fault drilled, seen as oil, gas migration pathway, *Oil and Gas Journal*, June 6, 97-103.
- Armstrong, P.A., D.S. Chapman, R.H. Funnell, R.G. Allis and P.J.J. Kamp, 1996, Thermal Modeling and Hydrocarbon Generation in an Active-Margin Basin: Taranaki Basin, New Zealand, *AAPG Bull.*, 80(8), 1216-1241.
- Bachu, S., J.C. Ramon, M.E. Villegas, and J.R. Underschultz, 1995, Geothermal Regime and Thermal History of the Llanos Basin, Colombia, *AAPG Bull.*, 79(1), 116-129.
- Batzle, M., and Z. Wang, Seismic properties of pore fluids, *Geophysics*, 57(11):1396-1408, 1992.
- Bodner D.P. and J.M. Sharp, 1988, Temperature Variations in South Texas Subsurface, *AAPG Bull.*, 72(1), 21-32.
- Bodvarsson, G. S., Mathematical modeling of the behavior of geothermal systems under exploitation, Ph.D. thesis, 353 pp., Univ. of Calif., Berkeley, 1982.

- Burnham, A.K., 1995, Chemical kinetics and shale process design, *in* C. Snape (ed.), *Composition, Geochemistry and Conversion of Oil Shales*, Kluwer Academic Publishers, 263-276.
- Castoviejo R., R. Gable, R. Cueto, J.C. Foucher, M. Soler, J. Gounot, J.C. Batsale, A. Lopez and M. Joubert, 1996, Ensayo de una metodologia innovadora para la deteccion de masas polimetlicas profundas: Modelo geologico y exploracion geotermica preliminares de la Masa Valverde (Huelva), *Boletin Geologico y Minero*, 107(5-6), 485-509.
- Coelho, D., A. Erendi, and L.M. Cathles, 1996, Temperature, pressure and fluid flow modelling in Block 330, South Eugene Island using 2D and 3D finite element algorithms, *in* Annual Meeting Abstracts - AAPG and SEPM, v. 5, p. 28.
- England, W.A., A.S. Mackenzie, D.M. Mann and T.M. Quigley, 1987, The movement and entrapment of petroleum fluids in the subsurface, *J. of the Geol. Soc., London*, 144, 327-347.
- Fisher, A.T., K. Becker and T.N. Narasimhan, Off-axis hydrothermal circulation: parametric test of a refined model of processes at Deep Sea Drilling Project/Ocean Drilling Program site 504, *J. Geophys. Res.*, 99(B2), 3097-321, 1994.
- Flemings, P., Zoback, M.D., Bishop, B.A., and Anderson, R.N., 1995, State of stress in the pathfinder well, *in* Anderson, R.N., Billaud, L. B., Flemings, P., Whelan, J., and Losh, S., *The GBRN/DOE Eugene Island Dynamic Enhanced Recovery project*, CD-ROM, Lamont Press, Part IV-3.
- Gable, R., 1977, Temperature and heat flow in France, Seminar on Geothermal Energy, Brussels, 6-8 December 1977, *in* Commission of the European Communities, Directorate General for Research, Science and Education, EURO 5920, Vol. 1: 113-131.
- Gable, R., 1986, Acquisition et Interpretation de données Géothermales, Doctor es-Sciences Thesis, Université Pierre et Marie Curie, *Documents du BRGM*, 104.

- Hart, B.S., P.B. Flemings, and A. Deshpande, Porosity and pressure: Role of compaction disequilibrium in the development of geopressures in a Gulf Coast Pleistocene basin, *Geology*, 23(1), pp 45-48.
- Holland, D. S., Leedy, J. B., and Lammlein, D. R., 1990, Eugene Island Block 330 field-U.S.A., offshore Louisiana, in Beaumont, E.A., and Foster, N. H., compilers, *Structural traps III, tectonic fold and fault traps: AAPG Treatise of Petroleum Geology Atlas of Oil and Gas Fields*: 103-143.
- Hooper, E.C.D., 1991, Fluid migration along growth faults in compacting sediments, *J. of Pet. Geology*, 14(2): 161-180.
- Humphris, C. C., Jr., 1978, Salt movements on continental slopes, northern Gulf of Mexico, in A. H. Bouma et al., eds., *Framework, facies, and oil trapping characteristics of the upper continental margin: American Association of Petroleum Geologists Studies in Geology* 7: 69-85.
- Lachenbruch, A.H., and Brewer, M. C., 1959, Dissipation of the temperature effect of drilling a well in Arctic Alaska, *U.S.G.S. Bull.*, 1083-C: 73-106.
- Losh, S., 1998, Oil Migration in a Major growth fault: Structural Analysis of the Pathfinder Core, South Eugene Island Block 330, Offshore Louisiana, *A.A.P.G. Bull.*, 82(9), 1694-1710.
- Losh, S., L. Eglinton, M. Schoell, and J. Wood, 1999, Vertical and Lateral fluid flow related to a large growth fault, South Eugene Island Block 330 field, Offshore Louisiana, *A.A.P.G. Bull.*, 83(2), 244-276.
- Mallard, W.G. and P.J. Linstrom, Eds., NIST Chemistry WebBook, NIST Standard Reference Database Number 69, March 1998, National Institute of Standards and Technology, Gaithersburg MD, 20899 (<http://webbook.nist.gov>).
- McCarthy, J.F., 1991, Analytical models of the effective permeability of sand-shale reservoirs, *Geophys. J. Int.*, 105, 513-527.

- Mello, U.T., R.N. Anderson and G.D. Carner, 1994, Salt restrains maturation in subsalt plays, *Oil and Gas Journal*, Jan. 31:101-107.
- Narasimhan, T.N. and P.A. Witherspoon, 1976, An integrated finite difference method for analyzing fluid flow in porous media, *Water Resour. Res.*, 12(1), 57-64.
- Press, W.H., S.A. Teukolsky, W.T. Vetterling and B.P. Flannery, 1992, Numerical recipes in C: the art of scientific computing - 2nd edition, Cambridge University Press, New York.
- Roberts, H.H., 1998, Evidence of episodic delivery of fluids and gases to the seafloor and impacts of delivery rate on surficial geology (Gulf of Mexico), AAPG 1998 annual meeting, expanded abstracts.
- Roberts, S.J., J.A. Nunn, L. Cathles, and F.D. Cipriani, 1996, Expulsion of abnormally pressured fluids along faults, *J. Geophys. res.*, 101, B12, 28,231-28,252.
- Rowan, M.G., B.S. Hart, S. Nelson, P.B. Flemings and B.D. Trudgill, Three-dimensional geometry and evolution of a salt-related growth-fault array: Eugene Island 330 Field, offshore Louisiana, Gulf of Mexico, *Mar. and. Pet. Geol.*, 15, 309-328.
- Rybach, L., 1981, Geothermal Systems, Conductive Heat Flow, in Geothermal Systems: principles and case histories, edited by L. Rybach and L.J.P. Muffler, John Wiley and Sons, Ltd.
- Sharp, J.M., and Domenico, P.A., 1976, Energy transport in thick sequences of compacting sediments, *Geol. Soc. of Am. Bull.*, 87: 390-400.
- Wang, C.Y., and X. Xie, 1998, Hydrofracturing and Episodic Fluid Flow in Shale-Rich Basins - A numerical Study, *A.A.P.G. Bull.*, 82(10), 1857-869.
- Whelan, J., Eglington, L., Requejo, R., and Kennicutt, M. C., 1995, Pathfinder well organic geochemistry - Indicators of Oil source and Maturity and fluid flow mechanisms, in Anderson, R.N., Billeaud, L. B., Flemings, P., Whelan, J., and Losh, S., *The GBRN/DOE Eugene Island Dynamic Enhanced Recovery project*, CD-ROM, Lamont Press, Part V.

**Table 1 : Principal physical properties of the sediments in the models**

Property	Salt	Shale	Proximal Deltaic Sands	Fluvial Sands
Thermal Conductivity	6	1.9	1.9 - 2.2	2.0
Vertical Permeability (m <sup>2</sup> )	10 <sup>-19</sup>	10 <sup>-17</sup>	10 <sup>-15</sup>	10 <sup>-14</sup>
Horizontal Permeability (m <sup>2</sup> )	10 <sup>-19</sup>	10 <sup>-15</sup> - 10 <sup>-14</sup>	10 <sup>-13</sup> - 10 <sup>-12</sup>	10 <sup>-13</sup>
Permeability increase	no fracture	10 <sup>3</sup>	10 <sup>2</sup> -10 <sup>3</sup>	10 <sup>1</sup> - 10 <sup>2</sup>
% of overburden for opening	no fracture	85%	85%	85%
% of overburden for closing	no fracture	75-85%	75-85%	75-85%
Porosity (%)	10	10	30	40

**Table 2: Numerical parameters**

Parameter	Value
Seafloor Temperature	18°C
Uniform Vertical Heat Flow at the base	60 mW/m <sup>2</sup>
Seafloor Pressure	10 <sup>6</sup> Pa
Bottom Pressure	1.4 10 <sup>8</sup> Pa

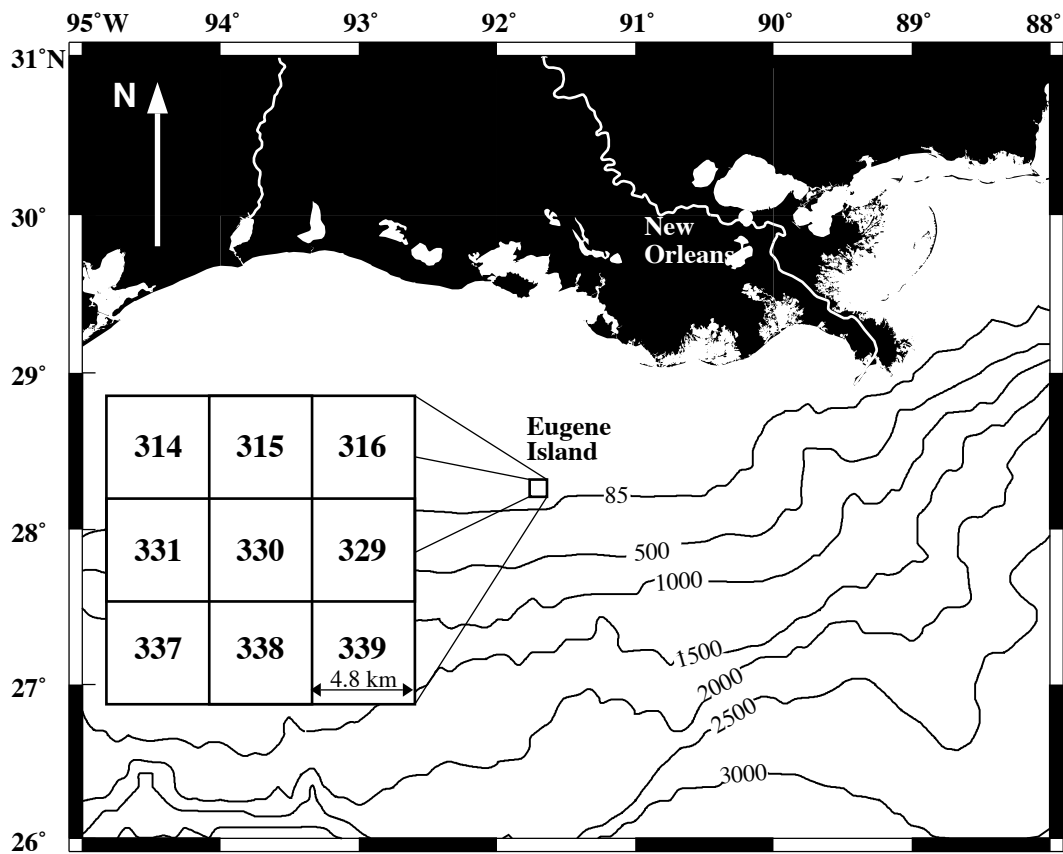


**Figure 4.1:** Location of the Eugene Island Block 330 field, on the continental slope of the Gulf of Mexico, off-shore Louisiana. The study area is composed of nine 3-mi.×3-mi. property blocks.

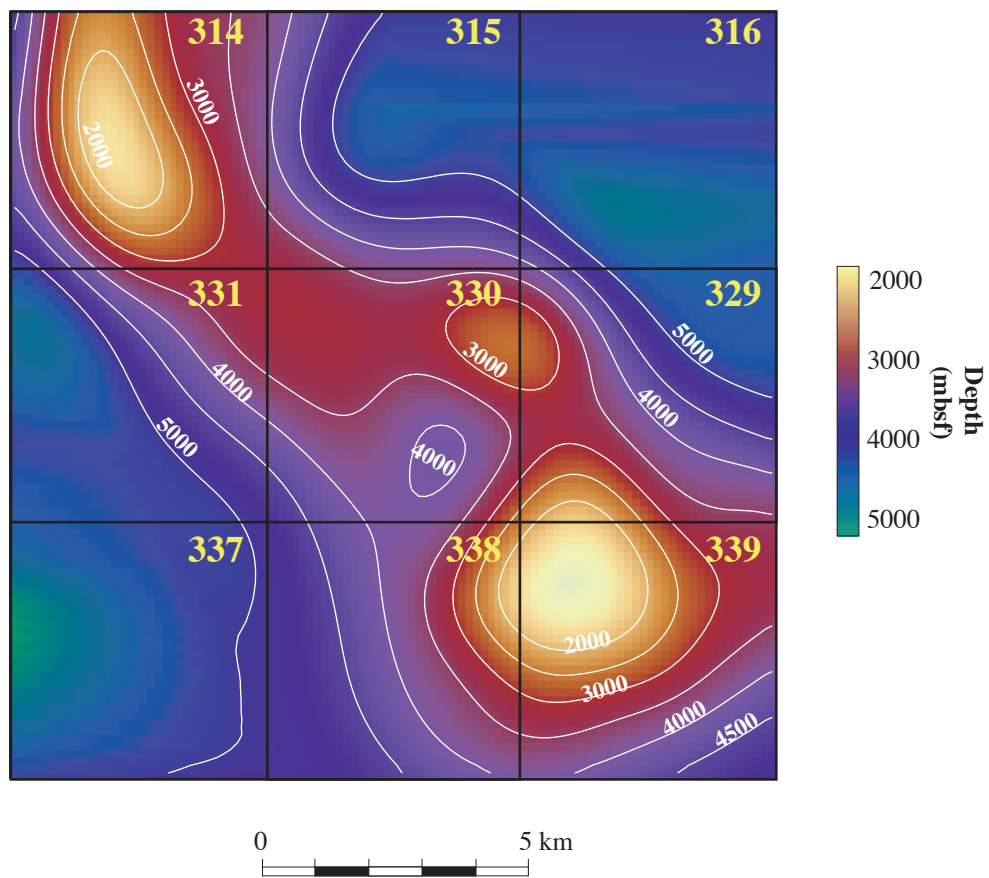


**Figure 4.2:** Top of salt map interpreted from the 3D seismics. The contours indicate the depth, in meters. The two major diapirs in Blocks 314 and 339 are shown by the brighter hues.

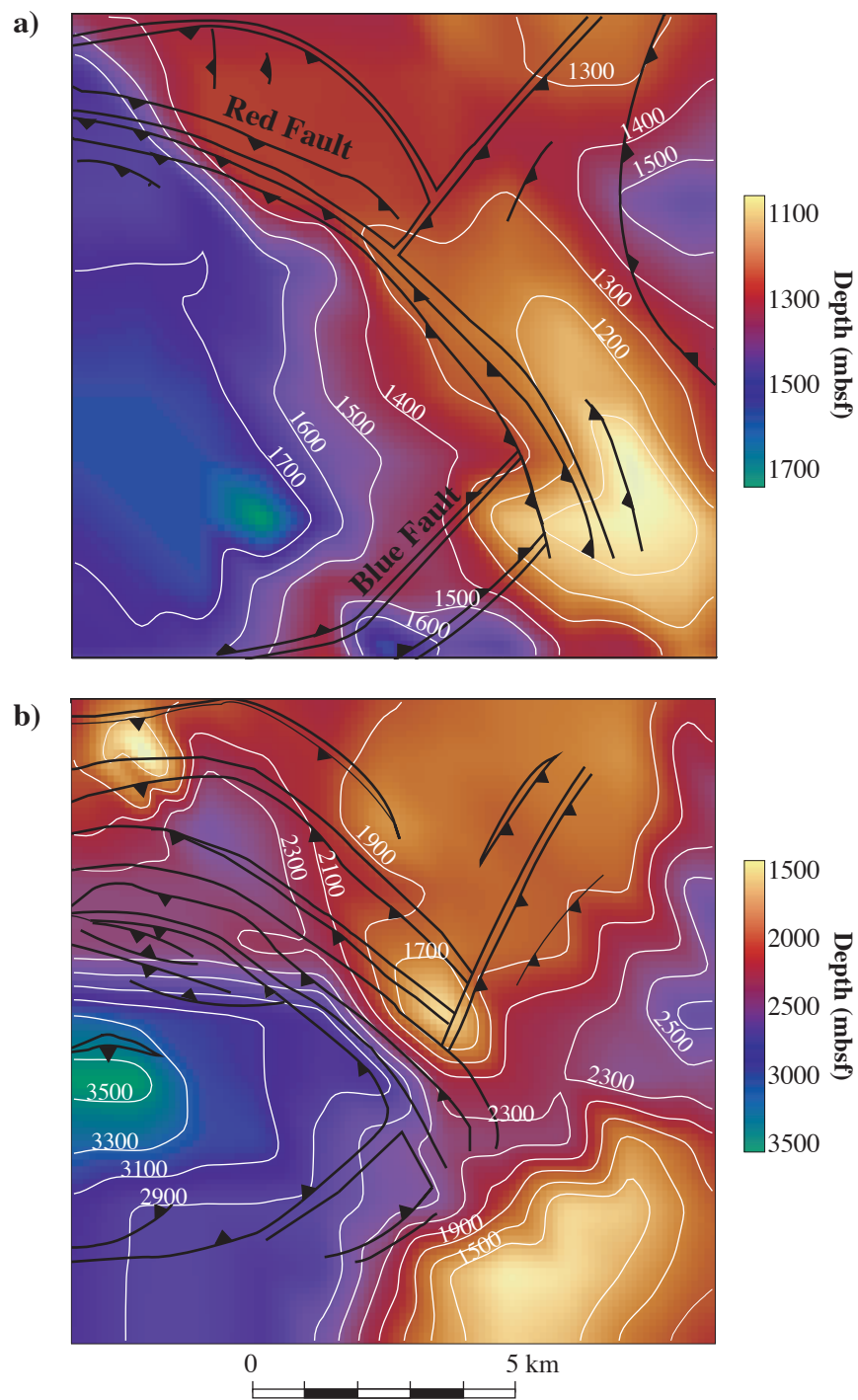


**Figure 4.3:** Two of the transgressive surfaces interpreted from the 3D seismic surveys of the data cube. *Sm. Gep 2* (a) and *Cris S* (b) correspond respectively to the top and the bottom of the proximal deltaic depositional phase of the minibasin. The black lines show the fault pattern at these depths (from *Alexander and Flemings*, [1995]), in particular the Red Fault (down to the South-West) and the Blue Fault (down to the North-West).

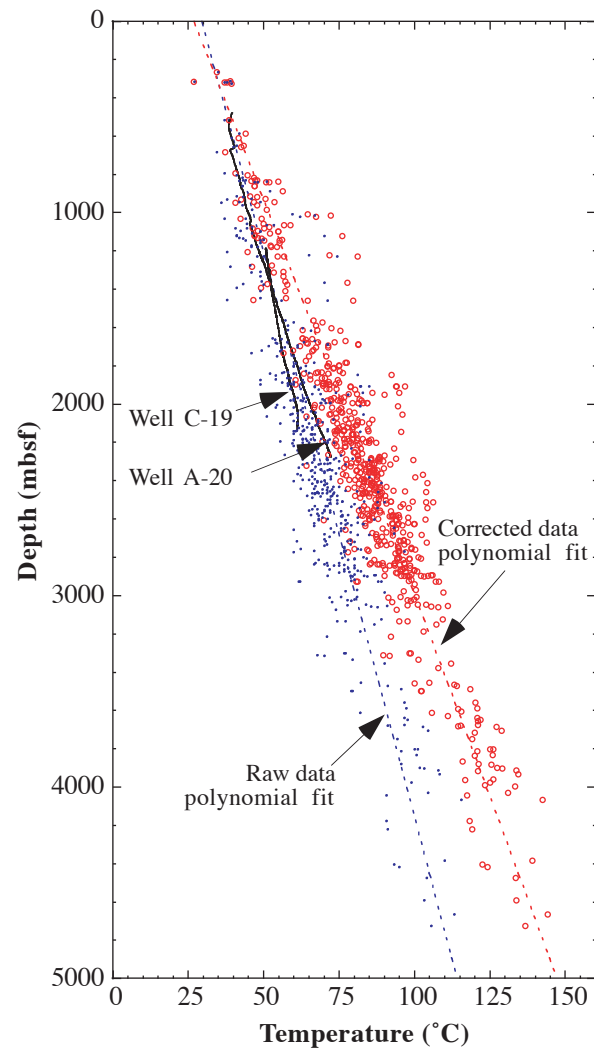


**Figure 4.4:** Bottom Hole Temperatures collected in the study area, before (blue dots) and after (red circles) correction. For comparison, two temperature logs in the same area are shown (Wells C-19 and A-20, black lines). The dotted line represent the second order polynomial fits for the raw and corrected BHT used in the data correction.

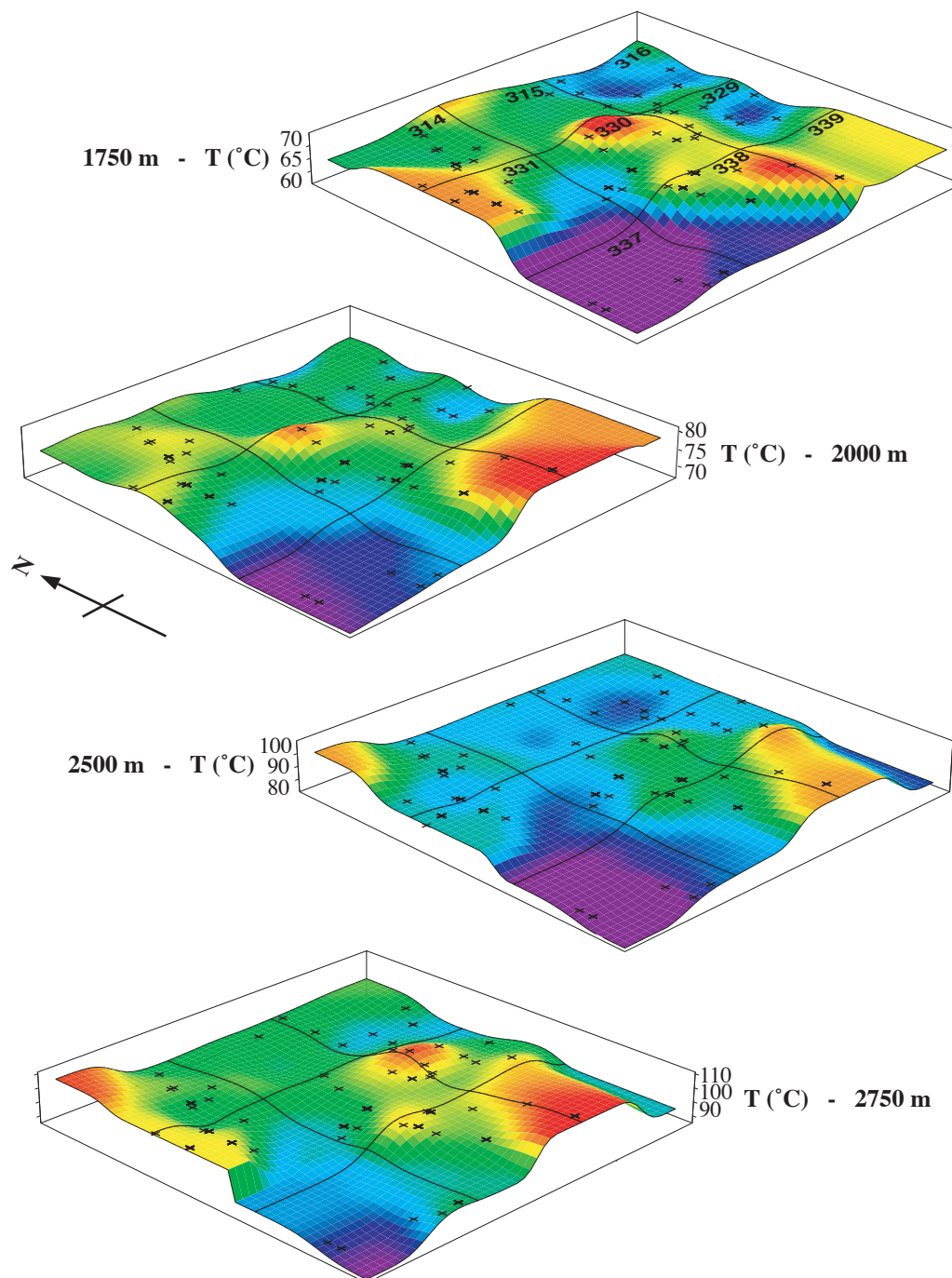


**Figure 4.5:** Temperature distribution at four different depths, after correction and interpolation of the BHT. The grid superimposed on the surfaces represents approximately the 9 blocks of the study area. The crosses show the location of the BHT measurements.

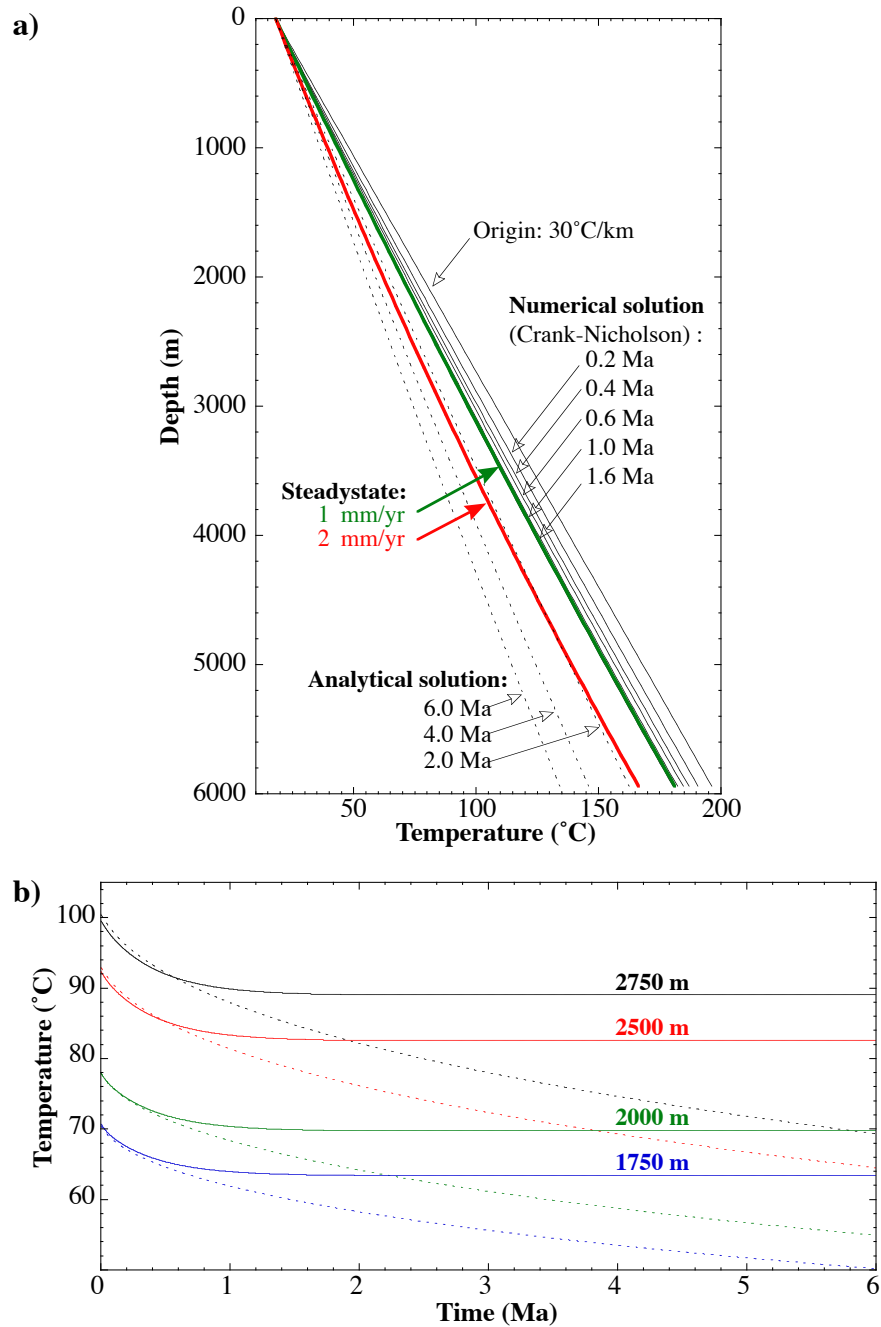


**Figure 4.6:** 1-D Estimation of the influence of sedimentation on the conductive regime. **(a)** Evolution through time of the temperature profiles vs. depth predicted by the analytical solution of Jaeger (1965) (dotted lines) and by a Crank-Nicholson discretization (continuous lines) for a 1mm/year sedimentation rate. The thick lines indicate the steady state limit of the numerical model at sedimentation rates of 1mm/year (green) and 2mm/year (red). **(b)** Evolution with time of the temperature calculated by the same analytical (dotted) and numerical (continuous lines) formulations at the depths of the surfaces of Figure 4.5.

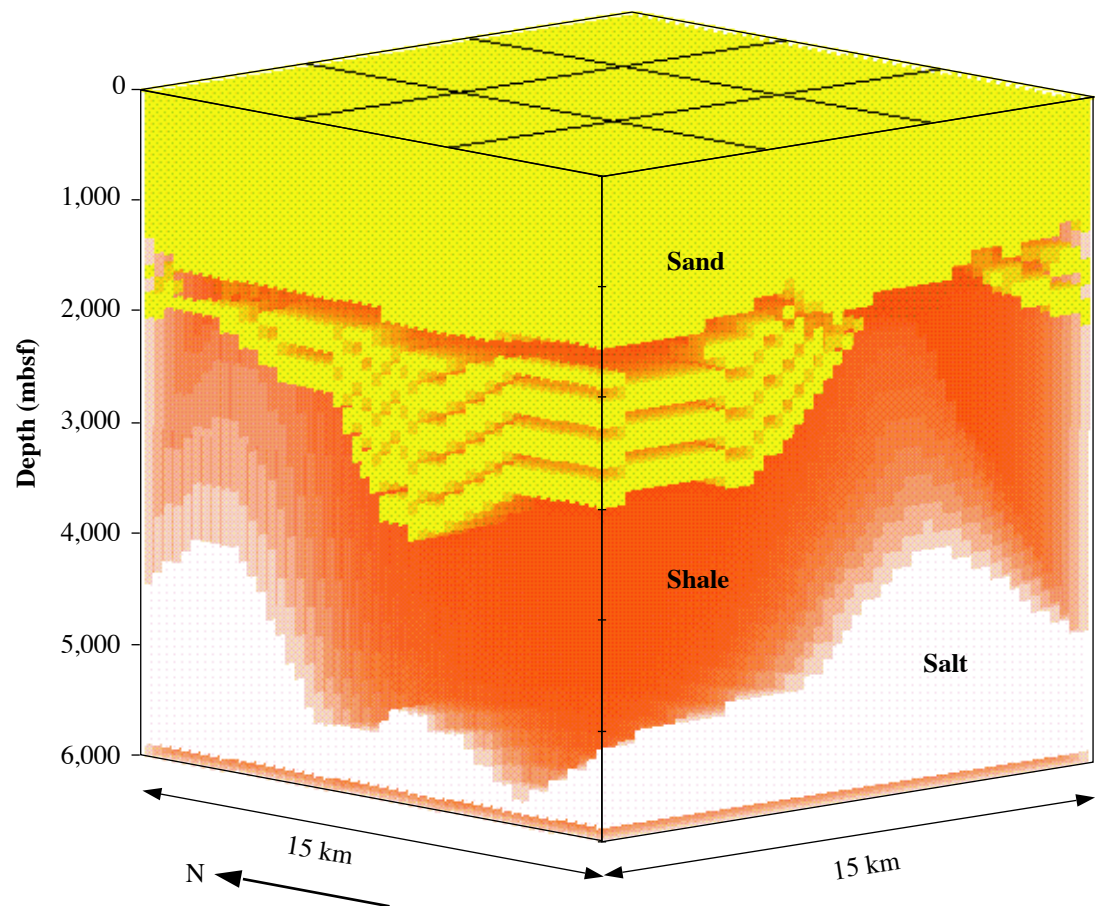


**Figure 4.7:** Representation of the lithology used in the conductive model (50×50×50 elements). The partially translucent shales (brown) allow to visualize the underlying salt diapirs (white). Four sand units (yellow) are used to represent the proximal deltaic depositional phase. The squares actually represent the different elements. (Vertical exaggeration x2)

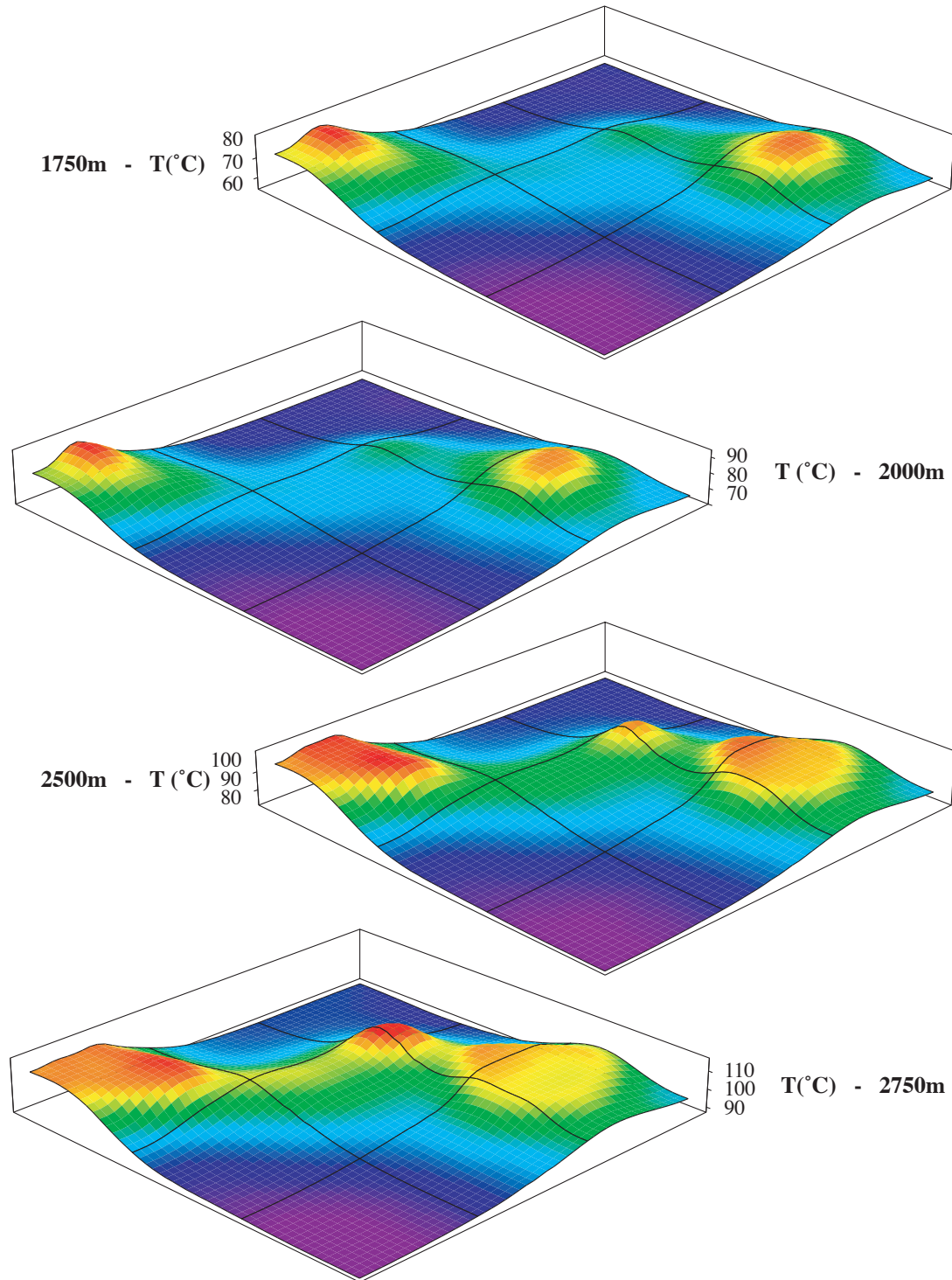


**Figure 4.8:** Result of the conductive regime simulation at the same depth as Figure 4.5. The anomalies are only related to the presence of the salt.

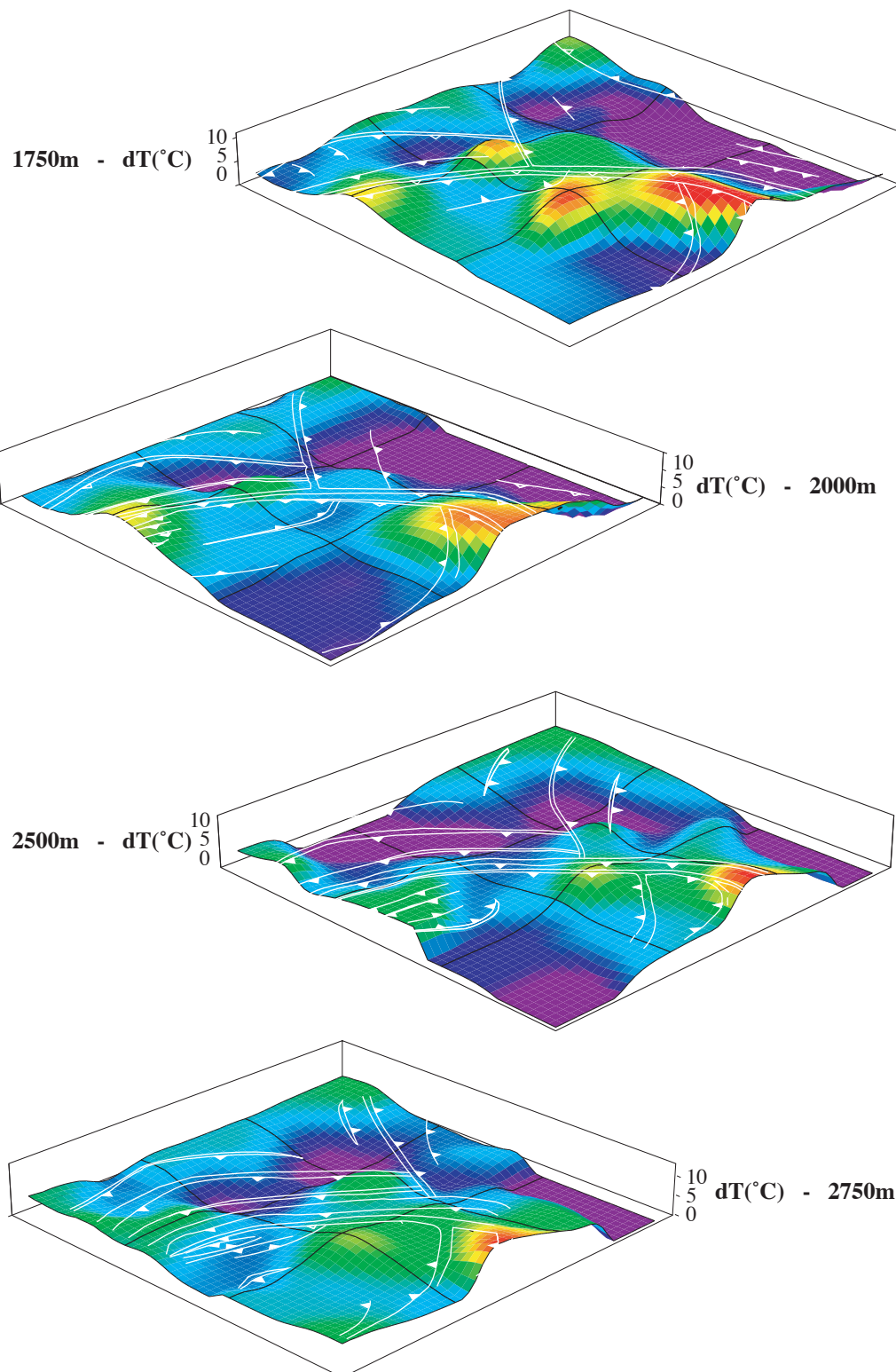


**Figure 4.9:** Difference (subtraction) between the measured temperatures (Figure 4.5) and the simulated conductive regime (Figure 4.8). Superimposed in white are the fault patterns approximately at the same depths (from *Alexander and Flemings*, [1995])

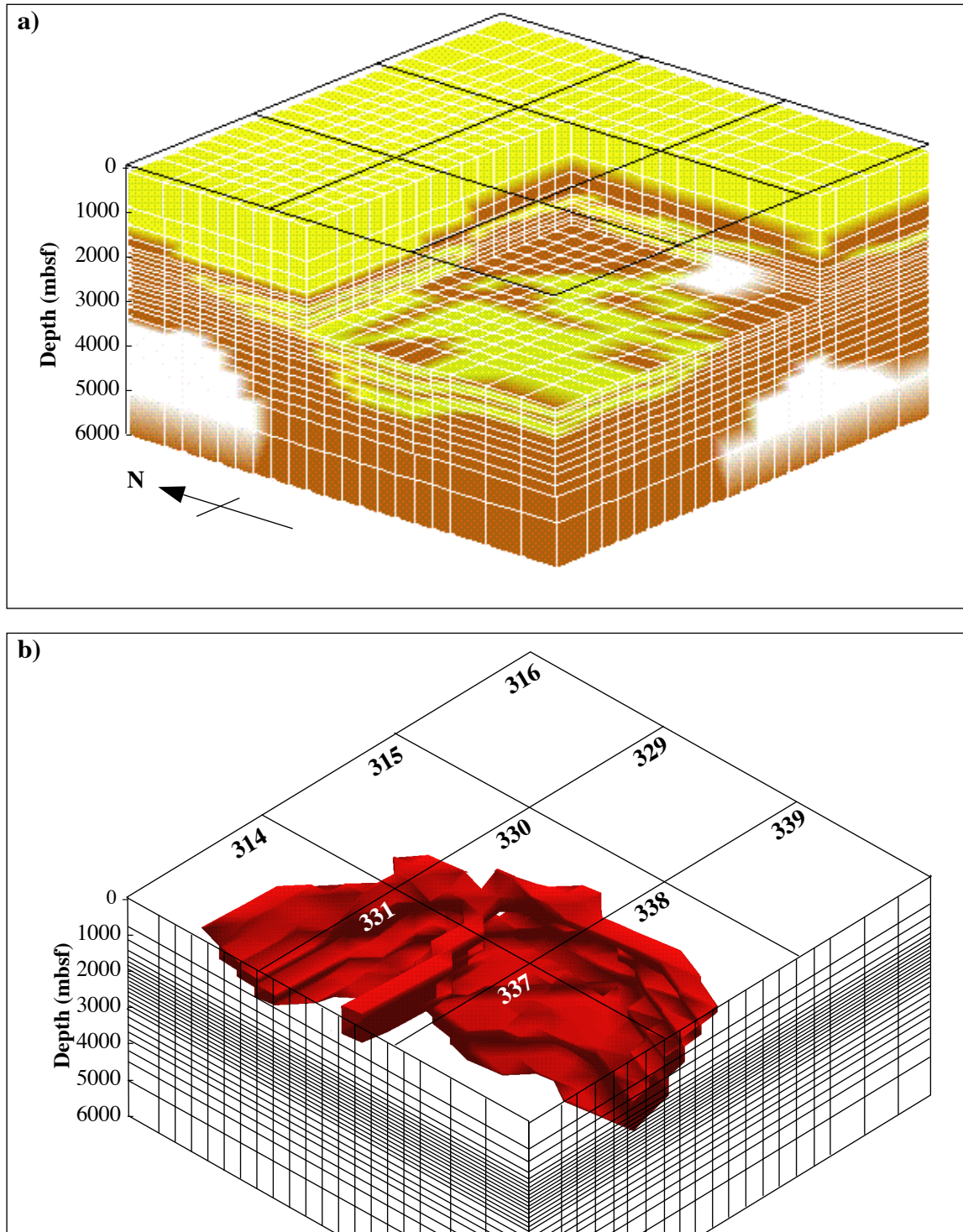


**Figure 4.10:** a) Representation of the lithology and of the grid (white lines) used in the numerical simulation of the complete thermal regime. Colors are the same as in Fig. 4.7. No vertical exaggeration. b) Representation of the fault nodes used in the simulation, derived from the fault planes interpreted in 3D seismics.

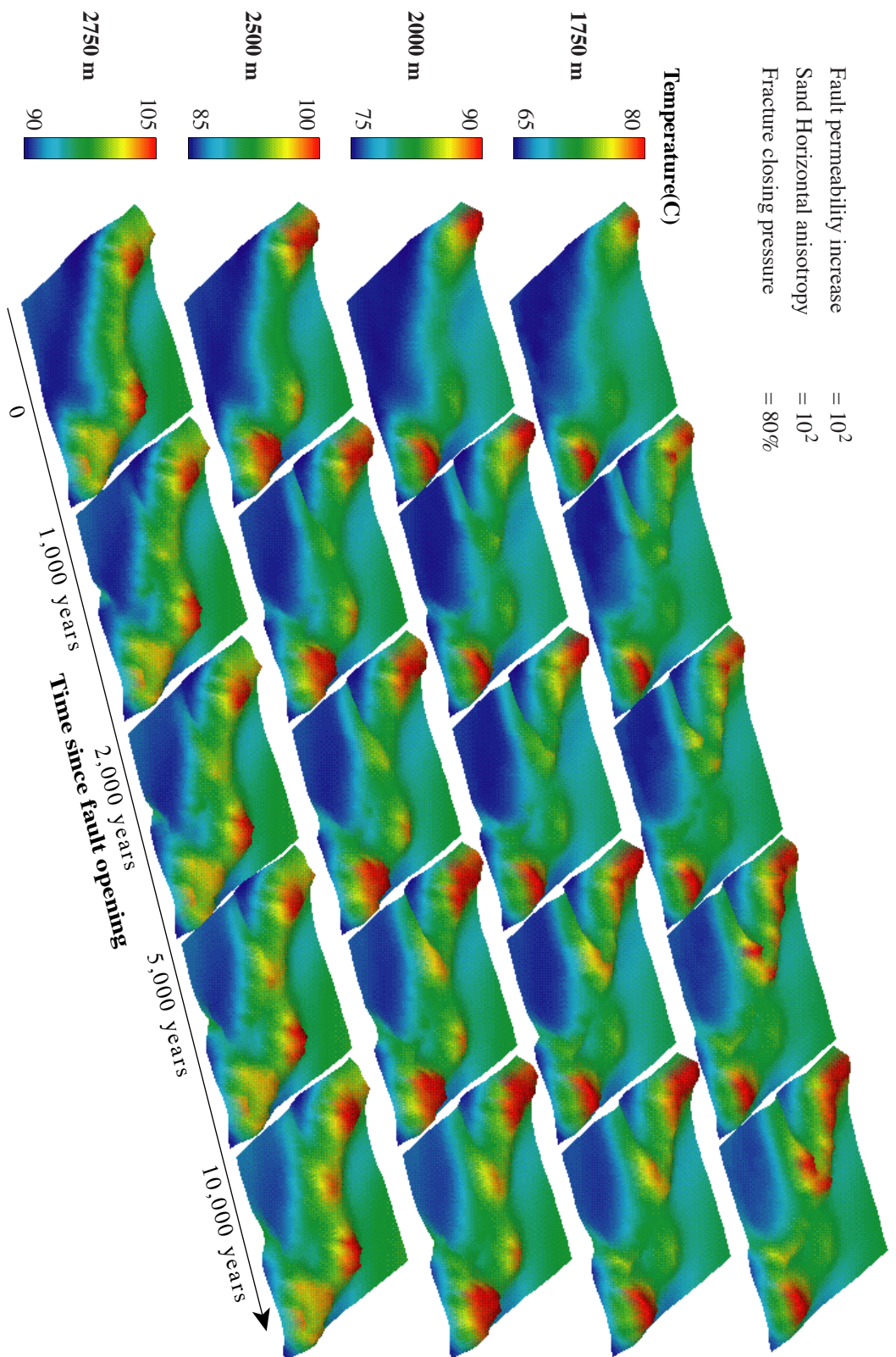


**Figure 4.11: (a)** Evolution through time of the simulated temperature distribution when the fault permeability is uniformly increased by  $10^2$ , the sand horizontal anisotropy is  $10^2$  and the fault closes when pressure falls below 80% of the lithostatic pressure.

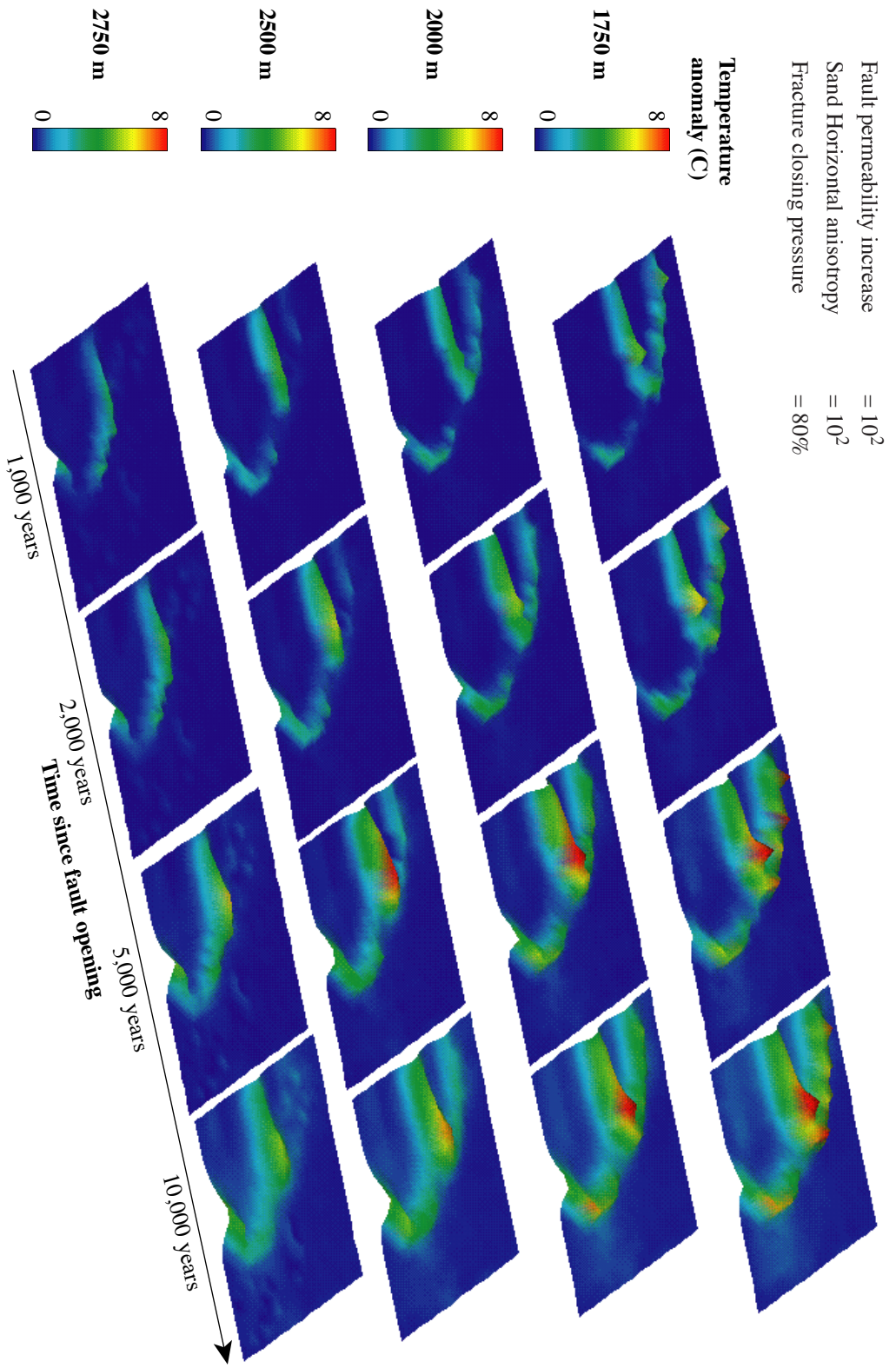


**Figure 4.11:** (b) Evolution through time of the temperature anomaly generated by fluid circulation, after removal of the conductive regime. (same parameters as Figure 11a)

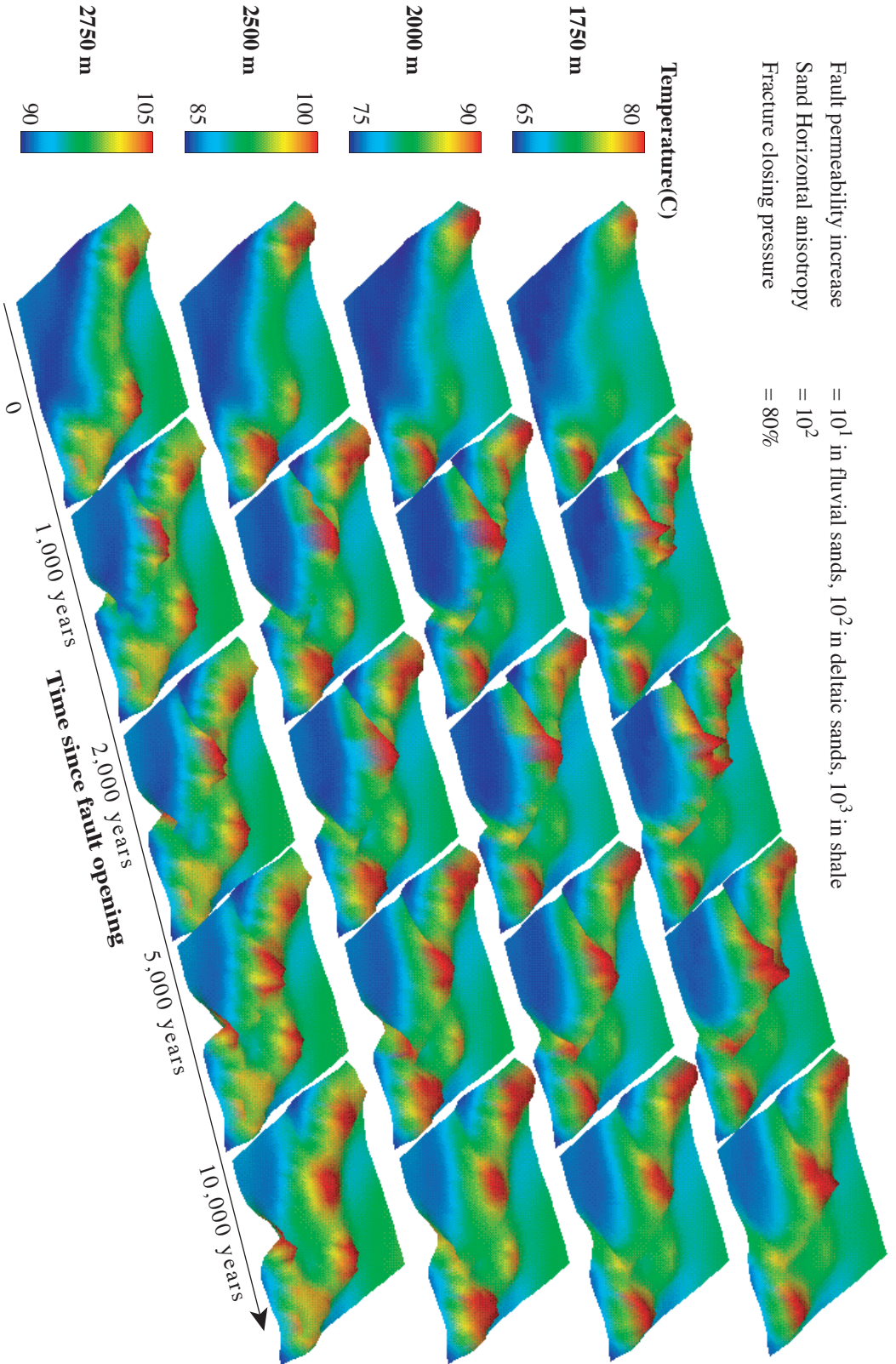


**Figure 4.12: (a)** Same as Figure 4.11a except for the fault permeability increasing by  $10^1$  in the fluvial sands, by  $10^2$  in the deltaic sands and by  $10^3$  in shales.

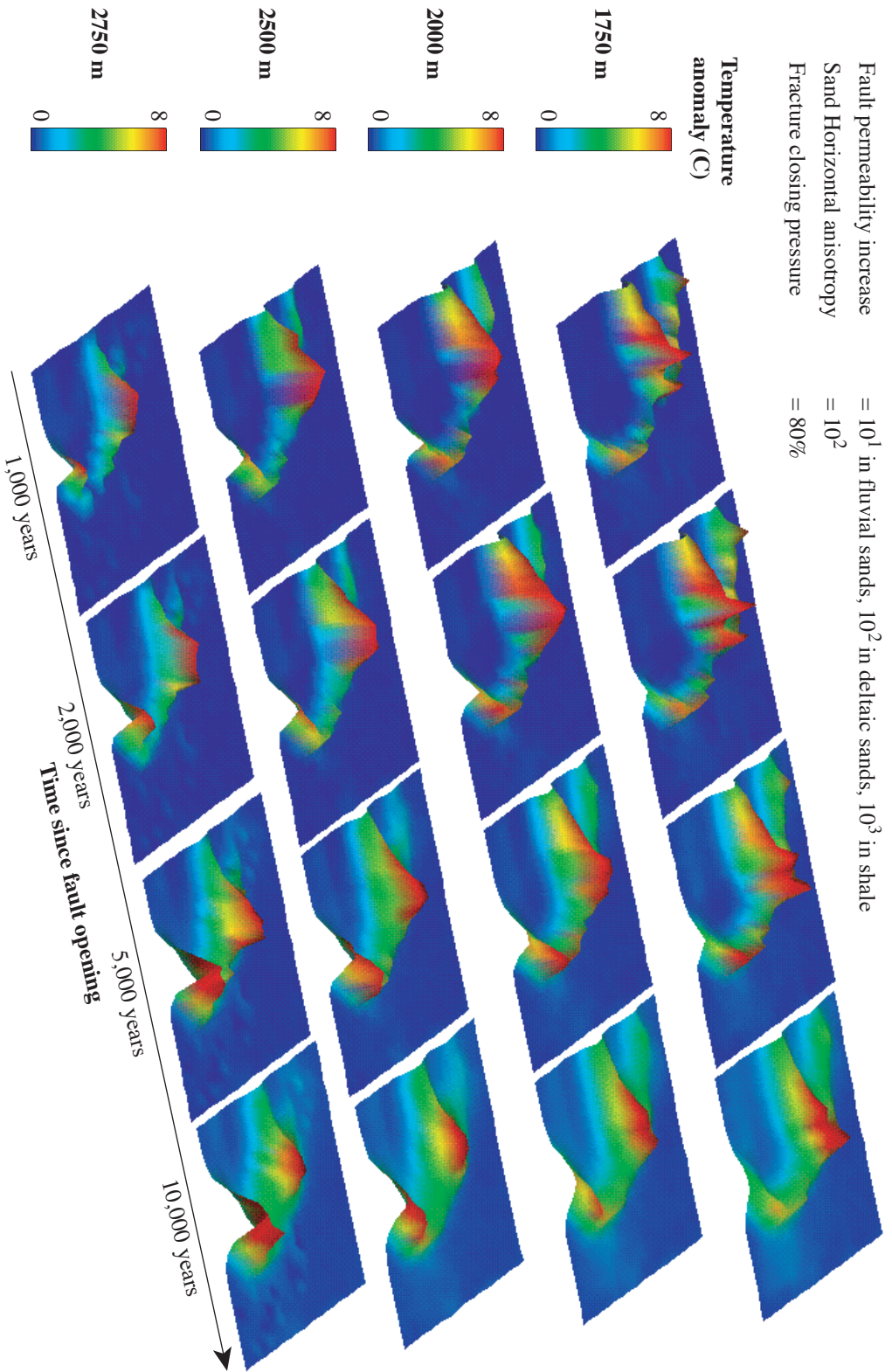


**Figure 4.12: (b)** Same as Figure 4.11b except for the fault permeability increasing by  $10^1$  in the fluvial sands, by  $10^2$  in the deltaic sands and by  $10^3$  in shales.

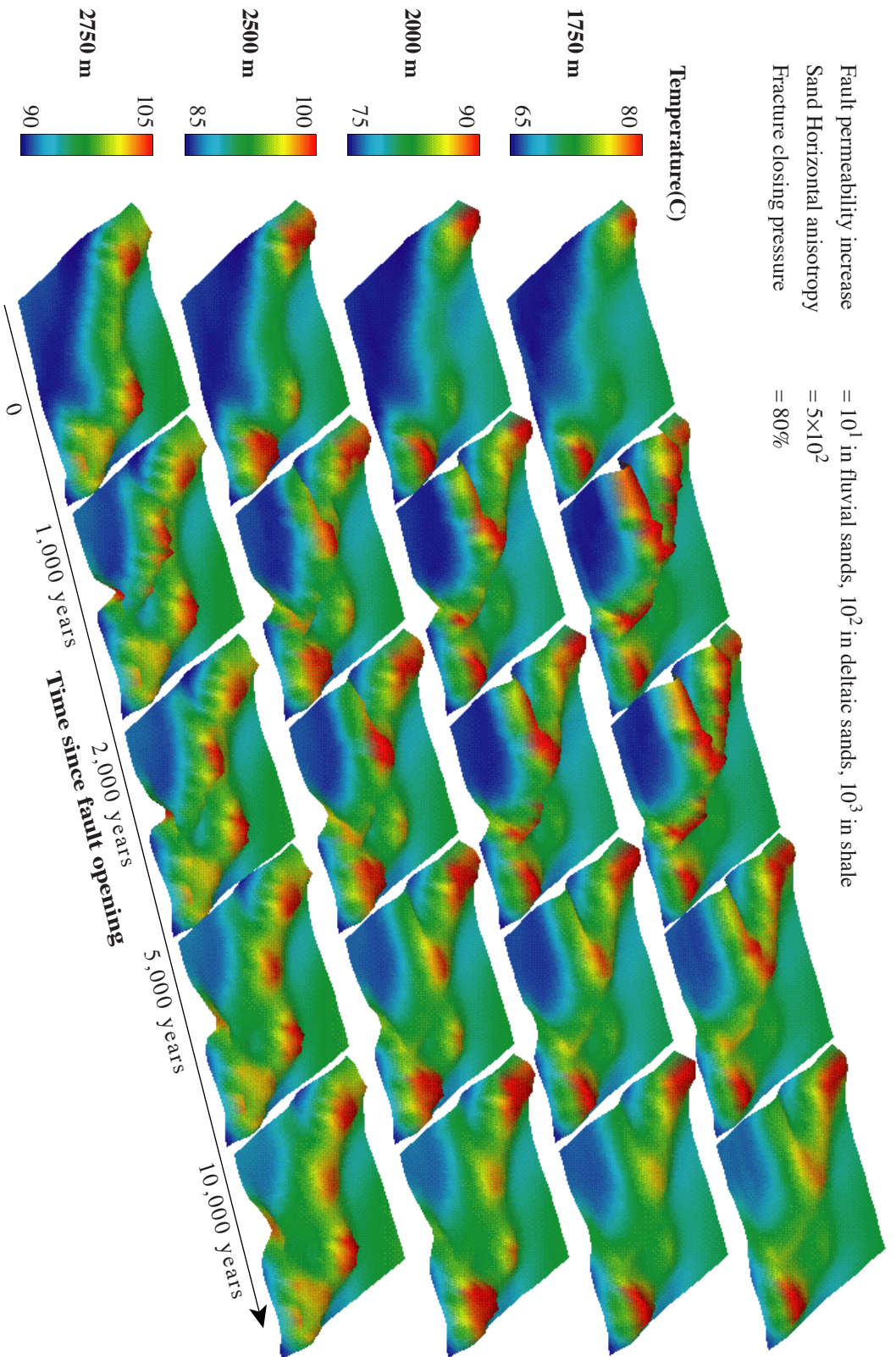


**Figure 4.13:** (a) Same as Figure 4.12a except for a higher ( $5 \times 10^2$ ) permeability in the deltaic sand.

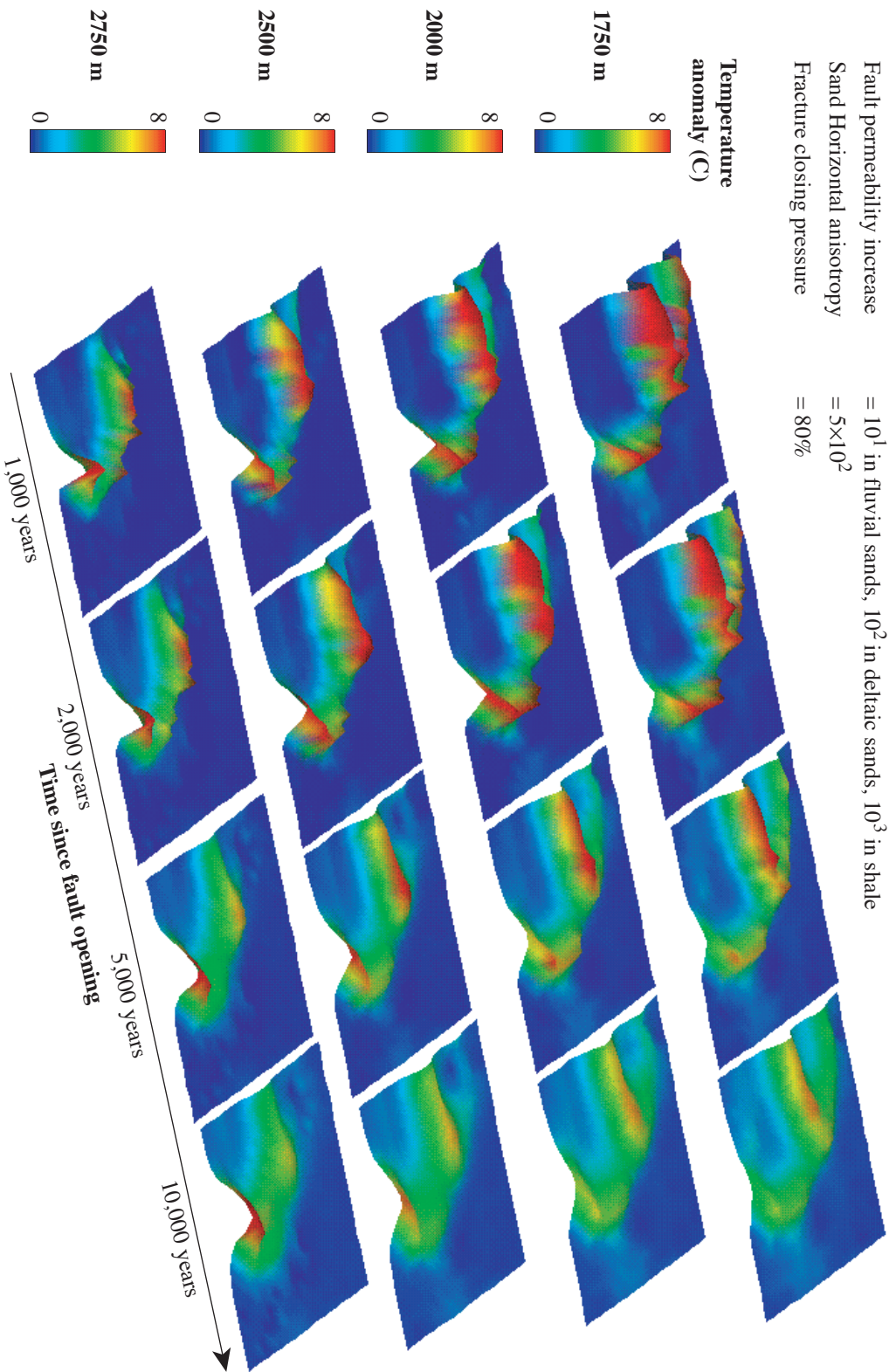
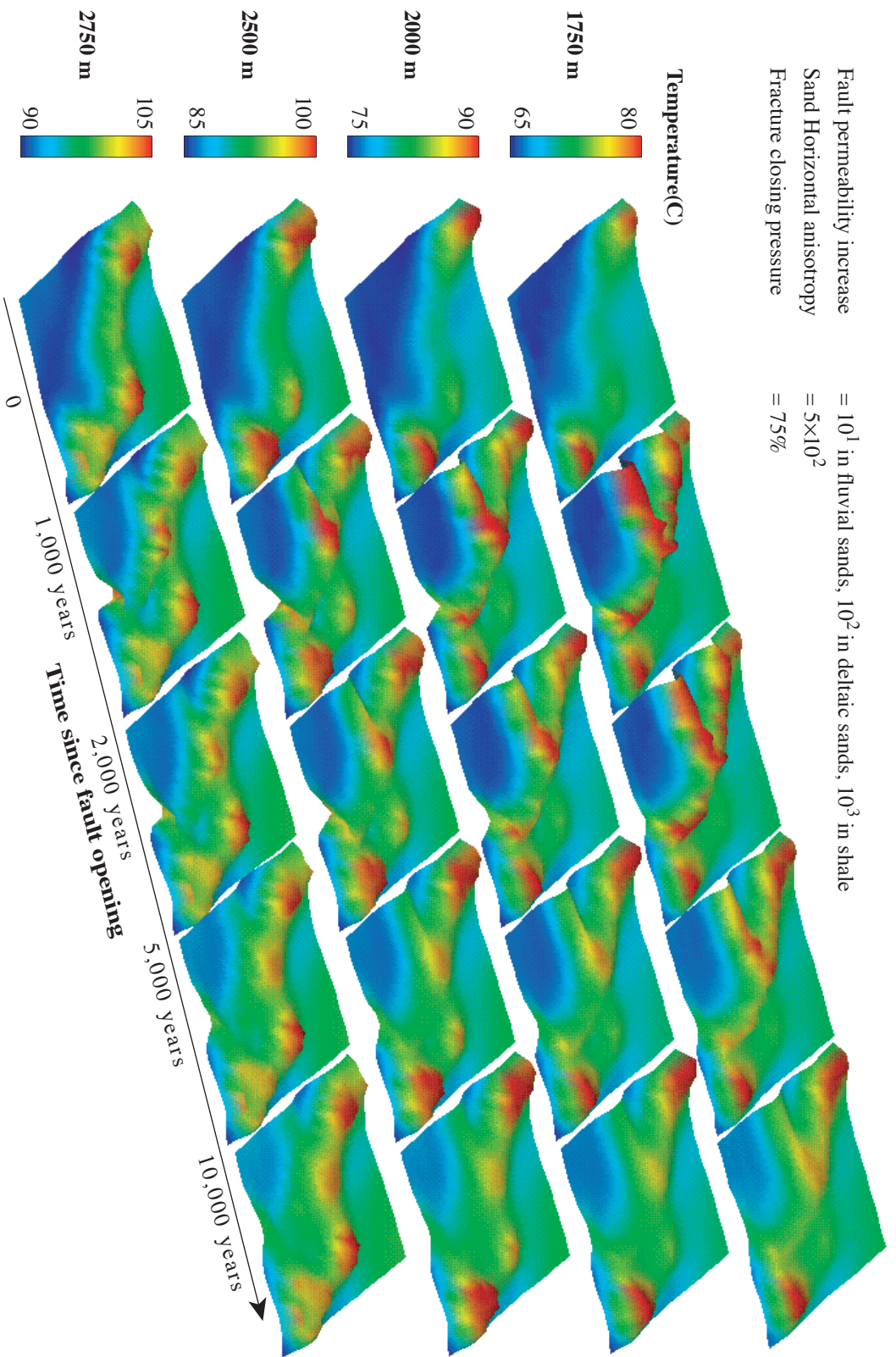
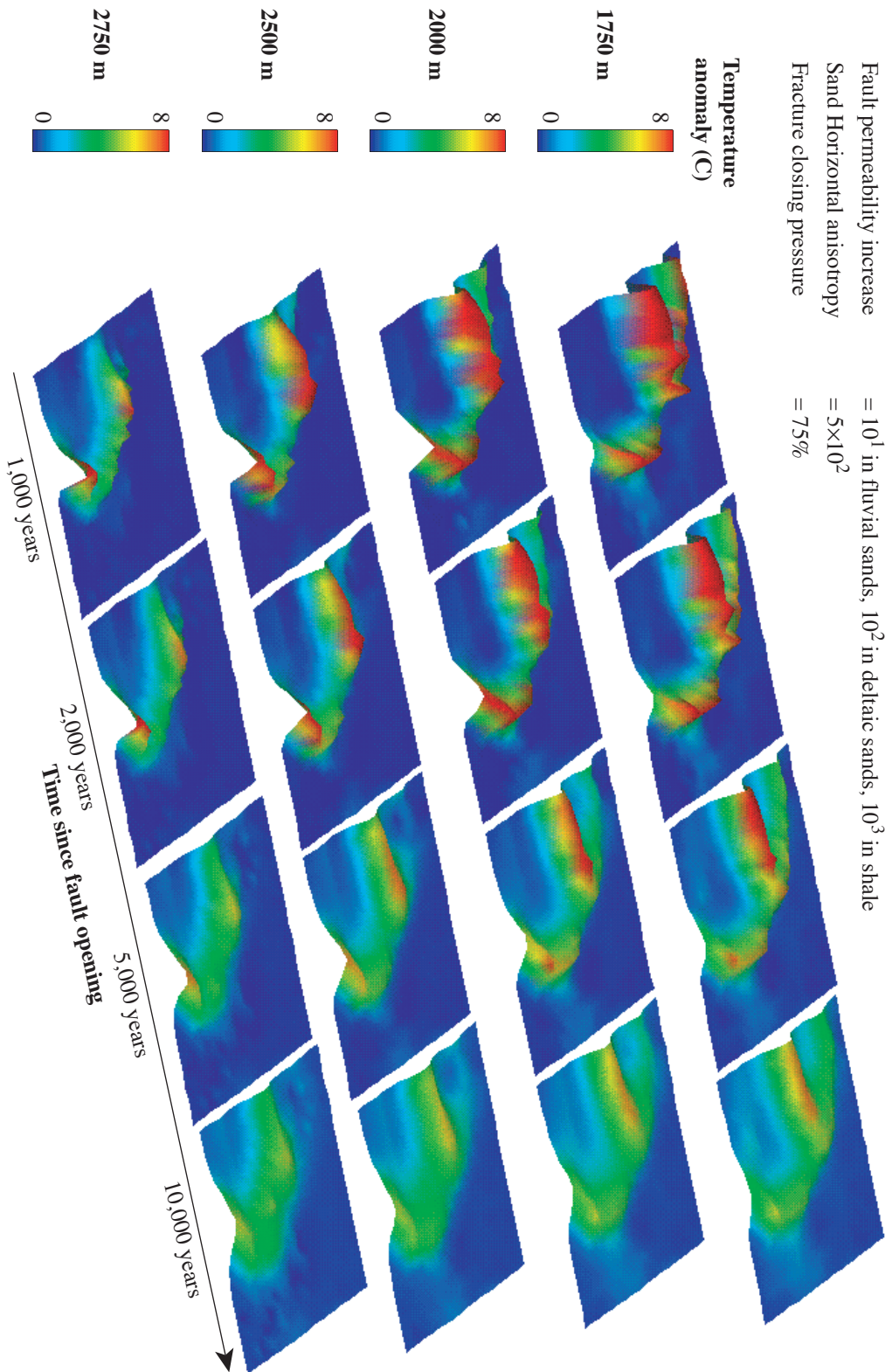


Figure 4.13: (b) Same as Figure 4.12b except for a higher ( $5 \times 10^2$ ) permeability in the deltaic sand.



**Figure 4.14:** (a) Same as Figure 4.13a except for the fault closing when pressure falls below 75% of the lithostatic pressure.



**Figure 4.14: (b)** Same as Figure 4.13b except for the fault closing when pressure falls below 75% of the lithostatic pressure.

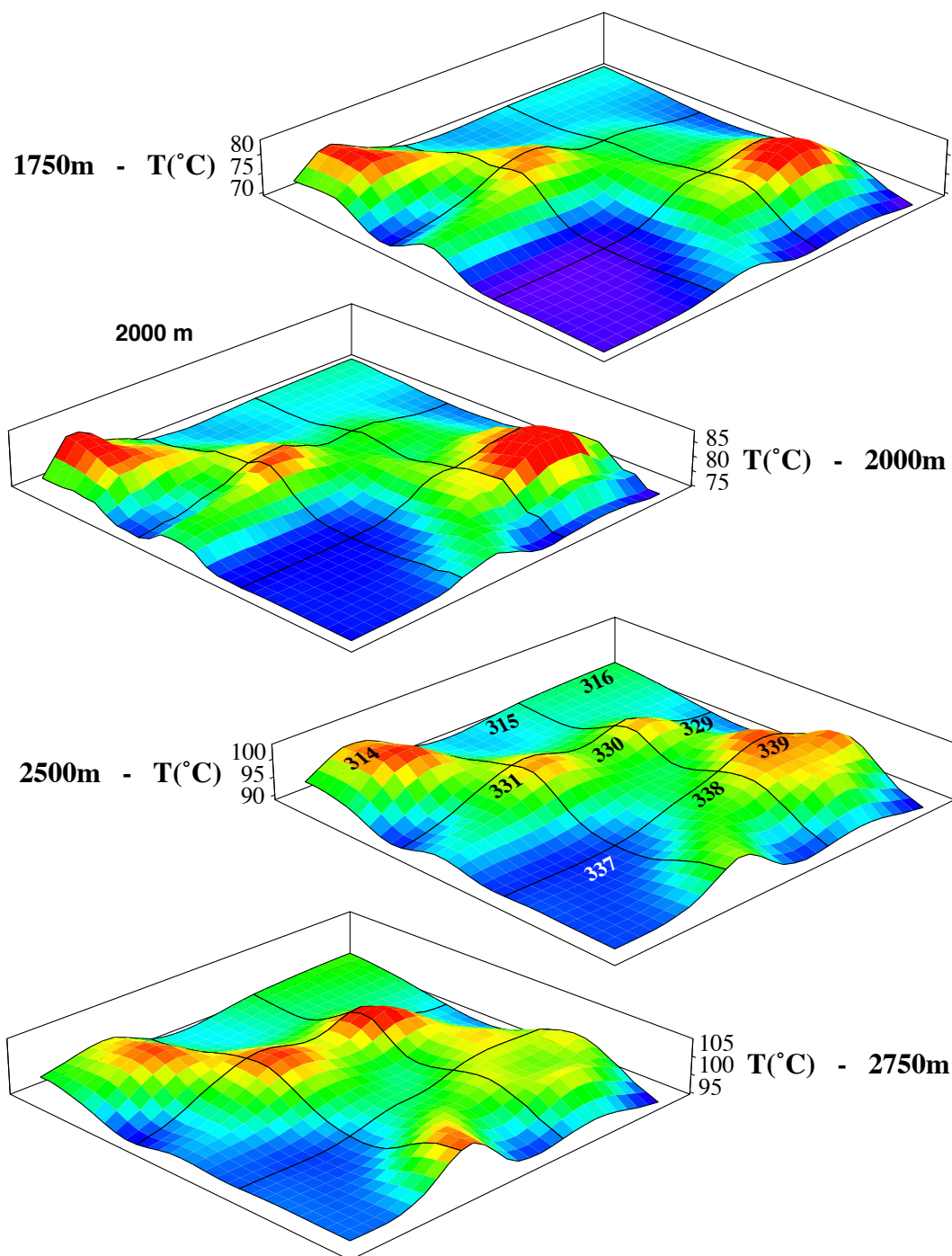


**Figure 4.15:** Result of the simulation after 5,000 years in the case corresponding to Figure 4.13: the fault permeability enhancements are  $10^3$ ,  $10^2$  and  $10^1$  in the shales, proximal deltaic sands and fluvial sands, respectively, the horizontal permeability in the sand is 500 and the closing pressure is 75% of the overburden. Compare with Figure 4.5.

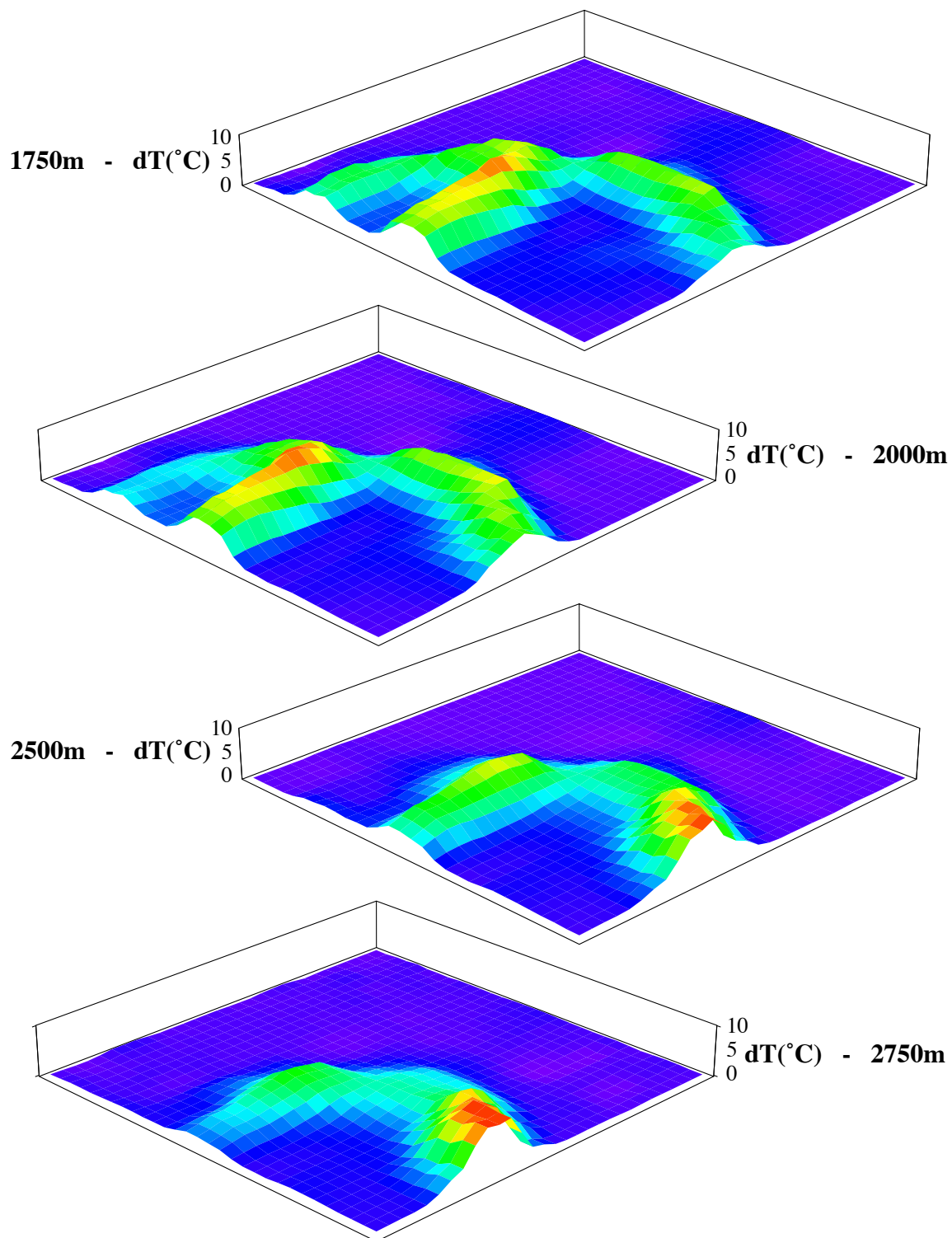


**Figure 4.16:** Anomalies produced by the fluid circulations in the fault after 5,000 years in the same case as Figures 4.15 and 4.13. Compare with Figure 4.9.